UNIVERSITÉ
YORK
UNIVERSITY

FACULTY OF GRADUATE STUDIES

I recommend that the dissertation prepared

under my supervision by

Henry Lee

entitled

The Environmental Impact of the Virgo Cluster
on the Evolution of Dwarf Irregular Galaxies

be accepted in partial fulfillment of the

requirements for the degree of

DOCTOR OF PHILOSOPHY

November 2001

M. McCall Supervisor

Recommendation concurred in by the following

Examining Committee

December 2001

Abstract

Dwarf galaxies are the greatest contributor to the total number of galaxies and most are believed to be systems consisting of matter in a near–primordial state. Containing H I gas and H II regions, dwarf irregular galaxies (dIs) can be used as test bodies to evaluate the impact of the environment on their evolution. Oxygen abundances relative to hydrogen within H II regions are a measure of how far the conversion of gas in the interstellar medium into stars has proceeded as a whole, as abundances do not vary significantly with galactocentric radius in dIs. Measurements of the [O III]λ4363 emission line from H II region spectroscopy provide accurate probes of the electron temperature from which oxygen abundances are directly computed.

The impact of the Virgo Cluster environment is investigated by comparing the properties of a set of Virgo dIs with those of a set of dIs in the field. In particular, two diagrams are used as diagnostics of evolution. The relationship between metallicity (as represented by the oxygen abundance) and galaxy luminosity is roughly indicative of the link between metallicity and mass. The relationship between oxygen abundance and the fraction of baryons in the form of gas can be used to evaluate the significance of gas flows during evolution.

To ensure accurate measures of luminosity and abundance, dIs in the field are chosen to have distance determinations from well–calibrated techniques and oxygen abundances derived from [O III]λ4363 measurements. Spectroscopic data are obtained for H II regions in 11 dIs distributed in the central and outer regions of the Virgo Cluster. To ensure that oxygen abundances are derived in a homogeneous manner, oxygen abundances for field and Virgo dIs are computed using an indirect bright–line method and compared with abundances directly obtained from [O III]λ4363, where available. They are found to agree to within about 0.2 dex with no systematic offset.

There is no systematic difference in oxygen abundance between field dIs and Virgo

dIs at a given luminosity, showing that there is no detectable difference in their stellar populations. Because there has been no significant fading or brightening of Virgo dIs with respect to field dwarfs and the metallicity–luminosity relation does not allow for any effects on the gas to be shown, this diagram is by itself insufficient to determine whether the environment has affected the evolution of dIs.

Oxygen abundances for field dIs are well correlated with the gas fraction in a way which shows definitively that evolution has been isolated, i.e., consistent with the "closed–box" model of chemical evolution. Four of the eleven Virgo dIs exhibit much lower gas fractions than field dIs at comparable oxygen abundances. Using field dIs as a reference, a gas–deficiency index, GDI, for dIs can be constructed, making it possible quantitatively to identify which objects have lost gas. There is no systematic difference in luminosity between gas–poor and gas–normal dIs at a given abundance.

For the gas–poor dI UGC 7636 (VCC 1249), the oxygen abundance of a newly discovered intergalactic H II region is combined with the optical luminosity of the dI and the gas mass of the adjacent H I cloud (STE1) to show that STE1 must have once been the interstellar medium of the dI. Tidal interactions of the dI with the elliptical NGC 4472 combined with ram–pressure stripping by the intracluster medium (ICM) best explain the observed properties of the detached cloud and the dI. That STE1 has remained intact and that there is no H I trail between the cloud and UGC 7636 suggest that the duration of the stripping event was short compared to the crossing timescale in the cluster.

A "staged" model is described to examine the chemical evolution of a gas–poor dI in the Virgo Cluster. Motivated by the observations, the model is characterized by three phases: isolated evolution, then sudden stripping which removes most of the gas, followed by a second stage of isolated evolution for the residual gas. The time since a typical stripping event is found to be approximately 1 Gyr or less. The GDIs for Virgo dIs correlate roughly with values of the projected X–ray surface brightness of the intracluster gas at the positions of the dIs. Thus, ram–pressure stripping best explains the observed gas–poor dIs in the Virgo sample. Together with the lack of significant fading, these observations suggest that dIs have recently encountered the ICM for the first time. A faded remnant of a gas–poor dI in Virgo will resemble a bright dE/dSph–like object like those presently seen in the cluster core.

Acknowledgments

"There is one thing even more vital to science than intelligent methods; and that is, the sincere desire to find out the truth, whatever it may be."
Charles Sanders Pierce

I am very grateful to Marshall McCall for his instruction, patience, encouragement, guidance, and financial support. Thanks also to Michael Richer for his help during observing runs at KPNO, CFHT, and OAN, for comments and advice on research, and for an introduction to the finer aspects of wine, cheese, and single–malts.

I would also like to thank specifically the following people at York University: Marlene Caplan for all of her masterful troubleshooting – I'm convinced (as others are, too) that no one survives a graduate degree without her help; Paul Delaney for a varying perspective – whose calm and patience showed me that any fire could be put out with grace, aplomb, and ease; Michael De Robertis for all things actively galactic (or anything that might even remotely lean to the right) – who always comes up with thought–provoking questions of all kinds; and Shanil Virani for continuing to ask pointed critical questions – whose ear towards music naturally extended into leading my own into the great number of gigs in the last few years. Others at York without whom I could not have survived my time include: Mel Blake, Robin Fingerhut, Houman Khosvarani, Curtis Krawchuk, Brigette Hesman, Jason Marshall, Gordon Mosher, Ryan Ransom, Chris Ryan, Ana Luisa Alfaro Suzán, Marcel Vandalfsen, and Peter White. For providing supplemental funding support at York, thanks are directed to the Faculty of Graduate Studies and the Graduate Student Association.

A special note of thanks go to Thuan Trinh for serving as the external examiner on my defense committee and for our discourse on the nature of dwarf galaxies.

Additional thanks are extended to: Bruno Binggeli for providing an updated electronic version of the Virgo Cluster Catalog; Stephane Charlot for clarifications to the GISSEL galaxy evolution code; Deidre Hunter for a copy of their Hα imaging; Stacy McGaugh for generously supplying his analytical formulation of the bright–line method; and Sabine Schindler for copies of ROSAT X–ray maps of the Virgo Cluster. Thanks also to Wayne Barkhouse, Elias Brinks, Patrick Durrell, Jay Gallagher, Brad Gibson, Eva Grebel, Buell Jannuzi, Martha Haynes, Robert Kennicutt, Stefanie Wachter, Dennis Zaritsky, and Konstanze Zwintz for their encouragement and helpful comments.

With research based mostly on observations, I am indebted to the following people. The staff at Kitt Peak National Observatory, in particular Jim DeVeny, is to be commended for their assistance with observations on the 4–metre telescope. Although we experienced a disproportionate amount of snow and ice at the summit, the staff at the Canada–France–Hawaii Telescope was extremely accommodating, especially in helping us to survive our own little transported piece of wintry Canada – which was distracting on its own, since we were able to look down from the summit towards the resorts around Kawaihae along the western side of the Big Island. Additional thanks go to the staff at Observatorio Astronómico Nacional in México for their assistance with imaging at the 2.1–metre telescope, and to the staff at the Cerro Tololo Inter–American Observatory in Chile for their assistance at the 1.5–metre telescope. Thanks also to Rodney Smith and many others at the University of Wales in Cardiff for their generosity during my short stay there, and to the Instituto de Astronomía at the Universidad Nacional Autónoma de México in México City, the Astronomy Dept. at the Universidad de Guanajuato, and the Dept. of Astronomy & Astrophysics at Pontificia Universidad Católica de Chile in Santiago for their invitations to give seminars about my research.

Finally, I'd like to send personal thanks to the following people: Naomi and René Bilodeau for their hospitality and the fact that "the year of hell" surpasses everything and leaves behind a sense and thread of shared experiences; Norm Rothery for providing an honest sense of the "big picture" on the other side of the gold coin; Lauren Jones for her encouragement and for telling me to persevere though the difficult times; Kristin von Czapiewski and Tommaso Gori, for helping to keep things

real and for their promise that it would be much better on the "other side;" Jeff and Lonni Lange, for remembering what this difficult journey entails; Steve and Lisa Wilcox, for always making me laugh and allowing me to feel like I was always home; and to my parents, my sister Shirley, and my brother–in–law Steve, all to whom I owe a tremendous debt for their support, patience, and for allowing me to go forward on this spectacularly crazy journey.

Finally ...

"Echa atrás la cara, hijo, y recibe las estrellas!"
"Cerro del Cielo" - Gabriela Mistral

"For everyone, as I think, must see that astronomy compels the soul to look upwards and leads us from this world to another."
"The Republic," Book VII, 1.529 - Plato

Looking up curiously into the Vancouver night sky as a wae lad, I realized in amazement that beyond the city lights were distant objects, seeing them as other stars similar in nature to our own Sun. I understood then what I wanted to do. It all seemed perfect in Chile that very first time, standing on top of Cerro Las Campanas at 2400 metres, alone with the (former UTSO) 60–cm telescope with just the wind for company, surrounded by the mountainous landscape in complete darkness, and the only illumination provided by the ceiling of stars in the Milky Way. A lifelong goal had finally been met in that singular moment.

Until now, I've been fortunate for the opportunity to have been a participant, which has only offered a tiny glimpse. From here, another journey awaits, pushing ever into the unknown, to fuel further answers to questions we haven't yet learned how to ask.

De una parte de espojos,	To one side, a sea of mirrors
de la otra serranía,	To the other mountain ranges,
y partiéndonos la noche	And cutting across the night
el tambor de la alegria.	The drum of happiness.[1]

"Panamanian Tamborito Dance" - Gabriela Mistral

[1] translation from "Selected Poems:" Translation by Langston Hughes (Bloomington-Indiana University Press, 1959)

Contents

Abstract iv

Acknowledgments vi

List of Tables xv

List of Figures xviii

1 Introduction 1

1.1 The Grand Picture 1

1.2 Dwarf Galaxies 5

1.2.1 dEs, dSphs, LLEs, and BCDs 7

1.2.2 Dwarf Irregular Galaxies 9

1.3 Physics of H II Regions 11

1.4 Metallicities 14

1.5 Physical Connections 15

1.5.1 Can Dwarfs Lose Mass? 20

1.6 The Environment of Galaxies 23

1.6.1 The Field 23

1.6.2 The Virgo Cluster 24

1.7 Thesis Outline 26

2 The Samples of Dwarf Irregular Galaxies 28

2.1 Dwarf Irregulars in the Field 29

2.1.1 Introduction 29

2.1.2 Distances 31

2.1.3 Oxygen Abundances 33
2.1.4 Individual Galaxies with New Spectra 34
2.2 Dwarf Irregulars in the Virgo Cluster 35
2.2.1 A General Description of the Virgo Cluster 35
2.2.2 Distance to the Virgo Cluster 37
2.2.3 The Spatial Distribution of Galaxies in the Cluster 37
2.2.4 Constituents of the Intracluster Medium in Virgo 40
2.3 The Nature of HI Deficiency in Virgo 43
2.3.1 Gas–Deficient Spiral Galaxies in Virgo 43
2.3.2 Gas–Deficient Dwarf Galaxies in Virgo 44
2.4 Studies of Virgo Dwarf Galaxies 46
2.5 The Sample of Dwarf Irregulars in Virgo 48
2.6 Individual Galaxies in the Virgo Sample 51
2.6.1 VCC 0512 51
2.6.2 VCC 0848 51
2.6.3 VCC 0888 52
2.6.4 VCC 1114 52
2.6.5 VCC 1179 52
2.6.6 VCC 1200 53
2.6.7 VCC 1249 53
2.6.8 VCC 1448 53
2.6.9 VCC 1554 54
2.6.10 VCC 1585 55
2.6.11 VCC 1789 56
2.6.12 VCC 2037 56

3 Observations & Reductions **57**
3.1 Observations of Field dIs 57
3.1.1 H II Regions in Holmberg II 58
3.1.2 H II Regions in IC 10 58
3.1.3 H II Regions in NGC 1560 60
3.1.4 H II Regions in NGC 3109 61
3.1.5 H II Regions in UGC 6456 61

3.1.6 Reductions 63
3.2 Observations of Virgo dIs 63
3.3 Optical Spectroscopy at Kitt Peak 65
3.3.1 Instrument Configuration 65
3.3.2 Image Acquisition 65
3.3.3 Reductions 70
3.3.4 Zero Corrections 70
3.3.5 Flat–Field Corrections 72
3.3.6 Geometric Corrections 72
3.3.7 Background Subtraction 73
3.3.8 Flux Calibration 73
3.3.9 Combining Frames 74
3.3.10 Aperture Extractions 76
3.3.11 Checks 77
3.4 Optical Spectroscopy at CFHT 77
3.4.1 Instrument Configuration and Image Acquisition 77
3.4.2 Reductions 83
3.5 Optical Spectra of Dwarf Galaxies 86
3.5.1 Spectra of Dwarf Irregulars in the Field 86
3.5.2 Spectra of Dwarf Irregulars in Virgo 86

4 Measurements and Analyses of Spectra 97
4.1 Measuring Line Fluxes 97
4.1.1 Underlying Balmer Absorption 99
4.2 Correcting Emission Line Data 102
4.3 Flux and Intensity Ratios: Field dIs 105
4.3.1 Holmberg II 106
4.3.2 IC 10 106
4.3.3 NGC 1560 109
4.3.4 NGC 3109 109
4.3.5 UGC 6456 114
4.3.6 DDO 187 114
4.4 Flux and Intensity Ratios: Virgo dIs 115

5 Deriving Nebular Abundances **121**
5.1 Direct ([O III]λ4363) Oxygen Abundances 121
5.2 The Bright–Line Method 124
5.2.1 The McGaugh Discriminant 128
5.2.2 Analytical Expressions 130
5.3 Abundance of Nitrogen Relative to Oxygen 136
5.4 Derived Properties for the Field dIs 137
5.4.1 Holmberg II 138
5.4.2 IC 10 138
5.4.3 NGC 1560 140
5.4.4 NGC 3109 140
5.4.5 UGC 6456 141
5.4.6 DDO 187 141
5.5 Derived Properties for the Virgo dIs 142

6 UGC 7636 Revealed: A Stripped dI in Virgo **146**
6.1 Recent Observations from the Literature 147
6.2 LR1 : A New Intergalactic H II Region 150
6.2.1 Heliocentric Velocity 152
6.2.2 Oxygen Abundance 154
6.3 Linking LR1 and STE1 with UGC 7636 155
6.4 Revealing the Stripping Process 160
6.4.1 Tidal Stripping 160
6.4.2 Ram–Pressure Stripping 161
6.4.3 Are Both Processes Required? 164

7 The Evolution of Dwarf Irregulars in Virgo **166**
7.1 Introduction 166
7.2 Derived Parameters 167
7.2.1 Absolute Magnitude, M_B, and Luminosity, L_B 167
7.2.2 Gas, Stellar, and Baryonic Masses 168
7.2.3 Gas–to–Light Ratio, M_{HI}/L_B and Gas Fraction, μ 169
7.3 Two–Component Method for Deriving M_*/L_B 170

7.3.1 Ingredients and Equations for M_* . . . 172
7.3.2 Colour and Surface Brightness of the Galactic Disk . . . 176
7.3.3 Effective Radius of the Galactic Disk . . . 179
7.3.4 Surface Brightnesses of the Young and Old Galactic Disk . . . 179
7.3.5 Colour of the Old Galactic Disk . . . 180
7.3.6 Luminosity of the Old Galactic Disk . . . 181
7.3.7 Mass–to–Light Ratio of the Old Galactic Disk . . . 182
7.3.8 The Variation of $(M_*/L_B)_{\rm old}$ with $L_{B,\rm old}$ . . . 183
7.3.9 A Final Equation For M_* . . . 183
7.3.10 Results . . . 184
7.3.11 Testing the Two–Component Method . . . 184
7.3.12 Comparison with the Bruzual & Charlot Code . . . 188
7.3.13 Variation of M_*/L_B with M_B . . . 190
7.4 Correlations . . . 192
7.4.1 Fitting Procedure . . . 192
7.4.2 (O/H) vs. M_B . . . 193
7.4.3 $B-V$ vs. M_B . . . 196
7.4.4 Effect of Star Formation on (O/H) vs. M_B Relation . . . 199
7.4.5 (O/H) vs. M_* . . . 200
7.4.6 (O/H) vs. $M_{\rm HI}/L_B$ . . . 203
7.4.7 $M_{\rm HI}/L_B$ vs. M_B . . . 203
7.4.8 (O/H) vs. $M_{\rm gas}$ . . . 206
7.4.9 $M_{\rm gas}$ vs. M_* . . . 208
7.4.10 (O/H) vs. $M_{\rm bary}$ . . . 208
7.5 Chemical Abundances and Gas Fractions . . . 212
7.5.1 The "Closed Box" Model of Chemical Evolution . . . 213
7.5.2 Gas–Deficiency Index (GDI) for dIs . . . 217
7.5.3 Sensitivity of μ to M_*/L_B, $(M_*/L_B)_{\rm old}$, and $(B-V)_{\rm old}$ . . . 219
7.5.4 N/O Measurements: Field and Virgo dIs . . . 222
7.6 The History of Virgo dIs . . . 227
7.6.1 The Staged Model of Chemical Evolution . . . 227
7.6.2 Staged Model for VCC 1249 (UGC 7636) . . . 234

7.6.3 Evolution of an Average Gas–Poor dI in Virgo 236
7.7 Gas–Poor Dwarfs and the Intracluster Medium 239
7.8 The Evolution of a Gas–Poor dI in Virgo 245
7.8.1 Fate of the Stripped Gas 247
7.8.2 Fading: The Fate of a Gas–Poor dI 249
7.9 Final Remarks 254
7.9.1 Distance Variations 254
7.9.2 Dispersion in M_*–μ Relationship 256

8 Conclusions **259**
8.1 Summary of Results 259
8.2 Future Projects 264

List of Tables

1.1 Comparison of dwarf and giant galaxies. 2
1.2 Basic properties of dwarf galaxies. 6
1.3 Distribution of galaxies in the field and in the Virgo Cluster. 23
2.1 Sample of dwarf irregular galaxies (dIs) in the field. 30
2.2 Revisions to distances for the sample of dIs in the field. 31
2.3 Revisions to oxygen abundances for the sample of dIs in the field. . . 33
2.4 Basic properties of the Virgo Cluster. 36
2.5 Observed properties for the sample of dIs in the Virgo Cluster. 50
3.1 Spectroscopy of field dwarfs acquired at Steward and SPM. 58
3.2 Instrument configurations at Steward and SPM. 59
3.3 Identification of H II regions in Holmberg II (Ho II). 59
3.4 Identification of H II regions in IC 10. 60
3.5 Identification of H II regions in NGC 1560. 61
3.6 Identification of H II regions in NGC 3109. 62
3.7 Identification of H II regions in UGC 6456. 62
3.8 Spectroscopy of Virgo dIs acquired at KPNO and CFHT. 64
3.9 Ritchey–Chrétien Spectrograph configuration at KPNO. 66
3.10 Multi–Object Spectrograph configuration at CFHT. 78
4.1 Equivalent widths at Hβ for H II regions in Virgo dIs. 101
4.2 Observed and corrected line ratios for Holmberg II. 107
4.3 Observed and corrected line ratios for IC 10 (SPM). 108
4.4 Reddening values for IC 10 (SPM). 108
4.5 Observed and corrected line ratios for IC 10 (Steward). 110
4.6 Observed and corrected line ratios for NGC 1560 (red spectra, Steward). 111
4.7 Reddening values for NGC 1560 (red spectra at Steward). 111

4.8 Observed and corrected line ratios for NGC 1560 (blue spectra). . . . 112
4.9 Observed and corrected line ratios for NGC 3109. 113
4.10 Observed and corrected line ratios for UGC 6456. 114
4.11 Line ratios for DDO 187. 115
4.12 Observed and corrected line ratios for H II regions in Virgo dIs (1). . 117
4.13 Observed and corrected line ratios for H II regions in Virgo dIs (2). . 118
4.14 Observed and corrected line ratios for H II regions in Virgo dIs (3). . 119
4.15 Observed and corrected line ratios for H II regions in Virgo dIs (4). . 120
5.1 Data for nitrogen and oxygen: Transition probabilities and collision strengths. 123
5.2 Derived properties for H II regions in field dIs. 139
5.3 Derived properties for the two H II regions in DDO 187. 141
5.4 Derived properties for H II regions in Virgo dIs (1). 143
5.5 Derived properties for H II regions in Virgo dIs (2). 144
5.6 Derived properties for H II regions in Virgo dIs (3). 145
5.7 Oxygen abundances adopted for each dI in the Virgo sample. 145
6.1 Basic data for UGC 7636, STE1, and LR1. 148
6.2 Observations of UGC 7636 from the literature. 149
6.3 Emission line data for LR1 (VCC 1249–1). 152
6.4 Derived properties for LR1 (VCC 1249–1). 153
6.5 Heliocentric velocities for five H II regions in VCC 1554. 154
7.1 List of observables and derived parameters. 167
7.2 Stars and gas in field and Virgo dIs. 185
7.3 M_B, $M_{B,\mathrm{old}}$, and their difference for field and Virgo dIs. 187
7.4 Properties of an average field and an average Virgo dI. 188
7.5 Models with constant star formation rate from synthesis code by Bruzual and Charlot (1996). 190
7.6 Properties of a test dI: two-component formalism versus Bruzual and Charlot (1996) code. 192
7.7 Gas–deficiency indices (GDIs) for field and Virgo dIs. 220
7.8 Effects of constant M_*/L_B, $(M_*/L_B)_{\mathrm{old}}$, and $(B-V)_{\mathrm{old}}$ on the fit to log(O/H) vs. log log$(1/\mu)$. 223

7.9 Staged evolutionary models for VCC 1249. 235
7.10 Staged evolutionary model for an average gas–poor dI in Virgo. . . . 239

List of Figures

1.1 Bivariate brightness distribution for galaxies. 16
2.1 Map of galaxies in the Virgo Cluster. 38
2.2 X–ray map of the Virgo Cluster. 41
2.3 Locations of sample dIs in the Virgo Cluster. 49
3.1 H II regions in VCC 0848 (A1223+06). 66
3.2 H II regions in VCC 0888 (8°26) and VCC 2037 (10°71). 67
3.3 H II regions in VCC 1179 (IC 3412) and VCC 1200 (IC 3416). 68
3.4 H II regions in VCC 1585 (DDO 136) and VCC 1789 (A1236+05). . . 69
3.5 Reductions flowchart for KPNO data. 71
3.6 Hα image of VCC 0512 from MOS at CFHT. 79
3.7 Hα image of VCC 1114 from MOS at CFHT. 80
3.8 Hα image of VCC 1249 from MOS at CFHT. 81
3.9 Hα image of VCC 1554 from MOS at CFHT. 82
3.10 Reductions flowchart for CFHT data. 84
3.11 Spectra of Holmberg II–9, IC 10–2, and NGC 1560–2. 87
3.12 Spectra of NGC 3109–3 and UGC 6456–2. 88
3.13 Spectra of VCC 0848–1 and VCC 1554–1. 89
3.14 VCC 0848–1: Blue region (3700 Å to 5500 Å) of spectrum. 90
3.15 VCC 0848–1: Red portion (5500 Å to 7300 Å) of spectrum. 91
3.16 VCC 1554–1: Blue portion (3700 Å to 5500 Å) of spectrum. 92
3.17 VCC 1554–1: Red portion (5500 Å to 7300 Å) of spectrum. 93
3.18 Spectra of VCC 0512–3, VCC 0888–1, and VCC 1114–1. 94
3.19 Spectra of VCC 1179–1, VCC 1200–1, and VCC 1249–1. 95
3.20 Spectra of VCC 1585–1, VCC 1789–1, and VCC 2037–1. 96

4.1 Line profile fits at Hβ, [O III]λ4959, and [O III]λ5007 for H II region VCC 1179–1. 100
4.2 Method to correct flux ratios for reddening. 103
5.1 Standard method to obtain nebular abundances from the spectra of H II regions. 122
5.2 Oxygen abundance vs. R_{23} for H II regions in field and Virgo dIs. . . 127
5.3 [N II]/[O II] versus R_{23} for H II regions in field and Virgo dIs. 131
5.4 [N II]/[O II] versus log(O/H) for H II regions in field and Virgo dIs. . 132
5.5 Direct ([O III]λ4363) oxygen abundances versus empirical abundances for H II regions in field and Virgo dIs. 135
5.6 Temperatures derived using the bright–line method. 137
6.1 log(O/H) versus M_B for field dIs and UGC 7636. 156
6.2 log(O/H) versus M_{HI}/L_B for field dIs and UGC 7636. 157
7.1 M_*/L_B vs. M_B for field and Virgo dIs. 191
7.2 log(O/H) versus M_B for field and Virgo dIs. 195
7.3 log(O/H) residuals versus M_B for field and Virgo dIs ($-15 \gtrsim M_B \gtrsim -17$). 197
7.4 $B-V$ versus M_B for field and Virgo dIs. 198
7.5 log(O/H) versus $M_{B,\mathrm{old}}$ (old disk) in field and Virgo dIs. 199
7.6 log(O/H) versus M_B and $M_{B,\mathrm{old}}$ for field dIs. 201
7.7 log(O/H) versus M_* for field and Virgo dIs. 202
7.8 log(O/H) versus M_{HI}/L_B for field and Virgo dIs. 204
7.9 M_{HI}/L_B versus M_B for field and Virgo dIs. 205
7.10 log(O/H) versus M_{gas} for field and Virgo dIs. 207
7.11 M_{gas} versus M_{star} for field and Virgo dIs. 209
7.12 log(O/H) versus M_{bary} for field and Virgo dIs. 210
7.13 Linear (O/H) versus log M_{bary} for field and Virgo dIs. 211
7.14 log(O/H) versus gas mass fraction for field and Virgo dIs. 216
7.15 Histograms of the gas deficiency index (GDI) for field and Virgo dIs. 221
7.16 log(N/O) versus log(O/H) for H II regions in field and Virgo dIs (1). 225
7.17 log(N/O) versus log(O/H) for dwarf galaxies (2). 226
7.18 log(O/H) versus gas fraction, μ: evolutionary models for VCC 1249 (UGC 7636). 229

7.19 log(O/H) versus M_* for VCC 1249 (UGC 7636). 230
7.20 log(O/H) versus gas fraction, μ: evolutionary models for an average gas-poor Virgo dI. 237
7.21 log(O/H) versus M_* for an average gas–poor Virgo dI. 238
7.22 Locations of gas–deficient dIs within the Virgo Cluster. 240
7.23 GDI versus relative velocity for Virgo dIs. 241
7.24 GDI versus X–ray surface brightness for Virgo dIs. 242
7.25 GDI versus ram–pressure for Virgo dIs. 244
7.26 r_0 versus M_B for gas–poor Virgo dwarfs. 252
7.27 $\mu_{\mathrm{eff},B}$ versus M_B for gas–poor Virgo dwarfs. 253
7.28 Suggested evolutionary path of a gas–poor dI in the Virgo Cluster. . . 255
7.29 log M_* versus log log $(1/\mu)$ for field and Virgo dIs. 258

Chapter 1

Introduction

1.1 The Grand Picture

Extragalactic astronomy as it pertains to the study of galaxies shares some analogies with the study of biological systems. A general understanding of biological systems and their properties begins with the study of the workings of the cell. Indeed, the picture is incomplete without knowing something about fundamental "units" (cells, proteins, complex molecules, etc.). In determining how animals are born, live and function, and eventually die, interactions with other animals and the effect of their surroundings play an important role. In an analogous fashion, insight on how galaxies trace the overall structure of the universe can be augmented by learning about the interaction of galaxies with each other and their environment.

A fundamental idea about how galaxies are created is one of "monolithic collapse" (e.g., Eggen et al. 1962), where a galaxy is formed from a sudden and large burst of stars and whose stellar population evolves passively over time; Burkert (1994) gives a modern treatment of this model for elliptical galaxies. A collapse model is in contrast with one of "galaxy assembly" over time. For example, Searle and Zinn (1978) suggested that independent fragments were captured and disrupted to form

the halo of the Milky Way galaxy over a time comparable to the age of the universe.

An accepted paradigm of large–scale structure in the universe is the hierarchical or "bottom–up" model (e.g., Peebles 1993; Bertschinger 1998; Longair 1998). In a typical cosmological model, galaxies are assumed to arise from local maxima in the background density field, which grow via a gravitational instability. While masses requiring large (e.g., $\sim 3\sigma$) fluctuations may be rare, smaller ($\sim 1\sigma$) and more common fluctuations would give rise to dwarf galaxies (Dekel and Silk 1986). These small concentrations of mass then grow by accretion or merging, eventually becoming giant disk and elliptical galaxies (e.g., Baugh et al. 1996). Other alternatives include the formation of ellipticals through the merging of spirals (e.g., James et al. 1999; Naab and Burkert 2001) and the transformation of spirals into spheroidal systems through interactions (Moore et al. 1996; Bekki et al. 2001).

Table 1.1 gives a comparison of the properties of dwarf and giant galaxies. A

Property	Dwarf Galaxies	Giant Galaxies
M_B (mag) [a]	-8 to -18	-18 to -21
μ_0^B (mag arcsec^{-2}) [b]	$\gtrsim 20$	$\lesssim 20$ [c]
L ($L_\odot$) [d]	$\sim 10^5$ to 10^9	$\sim 10^9$ to 10^{12}
M ($M_\odot$) [e]	$\sim 10^6$ to 10^9	$\sim 10^9$ to 10^{12}
r (kpc) [f]	$\lesssim 10$	$\gtrsim 10$
$v_{\rm rot}$ (km s^{-1}) [g]	$\lesssim 100$	$\gtrsim 100$
σ (km s^{-1}) [h]	$\approx$ 10–20	$\gtrsim 100$
[O/H] (dex) [i]	~ -1.5 to -0.5	~ -0.3 to $+0.3$

Table 1.1: Comparison of dwarf and giant galaxies. NOTES: [a] Absolute magnitude in B. [b] Central surface brightness in B. [c] Except giant low surface brightness galaxies (LSBGs, $\mu_0^B > 22$ mag arcsec^{-2}), which are physically large and massive. [d] Total luminosity. [e] Dynamical mass. [f] Characteristic size. [g] Neutral hydrogen rotational velocities for gas–rich disk–like systems. [h] Velocity dispersions of stars. [i] Average oxygen abundance by number relative to the Sun: [O/H] $\equiv$ log(O/H) $-$ log(O/H)$_\odot$, where log(O/H)$_\odot = -3.13$ (Grevesse et al. 1996).

general description of dwarf galaxies is deferred to the next section, while the giants

are briefly described here. Like the Milky Way galaxy, disk or spiral galaxies are flattened systems of stars, gas, and dust, supported by rotational motion. Most of these galaxies exhibit a pattern of spiral arms, which are delineated by star–forming regions. Supported by random motions, elliptical galaxies are large, smooth spheroidal systems of stars and contain very little gas and dust.

Through gravitational assembly, galaxies are collected into groups, clusters, and superclusters. Observations of spatial and velocity distributions of galaxies at ~ 100 Mpc scales (e.g., Bahcall 1997 for a recent review) appear to agree best with numerical simulations of hierarchical models. The largest structures observed are assumed to trace the underlying mass distribution in the universe.

The smallest units in the hierarchical model of structure formation are likely to be objects with properties closely resembling those of globular clusters and dwarf galaxies. In fact, dwarf galaxies are still merging with the Milky Way galaxy. The recent discovery of the Sagittarius dwarf galaxy (Ibata et al. 1994) and evidence for its tidal destruction and eventual consumption by the Milky Way point to the ongoing process of assembly (e.g., Johnston 1998; Helmi et al. 1999). A similar process may be happening in the Andromeda Galaxy (M 31; Ibata et al. 2001). Large galaxies may hide past merger episodes where smaller objects were consumed, so the observed properties of large galaxies today may reveal little about their "history of assemblage".

However, the problem of "overcooling" exists within hierarchical models. The models predict the formation of too many dwarfs, which would populate the faint end of the local galaxy luminosity function (see, e.g., Cole 1991; Cole et al. 1994 and references therein), but are not observed in the counts. Dwarf galaxies should also be seen in high–density regions and in low–density regions (Dekel and Silk 1986). However, Thuan et al. (1987) and Binggeli et al. (1990) showed that the spatial clustering of dwarf galaxies is similar to that of giant galaxies and that dwarfs also

tended to avoid voids. A way to bring the models into better agreement with observed counts is to have the formation of dwarfs delayed until $z \lesssim 1$, where the presence of a hot photoionized gas ejected by protogalaxies at earlier epochs into the intergalactic medium would suppress the number of dwarfs formed (Babul and Rees 1992; Babul and Ferguson 1996; Navarro and Steinmetz 1997; Ferguson and Babul 1998).

To study galaxy evolution, one attempts to connect the distant universe, which is young, to the local universe, which should contain the fossil records of galaxies in their youth. The following observations at distant epochs emphasize the importance of dwarf galaxies in the study of evolution. Excess counts of faint blue galaxies at $z \lesssim 1$ (Koo and Kron 1992; Ellis 1997) may in fact be the progenitors of dwarf galaxies observed in the nearby universe. Compact emission-line galaxies at $z \lesssim 1$ (Phillips et al. 1997; Guzman et al. 1997; Guzman et al. 1998) may be low mass, starbursting systems with physical properties similar to those of nearby dwarf galaxies. These data in addition to independent observations from the CFRS survey by Lilly et al. (1996) point to the fact that star formation activity peaked near $z \sim 1$. Observations at $1 < z < 3$ reveal distant galaxies with a range of physical sizes which exhibit irregular, multi-component structure (Williams et al. 1996; Ellis 1998). This implies that galaxy construction was well under way by these epochs. By redshifts $0 < z < 1$, the population of giant galaxies was in place and has not evolved significantly to the present day (Driver et al. 1995). However, the following issues remain unresolved: (1) why dwarfs and giants might both be involved in a "conspiracy" that both kinds of systems are vigorously forming stars near $z \simeq 1$, and (2) whether a majority of the descendants of distant blue objects have been observed or even recognized in the nearby universe.

A number of questions about dwarf galaxies arise. What are their properties? How do these galaxies evolve over time? Is the rate of recent star formation now

different from what has occurred in the past? Because of their relatively low masses and luminosities, is the evolution of dwarf galaxies inconsequential compared to that of giant galaxies? Have significant changes in galaxies occurred recently? Are these changes of short or long duration? Are galaxy properties affected by their surroundings or are galaxy properties set into place from birth ("nature versus nurture")? Or is the picture of galaxy evolution coloured by some mix of birth conditions and their surroundings?

Dwarf galaxies in the field provide clues to evolution in relative isolation. In this thesis, star–forming dwarf galaxies in the Virgo Cluster are studied and compared with field dwarfs to examine whether galaxy evolution has been affected by environment. The remainder of this chapter is organized as follows. An extended description of dwarf galaxies is presented in § 1.2. The different types of dwarf galaxies, and in particular, dwarf irregular galaxies, are described. The physics of H II regions and metallicities in dwarf galaxies are briefly discussed in § 1.3 and § 1.4, respectively. Arguments for and against an "evolutionary sequence" for dwarf galaxies are presented in § 1.5. A brief description of clusters of galaxies and the implications of how the living conditions within clusters can affect galaxy evolution are discussed in § 1.6. Finally, an outline of the entire thesis is presented in § 1.7.

1.2 Dwarf Galaxies

Dwarf galaxies are low mass, relatively low luminosity, intrinsically small, metal–poor[1] galaxies. They constitute the largest contribution to galaxies by number and type (e.g., Binggeli et al. 1985; Ferguson 1989a; Marzke and Costa 1997; Secker et al. 1997; Phillipps et al. 1998; Driver and Cross 2000). However, the total masses and

[1] A metal is any chemical element other than hydrogen and helium.

luminosities of all dwarf galaxies are several orders of magnitude smaller than giant galaxies (Table 1.1). Because dwarf galaxies are metal–poor, they represent systems which consist of matter in a near–primordial state. Although some dwarf galaxies are exceedingly faint, they may contain large amounts of dark matter. Recent reviews of dwarf galaxies include those by Grebel (1997, 1999, 2000, 2001), Kunth and Östlin (2000), Mateo (1998), and Tolstoy (2001).

There are five types of dwarf galaxies: dwarf elliptical galaxies (dEs) and dwarf spheroidal galaxies (dSphs), low–luminosity ellipticals (LLEs), blue compact dwarf galaxies (BCDs), and dwarf irregular galaxies (dIs). Henceforth, dSphs and dEs will be called "early–type" dwarfs, whereas dIs and BCDs will be called "late–type" dwarfs. Table 1.2 compares the basic properties of the various types of dwarf galaxies.

Property	dEs/dSphs	LLEs	BCDs	dIs
Examples	NGC 147 / Draco	M 32	I Zw 18	IC 1613
M_B (mag) [a]	$\gtrsim -17$	$\gtrsim -17$	$\gtrsim -18$	$\gtrsim -18$
μ_B (mag arcsec^{-2}) [b]	$\gtrsim 22$	$\gtrsim 21$	$\lesssim 22$	$\gtrsim 22$
$I(r)$ [c]	e^{-r}	$r^{1/4}$	e^{-r}	e^{-r}
I with increasing L [d]	brighter	fainter	brighter	brighter
$M_{\rm HI}$ ($M_\odot$) [e]	$\lesssim 10^8$	$\lesssim 10^8$	$\lesssim 10^9$	$\lesssim 10^9$
$M_{\rm tot}$ ($M_\odot$) [f]	$\lesssim 10^9$	$\lesssim 10^9$	$\lesssim 10^{10}$	$\lesssim 10^{10}$
H II regions?	no	no	central	many
Nucleation? [g]	yes	yes	yes	no

Table 1.2: Basic properties of dwarf galaxies: dwarf elliptical galaxies (dEs) and dwarf spheroidal galaxies (dSphs), low–luminosity ellipticals (LLEs), blue compact dwarf galaxies (BCDs), and dwarf irregular galaxies (dIs). NOTES: [a] Absolute magnitude in B. [b] Typical logarithmic surface brightness in B. [c] Radial dependence of linear surface brightness. [d] Behaviour of surface brightness with increasing luminosity (see Figure 1.1). [e] Mass of neutral hydrogen. [f] Dynamical mass. [g] Some dEs show nucleation, whereas dSphs generally do not have prominent nuclei. The range of properties are obtained from the reviews by Grebel (1999, 2000) and Mateo (1998).

It was once assumed that early–type dwarfs were systems containing only old stars, and that late–type dwarfs were systems of young stars (Hodge 1971). However, recent

observations have shown that all dwarf galaxies contain stars with a wide variety of ages, indicating that the most recent episode of star formation has occurred in the last few Gyr; see e.g., reviews by Grebel (1997, 1999) and Mateo (1998). The specifications for each morphological type of dwarf galaxy are not entirely rigorous, as definitions are loosely based upon their visual appearance, and not uniquely characterized by physical criteria (mass, age, star formation, etc.). Indeed, there are mixed–type or "transition" dwarfs (e.g., Antlia, LGS 3, Peg DIG, Phoenix), whose properties resemble those of both dIs and dEs/dSphs.

1.2.1 dEs, dSphs, LLEs, and BCDs

Dwarf ellipticals and dwarf spheroidal galaxies are very numerous in the nearby universe (Wirth and Gallagher 1984; Ferguson and Binggeli 1994; Gallagher and Wyse 1994). These galaxies are diffuse, and have low mass and low surface brightness. Indeed, dSphs are some of the faintest galaxies known. Their radial light distributions are disk–like and the surface brightness falls off as an exponential. Some dEs/dSphs exhibit bright central nuclei (e.g., NGC 205); nucleated dwarfs are especially apparent in the Virgo Cluster. The absence of H II regions[2] indicates that there are no signs of any current star formation. While most dEs/dSphs are very gas–poor, a few in the Local Group appear to contain modest amounts of neutral hydrogen (H I) gas (Blitz and Robishaw 2000). Most dEs/dSphs are typically located in the vicinity of giant galaxies. dEs/dSphs are not supported by rotation, but their velocity dispersions are so large that they appear to be strongly dominated by dark matter (Faber and Lin 1983; Lin and Faber 1983; Ashman 1992).

Low–luminosity ellipticals (LLEs; also compact ellipticals) are structurally similar

[2]Ionized hydrogen is often called H II to reflect the first and only ionization state of hydrogen. Clearly, neutral hydrogen is often referred as H I.

to giant elliptical galaxies (Bender et al. 1992). LLEs have smooth radial light distributions and the surface brightness follows the $r^{1/4}$–law of de Vaucouleurs (1948). As well, their luminosity–surface brightness distribution seems to be similar to the locus defined by giant ellipticals. Generally, LLEs are devoid of gas and H II regions, and consist mostly of old stars, though a few LLEs exhibit signs of having recently formed stars in the last Gyr.

The literature has been ambiguous and confusing about distinctions between dEs, dSphs, and LLEs. A number of authors (e.g., Ferguson and Binggeli 1994) use the "dE" class to represent any low–mass spheroidal–like galaxy. In this thesis, dEs/Sphs and LLEs are distinguished primarily by their structural properties (Binggeli et al. 1984; Kormendy 1985; Bender et al. 1992; Binggeli 1994). LLEs exhibit a trend of decreasing surface brightness with increasing luminosity, whereas dEs/dSphs show a trend of increasing surface brightness with increasing luminosity (see Figure 1.1 in § 1.5 below). The structural discontinuity between dEs/dSphs and LLEs suggests different histories of star formation for these two types of galaxies. Moreover, Gorgas et al. (1997) have shown from spectroscopic data that there are differences in the stellar populations between dEs/dSphs and ellipticals.

Blue compact dwarf galaxies are gas–rich galaxies which are primarily characterized by a high central surface brightness, stemming from the strong burst of star formation at the centre. Because of the bright central H II region, the visible appearance of a BCD is that of a galaxy with a nucleus. However, the surface brightness distributions of the underlying host galaxies are smooth and follow an exponential. Their H I distributions tend to be centrally concentrated (e.g., van Zee et al. 1998). Typically, BCDs are supported by rotation; however, highly disturbed kinematics are observed in the H I gas for some BCDs (e.g., van Zee et al. 1998). The spectroscopic properties of BCDs are similar to those of giant extragalactic H II regions (Searle and

Sargent 1972). I Zw 18 and SBS0335−052 are BCDs with oxygen abundances $1/50^{\text{th}}$ of solar and $1/40^{\text{th}}$ of solar, respectively, which makes them the most metal-poor dwarf galaxies known (see, e.g., Kunth and Östlin 2000 for references). Because of their relatively pristine chemical conditions, BCDs have been used as probes of the primordial helium abundance (see, e.g., Izotov et al. 1997; Izotov and Thuan 1999).

Terlevich et al. (1991) observed in the nearby universe a population of so-called "H II galaxies," which contain very bright and compact H II regions. Their properties and emission-line spectra are quite similar to those of BCDs. However, H II galaxies as a classification include large, luminous galaxies, which are not dwarfs.

1.2.2 Dwarf Irregular Galaxies

Dwarf irregular galaxies are gas-rich dwarf galaxies with an irregular optical appearance. Within them, H II regions are widespread. dIs also have an underlying population of old- and intermediate-aged stars. The spatial distribution of H I gas can be somewhat irregular or even "patchy" (e.g., Puche et al. 1992) and can extend much farther than the underlying distribution of stars. Studies of nearby dIs suggest that star formation rates have been slow but constant when averaged over the age of the universe (Gallagher et al. 1984; van Zee 2001). However, they are known to burst, and the present activity of star formation in dIs is sufficiently strong that their H II regions can be used to probe the level of chemical enrichment.

Rotational motions have been measured for some dIs (e.g., Hoffman et al. 1996). Lower mass dIs, however, may be dominated by random motions, although Côté et al. (1997) claim that dIs may be supported by rotation at luminosities as faint as $M_B \sim -13$. Rotation curves have shown that dIs are dominated by dark-matter (see, e.g., Ashman 1992). Because of their similar structural properties, a possible evolutionary link between BCDs, dIs, and dEs/dSphs is discussed below in § 1.5.

Recent reviews of dIs include those by Gallagher and Hunter (1984), Hunter and Gallagher (1986, 1989), and Hunter (1997).

The primary features which distinguish dIs from BCDs are the relative strengths of their respective starbursts, the spatial distribution of H II regions, and differences in their structural parameters. Combining optical and near–infrared imaging with burst models, Thuan (1985) found that starbursts in BCDs involved at least 10% of the galaxian mass. This was in contrast to the situation in dIs, where only a few per cent of the galaxian mass was involved in recent star formation. In dIs, H II regions are generally distributed over the entire galaxy. The contribution of light from young stars does not overwhelm the light from the underlying old stellar population. In BCDs, however, H II regions are typically found at the centre and the bursts of star formation are sufficiently strong that the underlying population may be hidden.

Patterson and Thuan (1996) studied surface brightness profiles of dIs and BCDs and derived structural parameters for their underlying stellar components. The central surface brightness of the underlying exponential component in dIs is similar to that of dEs, but about one to two magnitudes fainter than that of BCDs. The dIs are separated into two groups in a diagram of scale length versus luminosity. At a given luminosity, the scale length of the underlying component in dIs in the first group is comparable to that of dEs and about a factor of two larger than that of BCDs (see also Papaderos et al. 1996). The scale length of dIs in the second group is comparable to that of BCDs and about a factor of two smaller than that of dEs. Additional studies (Papaderos et al. 1996; Marlowe et al. 1997; Marlowe et al. 1999) have shown that the B–band luminosity of the central burst in BCDs is $\lesssim 1$ mag brighter than the underlying host galaxies and that the surface brightness of the underlying component in BCDs is brighter than that of dIs at a given luminosity[3].

[3]For the nearby BCD I Zw 18, the expected surface brightness of the underlying stellar population

To further understand the process of star formation, there are three important reasons why dIs offer advantages over spiral galaxies. First, dIs contain very little dust (e.g., Lisenfeld and Ferrara 1998). The paucity of dust allows for relatively unobstructed observations of conditions within dIs. Second, dIs do not exhibit spiral arms. The general lack of spiral arms in dIs suggests that the dynamical conditions relevant to star formation are less complicated than in spiral galaxies, although an appreciable fraction of dIs do exhibit bars (e.g., Sag DIG). Third, the abundance of heavy elements within dIs does not vary greatly with galactocentric radius (e.g., Pagel et al. 1978; Pagel et al. 1980; Devost et al. 1997; Kobulnicky and Skillman 1996, 1997). However, chemical abundances in spiral galaxies decrease with increasing galactocentric radii (e.g., McCall et al. 1985; Zaritsky et al. 1994). An abundance gradient for the Milky Way has been observed in H II regions (Shaver et al. 1983; Simpson et al. 1995; Afflerbach et al. 1996) and in stars (Smartt and Rolleston 1997). So, in contrast to spirals, a measurement of the oxygen abundance in any H II region of a dI can be presumed to represent the chemical state for the entire galaxy.

1.3 Physics of H II Regions

H II regions are clouds of ionized gas composed mostly of hydrogen and helium (Aller 1984; Osterbrock 1989). A cluster of young massive stars at the centre of each H II region is the cause of ionization, as they emit ultraviolet photons of sufficient energy to ionize hydrogen atoms. Owing to the prodigious rate of photoionization, the resulting state of ionization equilibrium is one where almost all hydrogen atoms are ionized. Radiative recombinations simultaneously act to create neutral atoms. The number of photoionizations is balanced by an equal number of recombinations.

is much fainter ($\mu_V \lesssim 28$ mag arcsec^{-2}) than the current burst of star formation (Legrand 2001). Stars older than $\sim$ 1 Gyr have been found from the HST archival data (Aloisi et al. 1999).

Upon recombination, hydrogen atoms can be formed in any excited level. However, recombinations directly to the ground state in turn produce additional ionizing photons which may be absorbed by neighbouring hydrogen atoms. The lifetimes of atoms created by recombinations to higher excited states are short because transitions between energy levels are fast. Consequently, the probability of ionizing a hydrogen atom in an excited state is very low.

Upon ionization of hydrogen, the liberated electrons carry kinetic energy and share the energy with other electrons by collisions. Energy is eventually transferred to protons and neutral atoms; the redistribution of energy to the other "colder" particles occurs very quickly. As a result, all of the particles in the gas have the same Maxwellian velocity distributions. The entire gas can be described by a single kinetic temperature or by the temperature of the electron gas T_e. However, the gas is not in local thermodynamic equilibrium. The mean intensity of the radiation field seen by the ions is much smaller than the Planck blackbody function appropriate for the kinetic temperature, because the photoionization source is very distant and geometric effects dilute the radiation field. Moreover, the ionization source cannot even be described by a single Planck function, because the central source consists of many stars.

Ultimately, each recombination converts the kinetic energy of the recombining electron into radiant energy which is lost by the gas. The gas is "cooled" and the radiant energy is observed as permitted lines (e.g., Balmer transitions). However, in a pure hydrogen nebula, the predicted gas temperature is much higher than what is generally observed in H II regions.

Metals, in particular, oxygen, are far more efficient as coolants of H II regions. By number, oxygen is the most abundant metal known (Grevesse et al. 1996). The

ionization potential for neutral oxygen (about 1 Ryd) is practically the same as hydrogen[4]; the ionization potential for singly–ionized oxygen is about 2.5 Ryd. Typically, the ionizing stars within H II regions emit sufficiently energetic photons to produce singly– and doubly–ionized oxygen. Although recombinations lead to very weak emission, the ions have several energy levels[5] close enough to the ground state to be readily excited by collision with free electrons. In fact, for ions, collisional excitation is strongly favoured than recombination.

Despite the fact that oxygen is vastly underabundant relative to hydrogen, the energies required to excite these ions to the upper levels are only of order kT_e and are accessible via collisional excitation. The excited levels arise from the same electronic configuration as the ground level. At the low densities typical of H II regions, collisional de–excitation is not important and the ions de–excite radiatively. Radiative transitions to lower levels are forbidden by selection rules for electric dipole radiation, but are allowed by magnetic–dipole or electric–quadrupole transitions. Ions spend very little time in an excited level and at any instant nearly all ions are present in the lowest energy level. Because the transition probabilities of forbidden lines are low, the probabilities of absorbing radiated photons are also low. Consequently, radiation from forbidden transitions escapes from the nebulae. The forbidden lines can be much brighter than the permitted lines and can dominate the optical spectrum[6]. So, the presence of oxygen significantly cools the gas.

A state of thermal equilibrium exists in H II regions when the rate of heating by photoionization balances the rate of cooling by recombination and by radiative de–excitations. To solve for the population of each energy level, the condition of

[4]1 Rydberg (13.6 eV) is the energy required to ionize a neutral hydrogen atom.

[5]Ions with electronic ground configurations p^2, p^3, or p^4 have five low–lying levels; in particular, N^+, Ne^{+2}, S^+, among others (Osterbrock 1989).

[6]The strongest optical radiative transitions, in particular [O III]$\lambda\lambda$4959, 5007 and Hα, give H II regions their distinctive green and red colours, respectively.

statistical equilibrium is applied: the population of each discrete level is constant with time. That is, the rate at which a level is populated from both collisional and radiative processes is equal to the rate of de–population by the inverse processes. Equilibrium equations for each of the low–lying levels can be solved for the relative population of each level. Consequently, the emissivity[7] of a collisionally excited line can be determined as a function of the electron density and the electron temperature. The abundance of metals can be derived once emissivities are known.

1.4 Metallicities

Metallicities, i.e., abundances of heavy elements relative to hydrogen, are a consequence of the history of star formation, and reveal how far the conversion of gas in the interstellar medium into stars has proceeded. Oxygen abundances are relatively easy to measure in dwarf galaxies containing H II regions. Emission–line spectra probe information about the physical conditions within H II regions and measure the most recent state of chemical enrichment of the ionized gas. The spectra are very distinct at optical wavelengths, being dominated by bright and narrow emission lines of hydrogen, oxygen, nitrogen, and sulphur; emission from other elements such as helium, argon, and neon may also be detected.

As the most abundant metal, oxygen is the regulator of physical conditions and, thus, the primary coolant within H II regions, especially within metal–poor dIs (see, e.g., Osterbrock 1989; Dinerstein 1990). At the low metallicities typical of dIs, the cooling is accomplished primarily through the optical emission lines of oxygen (see discussion in § 1.3 above). Singly–ionized [O II]λ3727 and doubly–ionized [O III]λ5007

[7]The emissivity is defined in terms of energy units per unit volume per unit time per unit solid angle per unit frequency.

lines[8] can have intensities up to five times brighter than that of Hβ. Because all key ionization stages are observed, oxygen abundances can be reliably determined.

A key emission line is [O III]λ4363, because the intensity ratio, $\{I([\text{O III}]\lambda4959) + I([\text{O III}]\lambda5007)\}/I([\text{O III}]\lambda4363)$, is a direct and accurate measure of the electron temperature, T_e, within H II regions. Knowing the electron temperature, the oxygen abundance can be obtained directly from the strong oxygen lines (Osterbrock 1989; see also Chapter 5). Typically, the uncertainty in the abundance[9] is about 0.1 dex (e.g., Pagel 1997). However, even with the best available spectra, the intensity of [O III]λ4363 relative to Hβ is a few per cent at most. Typically, [O III]λ4363 is only detectable in metal–poor dwarf galaxies with H II regions of high surface brightness. At higher metallicities, where H II region surface brightnesses can typically be low, indirect methods or empirical relations utilizing bright lines are employed (see § 5.2).

1.5 Physical Connections

Connections among the various types of dwarf galaxies have been sought, primarily using structural properties and initial ideas about their evolution (e.g., Binggeli 1994; Ferguson and Binggeli 1994; Richer and McCall 1995; Skillman and Bender 1995). Possible physical connections between dwarf types may be seen with the use of the well–known Kormendy diagram for galaxies, which is a plot of surface brightness against total luminosity (Kormendy 1985; also Binggeli 1994, Driver and Cross 2000). The bivariate brightness distribution for galaxies is shown in Figure 1.1. High– and low–luminosity ellipticals form a sequence whereby surface brightness increases with decreasing luminosity. Almost at right angles is the distribution of disk–like objects, including spirals, dIs, dEs, and dSphs, whose surface brightness decreases with

[8] Wavelengths are denoted in Ångstroms (Å).

[9] A logarithmic value of n dex is equivalent to a factor of 10^n.

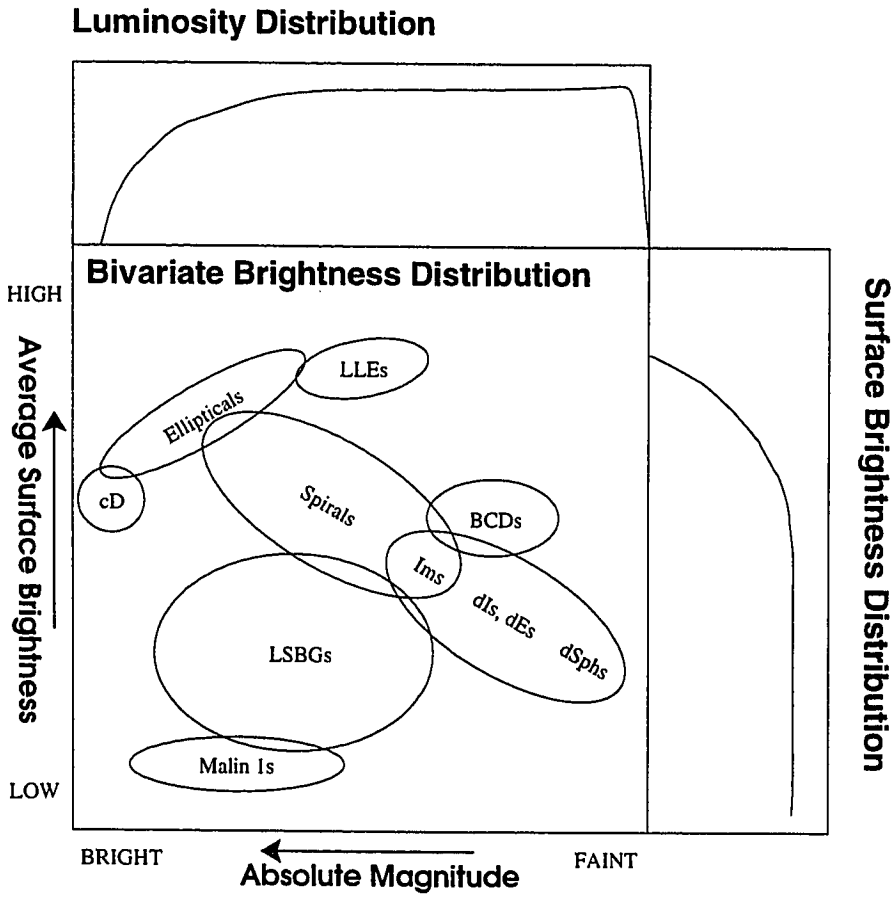

Figure 1.1: Bivariate brightness distribution for galaxies: average surface brightness is plotted against absolute magnitude. Arrows indicate directions of increasing surface brightness and luminosity. Regions of the bivariate brightness diagram are occupied by different types of galaxies: brightest cluster elliptical galaxies (cD), elliptical galaxies, low-luminosity ellipticals (LLEs), disk or spiral galaxies, low surface brightness galaxies (LSBGs, see e.g., Bothun et al. 1997; Impey and Bothun 1997), Malin 1-type galaxies (e.g., Bothun et al. 1987; Impey and Bothun 1989), blue compact dwarfs (BCDs), bright Magellanic irregulars (Ims), dwarf irregulars (dIs), dwarf ellipticals (dEs), and dwarf spheroidals (dSphs). Note that dwarf galaxies, with the exception of LLEs, appear to share the same phase space, which is almost at right angles to the phase space marked by high luminosity ellipticals. At the top and along the right are number distributions of galaxies as a function of absolute magnitude and surface brightness, respectively. Faint dwarf galaxies far outnumber other types of galaxies. This figure is based upon similar versions by Kormendy (1985), Binggeli (1994), and Driver and Cross (2000).

decreasing luminosity. BCDs have higher surface brightnesses than other dwarfs at similar luminosities. Number distributions of galaxies as functions of both luminosity and surface brightness show that faint dwarf galaxies dominate galaxy counts (e.g., Marzke and Costa 1997).

Figure 1.1 points to possible sequences for the evolution of dwarf galaxies. Because dIs, dEs, and dSphs all exhibit similar radial brightness profiles, an evolutionary connection between these three types of dwarfs might seem logical. Three basic scenarios have been examined.

1. Dwarf irregulars could fade to become dEs/dSphs, once the gas supply is exhausted either by star formation or by some other means (e.g., Faber and Lin 1983; Lin and Faber 1983; Dekel and Silk 1986).
2. Infall of gas onto dEs/dSphs could reignite star formation, turning them into BCDs, which subsequently fade into dIs or back into early–type dwarfs.
3. Sufficiently strong starbursts could transform dIs into BCDs with subsequent fading back into dIs and possibly into dEs/dSphs (Davies and Phillipps 1988, 1989).

On average, the surface brightness for bright dEs/dSphs is higher than dIs at the same luminosity, which rules out the fading of gas–poor dIs into dEs/dSphs (Bothun et al. 1986; Davies and Phillipps 1988). Also, dIs tend to have larger sizes than dEs/dSphs at a given luminosity. Although dIs cannot fade to become the population of relatively bright and compact dEs/dSphs observed today, the possibility that dIs may fade into large and faint dEs/dSphs cannot be excluded. It will be shown in Chapter 7 that successors to the current generation of gas–poor dIs in Virgo have not been found in the observed population of dEs/dSphs in the cluster.

Connections among dwarfs also can be elucidated from metallicities. Generally, nebular oxygen abundances are measured in gas–rich dwarfs with H II regions, whereas stellar iron abundances are measured in gas–poor dwarfs. Oxygen predominantly is created in Type II supernovae (Woosley and Weaver 1986; Wheeler et al. 1989). Iron, however, is produced in Type I and II supernovae, and its abundance is sensitive to the star formation history (Gilmore and Wyse 1991). Oxygen abundances measure the cumulative conversion of gas into stars and metals (see § 7.5), whereas the relative oxygen–to–iron abundance ratio[10], [O/Fe], conveys information about the rate at which gas is converted into stars.

Based on the presumption that [O/Fe] was the same for dEs as dIs, Skillman et al. (1989) concluded that dEs and dIs followed the same metallicity–luminosity relation. Richer and McCall (1995) and Richer et al. (1998) managed to measure oxygen abundances in dEs/dSphs directly using planetary nebulae. Contrary to the conclusions by Skillman et al., Richer et al. found that oxygen abundances were higher in dEs/dSphs than in dIs at similar luminosities, and showed that dEs/dSphs have higher [O/Fe] values than nearby dIs with similar oxygen abundances (see also Walsh et al. 1997). If dIs faded into dEs/dSphs, then dEs/dSphs would have higher oxygen abundances than dIs at the same luminosity, as is seen. However, [O/Fe] in dEs/dSphs would be like that in dIs at a comparable oxygen abundance, which is not the case.

If [O/Fe] is an indicator of the past star formation rate, then stars formed more rapidly in dEs/dSphs than in dIs. Indeed, van Zee (2001) has shown that past star formation activity within field dIs has been occurring at a slow, constant rate and that star formation has been evenly distributed within dIs. Thus, the rate at which energy is transferred into the interstellar medium may be regulating gas loss in dwarf

[10] $[O/Fe] = [\log(O/H) - \log(O/H)_\odot] - [\log(Fe/H) - \log(Fe/H)_\odot]$

galaxies.

Richer and McCall (1995) suggest that the more likely progenitor of a dE/dSph would be a BCD. At a given luminosity, the surface brightness of the underlying stellar component in BCDs is about 2 mag brighter than in dIs and the exponential scale length of the underlying component in BCDs is about a factor of two smaller than in dIs (Papaderos et al. 1996; Patterson and Thuan 1996; Terlevich et al. 1991; Meurer 1998; Marlowe et al. 1999). van Zee et al. (1998) have shown that the central mass concentrations of both stars and gas in BCDs are higher than in dIs. To transform BCDs into dIs, mass redistribution would be required. Patterson and Thuan (1996) have found that the $B-I$ colours of the underlying disks in dIs are redder than in BCDs, which suggests that the underlying component in dIs may either be older, more metal–rich, or both. However, the second possibility is ruled out, because oxygen abundances in dIs and BCDs are comparable at a given luminosity. Based upon their structural properties, there is not likely any connection between dIs and BCDs.

From their sample of BCDs in the field, Izotov and Thuan (1999) found that the average [O/Fe] for BCDs is $\simeq +0.4$ dex, which is comparable to nearby dEs/dSphs (Richer and McCall 1995; Walsh et al. 1997; Richer et al. 1998), but higher than dIs (Richer and McCall 1995). This suggests that the histories of star formation are similar for BCDs and dEs/dSphs (van Zee et al. 1997; Izotov and Thuan 1999). However, many BCDs appear to be rotationally supported (Côté et al. 1997; van Zee et al. 1998), while dEs/dSphs generally do not rotate. Transforming BCDs into dEs/dSphs would require that angular momentum is somehow dissipated in the process. BCDs are unlikely evolve to become objects resembling dEs/dSphs.

If the distinction between dIs and dEs/dSphs is traced back to an absence or presence of a strong star formation event early in their respective histories, photometry

of stars in nearby galaxies could in principle distinguish between them. However, the situation is complicated. While dEs/dSphs tend to have had discrete episodes of star formation in the past (as suggested by Marlowe et al. 1999), and dIs seem to have been forming stars at a slow, continuous rate (e.g., van Zee 2001), HST observations of resolved stellar populations in Local Group dwarfs have shown that no two dwarf galaxies share the same star formation histories, even within dwarfs of a given type (Tolstoy 2001). While there may be no evolutionary connection between early–type and late–type dwarfs, dwarf galaxies might instead have shared a common ancestor, which subsequently followed different paths of evolution. Environment seems to play to an important role in the Local Group (see Figure 3 in Grebel 1999), as most of the dEs/dSphs are found near spirals, whereas dIs are scattered and lie relatively undisturbed.

1.5.1 Can Dwarfs Lose Mass?

Many authors (e.g., Wyse and Silk 1985; Dekel and Silk 1986; Silk et al. 1987; Skillman and Bender 1995; Skillman 1997) have discussed models for the evolution of dwarf galaxies through gas loss. The basic idea is as follows. Massive stars are formed within star–forming H II regions. The rapid evolution of these stars eventually leads them to become Type II supernovae. Mechanical and thermal energy from these supernovae in addition to heavy metals are deposited into the interstellar medium. The continual build–up of thermal energy from multiple supernovae eventually raises the temperature to the virial temperature, and the gas is lost in a wind–like event.

The virial theorem is given by

$$\langle W \rangle + 2 \langle K \rangle = 0, \tag{1.1}$$

where $\langle K \rangle = \langle v^2 \rangle / 2$ and $\langle W \rangle = -GM/r$ are, respectively, the kinetic energy and

potential energy per unit mass, where the angle brackets represent averages in a steady state. $\langle v^2 \rangle$ describes the mean square velocity for the particles in the system, M is the total mass, r is the radius of the system, and G is the gravitational constant. Assuming that a spherical galaxy is in virial equilibrium, the average binding energy, $\langle E \rangle$, is

$$\langle E \rangle = \langle K \rangle + \langle W \rangle \tag{1.2}$$

$$= -\langle K \rangle = +\langle W \rangle / 2. \tag{1.3}$$

From the equality in Equation (1.3), the escape velocity, $v_{\rm esc}$, and the virial velocity, $v_{\rm vir}$, are given by

$$\langle v_{\rm esc}^2 \rangle = \frac{2GM}{r} \tag{1.4}$$

$$\langle v_{\rm vir}^2 \rangle = \frac{GM}{r}. \tag{1.5}$$

The effective gravity that dwarf galaxies exert on their contents is much less than that for giant galaxies. Assuming that an effective radius which encompasses half of the total light for the system is characteristic for the radius of a system, the ratio of the binding energy for a giant relative to a dwarf is

$$\frac{|E_g|}{|E_{\rm dw}|} = \frac{\langle v_{\rm vir,g}^2 \rangle}{\langle v_{\rm vir,dw}^2 \rangle} \tag{1.6}$$

$$= \frac{M_g / r_{\rm eff,g}}{M_{\rm dw} / r_{\rm eff,dw}} \tag{1.7}$$

$$= \frac{M_g}{M_{\rm dw}} \cdot \frac{r_{\rm eff,dw}}{r_{\rm eff,g}}$$

$$\approx 10 \text{ to } 1000. \tag{1.8}$$

So, dwarf galaxies should be more responsive to changes in internal energy and, therefore, should lose their contents more readily. In this scenario, supernovae–induced winds play an important role in regulating the flow of mass in dwarf galaxies and

are the driving force behind the supposed intrinsic evolution of gas–rich dwarfs into gas–poor dwarfs on short time scales.

Taking values for $M_{\rm tot}$ and $r_{\rm eff}$ from Mateo (1998) for Leo A and GR 8, which are two low–mass dIs ($M_{\rm tot} \simeq 10^7$ to 10^8 $M_\odot$), Equation (1.5) gives 16 km s^{-1} and 54 km s^{-1}, respectively, for the escape velocities. The velocity dispersions of the gas are about 9 km s^{-1} and 11 km s^{-1}, respectively (Mateo 1998). Thus, the gas is bound to these systems. Interestingly, a similar calculation for two nearby low–mass dEs/dSphs (Ursa Minor, Draco; $M_{\rm tot} \simeq 10^7$ $M_\odot$) shows that their escape velocities are comparable to the present–day velocity dispersions of their stars.

Low and Ferrara (1999) and Ferrara and Tolstoy (2000) have presented numerical models to examine whether dwarf galaxies are subject to mass loss. These models take into account the effect of dominant dark matter halos. Mass loss occurs only in very low–mass dwarf galaxies with $M_{\rm tot} \lesssim 10^6$ $M_\odot$.

Bubble–like structures on subkiloparsec and kiloparsec scales have been observed in dwarf galaxies (e.g., I Zw 18: Martin 1996; M 82: Strickland et al. 1997; NGC 1705: Meurer et al. 1998; NGC 4449: DellaCeca et al. 1997), which have likely arisen from energetic winds. However, even if the galaxy is experiencing a strong starburst, observations of NGC 1705 suggest it would take over a Hubble time to completely remove the interstellar medium (Meurer et al. 1998). Bothun et al. (1994) conducted ROSAT observations of five dwarf galaxies to search for X–ray haloes as evidence of supernovae–induced mass loss on galactic scales. No detections of haloes were seen. Upper limits to the halo luminosity were found to be much less than what would be expected, given the mass of stars formed. They concluded that either the ejection process was too weak, the outer halo was insufficiently massive to hold onto the ejected material, or that the ejection process cleared out all of the gas.

Skillman (1997) claimed that the situation for or against wind-dominated evolution in dwarf galaxies will remain unclear until more is learned about what happens to the metals which are ejected into the hot gas residing within galactic halos. However, in this thesis, it will be shown that dIs in the field have suffered little or no gas loss.

1.6 The Environment of Galaxies

While the spatial distribution of dwarfs is similar to that of giants (Thuan et al. 1987; Binggeli et al. 1990), the morphology of dwarf galaxies seems to be dependent upon their surroundings (Dressler 1980). In the field, dIs are distributed rather uniformly, whereas dEs/dSphs tend to cluster around giant galaxies. Furthermore, the number density of dIs is much higher than that of dEs/dSphs. Within clusters of galaxies, however, dEs/dSphs are predominant, tending to lie at or near the core, whereas dIs tend to lie in the outer regions where the galaxy number density is low. Table 1.3 shows the percentage of galaxy type in the field and in the nearby Virgo Cluster.

Type	Field [a]		Virgo Cluster [b]	
	N	%	N	%
Spirals	31	19	123	11
Es, S0s	3	2	71	6
dEs, dSphs	28	17	871	76
dIs, BCDs	102	62	87	7
ALL	164	100	1152	100

Table 1.3: Distribution of galaxies in the field and in the Virgo Cluster by number (N) and by percentage (%) of the total. NOTES: [a] Galaxies in the Local Volume with distances less than about 7 Mpc. [b] Adopted from Table 1 in Ferguson (1989a).

1.6.1 The Field

Field dIs are dwarf galaxies with few neighbours. Actually, field dIs are normally members of loose groups (e.g., IC 342/Maffei, Centaurus A, Sculptor) and there are

few truly "isolated" field dIs. However, the evolution of field dwarfs is not likely to be complicated by external effects, such as those found in clusters of galaxies, which are populated with thousands of galaxies and contain a significant mass of gas in the intracluster medium. So, dwarf irregulars in the field provide an excellent control sample against which a sample of cluster dwarf galaxies can be compared to evaluate environmental effects on galaxy evolution.

Nearby galaxies are easy to observe from the ground. Galaxy surveys ($z \lesssim 0.05$; e.g., Terlevich et al. 1991; Patterson and Thuan 1996; Pildis et al. 1997) show that dIs and BCDs are abundant in the field. In particular, within about 7 Mpc of the Milky Way galaxy, there are many dIs, a subset of which will be adopted in Chapter 2 as a "field sample."

Have all of the faintest galaxies been discovered in the very nearby universe? Despite intense efforts, this question remains unanswered (e.g., Driver and Cross 2000). Very faint and low surface brightness dwarf galaxies in close proximity can pose an observational problem. Stars in a low–luminosity dwarf galaxy lying in the background could appear similar to faint stars in the foreground within our own Milky Way galaxy. Extremely deep photometry is required to correctly separate stars in our own galaxy from stars in the target galaxy.

1.6.2 The Virgo Cluster

Interactions between galaxies and their environments may be important factors in galaxy evolution. An important venue to test the impact of environmental conditions is clusters of galaxies, where huge numbers of galaxies of various sizes, luminosities, and morphologies, as well as a large mass of gas are confined within a specific volume of space.

A cluster of galaxies is composed of thousands of galaxies and is one of the largest

gravitationally–bound objects in the universe, with a total gravitational mass of about 10^{14} to 10^{15} $M_{\odot}$ (e.g., Donahue 1998; Bahcall 1999). Recent studies have shown that clusters are still forming (Binggeli et al. 1987; Binggeli et al. 1993; Boselli et al. 1997). For rich clusters, a small fraction (up to 10 per cent) of the cluster mass is in the form of stars within galaxies, roughly 10 to 20% of the cluster mass is in the form of hot gas residing in the space between galaxies, while the remaining and dominant portion of the mass is dark (e.g., White et al. 1993). Elliptical galaxies containing old stars dominate the optical luminosity and lie at the core of most rich clusters. The hot intracluster gas is a strong emitter of X–rays with an equivalent temperature of 10^{7} to 10^{8} K; the gas is concentrated in the central regions (e.g., Sarazin 1988). Based upon the correlation of the intracluster gas mass with the optical luminosity of cluster ellipticals (Arnaud et al. 1992) and the fact that the metallicity of intracluster gas in clusters out to $z \sim 0.3$ remains relatively constant (Mushotzky and Loewenstein 1997), the predecessors of cluster ellipticals may have supplied most of the metals to the intracluster gas. However, it has been suggested as well that most of the intracluster gas mass may be primordial in origin (Gibson and Matteucci 1997).

Various kinds of processes may act on a cluster galaxy: tidal forces from galaxy–galaxy and galaxy–cluster interactions (Byrd and Valtonen 1990; Henriksen and Byrd 1996), ram–pressure effects due to the intracluster medium (Gunn and Gott 1972), high–speed encounters between galaxies (Moore et al. 1996), collisions and mergers (Barnes and Hernquist 1991), or some combination of the above. In all, the conditions in which galaxies reside are detrimental to the "health" of individual galaxies, especially dwarf galaxies, which should be far less able to retain their contents.

The Virgo Cluster is the nearest example of a cluster which is observable from the northern hemisphere. It is sufficiently rich that there is a core dominated by ellipticals and substantial quantities of intracluster gas. The "living conditions" of

dwarf galaxies within or passing through the central regions of the Virgo Cluster are sufficiently different from the field that galaxy properties are worth noting and comparing. If dwarf galaxies which began their lives in the periphery are "falling" into the centre, what effect does the environment have on them? Can the interstellar gas within galaxies be removed? How does the removal of the neutral gas affect subsequent evolution? Do environmental effects manifest themselves in diagnostics such as the metallicity versus galaxy luminosity diagram (see, e.g., Skillman et al. 1989; Richer and McCall 1995) or the metallicity versus gas fraction diagram (see, e.g., Larsen et al. 2001)? Answers to these questions are the objectives of the present work, which focuses on Virgo Cluster dIs.

1.7 Thesis Outline

Environmental effects on the chemical evolution of dwarf galaxies is examined by comparing the properties of dwarf galaxies in a cluster with those of dwarf galaxies in the field. For this thesis[11], dIs are chosen over BCDs, because the contribution of light from the underlying old stellar population can be separated from the contribution from young stars (see also § 1.2.2). A field sample of dIs is drawn from Richer and McCall (1995). It is updated with recent distances obtained from the literature, and with new spectroscopic data from unpublished observations and from the literature. Spectroscopic data are obtained for a sample of dIs, which are located in the core and the periphery of the Virgo Cluster. The derived oxygen abundances are combined with available data in the literature to examine the evolution of Virgo dIs and to evaluate the degree to which the cluster environment has affected their properties.

[11]Data was accessed as Guest User at the Canadian Astronomy Data Center, which is operated by the Dominion Astrophysical Observatory for the National Research Council of Canada's Herzberg Institute of Astrophysics.

The outline of the thesis is as follows. Chapter 2 describes the sample of dIs in the field and in the Virgo Cluster. Updates to distances and abundances for field dIs are obtained from the literature. For the Virgo Cluster, an overall description, the observed H I gas deficiency in spiral galaxies, and the adopted sample of dIs are presented. Chapter 3 describes the observations and reductions of unpublished spectroscopic data obtained at the Steward Observatory and the Mexican National Astronomical Observatory, and data acquired by the author for this thesis at the Kitt Peak National Observatory and the Canada–France-Hawaii–Telescope. Measurements from spectra for dIs in the field and Virgo samples are presented in Chapter 4. Methods by which flux ratios are corrected for underlying Balmer absorption and reddening are discussed. Observed flux ratios and corrected intensity ratios are listed. In Chapter 5, the derivation of oxygen abundances is presented. A description of the standard or direct method of deriving oxygen abundances in the presence of [O III]λ4363, the bright–line or empirical method in the absence of [O III]λ4363, and a comparison of empirical with direct abundances are presented. The derived properties for field and Virgo dIs are listed. Spectroscopic observations for the gas–poor Virgo dwarf irregular galaxy VCC 1249 are presented and their implications are described in Chapter 6. In Chapter 7, the importance of dwarf galaxies as probes of evolution is considered by utilizing the acquired spectroscopic data in various diagnostic diagrams. The discussion revolves around the context in which the data address quantitatively the impact of the Virgo Cluster environment on the properties and evolution of dwarf irregular galaxies. Finally, chapter 8 summarizes the results and perspectives for future work.

Chapter 2

The Samples of Dwarf Irregular Galaxies

This chapter presents the samples of dIs in the field and in the Virgo Cluster. The folllowing presents mostly an update of the field sample discussed by Richer and McCall (1995). The sample of field dIs is described in § 2.1. Using recent literature, distances and oxygen abundances for a number of these galaxies are updated and briefly described in § 2.1.2 and 2.1.3. Spectra for five field dIs were also obtained by M. McCall at Steward Observatory and San Pedro Mártir. These five dIs are briefly described in § 2.1.4. The addition of DDO 187 into the field sample is discussed.

A general description of the Virgo Cluster is presented in § 2.2. In § 2.3, the nature of gas–deficient spiral and dwarf galaxies in Virgo is discussed. Recent imaging and spectroscopic investigations of Virgo dwarf galaxies from the literature are summarized in § 2.4. Finally, the sample of Virgo dIs selected for the present study is listed and a brief description of each galaxy in the sample is discussed in § 2.5.

2.1 Dwarf Irregulars in the Field

2.1.1 Introduction

In the rush to observe the farthest reaches of the universe, the nearby universe should not be forgotten. The following quote by Erasmus (1510) emphasizes this point:

> "We fools have a particular trick of liking best whatever comes to us from farthest away."

The field sample as compiled by Richer and McCall (1995) is defined by two criteria: (1) oxygen abundances are determined directly from measurements of the [O III]λ4363 emission line (§ 1.4), and (2) distances are determined from stellar properties following the prescription in the appendix of Richer and McCall (1995). The sample includes dwarfs within the Local Group, whose distances are $\lesssim$ 1 Mpc. Table 2.1 lists the field sample of 22 dwarf irregular galaxies along with their basic properties. A new addition to the Richer and McCall (1995) sample is DDO 187, which satisfies the criteria stated above.

To establish the best possible parameters for the field sample, the literature was searched for measurements more recent than those compiled by Richer and McCall (1995). Direct oxygen abundances and well–determined distances were obtained from data given in papers describing emission–line spectroscopy and resolved galaxy photometry, respectively. Tables 2.2 and 2.3 summarize the field dwarf galaxies whose distances and oxygen abundances have been updated (as of June 2000), respectively. Of note also are updates to values of the H I 21–cm flux for GR 8, IC 1613, and Sextans B from Hoffman et al. (1996).

Name	M_B (mag)	$(m-M)^0$ (mag)	$(B-V)_T^0$ (mag)	F_{21} (Jy km s^{-1})	12+log(O/H) (dex)
(1)	(2)	(3)	(4)	(5)	(6)
DDO 187	−15.07	29.32	0.38	14.2	7.69 ± 0.09
GR 8	−12.19	26.83	0.31	8.6	7.63 ± 0.14
Holmberg II	−15.98	27.50	0.42	359.7	7.76 ± 0.13
IC 10 [a]	−15.85	24.47	0.69	950.4	8.20 ± 0.14
IC 1613	−14.53	24.38	0.67	698	7.71 ± 0.15
IC 2574	−17.06	27.86	0.35	442.5	8.09 ± 0.07
IC 4662	−15.84	27.32	0.35	125.2	8.09 ± 0.04
Leo A	−11.35	24.20	0.32	68.4	7.36 ± 0.06
LMC	−17.94	18.58	0.45	1.044×10^6	8.35 ± 0.06
NGC 55	−18.28	25.94	0.46	2679	8.34 ± 0.10
NGC 1560	−16.37	27.07	0.49	443	> 7.97
NGC 1569 [b]	−16.54	26.39	0.35	74	8.19 ± 0.06
NGC 2366	−16.28	27.76	0.54	297.0	7.91 ± 0.08
NGC 3109	−15.30	25.72	0.49	1876.7	7.74 ± 0.33
NGC 4214	−18.04	28.25	0.46	368.8	8.24 ± 0.12
NGC 5408	−15.81	27.76	0.49	59.20	8.01 ± 0.02
NGC 6822	−14.95	23.46	0.59	2367.1	8.25 ± 0.11
Sextans A	−14.04	25.84	0.38	208.8	7.55 ± 0.11
Sextans B	−14.02	25.67	0.51	102.4	8.12 ± 0.12
SMC	−16.56	19.06	0.59	8.99×10^5	8.03 ± 0.10
UGC 6456	−13.90	28.31	0.38	16.20	7.64 ± 0.13
WLM	−13.92	24.86	0.42	299.8	7.78 ± 0.16

Table 2.1: The sample of dIs in the field. Column (1) lists the name of the galaxy in alphabetical order, column (2) lists the absolute magnitude in B, column (3) lists the extinction–corrected distance modulus, column (4) lists the total dereddened $B-V$ colour, column (5) lists the integrated flux density at the 21–cm H I line, and column (6) lists the logarithm of the oxygen abundance by number. NOTES: [a] Its optical appearance shares similarities with blue compact dwarfs (Richer et al. 2001). [b] This is likely a post–starburst dwarf galaxy (Heckman et al. 1995; Greggio et al. 1998).

2.1.2 Distances

Resolved photometry of nearby galaxies was made commonplace with the launch of the Hubble Space Telescope. Distance measurements founded upon the observations of Cepheid variable stars (e.g., Madore and Freedman 1991) or the location of the tip of the red giant branch (e.g., Lee et al. 1993) are preferred. A large number of references in Table 2.2 reflect the wealth of data from space–based photometry.

Galaxy (1)	New/Update (2)	Method [a] (3)	Distance References (4)
DDO 187	New	Ceph	6
GR 8	Update	Ceph, TRGB	2, 18
Holmberg II	Update	Ceph	5
IC 10	Update	Ceph, TRGB	12, 15, 21
IC 1613	Update	TRGB	1
Leo A [b]	Update	Ceph, TRGB	4, 20
LMC	Update	SN87, TRGB	11, 16
NGC 2366	Update	Ceph	19
NGC 3109	Update	Ceph, TRGB	9, 10
NGC 6822	Update	Ceph, TGRB	3
UGC 6456	Update	TRGB	7, 17
Sextans A	Update	Ceph, TGRB	13
Sextans B	Update	Ceph, TRGB	14
WLM	Update	TGRB	8

Table 2.2: Revisions to distances for the sample of dIs in the field. Galaxies are listed in alphabetical order. Column (1) lists the galaxy name, column (2) indicates whether the galaxy is an addition or being updated, column (3) lists the method by which distances were obtained, and column (4) lists their references. REFERENCES : [1] Cole et al. 1999; [2] Dohm-Palmer et al. 1998; [3] Gallart et al. 1996; [4] Hoessel et al. 1994; [5] Hoessel et al. 1998a; [6] Hoessel et al. 1998b; [7] Lynds et al. 1998; [8] Minniti and Zijlstra 1997; [9] Minniti et al. 1999; [10] Musella et al. 1997; [11] Panagia 1999; [12] Saha et al. 1996; [13] Sakai et al. 1996; [14] Sakai et al. 1997; [15] Sakai et al. 1999; [16] Sakai et al. 2000; [17] Schulte-Ladbeck et al. 1998; [18] Tolstoy et al. 1995 (GR 8); [19] Tolstoy et al. 1995 (NGC 2366); [20] Tolstoy et al. 1998; [21] Wilson et al. 1996. NOTES: [a] Distance method: "Ceph" denotes Cepheid variables, "SN87" denotes the expanding ring of the supernova remnant SN1987A, and "TRGB" denotes the tip of the red giant branch. [b] For Leo A, Tolstoy et al. (1998) dispute the claim of detected Cepheids by Hoessel et al. (1994); the Tolstoy result is adopted here.

Cepheid stars are bright, pulsating, variable stars, whose periods of variability are correlated with their luminosities (Madore and Freedman 1991). Distances from

Cepheid variables depend upon the value of the distance modulus to the Large Magellanic Cloud (LMC). Panagia (1999) measured the expansion of the ring in the supernova remnant SN1987A and derived a distance modulus of 18.58 mag. This value of the distance modulus to the LMC is adopted for the remainder of this work. Distance determinations from Cepheids ("Ceph"; Table 2.2) are founded upon the Cepheid calibration by Madore and Freedman (1991), whose value of the distance modulus to the LMC was 18.50 mag. Values of distance moduli from Cepheids in the recent literature are corrected by +0.08 mag to account for the revised distance to the LMC.

Lee et al. (1993) showed that the absolute magnitude in I of the tip of the red giant branch (TRGB), M_I, is a constant, independent of metallicity and age, so long as the stars are relatively metal–poor and older than a few Gyr. Thus, measurements of M_I for resolved galaxies are good gauges of distance. To account for modest variations in colour and metallicity in each galaxy, absolute magnitudes in I of the TRGB are obtained following the prescription of Richer and McCall (1995). Distance moduli are derived from observed magnitudes in I, corrected for extinction. In spite of the dispute regarding the range in distance moduli to the LMC, it is wholly reassuring that the TRGB measurements by Sakai et al. (2000) are consistent with and independent of the SN1987A measurement by Panagia (1999).

For galaxies with more than one kind of observation, derived distance moduli are averaged. Generally, the errors in distance moduli obtained from either Cepheids or the TRGB are about 0.2 mag. For the remaining galaxies in Table 2.1 with no recent updates in the literature since 1995, distance moduli derived by Richer and McCall are corrected by +0.208 mag, because the old value for the distance modulus to the LMC used by Richer and McCall (1995) was 18.372 mag.

2.1.3 Oxygen Abundances

A number of authors have acquired emission-line spectra of H II regions in field dIs since Richer and McCall (1995) published their results. Oxygen abundances have been computed from these spectra using the published measurements of [O II]λ3727, [O III]λ4363, and [O III]$\lambda\lambda$4959, 5007 emission lines. These recent updates are listed in Table 2.3. In addition, spectroscopic data for five field dIs obtained by M. McCall at the Steward Observatory and at San Pedro Mártir are utilized.

Galaxy (1)	New/Update (2)	Abundance References (3)
DDO 187	New	10
Holmberg II	Update	7
IC 10	Update	7
IC 2574	Update	9
NGC 1560	Update	7
NGC 1569	Update	6
NGC 2366	Update	1, 4
NGC 3109	Update	7
NGC 4214	Update	5
NGC 6822	Update	8
UGC 6456	Update	3, 4, 7
WLM	Update	2

Table 2.3: Revisions to oxygen abundances for the sample of dIs in the field. Galaxies are listed in alphabetical order. Column (1) lists the galaxy name, column (2) indicates whether the galaxy is an addition or being updated, and column (3) gives the references to spectra. REFERENCES : [1] González-Delgado et al. 1994; [2] Hodge and Miller 1995; [3] Hunter and Hoffman 1999; [4] Izotov et al. 1997; [5] Kobulnicky and Skillman 1996; [6] Kobulnicky and Skillman 1997; [7] this work; [8] Miller 1996; [9] Miller and Hodge 1996; [10] van Zee et al. 1997.

A description of each of DDO 187 and the five field dIs observed at Steward and at San Pedro Mártir is presented in § 2.1.4. The spectroscopic data are presented in subsequent chapters. In § 3.1, the spectroscopic observations and reductions will be described, as well as the matching of extracted spectra with identified H II regions in the literature. Plots of the best spectra for each galaxy are illustrated in § 3.5. The

observed and corrected line ratios are listed in § 4.3. Derived properties for all H II region spectra in each galaxy are listed in Table 5.2 in § 5.4.

2.1.4 Individual Galaxies with New Spectra

Holmberg II

Located in the M 81 group of galaxies, Holmberg II (Ho II) is a gas–rich dwarf irregular galaxy[1] with many H II regions (Hodge et al. 1994). The positions of many of these H II regions coincide with the locations of H I "holes" (Puche et al. 1992), suggesting an association with winds from stars in the H II regions.

IC 10

IC 10 is a nearby late–type dwarf galaxy experiencing a strong burst of star formation. The H I gas exhibits complex kinematical structure (Shostak and Skillman 1989), which implies that the galaxy may still be in the stages of being assembled (Wilcots and Miller 1998).

NGC 1560

NGC 1560 is an edge–on late–type dwarf galaxy whose absolute B magnitude is comparable to the Small Magellanic Cloud. A number of bright H II regions were observed along the plane of the galaxy (unpublished Hα images, M. McCall). NGC 1560 is also known to be a member of the IC 342/Maffei group of galaxies (Buta and McCall 1999).

NGC 3109

NGC 3109 is an edge–on late–type dwarf galaxy whose absolute B magnitude is comparable to that of the Small Magellanic Cloud. The galaxy contains many H II

[1] Alternate names include UGC 4305 and DDO 50.

regions along the major axis (Richer and McCall 1992).

UGC 6456

UGC 6456 (VII Zw 403) is a late–type, gas–rich dwarf galaxy with bright H II regions. The galaxy is considered to be a member of the M 81 group of galaxies, although Lynds et al. (1998) have found that the galaxy may in fact be somewhat farther away.

DDO 187

DDO 187 (UGC 9128) is an isolated late–type, gas–rich dwarf galaxy. H II regions have been observed by Strobel et al. (1991), Hunter et al. (1993), and van Zee et al. (1997). A distance based on the measurement of two Cepheids has been determined by Hoessel et al. (1998b). van Zee et al. (1997) obtained spectroscopy for the two brightest H II regions; an [O III]λ4363 measurement and an oxygen abundance were determined for the brighter (DDO 187–1) of the two H II regions. Their reported fluxes were reanalyzed here in a manner similar to that for the other five field dIs for which new spectra were acquired.

2.2 Dwarf Irregulars in the Virgo Cluster

2.2.1 A General Description of the Virgo Cluster

Owing to its proximity ($\sim$ 15 Mpc), the Virgo Cluster is an important nearby laboratory to probe the influence of the cluster environment on galaxy evolution (see, e.g., Schmidt and Boller 1995). The Virgo Cluster is considered to be a key stepping stone for determining extragalactic distances (e.g., Graham et al. 1999; Kelson et al. 1997; Kelson et al. 2000). Observations of galaxies in the Virgo Cluster provide two advantages. First, galaxies in the cluster lie at comparable distances. Second, the

cluster is sufficiently close that ground–based imaging and spectroscopy of galaxy constituents are feasible.

As one of the nearest clusters of galaxies in the northern hemisphere, the Virgo Cluster contains over 1000 member galaxies (Reaves 1956; Reaves 1983; Binggeli et al. 1984; Sandage and Binggeli 1984; Binggeli et al. 1985; Binggeli et al. 1987; Binggeli et al. 1993). A compilation of galaxies is available in the form of the Virgo Cluster Catalog (VCC; Binggeli et al. 1985; Binggeli et al. 1993). Table 2.4 lists basic properties of the Virgo Cluster.

Property (1)	Value (2)	Reference (3)
$(m-M)$ [a]	31.12 mag [b]	5
D [c]	16.75 Mpc [b]	5
$\langle v_\odot \rangle$ [d]	1050 km s^{-1}	2
R_c [e]	1.7° (0.5 Mpc)	1
σ_{cl} [f]	760 km s^{-1}	1
ρ_{gal} [g]	$\sim$ 264 Mpc^{-3}	1
T_{ICM} [h]	$\simeq$ 2.4 keV	3, 4
L_X [i]	8.3 $\times$ 10^{43} ergs s^{-1}	3
n_{ICM} [j]	10^{-3} to 10^{-4} cm^{-3}	3, 6
M_{cl} [k]	$\simeq 2.5 \times 10^{14}\ M_\odot$	3, 7
M_{gal} [l]	$\simeq 9 \times 10^{12}\ M_\odot$	7
M_{gas} [m]	$\simeq 2 \times 10^{13}\ M_\odot$	7
M_{gas}/M_{cl} [n]	$\sim$ 0.08	...

Table 2.4: Basic properties of the Virgo Cluster. Columns (1) and (2) list the property and its value, respectively, and column (3) lists the references. REFERENCES: [1] Binggeli et al. 1987; [2] Binggeli et al. 1993; [3] Böhringer et al. 1994; [4] Edge and Stewart 1991; [5] Ferrarese et al. 1996; [6] Irwin and Sarazin 1996; [7] Schindler et al. 1999. NOTES: [a] Distance modulus. [b] The value stated by Ferrarese et al. (1996) is shifted upwards by 0.08 mag to account for the updated distance modulus for the LMC (see § 2.2.2). [c] Distance. [d] Average heliocentric velocity of the cluster. [e] Core radius of the cluster from King model fit to dE/dSph population. [f] Velocity dispersion of the entire cluster. [g] Number density of galaxies at the centre. [h] Temperature of the intracluster medium (ICM). [i] Total X–ray luminosity of the cluster (0.1–2.4 keV). [j] Particle number density of the ICM. [k] Estimated total mass of the cluster. [l] Estimated mass of galaxies in the cluster. [m] Estimated mass of gas in the cluster. [n] Fraction of total cluster mass in the form of gas.

2.2.2 Distance to the Virgo Cluster

Based upon measurements of Cepheids in the Virgo spiral galaxy M 100, the distance modulus to the Virgo Cluster is 31.04 mag (Ferrarese et al. 1996), assuming a distance modulus of 18.50 mag for the Large Magellanic Cloud (Madore and Freedman 1991). To account for the updated distance modulus of 18.58 mag for the Large Magellanic Cloud (Panagia 1999), the distance modulus to the Virgo Cluster is shifted upwards by 0.08 mag. Thus, a value of 31.12 mag is adopted, which corresponds to a distance of 16.75 Mpc.

2.2.3 The Spatial Distribution of Galaxies in the Cluster

The number density of galaxies in the Virgo Cluster is at least an order of magnitude higher than that found in the Local Group (Binggeli et al. 1985). A map of all catalogued galaxies in the cluster is shown in Figure 2.1. Each galaxy is represented by an open symbol, where the size of the symbol is proportional to the galaxy luminosity. The galaxies are clustered mainly in three groups: (1) the region near the centre, which is dominated by Messier 87, a supergiant elliptical galaxy; (2) to the south, a group dominated by the supergiant elliptical Messier 49, and (3) to the west, a group dominated by the elliptical galaxies Messier 84 and Messier 86.

The population of galaxies in the Virgo Cluster is overwhelmingly dominated by dwarf galaxies, in particular by dSphs (e.g., Table 1.3; Binggeli et al. 1985; Binggeli et al. 1987; Ferguson 1989a). There is strong morphological segregation: ellipticals, dEs, and dSphs are concentrated towards the core, whereas spirals, dIs, and BCDs are distributed towards the outer regions of the cluster (Binggeli et al. 1987). This agrees with the "morphology–density" relation found by Dressler (1980), which states that early–type galaxies lie in regions of higher density and late–type galaxies lie in

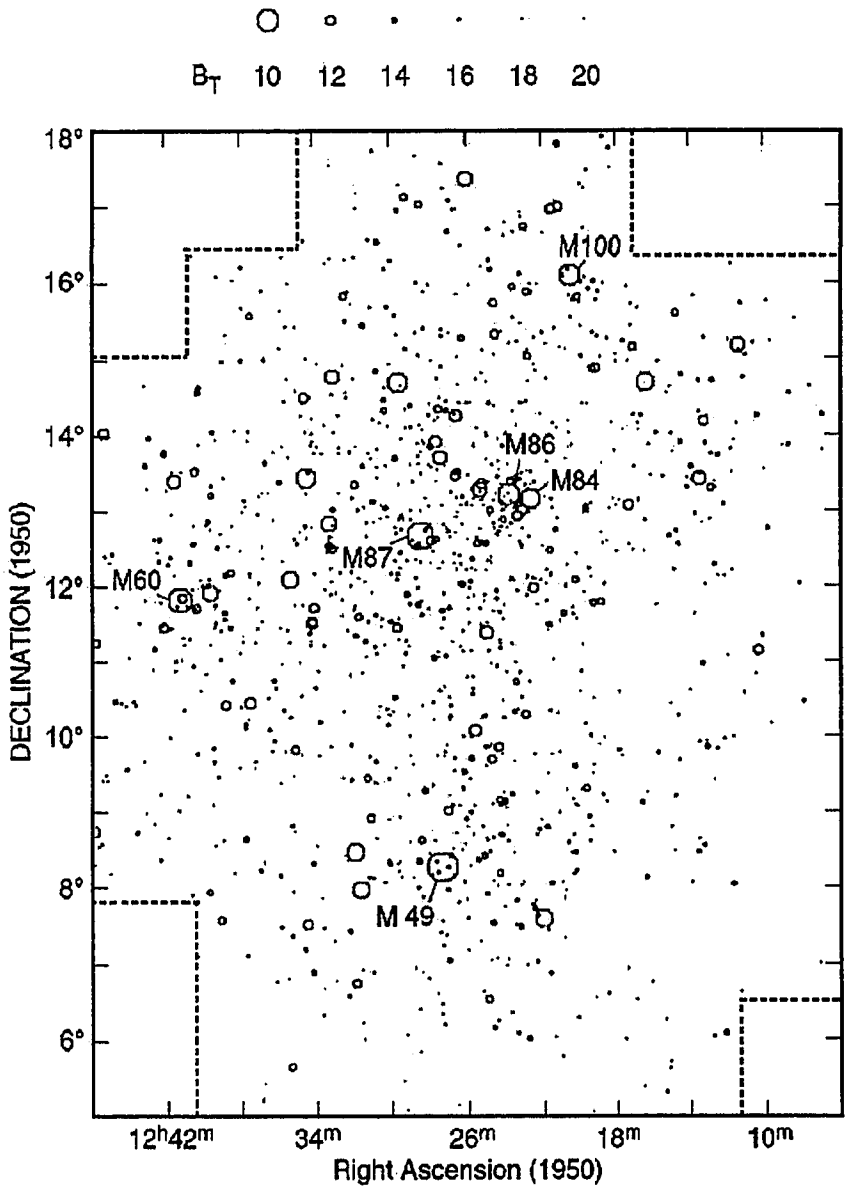

Figure 2.1: Map of galaxies in the Virgo Cluster (Epoch B1950): Declination (vertical axis) versus Right Ascension (horizontal axis). North is at the top and East is to the left. All objects in the Virgo Cluster Catalog (Binggeli et al. 1985) are indicated with open symbols, which are luminosity–weighted. A key at the top of the figure shows that the size of symbols is proportional to the apparent total blue magnitude. Six Messier galaxies (M 49, M 60, M 84, M 86, M 87, and M 100), all of whom are cluster members, are labeled. This figure is adapted from Binggeli et al. (1987) and Binggeli (2000).

regions of lower density.

Phillipps et al. (1998) undertook a deep survey of photographic plates of the Virgo Cluster acquired at the UK Schmidt Telescope. Their statistical analysis revealed an unusually large population of very faint dwarf galaxies (down to $M_B \simeq -10$) in the cluster. This suggests that there are far more faint dwarfs within a given luminosity interval in the Virgo Cluster than there are in the field (see also Driver and Cross 2000). However, it is unclear whether all of the faint dwarfs have been found in the nearby field.

Overall, the structure of the cluster is irregular and aspherical. Binggeli et al. (1987) and Gavazzi et al. (1999) have shown that the west group associated with M 84 and M 86 and the south group associated with M 49 are presently "falling" towards M 87. Although Gavazzi et al. (1999) claim that there is a ~ 1 magnitude discrepancy in distance modulus between the M 87 and M 49 groups, other authors have found otherwise. Here, a constant distance has been adopted for the entire cluster. The most significant conclusions of this thesis are not affected by distance variations.

An estimate of the crossing time for a typical galaxy in the Virgo Cluster can be computed from

$$t_{\rm cross} = \frac{2\langle \Delta r \rangle}{\pi \langle |\Delta v| \rangle}, \tag{2.1}$$

where $\langle \Delta r \rangle$ is the average projected radial distance from the centre of the cluster and $\langle |\Delta v| \rangle$ is the average radial velocity with respect to the cluster[2] (Côté et al. 1997). From the list of Virgo galaxies in Binggeli et al. (1993) and using a heliocentric velocity of 1050 km s^{-1}, one obtains $\langle \Delta r \rangle = 1.17$ Mpc, $\langle |\Delta v| \rangle = 599$ km s^{-1}, and $t_{\rm cross} = 1.2$ Gyr. The crossing time is about ten per cent of the Hubble time. Based

[2]A very rough estimate can be made from $t \simeq r/v$; the timescale is about 1 Gyr for $r \sim 1$ Mpc and $v \sim 1000$ km s^{-1}.

upon recent observations which support the existence of substructure and suggest that matter is continuing to fall into the centre of the cluster (Binggeli et al. 1987; Binggeli et al. 1993; Gavazzi et al. 1999), the Virgo Cluster is "young" to the extent that we are presently witnessing ongoing evolution.

2.2.4 Constituents of the Intracluster Medium in Virgo

The Virgo intracluster medium (ICM) consists mostly of X–ray emitting gas with old stars and planetary nebulae as additional minority constituents.

Hot gas permeating the intracluster medium is detected from X–ray emission, which is produced by free–free emission or thermal bremsstrahlung. The thermal temperature of the intracluster gas is about 3×10^7 K (Jones and Forman 1984; Giovanelli and Haynes 1985; Edge and Stewart 1991; Böhringer et al. 1994; Schindler et al. 1999). The gas is assumed to have originated from material ejected from stellar winds and supernovae from within elliptical galaxies and primordial material which never collapsed in the process of galaxy formation. The gas contains large random motions and collides with other intracluster gas, converting kinetic energy into heat. The only efficient cooling mechanism for the gas is thermal bremsstrahlung, because the particle density in the gas is low and the temperature is very high. For conditions found within clusters, the cooling timescale exceeds the age of the universe (Bothun 1982). This implies that clusters will remain immersed in hot gaseous baths for most of their lifetimes.

An X–ray map of the Virgo Cluster from the ROSAT All–Sky–Survey[3] is shown in Figure 2.2. The strongest concentration of X–ray emitting intracluster gas is located near the positions of M 87 and M 86. There also appears to be spurs of hot gas

[3]The X–ray map of the Virgo and other clusters may also be retrieved from the ROSAT image gallery at `http://www.xray.mpe.mpg.de/rosat/images/index`.

surrounding M 49 to the south and M 60 to the east. Aside from the "hot spots" near the centre of the cluster, the distribution of intracluster gas on the whole is rather irregular. Schindler et al. (1999) compared the spatial distributions of galaxies and the intracluster gas and found that both galaxies and gas are distributed similarly throughout the cluster. In particular, peaks in the spatial density of both galaxies and intracluster gas are found near the position of M 87.

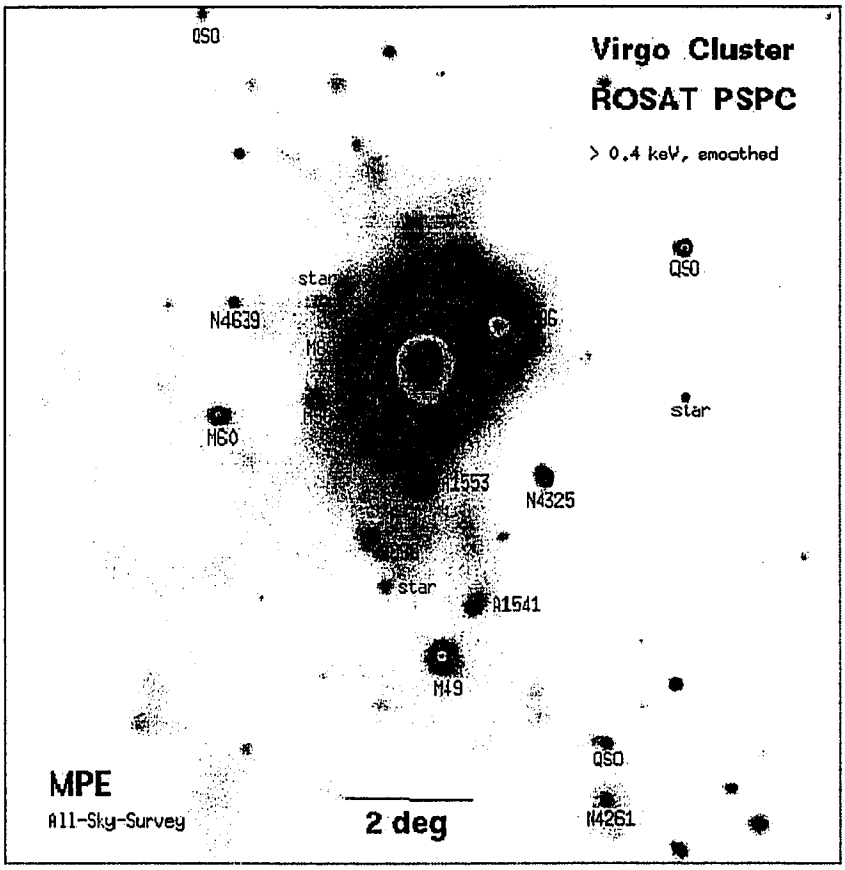

Figure 2.2: X–ray map of the Virgo Cluster from the ROSAT All–Sky– Survey. North is at the top and East is to the left. The extended X–ray emission comes from the hot intracluster gas distributed throughout the cluster. The large, dark spot is centred near the position of the giant elliptical M 87. A bright X–ray halo also surrounds M 86 to the west; halos of lesser degree surround M 60 to the east and M 49 to the south. Also indicated are foreground stars, Abell clusters (A1541, A1553) and quasars ("QSO") in the background, and Virgo Cluster member galaxies with NGC and Messier catalog designations. The image scale is roughly similar to the map of Virgo galaxies in Figure 2.1. This figure is adapted from Figure 5 in Binggeli (2000) and Figure 1 in Böhringer et al. (1994).

The fraction of total mass in the form of hot gas in the cluster is about seven to eight per cent (Table 2.4), which is consistent with the results found for weak X–ray clusters (e.g., Arnaud and Evrard 1999; Bahcall 1999). López-Cruz et al. (1997) have suggested that the intracluster medium was generated early in the history of the cluster through the tidal disruption of dwarfs. However, there is some doubt as to whether dwarf galaxies could have supplied the required amount of metals to explain the observed enrichment within the intracluster medium (e.g., Gibson and Matteucci 1997). The mass of metals (in particular, iron) in the intracluster medium is found to correlate with the luminosity of giant early–type galaxies in clusters (Arnaud et al. 1992; Jones and Forman 1992; Okazaki et al. 1993). This suggests that the chemical enrichment of the intracluster gas is caused mostly by material removed from elliptical galaxies. The metallicity of the gas is about one–third of solar, which points to stellar winds (as opposed to supernovae) as the primary origin for the gas enrichment. However, the mass of the lost material falls well short of what is required to account for the total gas mass, which suggests that the dominant portion of the intracluster gas is primordial in origin.

Measurements of the intracluster light in the Virgo Cluster have revealed a population of intergalactic red giant branch stars (Ferguson et al. 1998) and intracluster planetary nebulae (Méndez et al. 1997; Ciardullo et al. 1998; Feldmeier et al. 1998). These objects are likely to have been tidally stripped from galaxies during close encounters as the cluster was being formed. Intracluster stars are unlikely to have formed within the intracluster medium, because the cooling timescale far exceeds a Hubble time (see Table 2.4). Intracluster stars may contribute a significant fraction ($\sim$ 10–20%) of the stellar light and stellar mass of the cluster.

2.3 The Nature of HI Deficiency in Virgo

2.3.1 Gas–Deficient Spiral Galaxies in Virgo

Tully and Shaya (1984) and Binggeli et al. (1987) claimed that spirals and dIs observed today in the Virgo Cluster have likely fallen into the cluster on timescales much smaller than a Hubble time. This is borne out by the fact that late–type galaxies in Virgo exhibit a larger velocity dispersion than early–type galaxies (Binggeli et al. 1987; Conselice et al. 2001). Because they fall into the cluster at relatively high speeds, gas–rich galaxies ought to feel the effects of their surroundings. If so, there should be some kind of spatial segregation of gas–poor and gas–rich galaxies.

A variety of H I imaging studies (Haynes and Giovanelli 1986; Warmels 1988; Haynes 1989; Cayatte et al. 1994; Solanes et al. 2001) have shown that Virgo spiral galaxies are deficient in H I gas relative to spiral galaxies in the field. From a limited sample of Virgo spiral galaxies, Shields et al. (1991) and Skillman et al. (1996) found that (1) H I-deficient spirals residing in the central regions of the Virgo Cluster show on average higher chemical enrichment than field spiral galaxies of the same morphological type, and (2) that chemical abundances of spirals in the periphery of the cluster are indistinguishable from field spirals. This effect was attributed to less infall of metal–poor gas into centrally located spirals. That is, if H I gas is being removed from the outer regions of spirals as they travel through the core of the cluster, less metal–poor gas flows into the inner regions of spirals, allowing their oxygen abundances to grow more rapidly with time. A similar effect for two additional Virgo spirals was observed by Henry et al. (1992, 1994). Also, Koopmann and Kenney (1998) determined that early–type Virgo spirals exhibit reduced star formation rates compared to isolated spirals of similar type, suggesting that gas from Virgo spirals is being removed.

In their study of spiral galaxies in 18 clusters including Virgo, Solanes et al. (2001) determined that depletion of H I gas is related to galaxy morphology, and not to the optical size of the galaxy. Inside a projected radius of about 4 Mpc from the centre of the Virgo Cluster, early–type and very late–type disk galaxies show the strongest H I deficiency. As the spatial distributions of the gas–deficient spirals and the intracluster gas in the Virgo Cluster are found to be similar, Solanes et al. (2001) suggest that interactions with the intracluster gas have likely acted in recent times to remove the H I.

It is useful to examine three spiral galaxies in the Virgo Cluster to highlight the effects of stripping. NGC 4388 (VCC 0836), one of the most H I–deficient spirals in Virgo, is located close in projection to the centre of the cluster, and is travelling at a high speed relative to the cluster. Veilleux et al. (1999) obtained Fabry–Perot interferometric maps to provide kinematic details of the ionized gas within the galaxy. Their observations showed a complex interaction of the interstellar material with the surrounding intracluster gas. NGC 4438 (VCC 1043), located close in projection to M 87, shows an unusual visual appearance and an observed displacement of H I with respect to the stellar disk (Kotanyi et al. 1983). Finally, NGC 4522 (VCC 1522), which shows a stellar disk that is relatively undisturbed, has a truncated pattern of Hα emission above the disk plane, which is reminescent of a "bow–shock" (Kenney and Koopmann 1999). The appearance of extraplanar H II regions is interpreted as a consequence of star–formation occurring within the displaced gaseous material.

2.3.2 Gas–Deficient Dwarf Galaxies in Virgo

Dwarf galaxies in Virgo should exhibit a greater degree of gas deficiency, owing to their smaller gravitational potentials (see Equation 1.8). Hoffman et al. (1987) showed that Virgo dIs within a circle about 5° of the cluster centre are deficient in H I by

roughly a factor of two compared to dIs outside this circle. However, an additional and somewhat unexpected result was that although some dwarfs seemed to have lost gas, the degree to which dIs are deficient in H I is not more severe than for spirals (Hoffman et al. 1988). It should be noted that the quantity Hoffman et al. used to describe gas deficiency in dIs is based upon the "DEF" parameter given by

$$\mathrm{DEF} = \log M_{\mathrm{HI,exp}}(D_{\mathrm{opt}}, T) - \log M_{\mathrm{HI}}(D_{\mathrm{opt}}, T), \tag{2.2}$$

where the HI mass, M_{HI}, for a given morphological type, T, is computed within an optical diameter, D_{opt}, typically in B (Haynes and Giovanelli 1984; Giovanelli and Haynes 1985)[4]. The expected value, $M_{\mathrm{HI,exp}}$, was based upon an average for a mixture of gas–normal late–type *spirals* and dwarfs, and not based solely upon an average for gas–normal late–type dIs. Owing to its sensitivity to the star formation rate, the optical diameter in B could be zero if the surface brightness is never brighter than 25 mag arcsec^{-2}, which does not make for a useful indicator of mass in dwarfs. Moreover, the gas–poor dwarfs studied by Hoffman et al. (1988) in the Virgo Cluster were not compared with a sample of gas–normal dIs in the field.

It is useful to highlight three Virgo dwarf galaxies. Vigroux et al. (1986) showed that the extremely gas–poor dI VCC 1448 near the centre of the Virgo Cluster has optical properties similar to other dIs, except that it has an unusually large optical size and has almost no H I. A dust trail discovered inside the optical halo of the Virgo elliptical galaxy M 86 (Elmegreen et al. 2000) is believed to be stripped material from the nucleated dE galaxy VCC 0882. The ratio of the gas mass in the trail to the blue luminosity of the dwarf galaxy is comparable to a typical gas mass–to–luminosity ratio of roughly unity for dIs. Finally, VCC 1249 is a gas–poor dwarf galaxy which happens to have an H I cloud in its proximity (Sancisi et al. 1987). Various authors

[4]A gas–deficient galaxy would therefore have DEF > 0.

have attempted to link the H I cloud to the galaxy (e.g., Patterson and Thuan 1992; Henning et al. 1993; McNamara et al. 1994). Chapter 6 will present spectroscopic observations and a more extensive discussion which proves the connection.

2.4 Studies of Virgo Dwarf Galaxies

A brief review of recent work on Virgo dIs is given here. Bothun et al. (1985), Skillman et al. (1987), and Hoffman et al. (1987, 1989, 1996, 1999) have mapped many dIs and BCDs in H I. Much effort has been devoted to the study of dSphs, dEs, and BCDs in the Virgo Cluster at optical wavelengths (Drinkwater and Hardy 1991; Drinkwater et al. 1996; Durrell 1997; Phillipps et al. 1998; O'Neil et al. 1999). Some imaging studies of Virgo dIs at optical and near–infrared wavelengths have been carried out by Thuan (1985), Bothun et al. (1986), Gallagher and Hunter (1986), Impey et al. (1988), James (1991, 1994), and Boselli et al. (1997). Star formation in Virgo dwarf galaxies has been studied by Almoznino and Brosch (1998a), Almoznino and Brosch (1998b), Brosch et al. (1998), and Heller et al. (1999) via Hα imaging.

A few comments can be made about possible evolutionary links between dIs and dEs/dSphs in Virgo. Based upon a comparison of structural properties (Bothun et al. 1986; Drinkwater and Hardy 1991), it is generally believed that the dE/dSph population in Virgo as a whole could not have come from stripped dIs, although the possibility of a few stripped dIs evolving to become faint dEs/dSphs is not excluded. With near–infrared imaging, James (1994) found that dIs, BCDs, and dEs/dSphs are all structurally different, and concluded that the different types of dwarfs are not connected to each other in an evolutionary sense. Drinkwater et al. (1996) determined that the underlying stellar populations in BCDs have arisen from continuous star formation, as opposed to a burst–like mode which has been hypothesized for dEs/dSphs.

Thus, in Virgo, there is no clear evidence that late–type dwarfs are anything like the progenitors of early–type dwarfs.

Optical emission–line spectra of H II regions in Virgo Cluster late–type dwarfs have been presented by Gallagher and Hunter (1989), Izotov and Guseva (1990), and Vílchez (1995). In all, a total of 36 late–type dwarfs have been observed. Unfortunately, most of the galaxies in the samples of Gallagher and Hunter (1989) and Izotov and Guseva (1990) are BCDs, and not dIs. A comparison with dIs in the field requires a larger set of Virgo dIs. Another problem is that the temperature–dependent [O III]λ4363 emission–line was not detected for any of the 36 dwarfs, which means that none of the oxygen abundances could be obtained directly. Even empirical abundances could not be reliably determined, because the bright–line indicator, R_{23} (see § 5.2), is double–valued, and because the data do not allow for any discrimination between lower and upper branches of the calibration. Gallagher and Hunter (1989) and Izotov and Guseva (1990) simply assumed that all of their dwarf galaxies fell on the lower branch, since they were of relatively low luminosity.

A number of authors have obtained low–dispersion spectroscopy for other Virgo dwarfs. He and Impey (1986) observed emission–line spectra for three Virgo BCDs, but their spectral coverage was limited to the wavelength range between Hβ and [S II]$\lambda\lambda$6716, 6731. [O III]λ4363 was not observed, and the "bright–line" method could not be used to determine oxygen abundances, because [O II]λ3727 was not measured. Schulte-Ladbeck (1988) and Schulte-Ladbeck and Cardelli (1988) carried out spectroscopy of ten Virgo BCDs. The membership of the dwarf galaxies in the Virgo Cluster was judged from the radial velocities; only two were found to be members of the cluster. Although bright [O II] and [O III] lines were observed, [O III]λ4363 and [N II]λ6583 were not detected in either of the two dwarfs.

2.5 The Sample of Dwarf Irregulars in Virgo

To study the evolution of dwarfs in the cluster environment, a sample of dIs in the Virgo Cluster is constructed, for which new optical emission–line spectra are obtained and oxygen abundances are derived. The key goals are: (1) where possible, to measure [O III]λ4363 to derive direct oxygen abundances, and (2) if H II regions are too faint, to obtain spectra with sufficient wavelength coverage ([O II]λ3727 to [S II]$\lambda\lambda$6716, 6731) to derive empirical abundances.

From the Virgo Cluster Catalog compiled by Binggeli et al. (1985), dIs are selected according to the following criteria.

1. The candidates must be clearly identified as members of the cluster (Binggeli et al. 1985; Binggeli and Cameron 1993; Binggeli et al. 1993).
2. There must be suitably bright H II regions, as shown by published Hα images (Gallagher and Hunter 1989; Heller et al. 1999).
3. Candidate dwarfs must be located in the central and outer regions of the cluster to sample high–density and low–density conditions, respectively.
4. The galaxies must lie within a narrow luminosity range ($-15 \gtrsim M_B \gtrsim -17$) to test for an environmental effect on the metallicity–luminosity relation. This way, even a small offset from field dwarfs could be flagged in a statistical manner.
5. The galaxies must have a range of over ~ 100 in H I mass at a given luminosity.

Figure 2.3 shows where each dI in the final Virgo sample is located in the cluster and Table 2.5 lists their properties[5].

[5]This research has made use of the NASA/IPAC Extragalactic Database (NED) which is operated by the Jet Propulsion Laboratory, California Institute of Technology, under contract with the National Aeronautics and Space Administration.

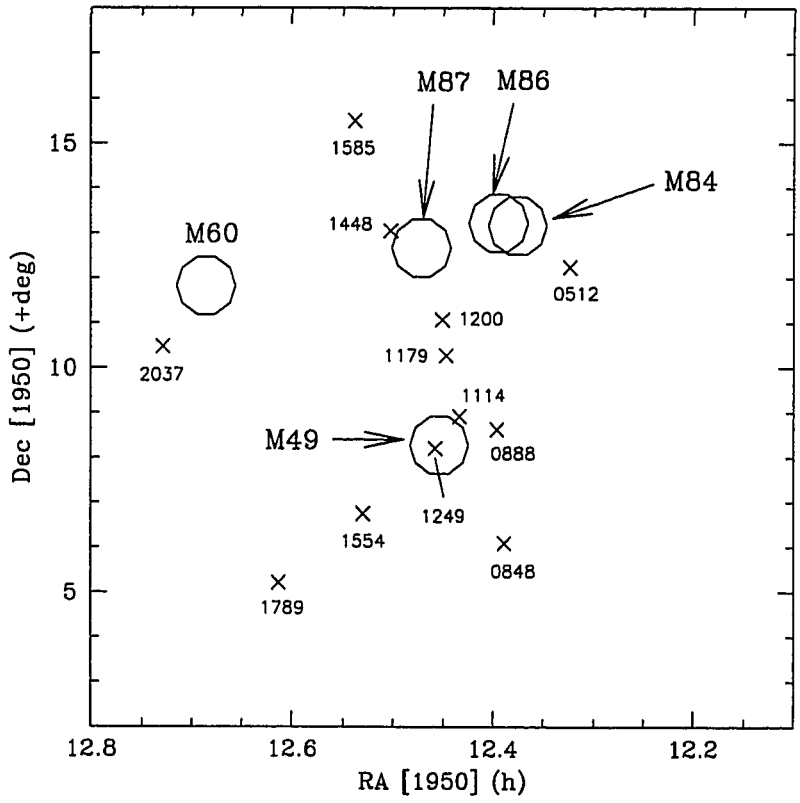

Figure 2.3: Locations of sample dIs within the Virgo Cluster (1950 epoch): Declination (vertical axis) versus Right Ascension (horizontal axis). North is at the top and East is to the left. Large circles show the positions of five giant elliptical galaxies. The crosses mark the locations of 12 dIs in the Virgo sample for which spectra were obtained; they are labelled with their numeric designations in the Virgo Cluster Catalog (Binggeli et al. 1985).

VCC #	Alternate Name	Type	B_T (mag)	$\mu_{0,B}$ (mag arcsec^{-2})	$r_{0,B}$ ($''$)	$B-V$ (mag)	$v_\odot$ (km s^{-1})	F_{21} (Jy km s^{-1})	W_{50} (km s^{-1})	V_{max} (km s^{-1})
(1)	(2)	(3)	(4)	(5)	(6)	(7)	(8)	(9)	(10)	(11)
0512	UGC 7421 [a]	SBm	15.30	23.67	16.22	0.49	153	3.69	108	157
0848	A1223+06	dI/BCD	14.73	...	...	0.42	1537	8.2	115	...
0888	8°26	dI	15.00	23.15	10.47	0.61	1090	1.442	79	...
1114	UGC 7596 [b]	dI	14.66	22.05	9.4	0.56	560	0.278	25	...
1179	IC 3412	dI/BCD	14.87	23.15	10.23	0.39	764	0.433	54	...
1200	IC 3416	dI	14.78	23.50	14.45	0.52	−123	< 0.395	...	...
1249	UGC 7636	dI/dSph	14.26	24.07	31.8	0.50	276	0.167	70	...
1448	IC 3475	dI/dSph	13.93	23.04	26.91	0.76	2572	< 0.507	...	...
1554	NGC 4532	Sm	12.15	19.77	19.39	0.39	2013	50.9	191	102
1585	IC 3522 [c]	dI	15.20	23.01	13.18	0.53	664	10.7	104	57
1789	A1236+05	dI	15.07	...	...	0.72	1620	1.065	98	...
2037	10°71	dI/BCD	15.80	23.60	11.48	0.34	1142	0.358	36	...

Table 2.5: Observed properties for the sample of dIs in the Virgo Cluster. Column (1) lists the galaxy designation in the Virgo Cluster Catalog (Binggeli et al. 1985). Column (2) lists the alternate name of the galaxy from the NASA Extragalactic Database (NED). Column (3) lists the galaxy type. Column (4) lists the total apparent blue magnitude of the galaxy from the Virgo Cluster Catalog (Binggeli et al. 1985). Columns (5) and (6) list in B the central surface brightness and exponential scale length (Binggeli and Cameron 1993; Hoffman et al. 1999; Patterson and Thuan 1996). Column (7) lists the observed $B-V$ colour (Bothun et al. 1986; Gallagher and Hunter 1986). Column (8) lists the heliocentric velocity (Binggeli et al. 1985, 1993). Column (9) lists the H I 21–cm flux integral (Hoffman et al. 1987, 1996). Column (10) lists the H I profile width at half–maximum (Hoffman et al. 1987, 1999; Patterson and Thuan 1992). Column (11) lists the H I maximum rotational velocity: VCC 0848 (Hoffman et al. 1996), VCC 1554 (Hoffman et al. 1999), VCC 1585 (Skillman et al. 1987). NOTES: [a] Also called 12°25. [b] Also called 8°30. [c] Also called DDO 136.

2.6 Individual Galaxies in the Virgo Sample

What follows are short descriptions of each dI in the Virgo sample.

2.6.1 VCC 0512

VCC 0512 is a barred Magellanic dwarf galaxy, whose luminosity is similar to that of the Small Magellanic Cloud. Bothun et al. (1986) and Binggeli et al. (1993) obtained structural parameters. R and Hα images are found in Figure 1 (Plate 26) of Gallagher and Hunter (1989). H II regions are found along the major axis of the galaxy.

2.6.2 VCC 0848

Gallagher and Hunter (1989) obtained R–band and Hα images, which are shown in their Figure 1 (Plate 24). A chain of bright H II regions is seen along the major axis. Surrounding the dI appear to be faint "shell–like" structures, which are more commonly found around elliptical galaxies. These shells may be debris from a merger with a very small object (Gallagher and Hunter 1989). Near–infrared imaging of this dI has been obtained by Boselli et al. (1997).

An emission–line spectrum covering 3400 to 6000 Å was reported by Gallagher and Hunter (1989). The spectrum and subsequent emission–line data are shown in Figure 2 and Table 3, respectively, in Gallagher and Hunter (1989). While [O II]λ3727 and [O III]$\lambda\lambda$4959, 5007 were observed, the [O III]λ4363 line was not detected and the spectral coverage did not include any emission lines near Hα. Because [N II]λ6583 was not measured, the appropriate branch in the empirical calibration could not be chosen. Their spectral data and the empirical calibration of the R_{23} bright–line indicator (see § 5.2) were used to derive an oxygen abundance on the lower branch of

12+log(O/H) = 7.88. The upper branch oxygen abundance would be 12+log(O/H) = 8.68, which is similar to abundances found in spiral galaxies.

Hoffman et al. (1996) obtained updated H I properties for VCC 0848 from resolved single–dish measurements with the Arecibo telescope. The resulting map shows a relatively smooth H I distribution. The rotational velocity was mapped at positions out to four times the optical radius. The maximum rotational velocity and the average line–of–sight velocity dispersion were found to be 157 km s^{-1} and 22 km s^{-1}, respectively.

2.6.3 VCC 0888

This dI has a relatively smooth appearance and contains a number of H II regions. R–band and Hα images of this dI are shown in Figure 1 (Plate 25) of Gallagher and Hunter (1989). Additional B–band photometry was obtained by Binggeli et al. (1993).

2.6.4 VCC 1114

This dI appears to have a smooth "elliptical" envelope. R–band and Hα images are shown in Figure 1 (Plate 21) of Gallagher and Hunter (1989). Two bright and compact H II regions are seen within the galaxy. Patterson and Thuan (1992) obtained additional photometry in B and I in their study of low surface brightness dIs.

2.6.5 VCC 1179

This dI/BCD galaxy has a smooth optical appearance. R–band and Hα images are found in Figure 1 (Plate 22) of Gallagher and Hunter (1989). A chain of H II regions is observed along the major axis of the galaxy. Heller et al. (1999) obtained Hα fluxes

for several H II regions. Additional B–band photometry was acquired by Binggeli et al. (1993).

2.6.6 VCC 1200

Optically, this dwarf appears smooth and relatively "boxy". R–band and Hα images are found in Figure 1 (Plate 23) of Gallagher and Hunter (1989). A number of compact H II regions are found throughout the galaxy. Additional B–band photometry has been published by Binggeli et al. (1993).

2.6.7 VCC 1249

This dI has an irregular appearance with optical "knots" throughout the body of the galaxy (see, e.g., Patterson and Thuan 1992). Gallagher and Hunter (1989) did not detect any distinct H II regions, although faint diffuse Hα emission was observed. At the Canada–France–Hawaii Telescope, a serendipitous discovery of an H II region in the H I cloud near VCC 1249 was made. An extensive discussion of the recent literature and this author's measurements are presented in Chapter 6.

2.6.8 VCC 1448

Of the entire dwarf sample, this galaxy is the closest (in projection) to M 87. It appears somewhat amorphous and featureless. R–band and Hα images are found in Figure 1 (Plate 23) of Gallagher and Hunter (1989).

Vigroux et al. (1986) interpreted optical and H I properties as being a consequence of the stripping of its gas. The large optical diameter of approximately 10 kpc is a problem for the scenario of a stripped dI fading to become a dE since typical dEs have sizes smaller than 10 kpc. Since stripping typically leads to an increase in size in response to the mass loss, VCC 1448 will not likely become an object resembling

a present–day dE. From optical and near–infrared surface photometry, Bothun et al. (1986) arrived at a similar conclusion based upon the much larger size and redder colours compared to a typical dE.

Knezek et al. (1999) considered VCC 1448 to be of mixed morphology (dI/dE) and labelled the galaxy a "transition" object. Although previous authors have claimed it is fading after having experienced its final bout of star formation, the measured $B-R$ colours (Knezek et al. 1999) are in conflict with those of dEs. With additional Hα imaging, Knezek et al. (1999) confirmed the results of Gallagher and Hunter (1989) and determined that the galaxy is devoid of bright H II regions.

This dwarf is included because its global optical properties are similar to those of VCC 1249.

2.6.9 VCC 1554

VCC 1554 is an example of a bright Magellanic irregular galaxy and appears to be the analog of the Large Magellanic Cloud (LMC) in the Virgo Cluster. The dwarf appears to host an H II region which resembles the 30 Doradus region in the LMC.

Although Gallagher and Hunter (1989) obtained imaging and spectrophotometric data of VCC 1554, an Hα image is not included in their paper. However, an emission–line spectrum and the resulting measurements are shown in their Figure 2 and Table 3, respectively. Their spectrum was limited to the wavelength range between [O II]λ3727 and [O III]λ5007, but [O III]λ4363 was not detected. From their reported data, the lower–branch oxygen abundance would be 12+log(O/H) = 8.00, while the upper–branch oxygen abundance would be 12+log(O/H) = 8.64. There is insufficient data to resolve the degeneracy of the empirical calibration of R_{23}.

Kenney and Young (1989) examined VCC 1554 to assess the effect of the Virgo Cluster environment on the properties of atomic and molecular gas in disk galaxies.

Young et al. (1996) included the galaxy in their Hα survey designed to study star formation in late–type galaxies. It was found that VCC 1554 is H I–normal (although there is little molecular gas found), and is forming stars at a rate that will eventually exhaust its gas supply in a Hubble time.

Ho et al. (1995, 1997) obtained a spectrum in the wavelength range 4200–6800 Å to search for an "active galactic nucleus." The galaxy was found not to exhibit any signs of photoionization arising from high energy shocks (see also Osterbrock 1989).

Hoffman et al. (1999) obtained H I synthesis maps at the VLA and optical (B, R) surface photometry. The derived H I mass for VCC 1554 is typical for dwarfs at comparable luminosities. The rotational velocity is 102 km s^{-1} at a radius of 1.'7 and the velocity dispersion is 24 km s^{-1}. While the inner gas is distributed somewhat smoothly, the outer H I appears disturbed towards the east and south. The disturbed appearance is likely due to an interaction with the neighbouring dwarf VCC 1581 (DDO 137).

2.6.10 VCC 1585

The optical appearance of this dwarf galaxy is somewhat irregular with bright "concentrations" throughout the body and a tail of "knots" curving away from the body towards the northwest. R–band and Hα images are found in Figure 1 (Plate 22) of Gallagher and Hunter (1989). H II regions are observed near the centre of the galaxy along the major axis. No emission lines were detected in an optical spectrum obtained by Gallagher and Hunter (1989; their Figure 2). Also, Heller et al. (1999) obtained Hα imaging and measured Hα fluxes for the H II regions.

A number of additional studies have focussed on this dI. Single–dish H I observations were obtained by Bothun et al. (1985) with the Arecibo radio telescope. Skillman and Bothun (1986) obtained H I synthesis observations at the VLA and

their resulting map shows a smooth H I distribution. Skillman et al. (1987) constructed a detailed H I map at the VLA and obtained a rotation curve, which extends well past the stellar–dominated exponential disk. The maximum rotational velocity was measured to be 57 km s^{-1} at a radius of 1.'3. Curiously, the rotation curve appears to "turn over" beyond about 1.'5. Bothun et al. (1986) reported optical and near–infrared surface photometry. Bothun et al. (1994) also conducted ROSAT observations to search for an X–ray halo as evidence of supernovae–induced mass loss on a galactic scale (see, e.g., Dekel and Silk 1986). There was no detection. The upper limit to the X–ray halo luminosity was found to be much less than what would be expected considering how much hot gas would have been expelled by star formation episodes over the life of the galaxy.

2.6.11 VCC 1789

Optically, this galaxy appears almost like a small elliptical galaxy. R–band and Hα images are found in Figure 1 (Plate 21) of Gallagher and Hunter (1989). A number of bright H II regions are observed. Only weak [O II]λ3727 emission was observed in an optical spectrum obtained by Gallagher and Hunter (1989; their Figure 2).

2.6.12 VCC 2037

This dI appears to have a bright central concentration, surrounded by a faint irregular envelope. R–band and Hα images are found in Figure 1 (Plate 26) of Gallagher and Hunter (1989). There appear to be two H II regions in the Hα image. Additional B–band photometry has been obtained by Binggeli et al. (1993).

Chapter 3

Observations & Reductions

Observations of field and Virgo dIs are discussed in this chapter. The spectroscopic data acquired and the IRAF reduction procedures are discussed below. Data obtained and the instrumentation employed are discussed in § 3.1 and 3.2 for field dIs and Virgo dIs, respectively. In particular, observations and reductions of data obtained at the Kitt Peak National Observatory and the Canada–France–Hawaii–Telescope are presented in § 3.3 and 3.4, respectively. Representative spectra are illustrated in § 3.5.

3.1 Observations of Field dIs

Between 1991 and 1994, M. McCall and co–workers undertook a program of long–slit spectroscopy with the 2.3–m Bok Telescope at Steward Observatory[1] and with the 2.1–m telescope at San Pedro Mártir (SPM)[2] in México to acquire optical spectra for a sample of dwarf galaxies in the vicinity of the Local Group. The primary focus was to obtain sufficiently long exposures to detect the [O III]λ4363 emission line, which was detected in four dIs; an upper limit was obtained for NGC 1560. Table 3.1 lists

[1]Bok Telescope, operated by the Steward University of the University of Arizona.

[2]Observatorio Astronómico Nacional, San Pedro Mártir, operated by Instituto de Astronomía, Universidad Nacional Autónoma de México.

the dwarf galaxies which were observed at Steward and SPM. The characteristics of

Galaxy (1)	Date (UT) (2)	Obs. (3)	N (4)	$t_{\rm total}$ (s) (5)	[O III]λ4363 (6)	δ(sens. func.) (7)
Holmberg II	1992 Mar. 23	Steward	1×300 s + 3×1200 s	3900	detected	3.7 %
IC 10	1991 Oct. 15	Steward	1×60 s + 3×1800 s	5460	detected	2.2 %
IC 10	1994 Dec. 1	SPM	1×1200 s	1200	...[a]	3.0 %
NGC 1560	1991 Oct. 15	Steward	3×1800 s	5400	upper limit	2.2 %
NGC 1560 "1" (NE)	1992 Jan. 27	SPM	1×1200 s	1200	...[a]	2.2 %
NGC 1560 "2" (SW)	1992 Jan. 27	SPM	1×900 s	900	...[a]	2.2 %
NGC 3109	1992 Mar. 23	Steward	1×300 s + 4×1200 s	5100	detected	3.7 %
UGC 6456	1992 Mar. 23	Steward	1×300 s + 4×900 s	3900	detected	3.7 %

Table 3.1: Spectroscopy of field dwarfs acquired at Steward and SPM. Column (1) lists the galaxy name in alphabetical order, column (2) lists the observation date, column (3) lists the observatory, column (4) lists the number of exposures obtained, column (5) gives the total exposure time, column (6) states whether [O III]λ4363 was detected, and column (7) lists the relative (root–mean–square) error of the sensitivity function obtained from observations of standard stars for the specified observing night. NOTES: [a] Spectra designed specifically to measure $F(\mathrm{H}\alpha)/F(\mathrm{H}\beta)$.

the instrumentation employed are listed in Table 3.2. A brief discussion of the H II regions in the five field dIs observed at Steward is presented below.

3.1.1 H II Regions in Holmberg II

Several of the H II regions in Holmberg II were spanned by the long slit employed. Table 3.3 lists the H II regions for which spectra were measured and the [O III]λ4363 line was detected. The locations of the H II regions were determined by comparing finding charts used by M. McCall against published Hα data (Hodge et al. 1994; Hunter and Gallagher 1985).

3.1.2 H II Regions in IC 10

Table 3.4 lists the H II regions for which spectra were measured. By inspection of the finding charts by M. McCall, the locations of the observed H II regions were matched

Property	Steward (blue)	Steward (red)	San Pedro Martír (red)
Telescope			
Aperture	2.3 metre		2.1 metre
Focus	f/9.0		f/7.5
Instrument	Boller & Chivens Spectrograph		Boller & Chivens Spectrograph
CCD			
Total area	TI 800 pix × 800 pix		Tektronix 1024 pix × 1024 pix
Usable area	800 pix × 350 pix		1024 pix × 400 pix
Pixel size	15 μm		24 μm
Image scale	0.8 arcsec pix^{-1}		0.92 arcsec pix^{-1}
Gain	2.8 e^- ADU^{-1}		1.22 e^- ADU^{-1}
Read-noise (rms)	7.4 e^-		3 e^-
Grating, Long slit			
Groove density	600 lines mm^{-1}	600 lines mm^{-1}	300 lines mm^{-1}
Blaze λ (1st order)	3568 Å	6690 Å	5000 Å
Dispersion	1.89 Å pix^{-1}	3.72 Å pix^{-1}	3.96 Å pix^{-1}
Effective λ range	3650–5100 Å	4200–7200 Å	3400–7500 Å
Slit width	2.5 arcsec	4.5 arcsec	2.2 arcsec

Table 3.2: Instrument configurations at Steward and SPM.

H II Region (1)	[O III]λ 4363 (2)	HSK94 (3)	HG85 (4)
Ho II - 1	upper limit	67	6
Ho II - 2 [a]	upper limit	67	6
Ho II - 3	upper limit	67	6
Ho II - 4	upper limit	69 ?	...
Ho II - 5	detected	70	5
Ho II - 6	upper limit	73	4
Ho II - 7 [b]	detected	73	4
Ho II - 8	detected	73	4
Ho II - 9	detected	71	3

Table 3.3: Identification of H II regions in Holmberg II (Ho II). Column (1) lists the H II region, column (2) lists whether [O III]λ4363 was detected or an upper limit was obtained, and columns (3) and (4) list the corresponding H II regions identified by Hodge et al. (1994, Figure 2: HSK94) and Hunter and Gallagher (1985, Figure 1 for DDO 50: HG85), respectively. The H II region number in column (1) increases along the slit towards the north. NOTES: [a] The H II region Ho II–2 encompasses two separate H II regions 1 and 3. Subsequent line intensities and derived quantities for Ho II–2 are not completely independent. [b] The H II region Ho II–7 encompasses two separate H II regions 6 and 8. Subsequent line intensities and derived quantities for Ho II–7 are not completely independent.

with Lequeux et al. (1979) and Hodge and Lee (1990).

H II Region (1)	[O III]λ 4363 (2)	LPRSTP (3)	HL90 (4)
IC 10 – 1 [a]	detected	1	111c,e
IC 10 – 2	detected	...	111c
IC 10 – 3	detected	...	111e
IC 10 – 4 [b]	upper limit	...	111b
IC 10 – 5	upper limit	...	106a
IC 10 – 6 [c]	...	...	106 south, diffuse

Table 3.4: Identifications of H II regions in IC 10. Column (1) lists the H II region, column (2) lists whether [O III]λ4363 emission was detected or an upper limit was obtained, and columns (3) and (4) list the corresponding H II regions identified by Lequeux et al. (1979, Figure 1: LPRSTP) and Hodge and Lee (1990, Figure 2: HL90), respectively. The H II region number in column (1) increases along the slit towards the south. NOTES: [a] The H II region IC 10–1 encompasses two separate H II regions 2 and 3. Subsequent line intensities and derived quantities for IC 10–1 are not completely independent. [b] Light from this H II region may include some light from the H II region 111a (HL90). [c] The observed spectrum was not of sufficient quality to be included in the subsequent analyses.

3.1.3 H II Regions in NGC 1560

The long slit was placed lengthwise along the major axis of the galaxy to obtain spectra of H II regions located in the disk. Table 3.5 lists the H II regions for which spectra were measured. From inspection of finding charts, Hα images provided by M. McCall, and the broadband images by Lee and Madore (1993), approximate locations of observed H II regions with respect to the measured stars in Lee and Madore (1993) were determined. The H II region NGC 1560–1 is identified by M. McCall as H II region "1" and is visible as the brightest "concentration" located near the centre of the galaxy in the V–band image of Lee and Madore (1993). For H II regions NGC 1560–6 and NGC 1560–7, Hγ was not detected because of the poor quality of the spectra.

H II Region (1)	[O III]λ 4363 (2)	Notes (3)
NGC 1560 – 1	upper limit	MLM "#1"
NGC 1560 – 2	upper limit	bright
NGC 1560 – 3	upper limit	faint
NGC 1560 – 4 [a]	upper limit	faint
NGC 1560 – 5	upper limit	faint
NGC 1560 – 6	...[b]	very faint
NGC 1560 – 7	...[b]	very faint

Table 3.5: Identifications of H II regions in NGC 1560. Column (1) lists the H II region, column (2) lists whether [O III]λ4363 emission was detected or an upper limit was obtained, and column (3) lists comments about the relative brightness observed for each H II region. The H II region number in column (1) increases along the slit towards the northeast. NOTES: [a] The spectrum for H II region NGC 1560–4 encompasses the signal from the two H II regions 3 and 5. Subsequent line ratios and derived quantities for NGC 1560–4 are not completely independent. [b] Hγ was not observed due to the poor quality of the spectrum.

3.1.4 H II Regions in NGC 3109

Table 3.6 lists the H II regions for which spectra were measured. By inspection of the finding charts by M. McCall, the locations of the observed H II regions were matched with Richer and McCall (1992). A continuum–subtracted Hα image may also be found in Hunter, Hawley, and Gallagher (1993, Figure 11), but it is difficult to match the H II regions seen in the [O III]λ5007 image by Richer and McCall (1992) with those seen in the Hα image by Hunter et al. (1993).

3.1.5 H II Regions in UGC 6456

The long slit was placed on the galaxy in an orientation similar to that employed by Tully et al. (1981). Table 3.7 lists the H II regions for which spectra were measured. By inspection of the finding charts by M. McCall, the locations of the observed H II regions were matched with Tully et al. (1981) and Lynds et al. (1998).

H II Region (1)	[O III]λ 4363 (2)	Notes (3)	RM92 (4)
NGC 3109 – 1	no Hγ	very faint	...
NGC 3109 – 2	*no [O III]λ 4959*	*very faint*	...
NGC 3109 – 3 [a]	detected	bright	5
NGC 3109 – 4 [b]	upper limit	bright	5

Table 3.6: Identifications of H II regions in NGC 3109. Column (1) lists the H II region, column (2) lists whether [O III]λ4363 emission was detected or an upper limit was obtained, column (3) lists notes about the H II regions, and column (4) lists the corresponding H II region identified by Richer and McCall (1992, Figure 1: RM92). The H II region number in column (1) increases along the slit towards the north. NOTES: [a] The extraction window was narrow (4.8 arcsec) to isolate the signal from the H II region. [b] The extraction window was wide (16.0 arcsec) and included the spectrum of an early–type field star adjacent to the H II region.

H II Region (1)	[O III]λ 4363 (2)	Lynds et al. 1998 (3)	Tully et al. 1981 (4)
UGC 6456 – 1	detected	5	2nd clump in slit
UGC 6456 – 2	detected	1	brightest clump in slit

Table 3.7: Identifications of H II regions in UGC 6456. Column (1) lists the H II region, column (2) lists whether [O III]λ4363 emission was detected, and columns (3) and (4) list the corresponding H II regions identified by Lynds et al. (1998, Figure 2) and Tully et al. (1981, Figure 2), respectively. The H II region number in column (1) increases along the slit towards the east.

3.1.6 Reductions

The data for each galaxy were reduced and calibrated in the standard manner with IRAF by a former M.Sc. student Robert Ross. The details are similar to those described below for the spectra of Virgo dIs. Relative errors in the sensitivity function (in magnitudes) for each galaxy are listed in Table 3.1. The author set apertures for the extraction of H II region spectra and redefined the "windows" used for sky subtraction. Final one–dimensional spectra for each aperture or H II region were obtained via "no–weights" summed extractions.

3.2 Observations of Virgo dIs

The author and M. Richer obtained optical spectra for eleven dIs in the Virgo sample at Kitt Peak National Observatory (KPNO)[3] and the Canada France Hawaii Telescope (CFHT)[4]. The data are presented in § 3.3 and § 3.4, respectively. A log of observations is given in Table 3.8. An angle of one arcsecond subtends a distance of 81.2 parsecs for a distance modulus of 31.12 mag for the Virgo Cluster. Thus, extragalactic H II regions comparable to the size of the 30 Doradus nebula[5] are resolved at the distance of the Virgo Cluster.

[3]Visiting Astronomer, Kitt Peak National Observatory, National Optical Astronomy Observatories, operated by the Association of Universities for Research in Astronomy, Inc. (AURA) under cooperative agreement with the National Science Foundation.

[4]Visiting Astronomer, Canada–France–Hawaii Telescope, operated by the National Research Council of Canada, the Centre National de la Recherche Scientifique de France, and the University of Hawaii.

[5]This bright nebula in the Large Magellanic Cloud has a linear diameter of approximately 200 pc (Walborn 1991).

Galaxy	Obs.	Date (UT)	N_{exp}	t_{total} (s)	$\langle \sec z \rangle$	$N_{H\,II}$	[O III]λ4363	δ(sens. func.)
(1)	(2)	(3)	(4)	(5)	(6)	(7)	(8)	(9)
VCC 0512	CFHT	1999 April 9	2×1800	3600	1.27	2	upper limit	5.0 %
VCC 0848	KPNO	1997 March 3	4×1800	7200	1.29	1	detected	4.9 %
VCC 0888	KPNO	1997 March 3	3×1800	5400	1.10	2	upper limit	4.9 %
VCC 1114	CFHT	1999 April 9	2×1800	3600	1.05	2	upper limit	5.0 %
VCC 1179	KPNO	1997 March 2	4×1800	7200	1.10	4	upper limit	5.5 %
VCC 1200	KPNO	1997 March 3	3×1800	5400	1.23	1	upper limit	4.9 %
VCC 1249	CFHT	1999 April 11	1×1800	816[a]	1.03	1	...[b]	4.3 %
VCC 1448	CFHT	1999 April 11	3×1800	5400	1.20	0	...[c]	4.3 %
VCC 1554	CFHT	1999 April 11	2×1800	3600	1.05	7[d]	detected	4.3 %
VCC 1585	KPNO	1997 March 2	2×1800	3600	1.59	1	upper limit	5.5 %
VCC 1789	KPNO	1997 March 2	3×1800	5400	1.30	1	upper limit	5.5 %
VCC 2037	KPNO	1997 March 2	3×1800	5400	1.22	2	upper limit	5.5 %

Table 3.8: Optical spectroscopy of Virgo dIs acquired at KPNO and CFHT. Column (1) lists the galaxy name from the Virgo Cluster Catalog (Binggeli et al. 1985), column (2) lists the observatory at which the spectra were acquired, column (3) lists the date on which data were acquired, column (4) lists the number of exposures obtained and the length of each exposure in seconds, column (5) indicates the total exposure time, column (6) lists the mean airmass, column (7) indicates the number of H II region spectra obtained, column (8) indicates whether [O III]λ4363 was detected, and column (9) lists the relative root–mean–square error in the sensitivity function obtained from observations of spectrophotometric standard stars for the specified observing night. NOTES: [a] 1800 second exposure terminated due to increasing cloud cover and rising humidity. [b] Hγ was not detected in the spectrum. [c] A spectrum was not detected. [d] Two galaxies were discovered in the background, each with $v/c \simeq 0.093$.

3.3 Optical Spectroscopy at Kitt Peak

Three nights (1997 March 1–3 UT) were awarded at KPNO. The first night was completely unusable due to inclement weather. Data were successfully obtained on the subsequent two nights and spectra were obtained for seven dIs. Attempts to acquire spectra of VCC 0512 failed because of insufficient signal; the slit was likely misaligned with the galaxy.

3.3.1 Instrument Configuration

Moderate–resolution optical spectroscopy was obtained using the Ritchey–Chrétien Spectrograph on the 4.0-metre telescope in the f/7.8 configuration. The spectrograph was used in long–slit mode for two–dimensional spectroscopy to cover the maximum possible number of H II regions. The characteristics of the instrumentation employed are listed in Table 3.9. The extreme ends of the CCD could not be used due to vignetting and defocusing effects. The effective wavelength coverage was 3500 to 7600 Å.

3.3.2 Image Acquisition

Figures 3.1 to 3.4 show the placement of the long slit over each dI. Individual exposures were 30 minutes and total exposure times ranged between one and two hours.

A single 1800–second "dark" frame was obtained to evaluate the contribution from the dark current. An inspection of the dark frame showed that the total counts registered were negligible compared to the counts from the sky background in a celestial image of comparable exposure time. Thus, no corrections for dark current were applied.

To correct for variations in the pixel–to–pixel sensitivity of the CCD, flat–field

Property	Value
Tektronix T2KB CCD	
Total area	2048 pix × 2048 pix
Usable area [a]	1500 pix × 471 pix
Pixel size	24 μm
Image scale	0.69 arcsec pix^{-1}
Gain	3.1 e^- ADU^{-1}
Read-noise (rms)	4 e^-
KPC-10A Grating	
Groove density	316 lines mm^{-1}
Blaze λ (1st order)	4000 Å
Dispersion	2.75 Å pixel^{-1}
Spectral resolution [b]	6.9 Å
Effective λ range	3500–7600 Å
Long slit	
Length	5.4 arcmin
Width	2 arcsec (300 μm)

Table 3.9: Ritchey–Chrétien Spectrograph configuration on the 4–m telescope at KPNO. NOTES: [a] Wavelength coverage (1500 pix), spatial coverage (471 pix). [b] Based on 2.5 pixels FWHM corresponding to a slit width of 2″.

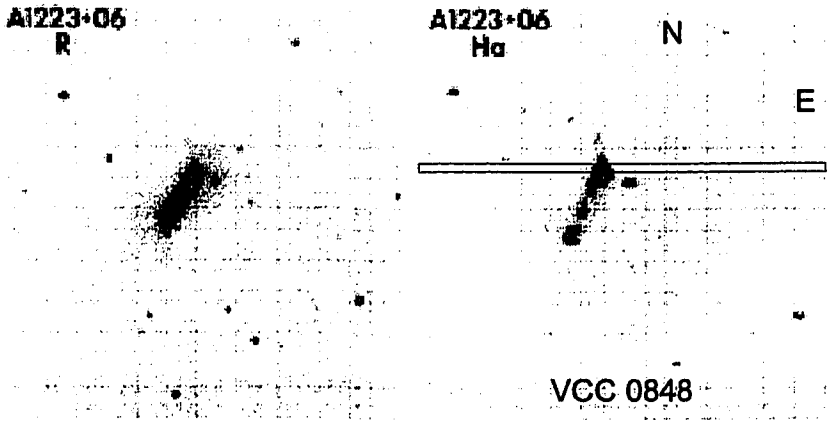

Figure 3.1: VCC 0848 (A1223+06): R and continuum-subtracted Hα images from Gallagher and Hunter (1989). The field of view in each frame is approximately 87″ by 87″. North is at the top and East is to the right. The orientation and placement of the long slit are indicated in the Hα image.

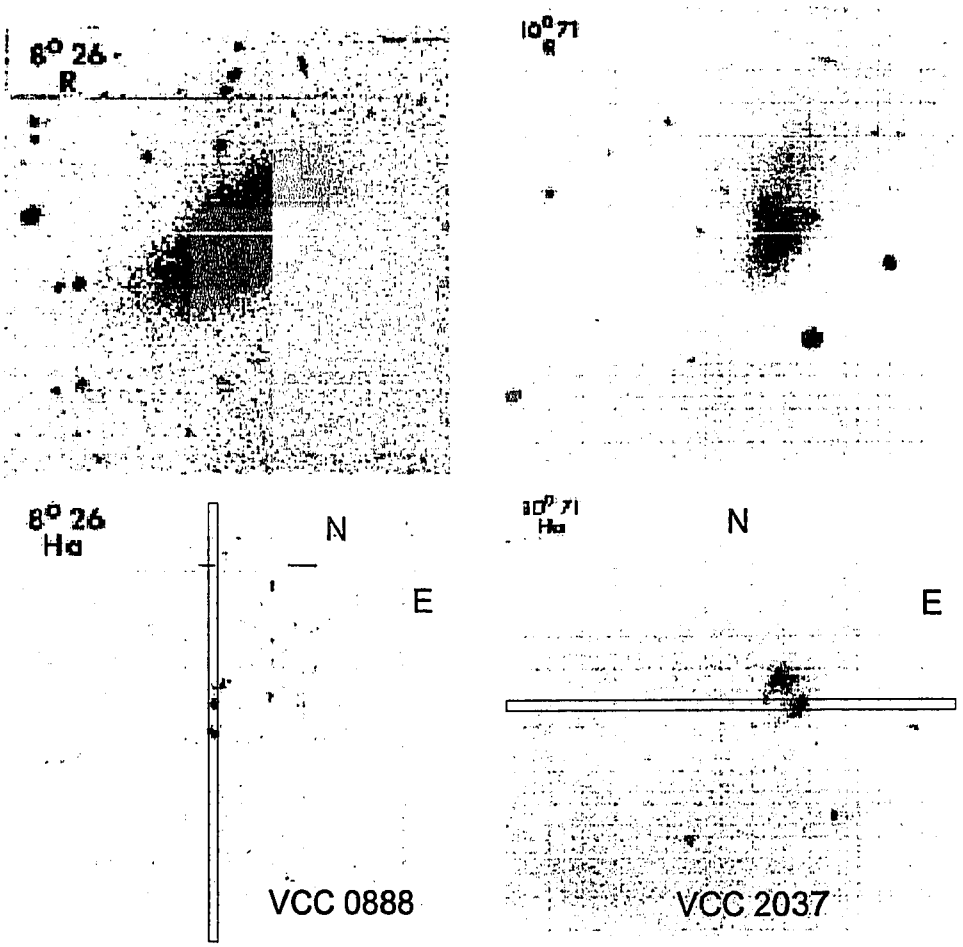

Figure 3.2: VCC 0888 (8°26; left) and VCC 2037 (10°71; right): R and continuum–subtracted Hα images from Gallagher and Hunter (1989). The field of view in each frame is approximately 87″ by 87″. North is at the top and East is to the right. The orientation and placement of the long slit are shown in each Hα image.

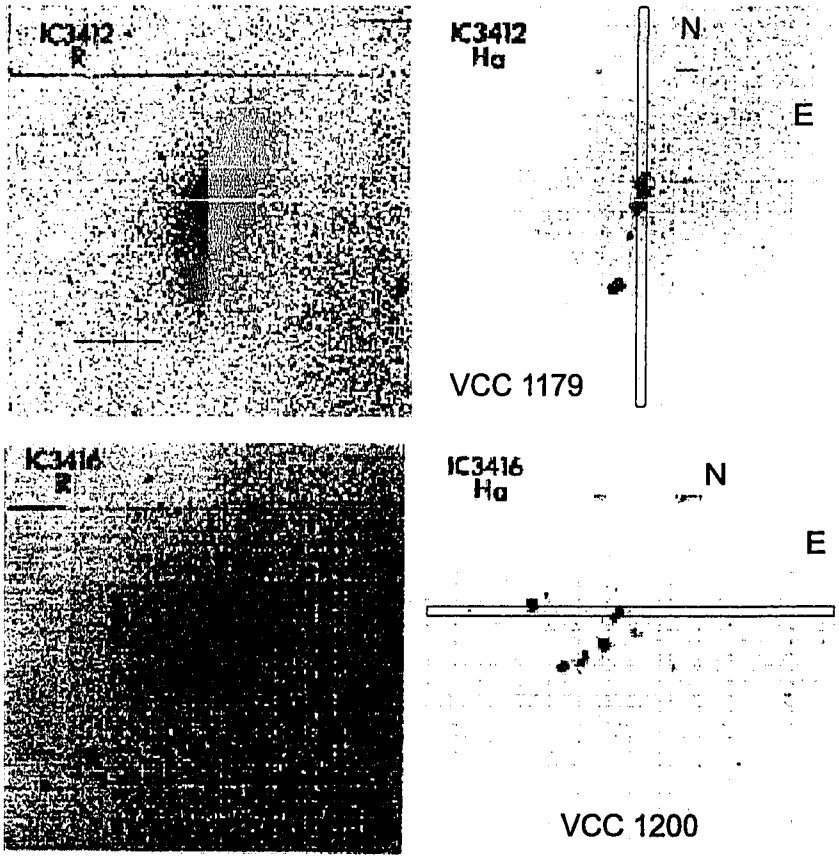

Figure 3.3: VCC 1179 (IC 3412; top), VCC 1200 (IC 3416; bottom): R and continuum-subtracted Hα images from Gallagher and Hunter (1989). The field of view in each frame is approximately 87″ by 87″. North is at the top and East is to the right. The orientation and placement of the long slit are shown in each Hα image.

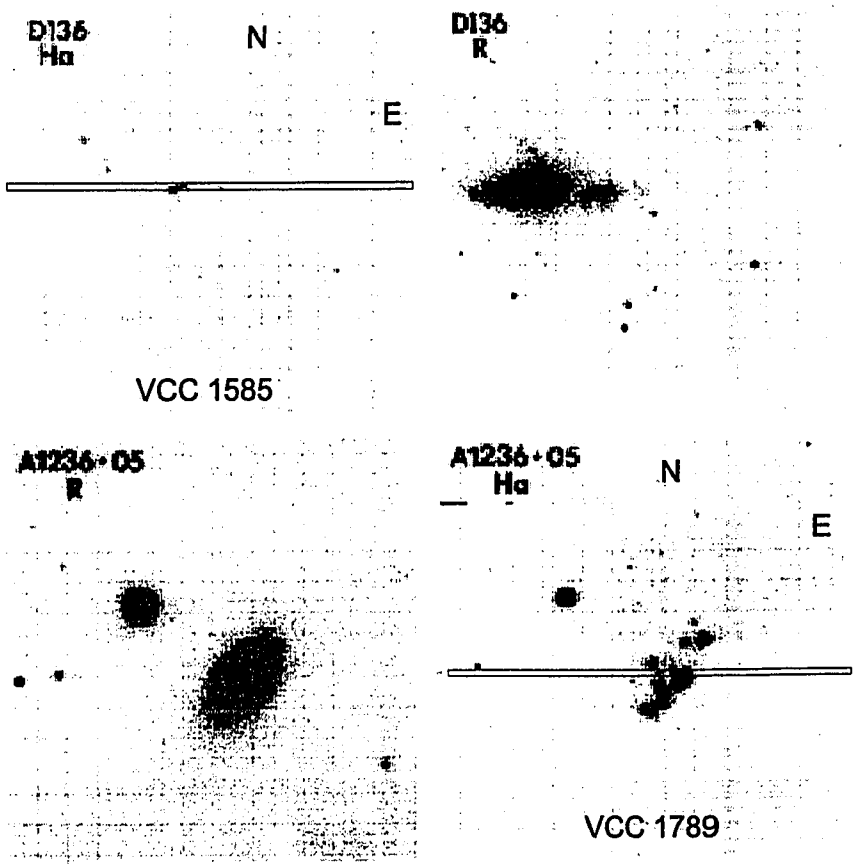

Figure 3.4: VCC 1585 (DDO 136; top), VCC 1789 (A1236+05; bottom) : R and continuum-subtracted Hα images from Gallagher and Hunter (1989). The field of view in each frame is approximately 87″ by 87″. North is at the top and East is to the right. The orientation and placement of the long slit are shown in each Hα image.

exposures of the internal quartz lamp within the spectrograph were taken at the beginning and end of each night. Twilight flats were acquired at dusk each night to correct for variations over larger spatial scales. To correct for the "slit function" in the spatial direction, the variation of illumination along the slit was taken into account using internal and twilight flats.

Two exposures of a helium–neon–argon ("HeNeAr") arc lamp were acquired on each night for wavelength calibration. Flux calibration was achieved by observing the standard stars G191B2B and Feige 67 (see Oke 1990) interspersed among observations of dIs. For all standard star exposures, the position of the star was set near the centre of the slit.

3.3.3 Reductions

Spectra were reduced using IRAF[6] routines, which are described in the documents by Massey (1992) (*noao.imred.ccdred*) and Massey et al. (1992) (*noao.imred.specred*). Additional routines in the *noao.onedspec* and *noao.twodspec.longslit* packages were used. A diagram showing the flow of reductions for KPNO data is shown in Figure 3.5. As calibration exposures were taken on each night, the reductions were performed independently for each night. Columns and rows were parallel to the spatial and wavelength axes, respectively.

3.3.4 Zero Corrections

The zero–offset for the individual bias frames was removed using the measured counts in the overscan section in the last thirty columns of the digital data. All images were then subsequently trimmed to remove the overscan section. Then, a "superbias" was

[6]IRAF is distributed by the National Optical Astronomy Observatories, which is operated by the Associated Universities for Research in Astronomy, Inc., under contract to the National Science Foundation.

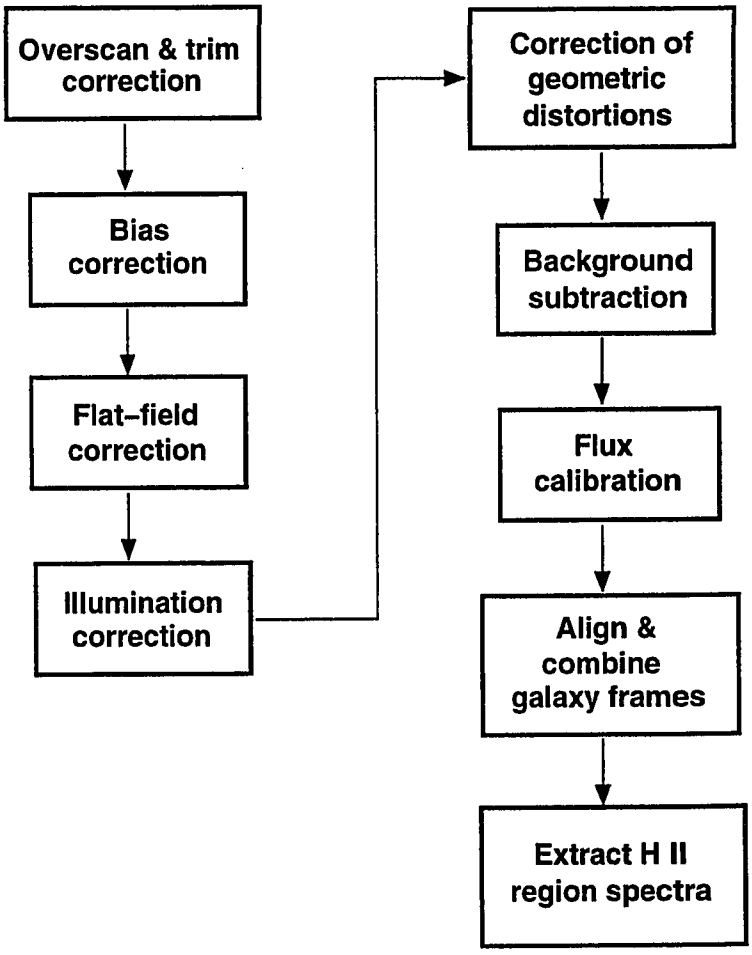

Figure 3.5: Reductions flowchart for KPNO data.

created by averaging bias frames. No structure in the final bias frame was visible.

3.3.5 Flat–Field Corrections

Internal flat and sky flat frames were averaged to make a single internal flat image ("Flat") and a single sky flat image ("Sky"), respectively. A spline function was fit in the dispersion direction to the "Flat" image to create a normalized "nFlat" image. The averaged sky flat "Sky" was flat corrected using the normalized flat–field frame "nFlat". The quality of flatness across the CCD field was evaluated by examining the newly flattened "Sky" image along the spatial direction. To correct for the illumination along the slit (slit function), a normalized illumination image, "nSky", was constructed using the flattened "Sky" image. The final flat field image, called "perfectFlat", was constructed by multiplying "nFlat" with "nSky." Subsequently, every object frame was simultaneously corrected for low– and high–frequency variations in response.

3.3.6 Geometric Corrections

The wavelength scale was linearized at all spatial positions. Emission lines in the comparison arc spectrum were selected along a given dispersion line. The emission lines were used to check and confirm the placement of the lines at a given pixel position in all rows. A two–dimensional polynomial function was fit to wavelength as a function of pixel position. This was used to transform the spectra to a linear wavelength scale. To ensure correct mapping, a comparison (arc lamp) frame and a sample object frame were transformed and a visual inspection was performed to compare the transformed frames with the original frames.

Standard star exposures were obtained with the stars positioned at the centre of the slit. No correction for spatial distortions was made, because the positions of

standard stars did not change along the slit.

3.3.7 Background Subtraction

To remove bright telluric lines, the sky background was fitted and subtracted from object spectra. Subtraction was done interactively for each object frame. A polynomial function was fitted along a set of selected columns. A subsequent median was taken to eliminate the effects of cosmic rays. The resulting average was then subtracted from each object frame.

3.3.8 Flux Calibration

Fluxes were calibrated from digital units (ADUs) to physical flux units (ergs cm^{-2} s^{-1} $Å^{-1}$) using the standard star frames. Apertures encompassing the spectra of G191B2B and Feige 67 were defined and spectra were extracted. Standard star spectra were integrated over the appropriate calibration bandpasses. Using tabulated fluxes (Massey et al. 1988), observed counts were used to derive the flux calibration at the sampling wavelengths. The grid was used as input to compute the sensitivity function, which would define the instrumental response to flux continuously with wavelength. Shifts were applied so that the mean sensitivity curve for each star was the same as the star giving the largest mean sensitivity. This process compensated for variable grey extinction due to changing transparency. A low–order polynomial function was fitted to the data, producing root–mean–square errors between five and six per cent. To check the quality of these fits, the sensitivity and their residuals (both in magnitudes) were plotted against wavelength. Anomalous data points for a given sensitivity curve were deleted interactively. Some curves were entirely removed, owing to anomalous shapes. These were associated with observations at high airmass. A single mean sensitivity function was obtained separately for each of the two nights.

Inspection of the standard star spectra acquired on March 3 (UT) showed that there appeared to be some "missing flux" blueward of column 500 (approximately 3727Å) compared to spectra from the same standard stars obtained on the previous night (March 2 UT). However, there appeared to be very little change in the overall shape of the sensitivity function redward of column 500 from one night to the next. No further attention was paid to this problem, since there were no strong emission features of value blueward of $\lambda \simeq 3727$Å.

Object spectra were flux-calibrated using the standard star spectra. The spectra were corrected for atmospheric extinction and calibrations were carried out in two dimensions by applying the same sensitivity function to each row.

3.3.9 Combining Frames

For each target frame, image sections were cropped to remove columns blueward of [O II]λ3727 and redward of [O II]$\lambda\lambda$7320, 7330. This was especially important, because there was significant noise in the "blue" part of the chip which affected how variances in the signal were computed in the procedure to remove cosmic rays. Consequently, cropping greatly improved the removal of cosmic rays. No cropping was performed in the spatial direction; no rows were removed.

The *imcombine* task was used to add the frames for a given galaxy, with *reject* set to "avsigclip." To determine the best way to combine, a test galaxy with three 30–minute frames was chosen. Two small (10 pix × 10 pix) "boxes" were selected to measure sky signal; one box was placed about 43 pixels ($\sim 30''$) from the top edge of the frame and the second box was placed about 43 pixels from the bottom edge. The three 30–minute frames were added to form two combined images, one with *combine* = *average* and the other with *combine* = *median*. The sky signal was measured in each of the combined images. Compared to the standard deviation of sky counts in

an individual frame, the standard deviation in sky counts of the combination was reduced by a factor of approximately 1.4 with median–averaging and by a factor of about 1.7 with normal averaging. Subsequently, object frames were combined by implementing *combine = average*.

For cosmic–ray rejection, the *avsigclip* parameter was preferred over *sigclip*, because the latter only worked well with more than ten frames. The parameter, *crreject*, which uses the CCD noise parameters in ADUs or counts, could not be used to reject cosmic rays, because object frames had already been flux–calibrated into physical flux units.

Small shifts in pixels might have been expected in different exposures of the same target due to flexure in the telescope. Thus, spatial profiles of emission–line features were visually examined in all frames to check the alignment in both the vertical and the horizontal directions. Fortunately, no significant shifts were found.

Individual frames for a given galaxy were scaled to a common flux before combining. Scaling and weighting factors were determined in the following manner. The mean flux was measured for a box around the [O III]λ5007 emission–line feature in each frame. The [O III]λ5007 feature was selected because it was generally bright and approximately midway in wavelength between [O II]λ3727 and Hα. The frame with the largest mean flux was set to unit scaling factor and unit weighting factor. The remaining scale factors were computed by determining the ratio of the box mean relative to the largest observed value. This yielded scale factors larger than unity. Weighting factors were computed as the reciprocal of the scale factors, which ensured that the contribution of each spectrum to the average was proportional to the flux in [O III]λ5007.

This procedure was successful for six of the seven dIs for which there were at least three exposures acquired. Since only two exposures were obtained for VCC 1585,

cosmic rays could not be removed by the procedure stated above. Instead, the following scheme was adopted (Wells and Bell 1994). The two exposures were aligned and added. A set of rows was defined as the aperture corresponding to the H II region. Cosmic rays in the proximity of emission lines were identified using *rimcursor*. Co-ordinates for identified cosmic rays were stored in a text file, which was used as input to the *imedit* task to remove cosmic rays within the aperture. Cosmic rays missed by this task were removed manually using *epix*.

Individual flux-calibrated frames were finally combined into a single sky-subtracted two-dimensional galaxy image with most of the cosmic rays removed. Any remaining cosmic rays were observed to lie far outside of the rows and columns corresponding to the spectra of H II regions.

3.3.10 Aperture Extractions

One-dimensional spectra of calibrated flux versus wavelength were extracted from pre-defined apertures on the two-dimensional images. An "aperture" was defined as a set of rows encompassing the spectrum of an H II region. The spatial profile of the Hβ emission line was used to set the limit of each aperture. In most cases, each aperture was ten pixels or 6.9 arcsec wide. Since the underlying continuum was weak, tracing was not performed and optimal or variance-weighted extraction described by Massey et al. (1992) was not used to sum the pixels.

Multiple spectra were extracted for those galaxies with more than one H II region. Spectra were examined visually and rough estimates of line widths and fluxes for specific emission lines were made in preparation for more precise measurements (see Chapter 4). Data for each one-dimensional spectrum were written into text files, consisting of two-column lists of flux and wavelength values.

3.3.11 Checks

To check the flux calibration, exposures of the well–studied Galactic planetary nebula IC 2149 (Kohoutek and Martin 1981; Kaler 1983; Feibelman et al. 1994) were obtained on the final night. The value of $F(\mathrm{H}\alpha)/F(\mathrm{H}\beta)$ was measured to be 3.766 $\pm$ 0.016, which is consistent with 3.52 $\pm$ 0.35 measured by Kaler (1983).

3.4 Optical Spectroscopy at CFHT

Three nights (1999 April 9–11 UT) were awarded at CFHT. Spectra for two dIs were obtained on the first night until thick clouds prevented further observing. The dome was not opened on the second night due to fog, snow, and ice. Spectra for another three galaxies were obtained on the final night until about local midnight, when fog and high humidity mercifully ended the observing run.

3.4.1 Instrument Configuration and Image Acquisition

Optical spectroscopy was obtained using the Multi–Object Spectrograph (MOS) in the f/8 configuration. The characteristics of the instrumentation employed are listed in Table 3.10.

The MOS spectrograph uses focal–plane masks created from previously obtained images (Lefévre et al. 1994). For each galaxy, five–minute Hα exposures were obtained in imaging mode to locate possible H II regions. Figures 3.6 to 3.9 inclusive show the raw Hα images of four dIs for which spectra were successfully acquired. An Hα exposure for VCC 1448 did not reveal any compact H II regions.

For each Hα image, every potential H II region was marked and the coordinates were recorded into a text file. Slit masks were subsequently constructed on–line using a YAG laser. Slits for each H II region were constructed to be approximately 2″ wide

Property	Value
STIS2 CCD	
Maximum area	2048 × 2048
Pixel size	21 μm
Image scale	0.44 arcsec pix^{-1}
Effective field of view [a]	$9' \times 10'$
Gain	4.52 e^- ADU^{-1}
Read-noise (rms)	9.3 e^-
B600 Grating	
Groove density	600 lines mm^{-1}
Blaze λ (1st order)	5000 Å
Dispersion	2.24 Å pixel^{-1}
Spectral Resolution [b]	5.6 Å
Effective λ range [c]	3600–7000 Å
Slits (targets)	
Length	10 arcsec (23 pix)
Width	2 arcsec (4.6 pix)
Hole diameters	
Faint stars	3 arcsec (6.9 pix)
Bright stars	5 arcsec (11.5 pix)

Table 3.10: Properties of the Multi–Object Spectrograph configuration at CFHT. NOTES: [a] Spatial direction (east–west) and spectral direction, respectively. [b] Based on 2.5 pixels FWHM. [c] For slits placed at the centre of the field.

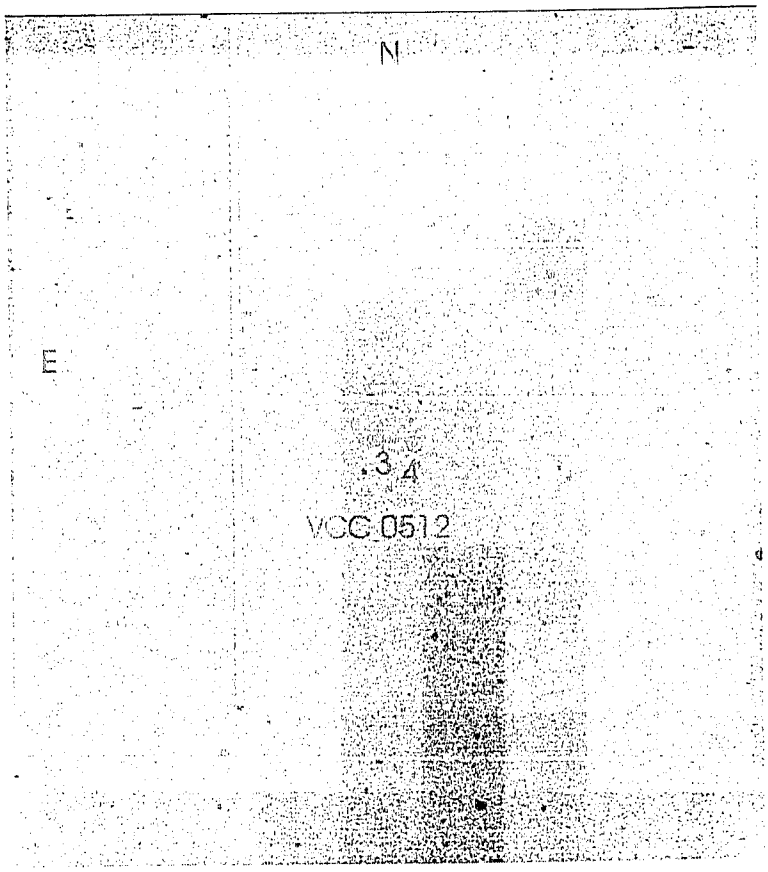

Figure 3.6: Five–minute Hα exposure of VCC 0512 (12°25) from MOS at CFHT. North is at the top and East is to the left. The image has not been corrected for continuum emission. The 5.'1 by 5.'7 frame is displayed as a "negative" so black objects on the image indicate bright sources. Two H II regions (labelled 3 and 4) are identified, over which small east–west slits were placed for spectrophotometry. The white vertical stripe is due to a set of bad columns on the CCD. This image may be compared with R–band and continuum–subtracted Hα images for 12°25 obtained by Gallagher and Hunter (1989: Fig. 1, Plate 26).

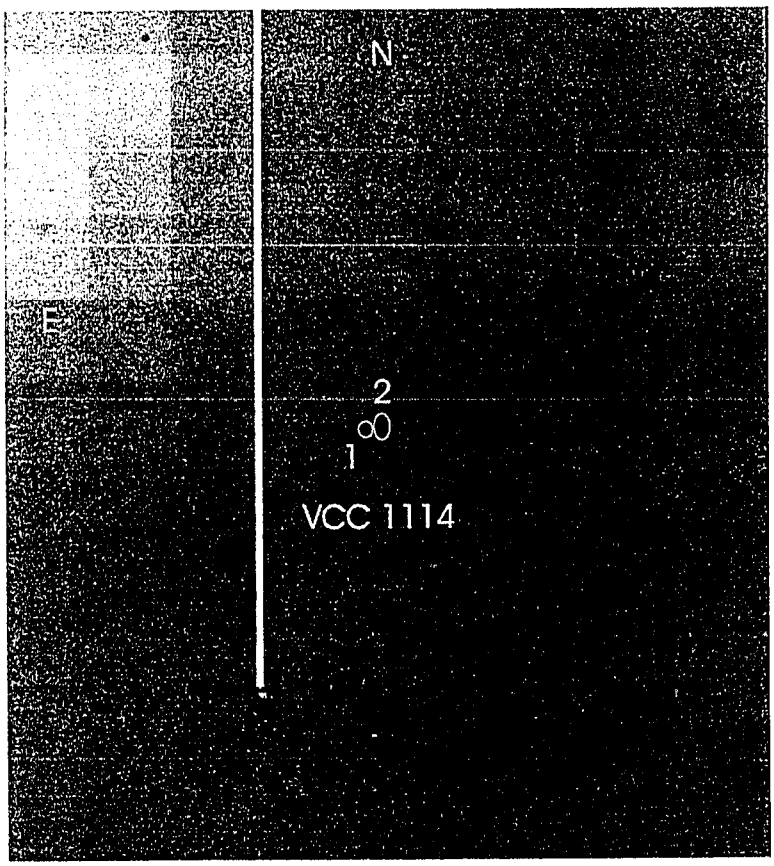

Figure 3.7: Five–minute Hα exposure of VCC 1114 (8°30) from MOS at CFHT. North is at the top and East is to the left. The image has not been corrected for continuum emission. The 5.'1 by 5.'7 frame is displayed as a "negative", so black objects on the image indicate bright sources. Two H II regions (labelled 1 and 2) are identified, over which small east–west slits were placed for spectrophotometry. The white vertical stripe is due to a set of bad columns on the CCD. This image may be compared with R–band and continuum–subtracted Hα images for 8°30 obtained by Gallagher and Hunter (1989: Fig. 1, Plate 21).

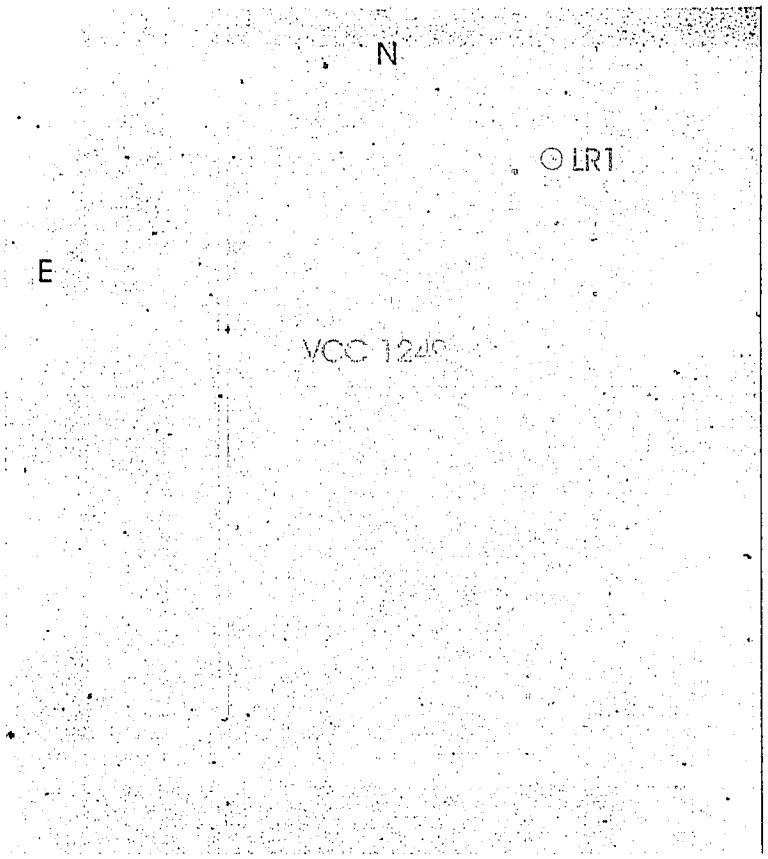

Figure 3.8: Five–minute raw Hα exposure of VCC 1249 (UGC 7636) from MOS at CFHT. North is at the top and East is to the left. The image has not been corrected for continuum emission. The 5.′1 by 5.′7 frame is displayed as a "negative" so black objects on the image indicate bright sources. There is faint, diffuse Hα emission at the position of the galaxy (centre of the image). To the northwest, a new H II region (LR1; see Chapter 6) was identified, over which a small east–west slit was placed for spectrophotometry. The white vertical stripe is due to a set of bad columns on the CCD.

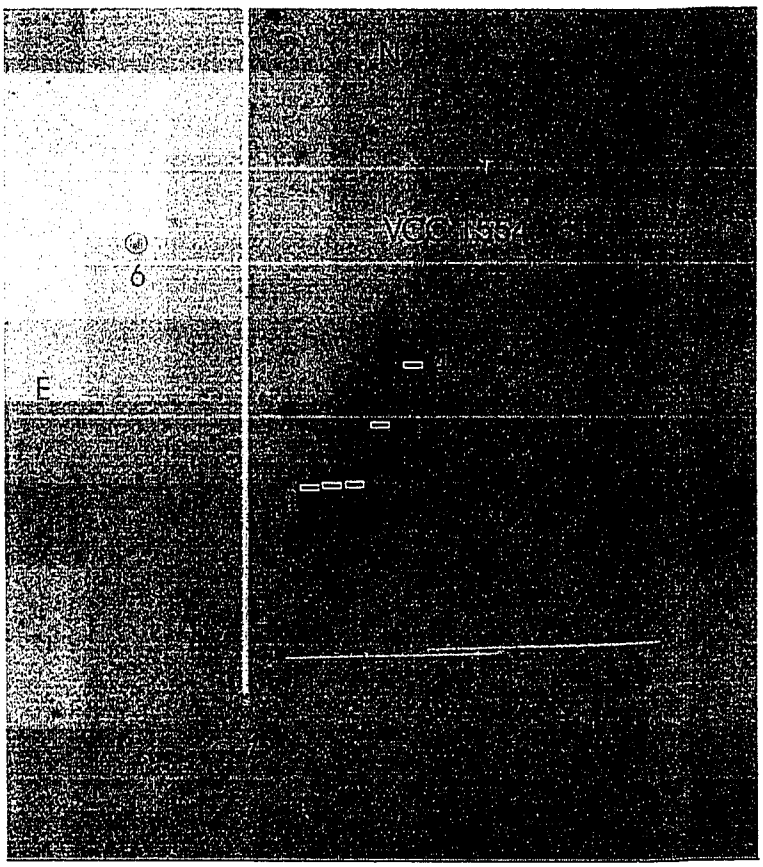

Figure 3.9: Five–minute raw Hα exposure of VCC 1554 (NGC 4532) from MOS at CFHT. North is at the top and East is to the left. The image has not been corrected for continuum emission. The 5′.1 by 5′.7 frame is displayed as a "negative" so black objects on the image indicate bright sources. Five large H II regions (labelled 1–5) and two additional emission–line objects (labelled 6 and 7) are identified, over which small east–west slits were placed for spectrophotometry. Slits for H II regions 1–5 are drawn here for visibility. The position of H II region "1" relative to the main body of the galaxy appears to be analogous to that of the 30 Doradus nebula in the Large Magellanic Cloud. The white vertical stripe is due to a set of bad columns on the CCD.

and 10″ long. Sky slits of the same size were placed near target slits. For pointing, holes with diameters 3″ and 5″ were created in the mask to transmit faint and bright stars, respectively, in the field of view.

The spectral coverage varied for each object, depending on its location within the field of view. For the most part, the spectral coverage was between 3600 Å and 7200 Å. For VCC 1249 (UGC 7636), the position of the H II region, LR1, was near the top of the field (Figure 3.8). Because of the position of the slit, the spectral range was cut off redwards of 6700 Å.

Spectral traces of objects at the centre of the field of view were aligned perpendicular to the slit. Spectra of objects farther away from the centre exhibited concave "bowing."

Spectra of a neon–argon–mercury (Ne–Ar–Hg) arc–lamp and the standard star Feige 67 were acquired to wavelength– and flux–calibrate, respectively, the object spectra. Illuminated dome flat–field exposures were obtained to remove pixel–to–pixel sensitivity variations. From the dome flats, a two per cent variation in raw counts was found from the edge to the centre of the slit. Since five slit masks (one for each galaxy) were inserted into the mask slide on a given night, there was insufficient time to accquire twilight flats for all masks. No emission–line flux standard was observed.

3.4.2 Reductions

A diagram showing the flow of reductions for the CFHT data is shown in Figure 3.10. Rows and columns were parallel to the spatial and wavelength axes, respectively. Reductions of the CFHT data proceeded similarly to those of the Kitt Peak data. However, there were four key differences. First, owing to the small slit sizes, the slit function or illumination across each slit was assumed to be constant over the

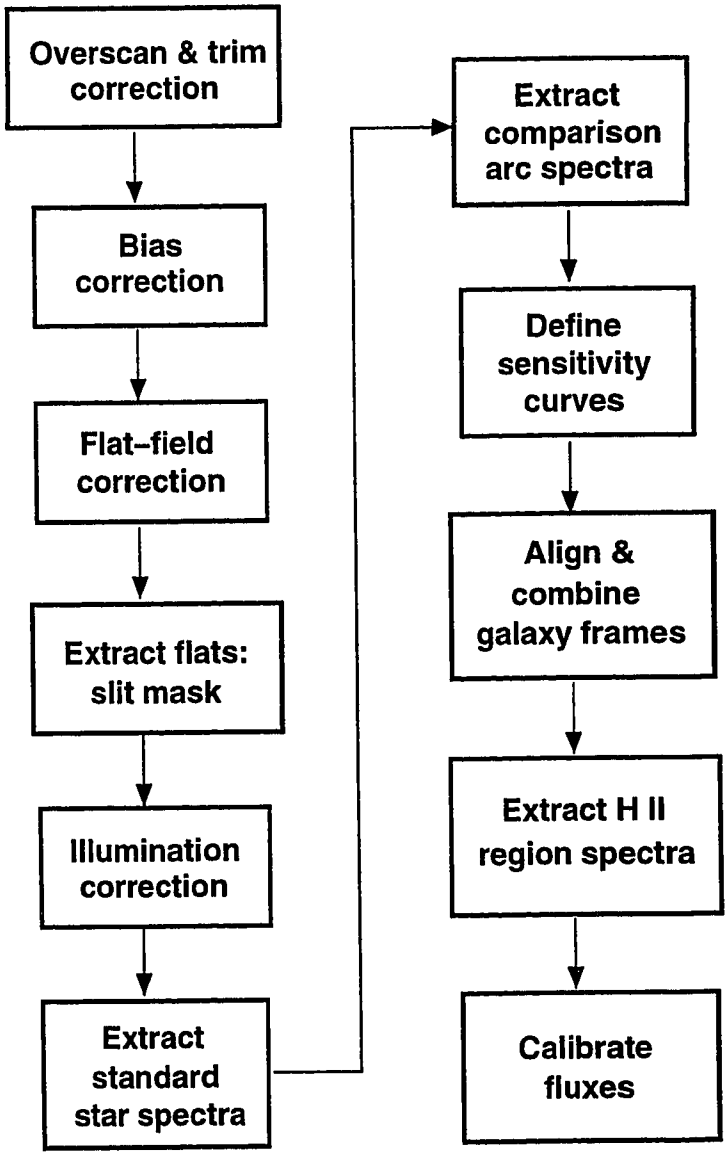

Figure 3.10: Reductions flowchart for CFHT data.

entire slit. Second, no correction for geometric distortions was required, because the position of each target galaxy was at the centre of the frame. Third, for a given galaxy, subsections of dome flat exposures corresponding to the positions of H II regions were extracted. A different task (*apflatten*) was used to remove large–scale response variations in the dispersion direction, leaving behind pixel–to–pixel variations only (Massey et al. 1996).

The sensitivity function was assumed to be constant from slitlet to slitlet on a given night. To check this, two exposures of Feige 67 were obtained with the slit mask for VCC 1114 on the first night and two exposures of Feige 67 were obtained with the slit mask for VCC 1448 on the final night. For the VCC 1114 mask, two five–minute exposures were obtained through the same slit (H II region #2 in Figure 3.7) near the centre of the galaxy. For the VCC 1448 mask, a one–minute exposure was taken with the star centred on a slit at the centre of the galaxy and a four–minute exposure was taken with the star centred on another slit, located 107 pixels (47 arcsec) from the first slit. The shapes of the sensitivity curves for each night were similar. For a given night, an average response curve was obtained and used to flux–calibrate object spectra.

Spectroscopic frames for each galaxy were aligned and combined. In the process, most cosmic rays were subsequently removed using *ccdclip*. After visual inspection of images, additional cosmic rays were identified and removed manually.

Apertures corresponding to H II regions were carefully defined to optimize signal quality. Good background subtraction was difficult to achieve, because the slit size was small and the background signal was dominated by the galaxy. Data were extracted for each aperture and averaged to yield one–dimensional spectra; sky subtraction was performed during extraction. These spectra were subsequently corrected onto a linear wavelength scale, and flux–calibrated using the standard star spectra.

3.5 Optical Spectra of Dwarf Galaxies

3.5.1 Spectra of Dwarf Irregulars in the Field

Representative spectra for each of the five field dIs observed at Steward Observatory are shown. [O III]λ4363 was detected in at least one H II region of all dIs except NGC 1560. The spectra are shown in Figures 3.11 and 3.12.

3.5.2 Spectra of Dwarf Irregulars in Virgo

Spectra observed for each Virgo dI are illustrated. The [O III]λ4363 line was detected in two H II regions: VCC 0848–1 and VCC 1554–1. These two spectra are shown in their entirety in Figure 3.13.

To highlight faint lines, Figures 3.14 and 3.15, respectively, give magnified views of the "blue" (3700 Å to 5500 Å) and the "red" (5500 Å to 7300 Å) portions of the spectrum of VCC 0848. In each figure, bright emission lines are labelled in the top panel and faint emission lines are labelled in the bottom panel. Similarly, magnified versions of blue and red spectra for VCC 1554–1 are shown in Figures 3.16 and 3.17, respectively.

For the remaining dIs where [O III]λ4363 was not detected, the spectra are shown in Figures 3.18 to 3.20 inclusive. The best spectrum for each dI is shown. The following emission lines were observed in all spectra: [O II]λ3727, Hβ, [O III]$\lambda\lambda$4959, 5007, Hα, [N II]λ6583, and [S II]$\lambda\lambda$6716, 6731, except VCC 1249–1 where the spectral range did not extend redwards of 6700 Å.

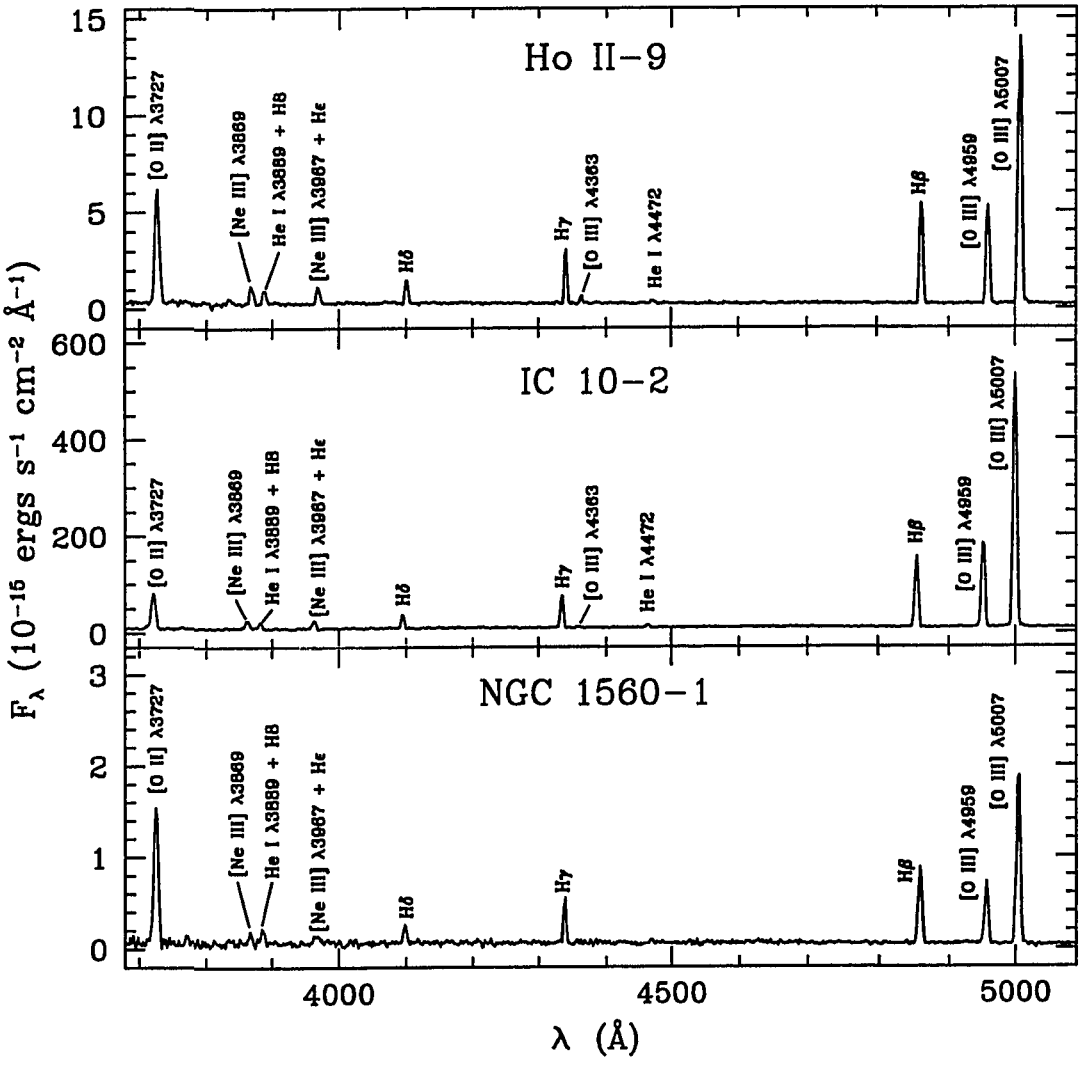

Figure 3.11: Optical emission-line spectra of Holmberg II-9, IC 10-2, and NGC 1560-2 from Steward Observatory. The observed flux per unit wavelength is plotted versus wavelength. Key emission lines are labelled.

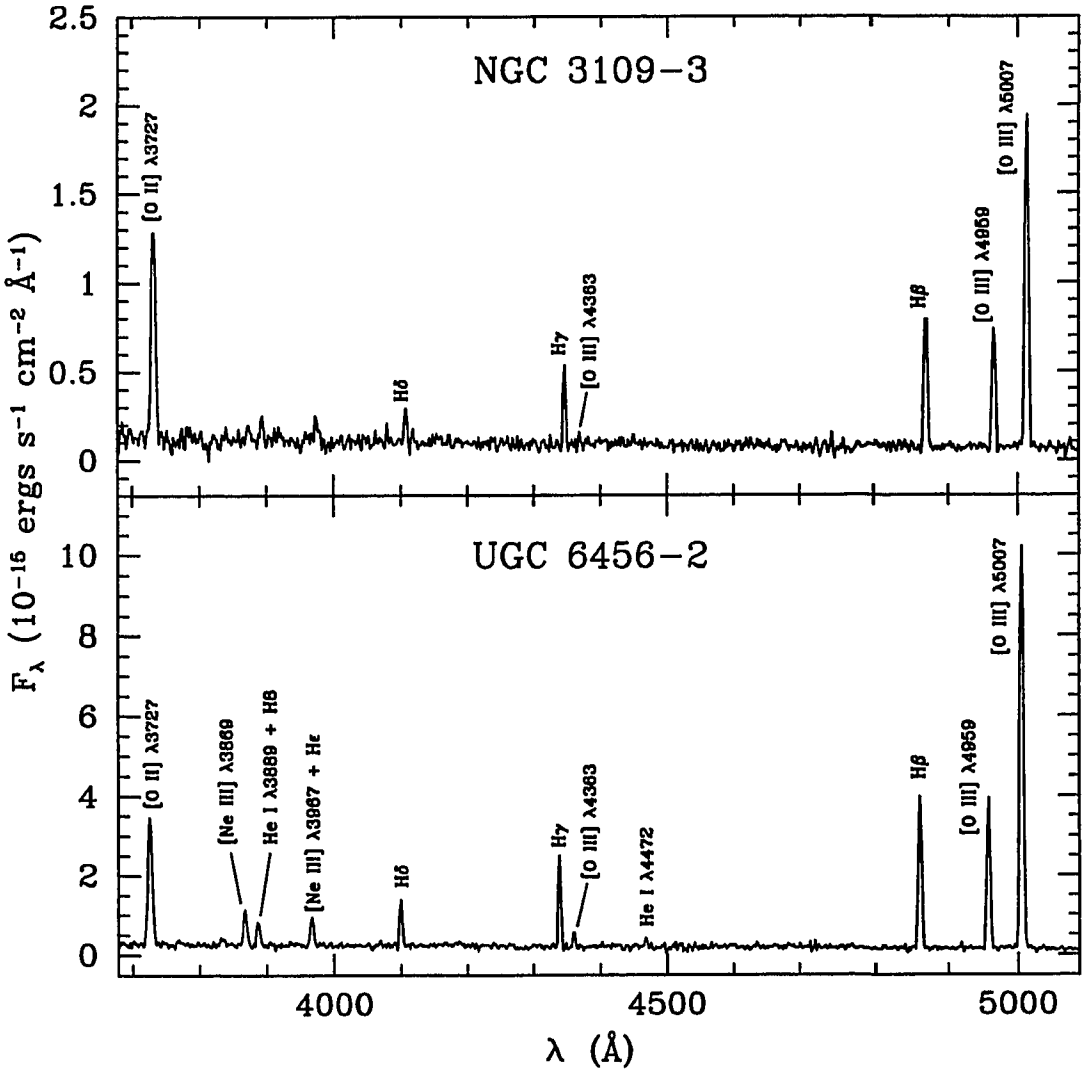

Figure 3.12: Optical emission–line spectra of NGC 3109–3 and UGC 6456–2 from Steward Observatory. The observed flux per unit wavelength is plotted versus wavelength. Key emission lines are labelled.

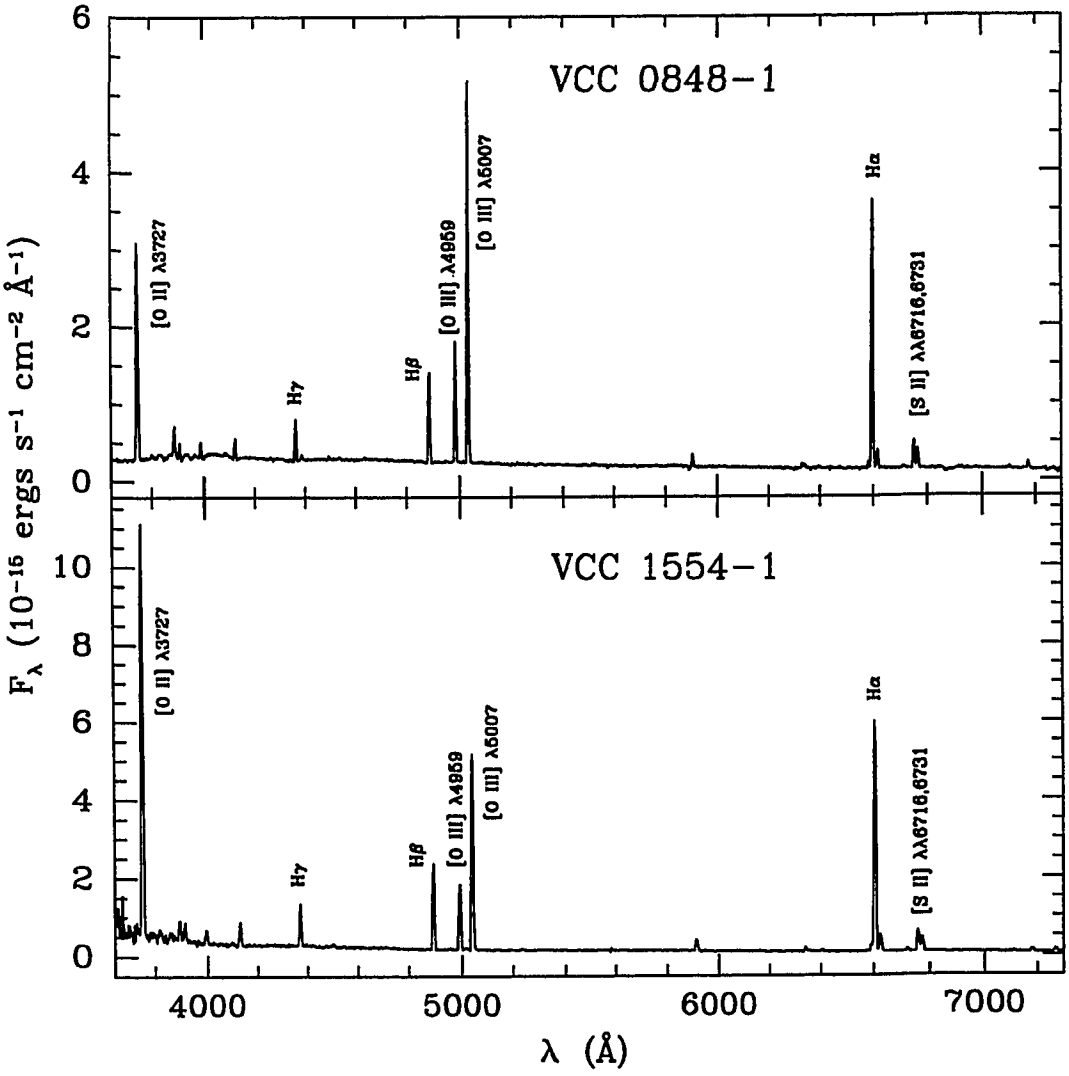

Figure 3.13: Optical emission-line spectra of VCC 0848–1 and VCC 1554–1: the observed flux per unit wavelength is plotted versus wavelength. Key emission lines are labelled.

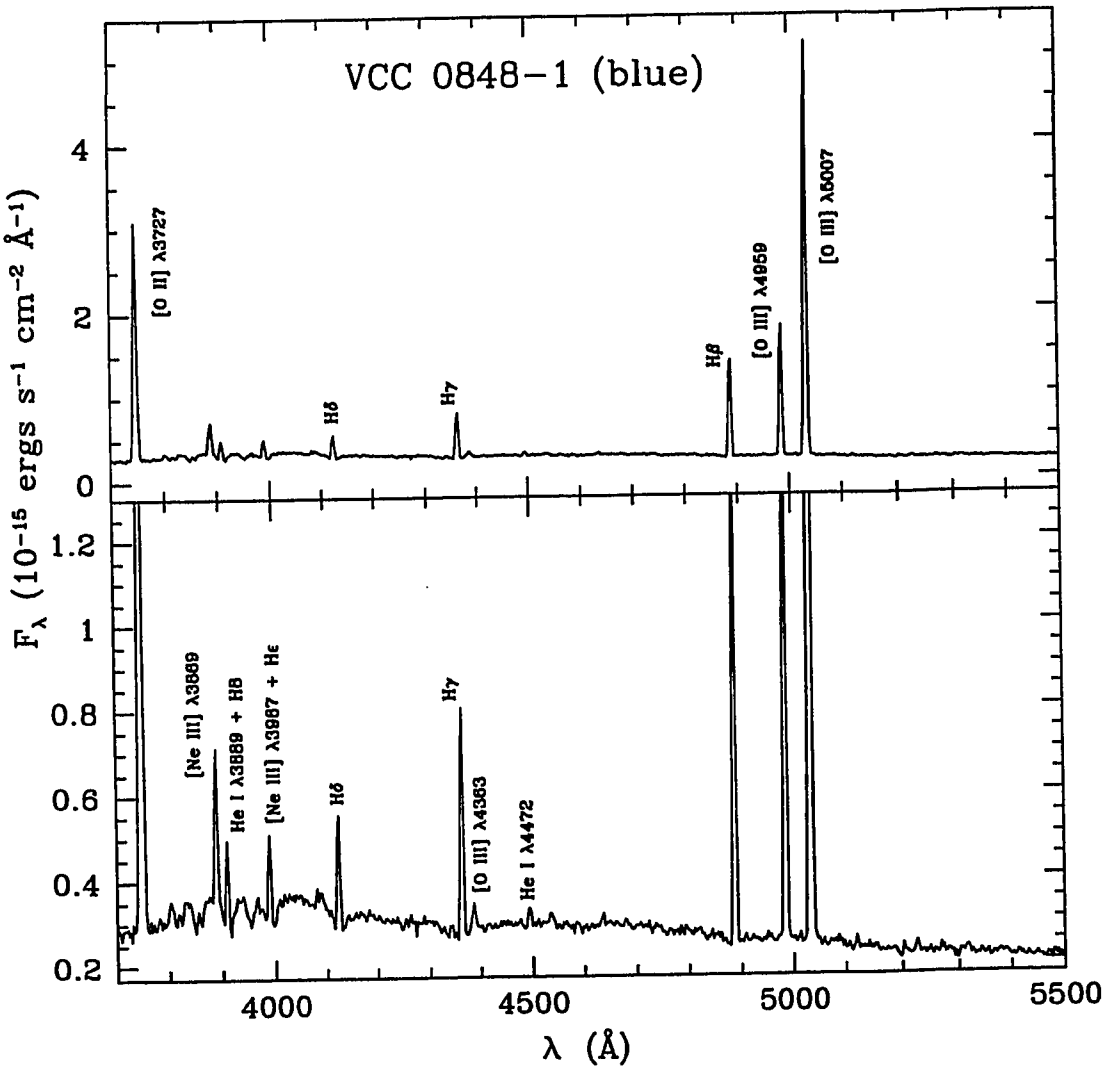

Figure 3.14: VCC 0848-1: "Blue" region (3700 Å to 5500 Å) of spectrum; observed flux per unit wavelength versus wavelength is shown. Top panel: Bright lines are labelled. Bottom panel: Additional faint lines are labelled, including [O III]λ4363.

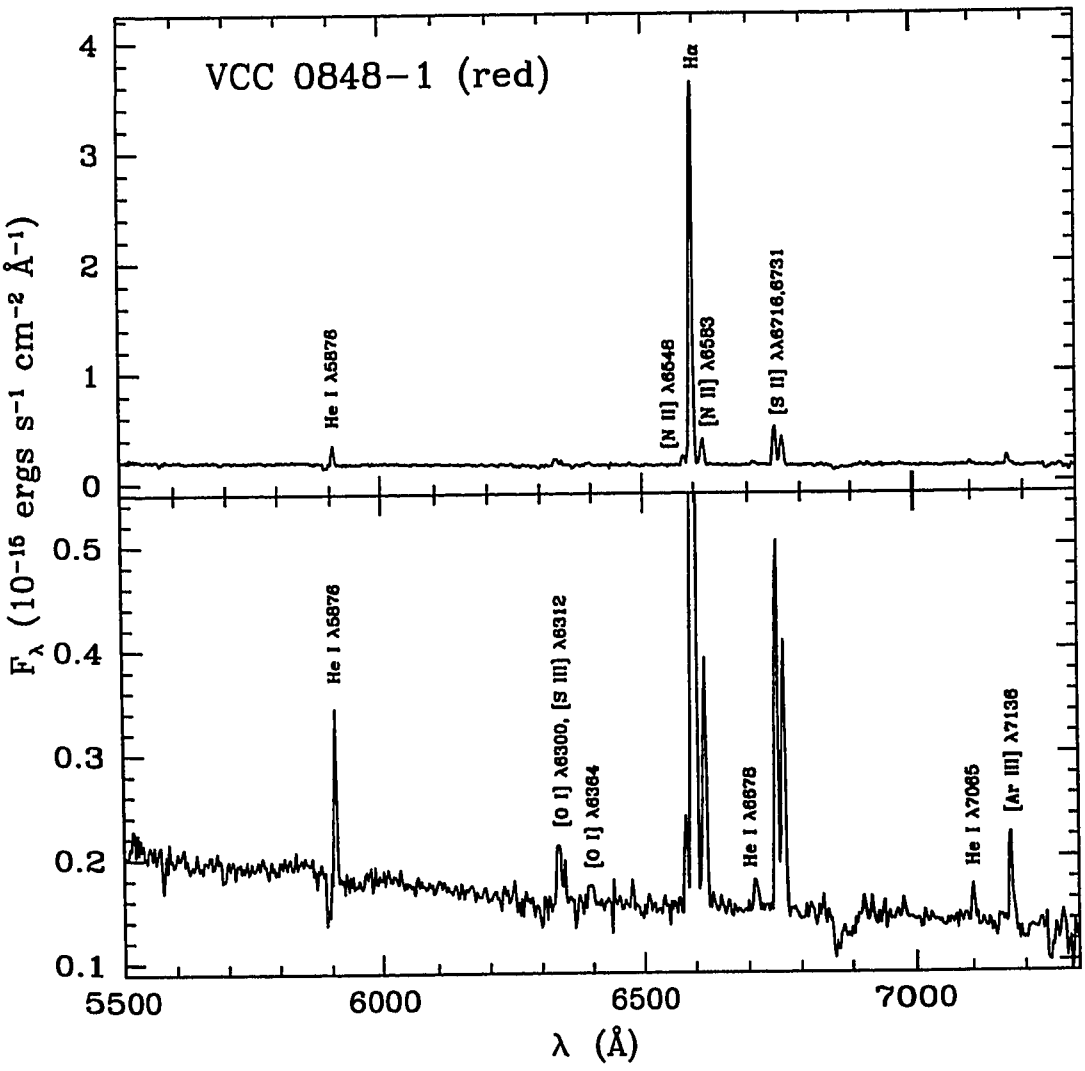

Figure 3.15: VCC 0848–1: "Red" portion (5500 Å to 7300 Å) of spectrum; observed flux per unit wavelength versus wavelength is shown. Top panel: Bright lines are labelled. Bottom panel: Additional fainter lines are indicated.

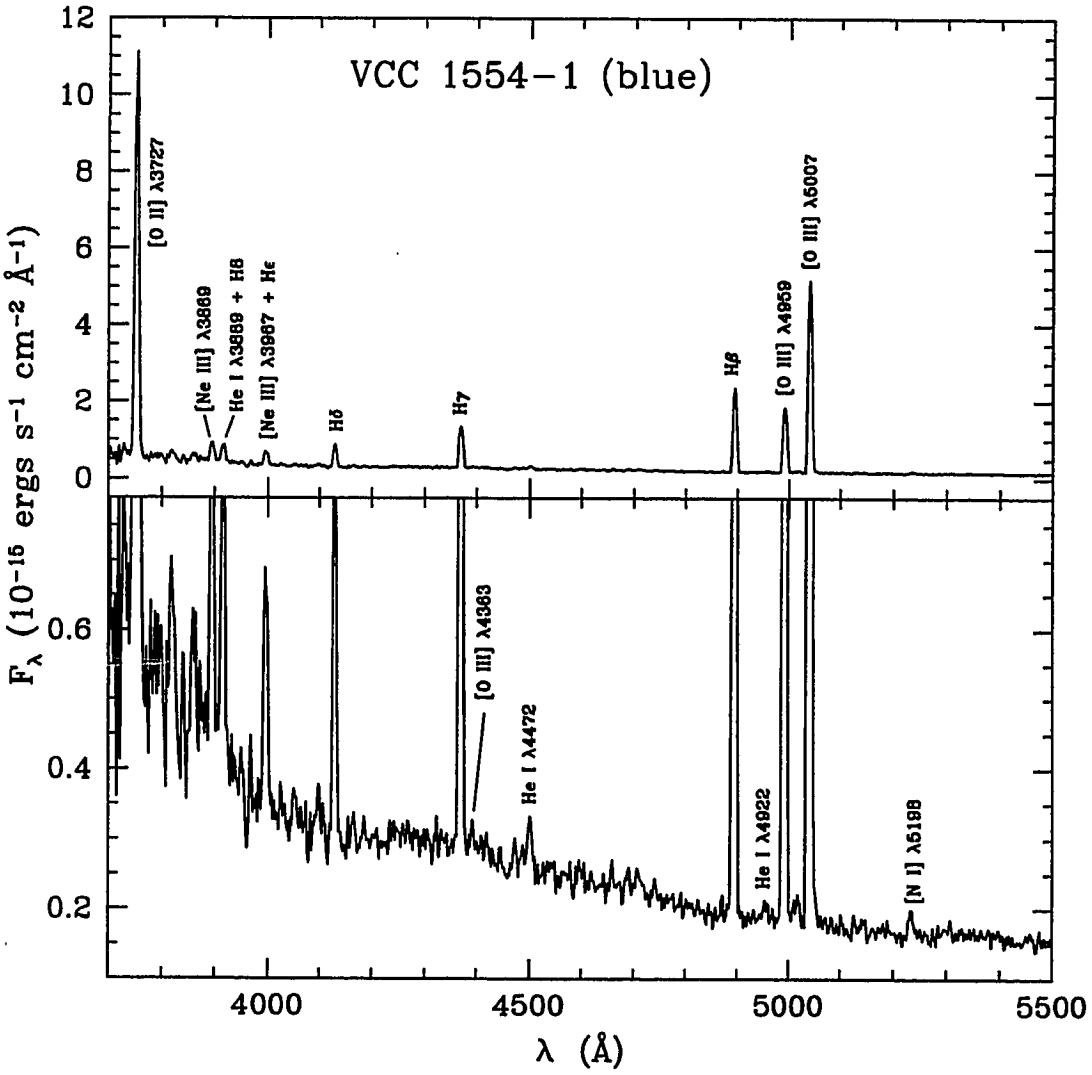

Figure 3.16: VCC 1554–1: "Blue" portion (3700 Å to 5500 Å) of spectrum; observed flux per unit wavelength versus wavelength is shown. Top panel: Bright lines are labelled. Bottom panel: Additional faint lines are labelled, including [O III]λ4363.

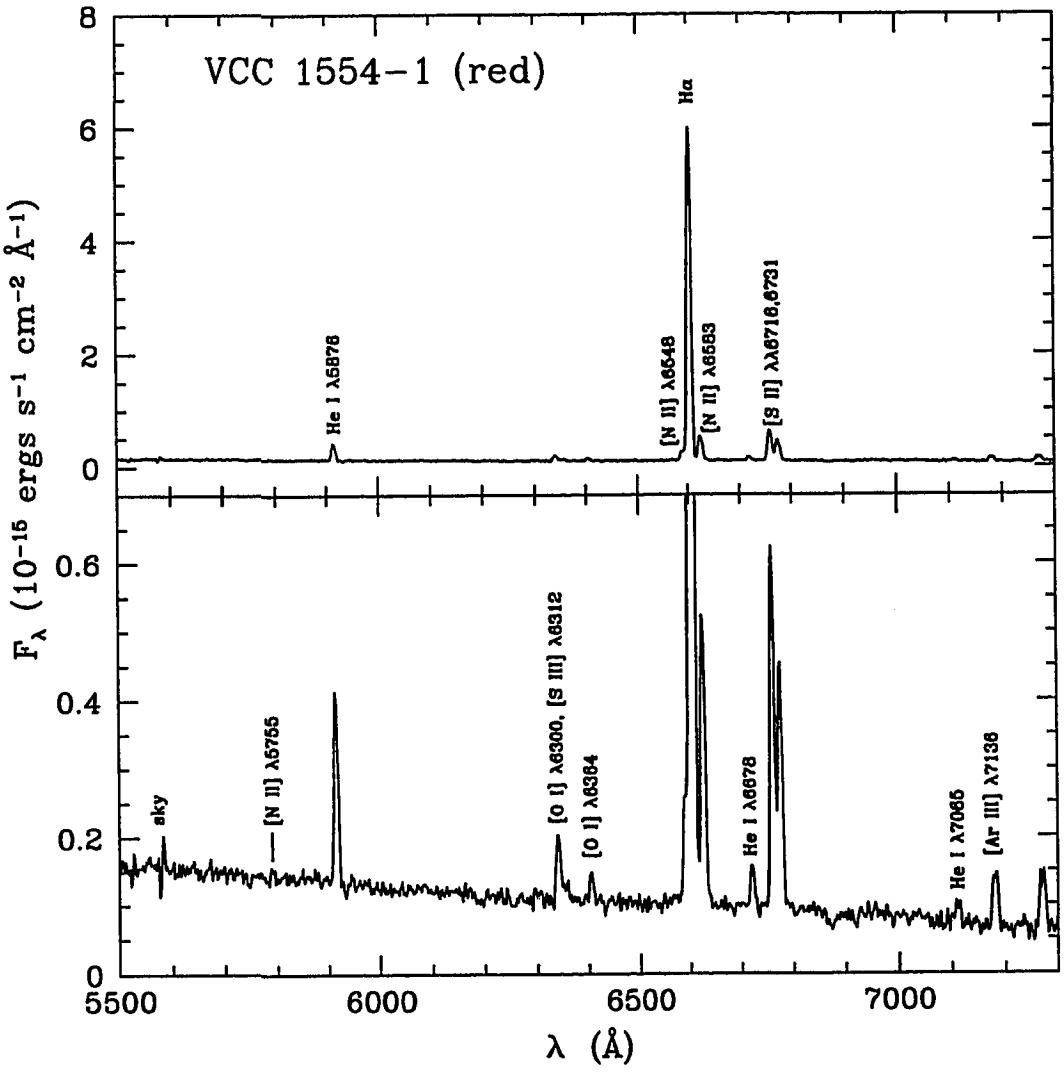

Figure 3.17: VCC 1554–1: "Red" portion (5500 Å to 7300 Å) of spectrum; observed flux per unit wavelength versus wavelength is shown. Top panel: Bright lines are labelled. Bottom panel: Additional faint lines are labelled, including [N II]λ5755.

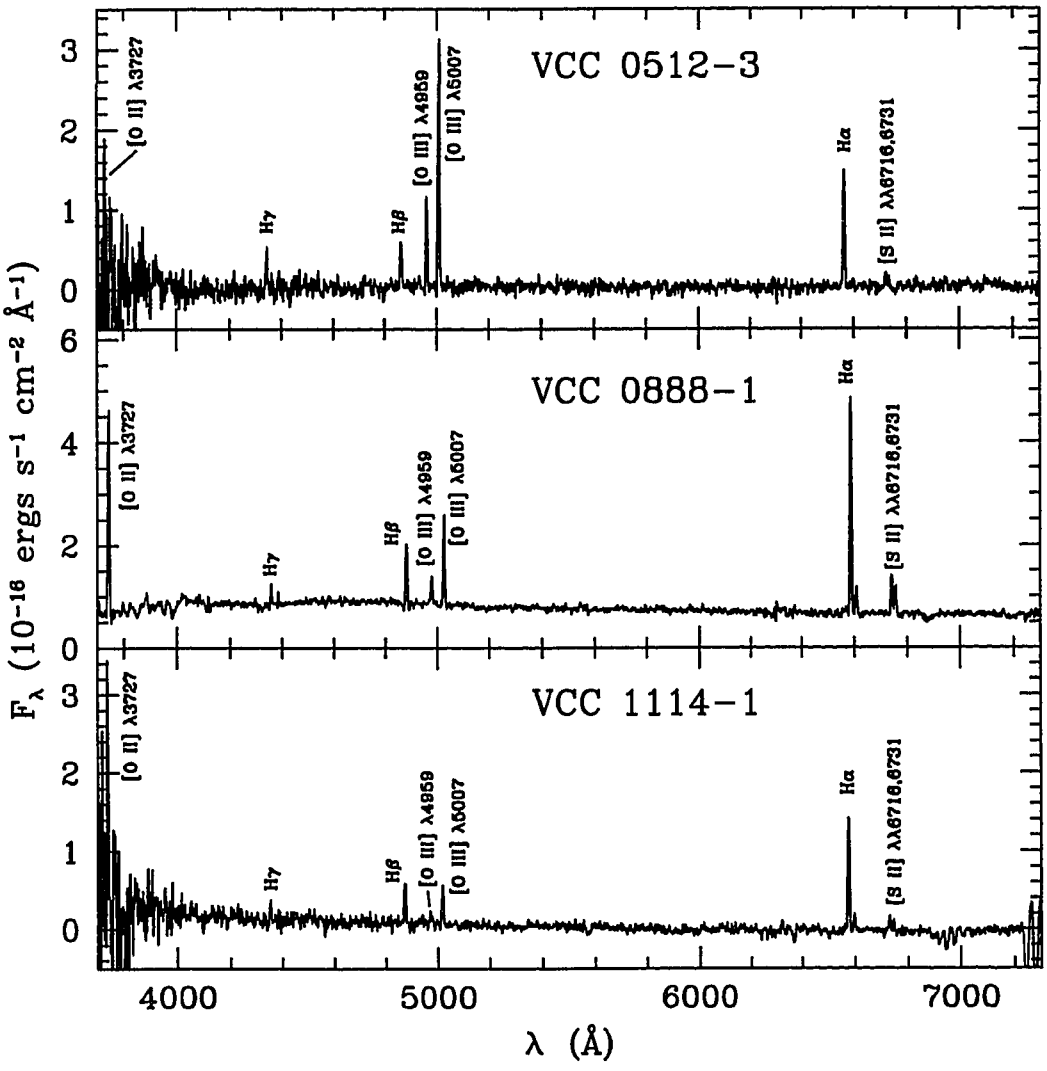

Figure 3.18: Optical spectra of VCC 0512–3, VCC 0888–1, and VCC 1114–1: observed flux per unit wavelength versus wavelength. Key emission lines are labelled.

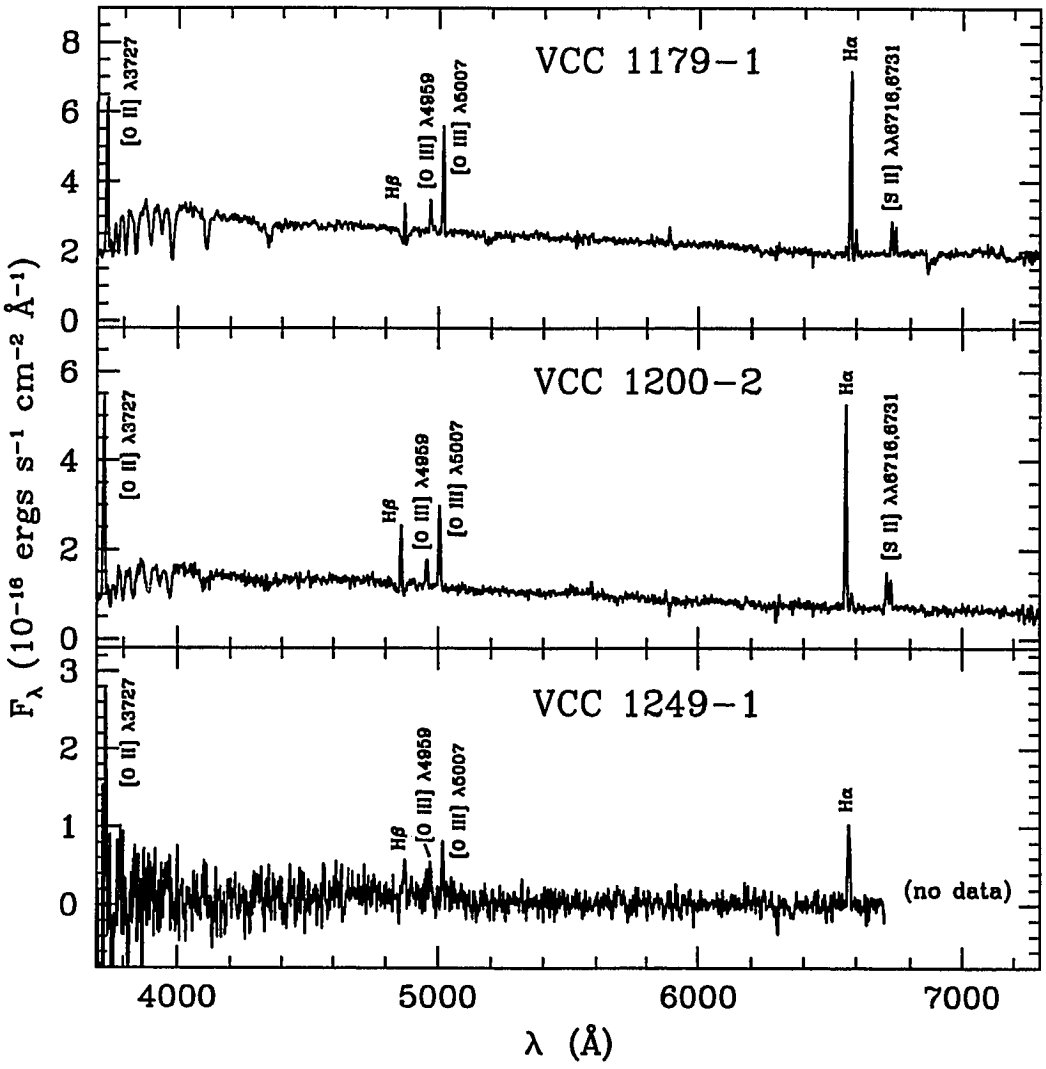

Figure 3.19: Optical spectra of VCC 1179–1, VCC 1200–1, and VCC 1249–1: observed flux per unit wavelength versus wavelength. Key emission lines are labelled. Note the underlying absorption at Hβ for VCC 1179–1 (see § 4.1.1) and VCC 1200–2.

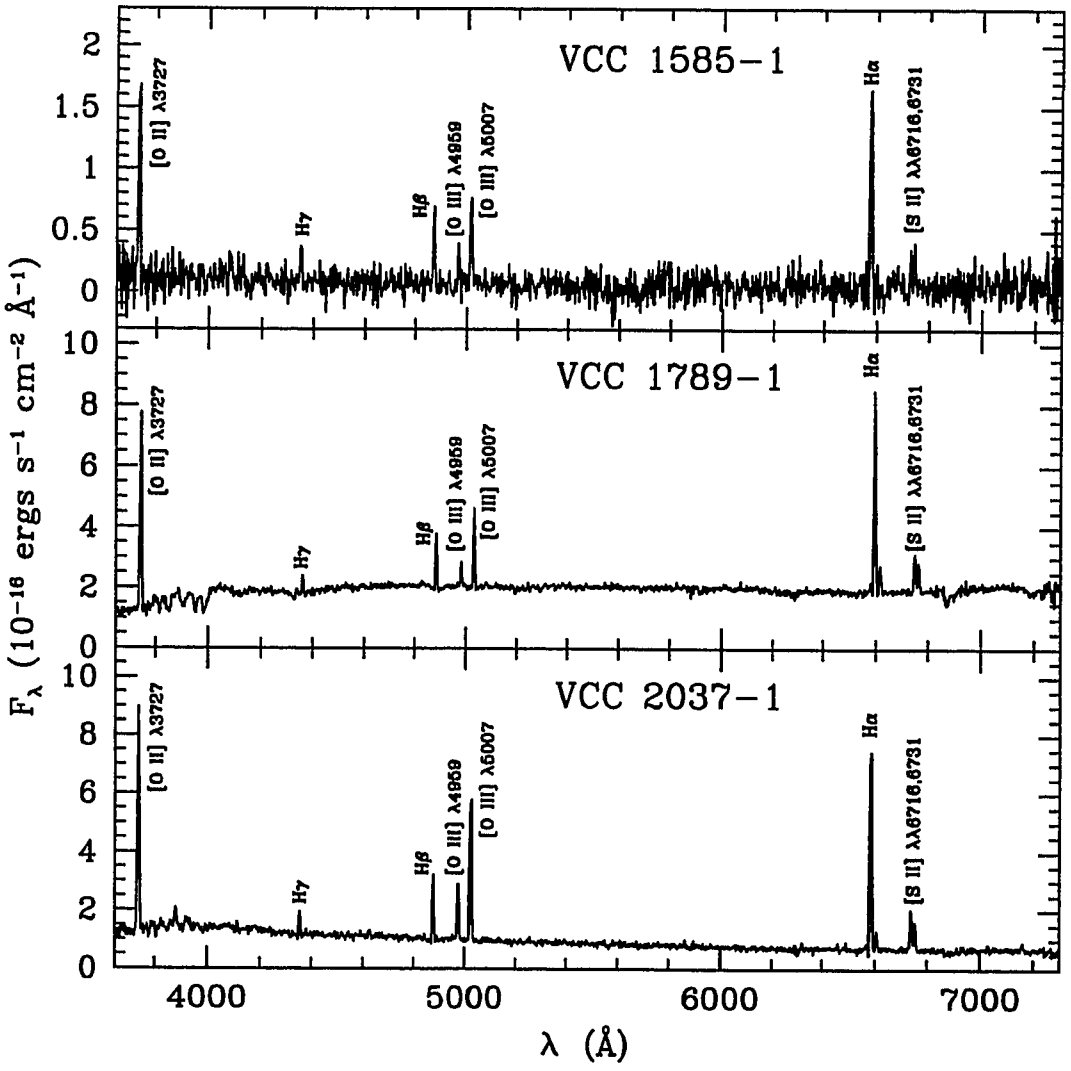

Figure 3.20: Optical spectra of VCC 1585–1, VCC 1789–1, and VCC 2037–1: observed flux per unit wavelength versus wavelength. Key emission lines are labelled.

Chapter 4

Measurements and Analyses of Spectra

Measurements and the analyses of spectra are presented in this chapter. The method by which emission line fluxes are measured is explained in § 4.1. Methods to correct flux ratios for underlying Balmer absorption and reddening are presented in § 4.2. Flux and intensity ratios for H II regions in field dIs and Virgo dIs are listed in § 4.3 and § 4.4, respectively. Derived quantities will be discussed and presented in the next chapter.

4.1 Measuring Line Fluxes

The method used to measure fluxes in emission lines is described here. Underlying Balmer absorption arising from the stellar continuum is also discussed. At Hβ, it was possible to fit simultaneously the emission line and the underlying absorption to obtain directly the equivalent width of each. The determination of upper limits to undetected emission lines (e.g., [O III]λ4363) is discussed also. Note that the heliocentric velocities of Virgo dIs are generally $\gtrsim 250$ km s^{-1}, which shifts the [O III]λ4363 line to longer wavelengths, away from contamination due to the Hg Iλ4358 sky line.

Measurements of emission lines were obtained with INTENS software which was developed by M. McCall and L. Mundy. The software is a non–interactive nonlinear least–squares fitting program which can derive the properties of emission and/or absorption lines in one–dimensional spectra (flux versus wavelength) or two–dimensional spectra (flux versus wavelength as a function of position in an image). All spectra analyzed in the present study were one–dimensional.

To measure line properties, especially fluxes, the user creates an input file containing information about the spectral data. The user specifies wavelength zones, where each zone is defined by a lower and an upper wavelength limit. Within each zone, the user can list up to five spectral lines to be simultaneously fitted. The software fits an integrated Gaussian profile[1] to each spectral line and solves for the velocity, the full width at half maximum, integrated flux, and equivalent width. The returned output includes a text file, summarizing the results and their errors, and plots of fits and residuals for the spectral lines in each wavelength zone. Fits were made to the following emission lines:[2] [O II]λ3727, Hγ, [O III]λ4363 (when detected), Hβ, [O III]λ4959, [O III]λ5007, [N II]λ6548, Hα, [N II]λ6583, and [S II]$\lambda\lambda$6716, 6731.

The [O III]λ4363 line was detected in only two of the dIs in the Virgo sample, so an upper limit to the flux was estimated for the remaining dwarfs. A two–sigma upper limit to the [O III]λ4363 flux was computed as the product $2.51Aw$, where A is two times the root–mean–square of the underlying counts in the continuum immediately surrounding the [O III]λ4363 line, w is the full width at half maximum of the line obtained from a fit of the nearest strong line, and the numerical factor is the square root of 2π. Because of its close proximity, the width of Hγ was adopted for the width

[1] An integrated Gaussian profile is a Gaussian profile which is discretely sampled by bins of width equal to the width of each pixel.

[2] These lines are observed in most cases, but this is by no means a complete list; see VCC 0848–1 (Table 4.12) and VCC 1554–1 (Table 4.14).

of [O III]λ4363. Where appropriate, two-sigma upper limits to [O III]λ4363 are given in Tables 4.12 to 4.15.

4.1.1 Underlying Balmer Absorption

McCall et al. (1985) found that stellar flux contributes most to the continuum in the optical in the spectra of extragalactic H II regions. Underlying Balmer absorption results in smaller Balmer line fluxes and can lead to underestimates of Balmer emission equivalent widths[3], overestimates of the reddening, and, because emission lines are referenced to Hβ, overestimates of fluxes of forbidden lines relative to Hβ. Most workers have reported in the literature a correction of about 2 Å for the underlying Balmer absorption (see McCall et al. 1985). Here, it was possible to make a direct measurement of the underlying Balmer absorption.

Owing to sufficient spectral resolution and strong continua, a few of the spectra exhibited obvious underlying Balmer absorption, especially at Hβ (e.g., Figure 3.19). Fits of emission and absorption profiles at Hβ allowed for a direct determination of the equivalent width of the underlying Balmer absorption. A measurement of the Hβ equivalent width is applicable to any Balmer line, owing to the flatness of the Balmer decrement in absorption.

Using INTENS, "emission-only" and "emission-plus-absorption" profiles were fitted separately at Hβ. Emission and absorption profiles were both assumed to be integrated Gaussians. Profile fits for the H II region VCC 1179–1 are illustrated in Figure 4.1, where fits at Hβ, [O III]λ4959, and [O III]λ5007 are shown.

The effective equivalent width of the underlying absorption at Hβ is obtained by taking the difference of the emission equivalent width of the "emission-only" line fit

[3]An equivalent width of a spectral line, W (in Å), is the width of the continuum containing the same energy as the line.

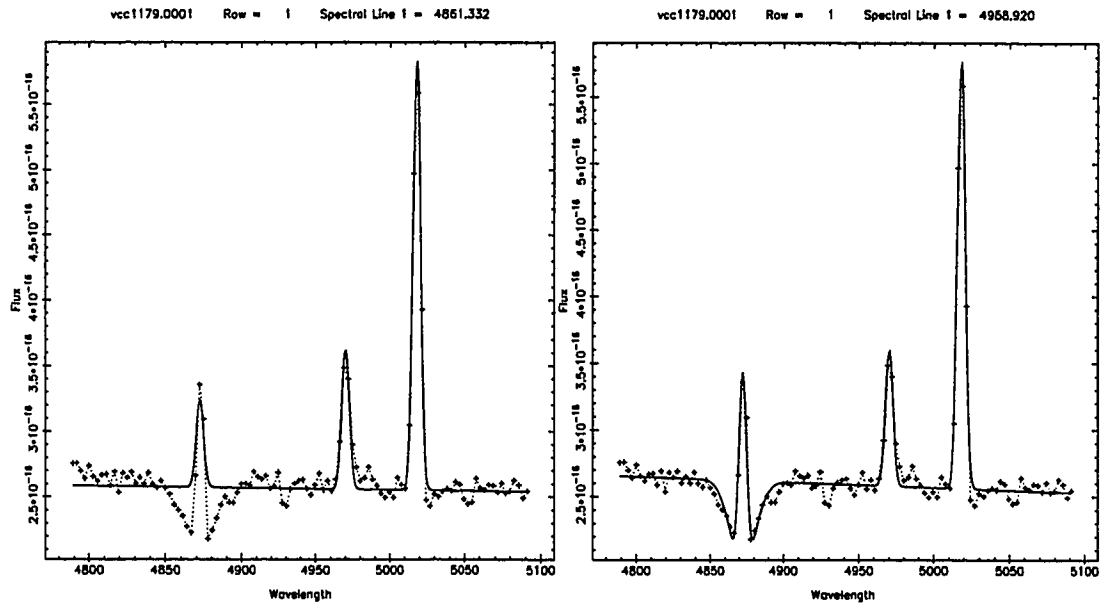

Figure 4.1: Line profile fits at Hβ, [O III]λ4959, and [O III]λ5007 for H II region VCC 1179–1: observed flux (ergs s^{-1} cm^{-2} $Å^{-1}$) versus wavelength (Å). The dotted line connects consecutive data points. The solid line is a fit to the lines and continuum. LEFT panel: A profile fit at Hβ is obtained assuming that the line consists only of emission. The equivalent width of the emission line profile is 1.61 ± 0.23 Å. RIGHT panel: An emission line profile and an absorption line profile are simultaneously fit at Hβ. The equivalent widths of the emission line and the absorption line are 3.73 ± 0.21 Å and 5.44 ± 0.42 Å, respectively. Thus, the effective equivalent width of the underlying absorption at Hβ is 2.12 ± 0.31 Å, which is the difference between the emission equivalent width derived from the "emission–only" fit and the emission equivalent width from the "emission–plus–absorption" fit.

and the emission equivalent width determined from the "emission plus absorption" fit. Effective equivalent widths for underlying Balmer absorption at Hβ are given in Table 4.1. From the values listed in column (5), the average equivalent width for

VCC dI H II region (1)	EW at Hβ in emission only, $W(\mathrm{H}\beta)_e$ (Å) (2)	EW of Hβ emission in simultaneous fit (Å) (3)	EW of Total Absorption at Hβ (Å) (4)	Eff. EW of underlying absorption at Hβ, $W(\mathrm{H}\beta)_{abs}$ (Å) (5)
0848–1	33.69 ± 0.57	...	...	...
0888–1	9.01 ± 0.33	10.40 ± 0.40	4.99 ± 0.94	1.38 ± 0.52
0888–2	6.59 ± 0.31	7.77 ± 0.37	4.61 ± 0.95	1.19 ± 0.49
1114–1	47.0 ± 5.9	...	...	...
1114–2	260 ± 130	...	...	...
1179–1	1.61 ± 0.23	3.73 ± 0.21	5.44 ± 0.42	2.12 ± 0.31
1179–2	6.09 ± 0.28	7.80 ± 0.32	4.58 ± 0.58	1.72 ± 0.43
1179–3	13.79 ± 0.66	...	...	...
1179–4	16.0 ± 1.9	...	...	...
1200–2	6.85 ± 0.43	9.52 ± 0.51	7.3 ± 1.0	2.67 ± 0.66
1249–1	26.8 ± 5.9	...	...	...
1554–1	112.3 ± 6.8	...	...	...
1554–2	...[a]	...	...	...
1554–3	...[a]	...	...	...
1554–4	4.33 ± 0.33	...	...	...
1554–5	...[a]	...	...	...
1585–1	66 ± 13	...	...	...
1789–1	6.18 ± 0.18	7.13 ± 0.22	2.84 ± 0.45	0.94 ± 0.29
2037–1	15.03 ± 0.38	16.27 ± 0.49	4.29 ± 0.93	1.24 ± 0.62
2037–2	3.85 ± 0.47	5.33 ± 0.67	4.3 ± 1.4	1.48 ± 0.82

Table 4.1: Equivalent widths (EW) at Hβ for H II regions in Virgo dIs. Column (1) lists the H II region. Column (2) lists the equivalent width of the fitted line profile in emission only at Hβ (see Figure 4.1). Column (3) lists the equivalent width of the Hβ emission obtained from a simultaneous fit of absorption and emission (Figure 4.1). Column (4) lists the total equivalent width of the entire absorption profile from the simultaneous fit. Column (5) lists the effective equivalent width of the underlying absorption affecting Hβ emission. This effective equivalent width is the difference of column (2) and column (3). NOTE: [a] Negative equivalent width, because the continuum is negative.

underlying absorption at Hβ is

$$\langle W(\mathrm{H}\beta)_{\mathrm{abs}} \rangle = 1.59 \pm 0.56 \text{ Å}. \tag{4.1}$$

The error listed is the standard deviation. This result is consistent with that obtained by McCall et al. (1985), Díaz (1988), and González-Delgado et al. (1999).

Column (4) in Table 4.1 lists the equivalent width of the entire absorption line profile at Hβ. Results lie in the range between 3 to 7 Å. These values are consistent

with what is expected for OB associations with a normal initial mass function (McCall et al. 1985; Jaschek and Jaschek 1995). They imply that the H II regions have ages between 4 and 40 Myr (González-Delgado et al. 1999).

4.2 Correcting Emission Line Data

Corrections and analyses were performed with SNAP (Spreadsheet Nebular Analysis Package, Krawchuk et al. 1997). SNAP is an Excel module or add–in, where users can enter into spreadsheets observed fluxes, equivalent widths, and their errors for each spectral line in a given spectrum. Users can compute the reddening using a specified reddening law, apply equivalent width (underlying Balmer absorption) and reddening corrections to flux ratios, compute electron temperatures and electron densities from specified line ratios, and compute nebular (e.g., oxygen) abundances.

All observed Balmer flux ratios were first corrected for underlying Balmer absorption. An equivalent width of 2 Å (McCall et al. 1985) for the underlying absorption was adopted for spectra of H II regions in field dIs. For each spectrum of an H II region in a Virgo dI where underlying Balmer absorption was directly measured, the effective equivalent width (see Table 4.1) for the corresponding H II region was used to compensate for underlying Balmer absorption. In the remaining spectra where underlying Balmer absorption was not directly measured, the average equivalent width from Equation (4.1) was used. For these spectra, the emission equivalent widths at Hβ exceeded 15 Å. Using 2 Å as the equivalent width for the underlying absorption did not significantly alter the results[4].

Next, flux ratios were corrected for reddening. A sketch of this method is shown

[4]A possible exception is VCC 1554–4 where $W(\mathrm{H}\beta)_{\mathrm{e}} \sim 4$ Å. However, the oxygen abundance for VCC 1554 is adopted from the abundance derived from the [O III]λ4363 detection in the spectrum for VCC 1554–1, where $W(\mathrm{H}\beta)_{\mathrm{e}} \sim 110$ Å.

in Figure 4.2. A reddening, $E(B-V)$, was computed from Balmer flux ratios using

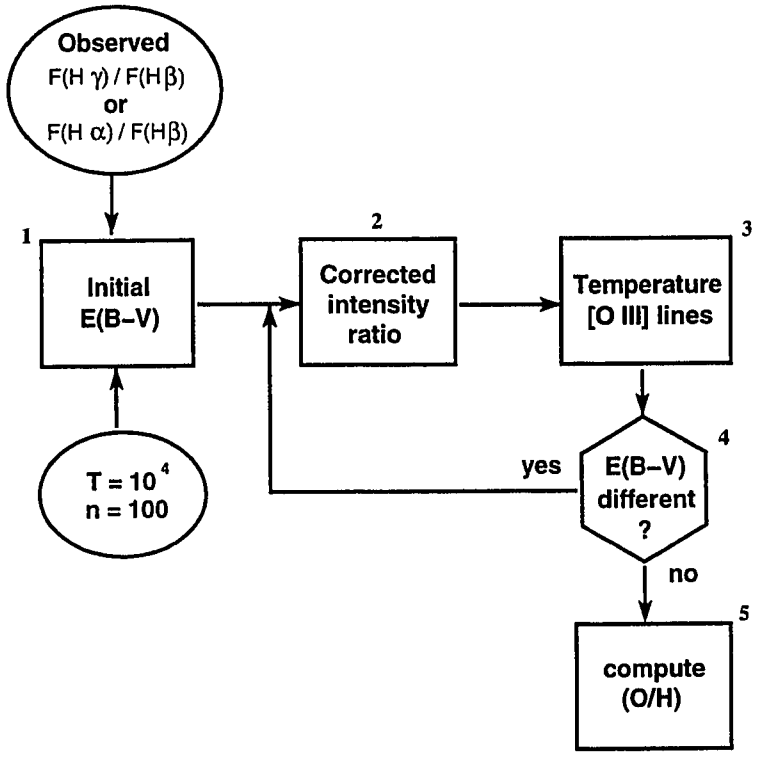

Figure 4.2: Method to correct flux ratios for reddening. Step 1: an initial estimate of the reddening, $E(B-V)$, is computed from $F(\mathrm{H}\gamma)/F(\mathrm{H}\beta)$ or $F(\mathrm{H}\alpha)/F(\mathrm{H}\beta)$, assuming an electron temperature of 10^4 K, and assuming an electron density 100 cm^{-3}. Step 2: flux ratios are corrected for reddening. Step 3: an electron temperature is computed from [O III]λ4363 and [O III]$\lambda\lambda$4959, 5007. Step 4: another reddening value is computed with the "new" temperature. If the new reddening is significantly different from the initial value in step 1, go back to step 2. Step 5: if the new reddening is not significantly different, adopt the temperature from step 3 and compute the oxygen abundances following the flow–chart in Figure 5.1.

$$\log \frac{I(\lambda)}{I(\mathrm{H}\beta)} = \log \frac{F(\lambda)}{F(\mathrm{H}\beta)} + 0.4\, E(B-V)\, [A_1(\lambda) - A_1(\mathrm{H}\beta)]\,. \qquad (4.2)$$

$F(\lambda)/F(\mathrm{H}\beta)$ and $I(\lambda)/I(\mathrm{H}\beta)$ are the observed flux ratio and corrected intensity ratio, respectively, at wavelength λ. $A_1(\lambda)$ is the extinction in magnitudes for $E(B-V) = 1$, i.e., $A_1(\lambda) = A(\lambda)/E(B-V)$, where $A(\lambda)$ is the monochromatic extinction in magnitudes. Values of A_1 were obtained from the Cardelli et al. (1989) reddening law as defined by a ratio of the total to selective extinction, R_V, equal to 3.07,

which in the limit of zero reddening is the value for an A0V star (e.g., Vega) with intrinsic colour $(B-V)^0 = 0$. For Hα– and Hγ–based reddenings, initially the ratios $I(\mathrm{H}\alpha)/I(\mathrm{H}\beta) = 2.86$ and $I(\mathrm{H}\gamma)/I(\mathrm{H}\beta) = 0.468$ were adopted, respectively, which are appropriate for typical conditions within H II regions ($T_e = 10^4$ K and $n_e = 100$ cm^{-3}; Osterbrock 1989).

To arrive at a final estimate of the reddening, an electron temperature was required to obtain a new value of $I(\mathrm{H}\alpha)/I(\mathrm{H}\beta)$ or $I(\mathrm{H}\gamma)/I(\mathrm{H}\beta)$ (Figure 4.2). In most cases, the electron density can be assumed to be $n_e = 100$ cm^{-3}. In the three–level atom approximation (see, e.g., McCall 1984), electron temperatures can be determined from the forbidden and collisionally excited [O III]λ4363 and [O III]$\lambda\lambda$4959, 5007 lines with the following equation (Osterbrock 1989)

$$\frac{I([\mathrm{O\ III}]\lambda 4959) + I([\mathrm{O\ III}]\lambda 5007)}{I([\mathrm{O\ III}]\lambda 4363)} = \frac{7.73\ \exp[(3.29 \times 10^4)/T_e]}{1 + 4.5 \times 10^{-2}\, T_e^{-1/2}} \qquad (4.3)$$

However, SNAP computes temperatures by directly solving the equations of statistical equilibrium and determining the emissivities for collisionally excited lines using a five–level atom approximation (see, e.g., DeRobertis et al. 1987). For oxygen, the O^+ and O^{+2} ions have only five levels within a few electron volts of ground (Osterbrock 1989), which are accessible via collisional excitation. In the absence of [O III]λ4363, the electron temperature is assumed to be $T_e = 10^4$ K.

The Hα, [N II]$\lambda\lambda$6548, 6583, and [S II]$\lambda\lambda$6716, 6731 lines were not detected in spectra of H II regions in field dIs, because the spectra acquired at Steward were obtained at wavelengths between 3600 Å and 5100 Å. Because the density–dependent line ratio, $I([\mathrm{S\ II}]\lambda 6716)/I([\mathrm{S\ II}]\lambda 6731)$, could not be formed, a value of $n_e = 100$ cm^{-3} was adopted. In a number of spectra of H II regions in Virgo dIs where n_e was derived (see Chapter 5), using the derived electron density did not produce significant differences, because line emissivities are not very sensitive to n_e (Osterbrock 1989).

After correcting line ratios for the initial estimate of the reddening, the temperature was estimated and a second value of the reddening was computed. It was found that the reddening values did not change significantly from the first to the second iteration. Also, the derived temperature in the second iteration was found to be very similar to the value from the first iteration. Errors in the reddening returned by SNAP were computed from the maximum and minimum values of the reddening based upon approximate 2σ errors in fits to emission lines from INTENS.

An Hγ–based reddening was used to correct spectra of H II regions in Holmberg II, NGC 3109, and UGC 6456. Hα–based reddenings were used to correct spectra of H II regions in IC 10, NGC 1560, and all Virgo dIs; $F(\mathrm{H}\gamma)/F(\mathrm{H}\beta)$ was not used in a number of spectra, because they exhibited severe absorption at Hγ.

In some cases, values for $I([\mathrm{O\ III}]\lambda5007)/I([\mathrm{O\ III}]\lambda4959)$ were found to be lower than the theoretical value by about 10%. To check the consistency of the computations, electron temperatures determined with $I([\mathrm{O\ III}]\lambda5007)/I([\mathrm{O\ III}]\lambda4363)$ were compared with those using $I([\mathrm{O\ III}]\lambda4959)/I([\mathrm{O\ III}]\lambda4363)$. There were no significant differences in electron temperatures obtained from either ratio. Errors in the electron temperature were based upon the maximum and minimum values possible given the errors in the [O III] emission lines.

4.3 Flux and Intensity Ratios: Field dIs

Observed and corrected line ratios for the five field dIs observed at Steward and at San Pedro Mártir are listed in Tables 4.2 to 4.10, respectively. The listed errors for the observed emission–line flux ratios at each wavelength λ include the errors in the fits to the line profiles, their surrounding continua, and the relative error in the sensitivity function stated in Table 3.1. Errors for observed ratios do not include the

error in the flux at the Hβ reference line. No error was assumed for the correction for underlying Balmer absorption. Note that the errors in the corrected intensity ratios account both for errors in the flux at the specified wavelength λ and flux at the Hβ reference line.

4.3.1 Holmberg II

Observed flux (F) and corrected intensity (I) ratios are listed in Table 4.2. No variations in T_e were observed to within the computed errors. The reddening values for Holmberg II were found to be small and consistent with zero. So, zero reddening was adopted and the observed flux ratios were subsequently compensated only for underlying Balmer absorption with equivalent width of 2 Å.

4.3.2 IC 10

In addition to Steward data, long–slit spectra between 3450 Å and 7450 Å were obtained with the 2.1–metre telescope at San Pedro Mártir (SPM) in México on 1994 December 1 (UT). Because the sensitivity of the SPM data at blue wavelengths was poor, these spectra were acquired specifically to measure Hα and Hβ. The increased coverage provided a larger baseline in wavelength to allow for a truer estimation of the reddening. The SPM spectra were reduced in a manner similar to the Steward data. H II regions identified at SPM were matched with those identified at Steward, so that the appropriate reddening corrections could be applied. The data obtained at SPM are listed in Table 4.3. Derived reddenings for each H II region are listed in Table 4.4 and are also listed in Table 5.2.

For Steward data, intensity ratios were derived from flux ratios by compensating for underlying Balmer absorption with equivalent width of 2 Å and for the reddening derived for each H II region from the SPM data. Observed flux and corrected intensity

	Ho II–1		Ho II–2		Ho II–3	
Identification (Å)	F	I	F	I	F	I
[O II] 3727	447 ± 11	443 ± 48	259.3 ± 4.7	257 ± 22	186.7 ± 4.5	185 ± 16
[Ne III] 3869	48.8 ± 4.8	48.3 ± 8.1	34.3 ± 2.6	34.0 ± 4.4	29.5 ± 2.6	29.2 ± 4.1
He I + H8 3889	34.1 ± 4.6	36.6 ± 8.0	26.4 ± 2.5	28.8 ± 4.9	25.1 ± 2.6	27.3 ± 4.6
[Ne III] + Hϵ 3970	48.6 ± 4.8	50.4 ± 9.0	37.7 ± 2.6	39.1 ± 4.6	33.3 ± 3.0	34.5 ± 5.2
Hδ 4101	44.4 ± 7.7	46 ± 12	37.2 ± 3.7	38.9 ± 6.2	34.8 ± 3.3	36.5 ± 5.7
Hγ 4340	61.2 ± 4.4	61.6 ± 9.3	58.4 ± 2.4	59.3 ± 6.1	57.1 ± 2.4	58.2 ± 6.0
[O III] 4363	< 9.1 (2σ)	< 6.8 (2σ)	8.3 ± 1.9	8.2 ± 2.3	9.0 ± 2.0	8.9 ± 2.4
Hβ 4861	100.0 ± 4.5	100.0 ± 6.3	100.0 ± 2.2	100.0 ± 4.5	100.0 ± 2.1	100.0 ± 4.4
[O III] 4959	87.8 ± 5.4	87 ± 12	79.7 ± 4.8	79.0 ± 9.1	69.4 ± 5.2	68.7 ± 8.8
[O III] 5007	260.2 ± 6.6	258 ± 28	192.9 ± 5.8	191 ± 18	159.8 ± 6.1	158 ± 15
	Ho II–4		Ho II–5		Ho II–6	
Identification (Å)	F	I	F	I	F	I
[O II] 3727	251.1 ± 8.1	246 ± 25	191.4 ± 2.6	188 ± 15	261.3 ± 3.2	257 ± 20
[Ne III] 3869	...	...	26.7 ± 1.2	26.2 ± 2.6	23.2 ± 1.9	22.8 ± 3.0
He I + H8 3889	...	...	17.2 ± 1.1	21.1 ± 2.7	21.0 ± 1.9	24.3 ± 3.8
[Ne III] + Hϵ 3970	18.7 ± 3.9	21.7 ± 6.5	21.9 ± 1.6	25.2 ± 3.3	21.5 ± 2.6	24.6 ± 4.5
Hδ 4101	20.2 ± 3.8	22.7 ± 6.2	24.3 ± 1.5	27.4 ± 3.3	29.7 ± 2.2	32.2 ± 4.2
Hγ 4340	50.0 ± 2.7	51.5 ± 6.3	47.72 ± 0.94	49.8 ± 4.1	43.8 ± 2.4	45.6 ± 5.1
[O III] 4363	< 4.7 (2σ)	< 3.5 (2σ)	6.02 ± 0.75	5.9 ± 1.0	< 3.0 (2σ)	< 2.2 (2σ)
He I 4472	...	...	2.65 ± 0.91	2.6 ± 1.0	4.1 ± 1.2	4.0 ± 1.3
He II 4686	...	...	2.90 ± 0.59	2.85 ± 0.71	...	...
Hβ 4861	100.0 ± 3.2	100.0 ± 5.2	100.0 ± 1.2	100.0 ± 4.0	100.0 ± 1.2	100.0 ± 4.0
[O III] 4959	41.9 ± 3.3	41.1 ± 5.7	96.0 ± 2.2	94.1 ± 7.7	72.7 ± 1.8	72.5 ± 6.0
[O III] 5007	139.2 ± 4.1	137 ± 14	269.5 ± 2.7	264 ± 21	213.5 ± 2.2	211 ± 16
	Ho II–7		Ho II–8		Ho II–9	
Identification (Å)	F	I	F	I	F	I
[O II] 3727	239.2 ± 2.1	235 ± 18	221.0 ± 2.0	217 ± 17	144.8 ± 2.2	143 ± 12
[Ne III] 3869	23.4 ± 1.1	23.0 ± 2.3	22.5 ± 1.2	22.1 ± 2.3	18.9 ± 1.1	18.6 ± 2.1
He I + H8 3889	20.3 ± 1.1	22.8 ± 2.5	19.5 ± 1.2	21.4 ± 2.6	15.1 ± 1.1	16.7 ± 2.2
[Ne III] + Hϵ 3970	22.2 ± 1.7	24.6 ± 3.3	22.4 ± 1.5	24.2 ± 3.0	17.54 ± 0.70	19.1 ± 1.9
Hδ 4101	27.3 ± 1.2	29.5 ± 3.0	25.5 ± 1.1	27.5 ± 2.7	21.56 ± 0.73	23.2 ± 2.2
Hγ 4340	47.3 ± 1.4	48.8 ± 4.3	49.5 ± 1.2	50.8 ± 4.3	42.85 ± 0.86	43.9 ± 3.7
[O III] 4363	3.2 ± 1.1	3.2 ± 1.2	4.30 ± 0.92	4.2 ± 1.1	5.69 ± 0.69	5.61 ± 0.94
He I 4472	2.95 ± 0.90	2.9 ± 1.0	3.43 ± 0.90	3.4 ± 1.0	3.11 ± 0.64	3.07 ± 0.77
Hβ 4861	100.00 ± 0.91	100.0 ± 3.9	100.0 ± 1.0	100.0 ± 3.9	100.0 ± 1.4	100.0 ± 4.0
[O III] 4959	73.7 ± 1.2	72.5 ± 5.7	75.0 ± 1.3	73.6 ± 5.9	105.3 ± 3.9	103.9 ± 9.6
[O III] 5007	215.1 ± 1.5	211 ± 16	217.6 ± 1.5	214 ± 16	300.7 ± 4.8	297 ± 24

Table 4.2: Observed and corrected line ratios for Holmberg II. Wavelengths are listed in Å. F is the observed flux ratio with respect to H$\beta \equiv 100$. I is the intensity ratio corrected only for underlying Balmer absorption. The reddening was assumed to be zero. The errors in the observed line ratios account for the errors in the fits to the line profiles, the surrounding continua, and the relative error in the sensitivity function listed in Table 3.1; flux errors in the Hβ reference line are not included in the ratio relative to Hβ. Errors in the corrected line ratios account for errors in the specified line and in the Hβ reference line.

SPM	IC 10-1		IC 10-2		IC 10-3	
Identification (Å)	F	I	F	I	F	I
Hβ 4861	100.0 ± 2.2	100.0 ± 3.8	100.0 ± 1.7	100.0 ± 3.5	100.0 ± 3.9	100.0 ± 5.1
Hα 6563	628.0 ± 4.0	286 ± 20	620.0 ± 3.4	286 ± 19	676.0 ± 5.3	286 ± 24
	IC 10-4		IC 10-5			
Identification (Å)	F	I	F	I		
Hβ 4861	100.0 ± 4.5	100.0 ± 5.7	100.0 ± 5.3	100.0 ± 6.3		
Hα 6563	703.0 ± 7.7	286 ± 26	961.0 ± 8.6	286 ± 27		

Table 4.3: Observed and corrected line ratios for IC 10 (SPM). Wavelengths are listed in Å. F is the observed flux ratio with respect to H$\beta \equiv 100$ and I is the intensity ratio corrected for underlying Balmer absorption of equivalent width of 2 Å and for reddening.

H II region	$E(B-V)$ (mag)
IC 10-1	+0.788 ± 0.070
IC 10-2	+0.773 ± 0.067
IC 10-3	+0.862 ± 0.083
IC 10-4	+0.897 ± 0.091
IC 10-5	+1.215 ± 0.096

Table 4.4: Reddening values for IC 10 (SPM), which were derived from the values of $F(\mathrm{H}\alpha)/F(\mathrm{H}\beta)$ listed in Table 4.3. These values are also listed in Table 5.2.

ratios are listed in Table 4.5 for all H II regions. Errors in the corrected intensity ratios account for errors in the flux at the specified wavelength λ, errors at the Hβ reference line, and errors in the reddening values obtained from the SPM data.

4.3.3 NGC 1560

Because NGC 1560 is a known member of the IC 342/Maffei Group (Buta and McCall 1999), there is expected to be non–negligible foreground extinction along the line–of–sight to NGC 1560. A second observing program was designed specifically to measure Hα and Hβ fluxes, because the Hγ fluxes were found to be unusable. At Steward (Table 3.1), the long slit was placed on the northeast and southwest regions of the galaxy for a selection of H II regions which are not the ones observed at blue wavelengths. The data are listed in Table 4.6. Reddening values were derived from $F(\mathrm{H}\alpha)/F(\mathrm{H}\beta)$, and are listed in Table 4.7. An average reddening of $E(B-V) = +0.36$ mag was computed from the H II regions 1 NE, 1 SW, 2 SW, 3 SW, and 6 SW. This value was adopted to correct line ratios for H II regions observed in the blue.

Observed flux and corrected intensity ratios are listed in Table 4.8. Flux ratios for the two H II region spectra NGC 1560–1 and NGC 1560–2 are in good agreement with those extracted independently by M. G. Richer (personal communication) from the same Steward data.

4.3.4 NGC 3109

Observed flux and corrected intensity ratios are listed in Table 4.9. The reddening values were found to be near zero, which is consistent with the small value listed in NED. Zero reddening was adopted and the observed flux ratios were subsequently compensated only for underlying Balmer absorption with equivalent width of 2 Å.

Steward	IC 10–1		IC 10–2		IC 10–3	
Identification (Å)	F	I	F	I	F	I
[O II] 3727	68.5 ± 1.1	198 ± 30	61.9 ± 1.3	175 ± 26	98.7 ± 2.6	312 ± 56
[Ne III] 3869	12.28 ± 0.70	29.6 ± 5.0	12.64 ± 0.69	30.0 ± 4.9	12.8 ± 1.9	33.2 ± 9.0
He I + H8 3889	8.64 ± 0.67	25.8 ± 5.2	9.36 ± 0.66	26.5 ± 5.0	7.5 ± 1.5	27 ± 11
[Ne III] + Hϵ 3970	10.99 ± 0.63	28.4 ± 4.8	11.21 ± 0.67	28.1 ± 4.7	10.6 ± 1.2	31.1 ± 8.0
Hδ 4101	15.32 ± 0.49	32.6 ± 4.2	15.49 ± 0.49	32.3 ± 4.0	15.5 ± 1.2	35.8 ± 6.7
Hγ 4340	34.18 ± 0.40	53.5 ± 4.8	35.28 ± 0.41	54.5 ± 4.7	29.36 ± 0.83	48.9 ± 5.4
[O III] 4363	1.65 ± 0.32	2.37 ± 0.60	1.53 ± 0.33	2.20 ± 0.60	2.77 ± 0.73	4.1 ± 1.4
He I 4472	3.48 ± 0.31	4.55 ± 0.66	3.46 ± 0.32	4.52 ± 0.66	3.71 ± 0.71	4.9 ± 1.3
He II 4686	...	...	...	...	1.44 ± 0.53	1.60 ± 0.65
Hβ 4861	100.0 ± 1.3	100.0 ± 5.4	100.0 ± 1.3	100.0 ± 5.2	100.0 ± 1.7	100.0 ± 5.8
[O III] 4959	134.5 ± 5.9	123.4 ± 8.6	136.7 ± 5.7	126.9 ± 8.6	127.7 ± 6.3	115.3 ± 8.8
[O III] 5007	404.8 ± 7.4	360 ± 17	409.1 ± 7.2	366 ± 17	391.6 ± 7.9	342 ± 17
	IC 10–4		IC 10–5			
Identification (Å)	F	I	F	I		
[O II] 3727	154.2 ± 2.9	517 ± 98	105.0 ± 6.2	550 ± 130		
[Ne III] 3869	...	...	...	...		
He I + H8 3889	9.2 ± 1.5	29.4 ± 9.8	...	...		
[Ne III] + Hϵ 3970	12.6 ± 2.1	34 ± 11	12.3 ± 2.8	44 ± 17		
Hδ 4101	10.9 ± 1.3	26.5 ± 6.8	20.4 ± 2.6	56 ± 15		
Hγ 4340	32.0 ± 1.3	52.9 ± 6.9	29.0 ± 2.6	55 ± 11		
[O III] 4363	< 1.6 (2σ)	< 2.5 (2σ)	< 4.8 (2σ)	< 8.7 (2σ)		
He I 4472	2.04 ± 0.60	2.8 ± 1.0	...	...		
He II 4686	...	...	...	...		
Hβ 4861	100.0 ± 2.5	100.0 ± 7.0	100.0 ± 3.6	100.0 ± 9.0		
[O III] 4959	63.3 ± 4.3	57.6 ± 5.7	102.9 ± 9.2	92 ± 12		
[O III] 5007	194.8 ± 5.4	171 ± 10	326.1 ± 11.8	278 ± 21		

Table 4.5: Observed and corrected line ratios for IC 10 (Steward). Wavelengths are listed in Å. F is the observed flux with respect to H$\beta \equiv 100$ and I is the intensity ratio corrected for underlying Balmer absorption and reddening. Reddenings derived from $F(\mathrm{H}\alpha)/F(\mathrm{H}\beta)$ values obtained at SPM are listed in Table 4.4. The errors in the observed line ratios account for the errors in the fits to the line profiles and surrounding continua, and the relative error in the sensitivity function stated in Table 3.1; flux errors in the Hβ reference line are not included in the ratio relative to Hβ. Errors in the corrected line ratios account for flux errors in the specified line and in the reference line, and errors in the reddening.

	NGC 1560–1 NE		NGC 1560–2 NE			
Identification (Å)	F	I	F	I		
Hβ 4861	100.0 ± 6.3	100 ± 14	100 ± 21	100 ± 47		
Hα 6563	396 ± 14	286 ± 44	183 ± 10	286 ± 86		
	NGC 1560–1 SW		NGC 1560–2 SW		NGC 1560–3 SW	
Identification (Å)	F	I	F	I	F	I
Hβ 4861	100.0 ± 8.3	100 ± 20	100.0 ± 8.2	100 ± 19	100.0 ± 8.5	100 ± 20
Hα 6563	523 ± 15	286 ± 39	465 ± 15	286 ± 40	397 ± 17	286 ± 43
	NGC 1560–6 SW		NGC 1560–7 SW			
Identification (Å)	F	I	F	I		
Hβ 4861	100.0 ± 7.9	100 ± 18	100 ± 34	100 ± 92		
Hα 6563	445 ± 13	286 ± 36	556 ± 15	286 ± 155		

Table 4.6: Observed and corrected line ratios for NGC 1560 (red spectra, Steward). Wavelengths are listed in Å. Two H II regions (1–2 NE) were detected when the long slit was placed in the northeast region of the galaxy. The observed value of $F(\mathrm{H}\alpha)/F(\mathrm{H}\beta)$ for NGC 1560–2 NE is anomalously low; a reddening was not computed for this spectrum. Five H II regions (1–3, 6, and 7 SW) were detected when the long slit was placed in the southwest region of the galaxy.

H II region	$E(B-V)$ (mag)
NGC 1560–1 NE	$+0.33 \pm 0.15$
NGC 1560–2 NE	...[a]
NGC 1560–1 SW	$+0.48 \pm 0.14$
NGC 1560–2 SW	$+0.38 \pm 0.14$
NGC 1560–3 SW	$+0.24 \pm 0.15$
NGC 1560–6 SW	$+0.38 \pm 0.13$
NGC 1560–7 SW	$+0.56 \pm 0.51$

Table 4.7: Reddening values for NGC 1560 from red spectra at Steward. These were derived from $F(\mathrm{H}\alpha)/F(\mathrm{H}\beta)$ data listed in Table 4.6. NOTE: [a] Reddening was not computed, because $F(\mathrm{H}\alpha)/F(\mathrm{H}\beta)$ was anomalously low.

	NGC 1560-1		NGC 1560-2		NGC 1560-3	
Identification (Å)	F	I	F	I	F	I
[O II] 3727	154.3 ± 6.7	254 ± 22	224.7 ± 4.8	359 ± 23	209 ± 20	338 ± 56
[Ne III] 3869	8.9 ± 3.8	13.5 ± 6.2	13.0 ± 2.1	19.2 ± 3.8	31.8 ± 7.2	48 ± 14
He I + H8 3889	...	...	19.2 ± 2.4	31.6 ± 5.6	...	...
[Ne III] + Hϵ 3970	12.2 ± 2.7	17.0 ± 5.2	10.7 ± 1.8	18.8 ± 4.5	...	...
Hδ 4101	31.4 ± 4.9	40.9 ± 8.4	21.0 ± 1.7	30.8 ± 4.0	26.2 ± 5.6	38 ± 12
Hγ 4340	40.7 ± 2.1	48.5 ± 4.6	43.9 ± 1.5	54.4 ± 4.3	50.0 ± 5.0	61 ± 11
[O III] 4363	< 2.8 (2σ)	< 3.4 (2σ)	< 2.8 (2σ)	< 3.3 (2σ)	< 11.5 (2σ)	< 13.6 (2σ)
He I 4472	...	...	4.02 ± 0.75	4.5 ± 1.0	...	...
He II 4686	...	...	...	...	...	...
Hβ 4861	100.0 ± 2.6	100.0 ± 3.6	100.0 ± 2.4	100.0 ± 3.4	100.0 ± 5.6	100.0 ± 7.0
[O III] 4959	124.6 ± 4.7	122.3 ± 9.8	81.8 ± 5.2	78.1 ± 8.0	150 ± 11	145 ± 21
[O III] 5007	324.8 ± 5.8	315 ± 20	238.1 ± 6.6	224 ± 16	426 ± 14	407 ± 44
	NGC 1560-4		NGC 1560-5		NGC 1560-6	
Identification (Å)	F	I	F	I	F	I
[O II] 3727	220 ± 18	363 ± 49	254 ± 18	423 ± 56	295 ± 37	385 ± 91
[Ne III] 3869	19.8 ± 6.9	30 ± 12	...	...	...	...
He I + H8 3889	...	...	38.7 ± 5.9	58 ± 13	...	...
[Ne III] + Hϵ 3970	23.2 ± 5.3	33.9 ± 9.0	27.8 ± 6.7	39 ± 13	...	...
Hδ 4101	34.8 ± 6.1	46 ± 11	29.3 ± 5.7	38 ± 10	...	...
Hγ 4340	52.1 ± 3.9	61.3 ± 8.4	44.5 ± 4.1	51.6 ± 8.4	...	...
[O III] 4363	< 6.7 (2σ)	< 8.1 (2σ)	< 4.4 (2σ)	< 5.3 (2σ)	...	...
Hβ 4861	100.0 ± 4.5	100.0 ± 5.3	100.0 ± 5.2	100.0 ± 6.0	100.0 ± 8.5	100 ± 11
[O III] 4959	110.5 ± 8.2	109 ± 14	58.5 ± 4.9	58.3 ± 8.5	40.3 ± 6.8	31.4 ± 8.7
[O III] 5007	318 ± 11	310 ± 29	175.8 ± 6.2	173 ± 18	130.1 ± 9.4	100 ± 18
	NGC 1560-7					
Identification (Å)	F	I				
[O II] 3727	182.1 ± 67.2	240 ± 140				
Hβ 4861	100.0 ± 16.2	100 ± 20				
[O III] 4959	37.1 ± 17.7	29 ± 20				
[O III] 5007	214.02 ± 23.2	163 ± 52				

Table 4.8: Observed and corrected line ratios for NGC 1560 (blue spectra). Wavelengths are listed in Å. F is the observed flux ratio with respect to H$\beta \equiv 100$ and I is the intensity ratio corrected for underlying Balmer absorption and constant reddening ($E(B-V) = +0.36$ mag) derived from red spectra (Tables 4.6 and 4.7). The errors in the observed line ratios account for the errors in the fits to the line profiles and surrounding continua, and the relative error in the sensitivity function listed in Table 3.1; flux errors in the Hβ reference line are not included in the ratio relative to Hβ. However, errors in the corrected line ratios account for flux errors in both the specified line and in the reference line.

	NGC 3109–1		NGC 3109–2	
Identification (Å)	F	I	F	I
[O II] 3727	418 ± 77	420 ± 200	385 ± 11	380 ± 43
[Ne III] 3869	...	...	...	...
He I + H8 3889	...	...	...	...
[Ne III] + Hϵ 3970	...	...	...	...
Hδ 4101	...	...	...	...
Hγ 4340	...	...	42.3 ± 5.6	45 ± 10
[O III] 4363	...	...	...	...
Hβ 4861	100 ± 26	100 ± 56	100.0 ± 5.2	100 ± 14
[O III] 4959	41 ± 23	41 ± 36	...	...
[O III] 5007	202 ± 30	204 ± 90	24.2 ± 4.6	23.9 ± 6.2
	NGC 3109–3		NGC 3109–4	
Identification (Å)	F	I	F	I
[O II] 3727	227.5 ± 6.2	220 ± 20	304.8 ± 7.4	283 ± 26
[Ne III] 3869	10.9 ± 2.1	10.5 ± 2.5	...	...
He I + H8 3889	16.5 ± 2.8	21.1 ± 5.6	...	...
[Ne III] + Hϵ 3970	16.7 ± 3.2	20.9 ± 6.1	...	...
Hδ 4101	20.9 ± 3.6	25.0 ± 6.4	17.3 ± 2.7	27.1 ± 7.6
Hγ 4340	45.3 ± 2.4	47.7 ± 5.5	41.1 ± 3.2	47.4 ± 7.1
[O III] 4363	5.7 ± 2.0	5.5 ± 2.2	< 6.5 (2σ)	< 6.0 (2σ)
Hβ 4861	100.0 ± 2.2	100.0 ± 8.8	100.0 ± 2.5	100.0 ± 9.4
[O III] 4959	105.7 ± 3.3	102.3 ± 9.5	100.6 ± 3.4	93.3 ± 9.1
[O III] 5007	313.4 ± 4.1	303 ± 25	280.6 ± 4.1	260 ± 23

Table 4.9: Observed and corrected line ratios for NGC 3109. Wavelengths are listed in Å. F is the observed flux ratio with respect to H$\beta \equiv 100$ and I is the intensity ratio corrected only for underlying Balmer absorption. The reddening was assumed to be zero. The errors in the observed lines account only for the errors in the fits to the line profiles and surrounding continua, and the relative error in the sensitivity function (Table 3.1). Flux errors in the Hβ reference line are not included in the ratio relative to Hβ. However, errors in the corrected line ratios account for flux errors in both the specified line and in the reference line.

4.3.5 UGC 6456

Observed flux and corrected intensity ratios are listed in Table 4.10. Values of the reddening derived from the $F(\mathrm{H}\gamma)/F(\mathrm{H}\beta)$ ratio were consistent with zero. Zero reddening was adopted and the observed flux ratios were subsequently compensated only for underlying Balmer absorption with equivalent width of 2 Å.

	UGC 6456–1		UGC 6456–2	
Identification (Å)	F	I	F	I
[O II] 3727	136.8 ± 6.1	133 ± 16	116.2 ± 1.9	114.6 ± 9.2
[Ne III] 3869	12.5 ± 2.5	12.1 ± 3.2	25.7 ± 1.2	25.3 ± 2.5
He I + H8 3889	12.9 ± 2.5	18.0 ± 5.9	16.4 ± 1.1	18.5 ± 2.3
[Ne III] + Hϵ 3970	...	...	19.9 ± 1.0	22.0 ± 2.4
Hδ 4101	21.7 ± 3.0	25.8 ± 6.0	26.0 ± 1.1	27.9 ± 2.9
Hγ 4340	46.2 ± 2.7	48.5 ± 6.6	50.2 ± 1.4	51.3 ± 4.6
[O III] 4363	8.6 ± 2.2	8.3 ± 2.7	8.3 ± 1.1	8.2 ± 1.5
He I 4472	...	...	4.41 ± 0.89	4.4 ± 1.1
He II 4686	...	...	1.54 ± 0.58	1.52 ± 0.61
Hβ 4861	100.0 ± 4.3	100.0 ± 6.0	100.0 ± 1.2	100.0 ± 4.0
[O III] 4959	87.9 ± 3.3	85.3 ± 9.7	112.0 ± 3.5	110.5 ± 9.8
[O III] 5007	237.3 ± 4.1	231 ± 23	308.5 ± 4.4	304 ± 24

Table 4.10: Observed and corrected line ratios for UGC 6456. Wavelengths are listed in Å. F is the observed flux ratio with respect to Hβ. I is the intensity ratio corrected for underlying Balmer absorption. The reddening was assumed to be zero. The errors in the observed flux ratios account for the errors in the fits to the line profiles, the surrounding continua, and the relative error in the sensitivity function (Table 3.1). Flux errors in the Hβ reference line are not included in the ratio relative to Hβ. However, errors in the corrected line ratios account for flux errors in both the specified line and in the reference line.

4.3.6 DDO 187

The fluxes reported by van Zee et al. (1997) are reanalyzed. Zero reddening was assumed and the observed flux ratios were corrected for underlying Balmer absorption with equivalent width of 2 Å. Observed and corrected line ratios are listed in Table 4.11.

	DDO 187–1		DDO 187–2	
Identification (Å)	F	I	F	I
[O II] 3727	180 ± 8.4	175.2 ± 8.4	256 ± 15	237 ± 15
[Ne III] 3869	27.5 ± 1.4	26.8 ± 1.4	...	...
Hγ 4340	44.3 ± 1.8	44.3 ± 1.8	35.3 ± 2.7	35.3 ± 2.7
[O III] 4363	2.7 ± 0.6	2.6 ± 0.6	...	...
Hβ 4861	100.0 ± 3.7	100.0 ± 3.7	100.0 ± 4.8	100.0 ± 4.8
[O III] 4959	64.5 ± 2.4	62.8 ± 2.4	16.6 ± 2.3	15.4 ± 2.3
[O III] 5007	187.8 ± 6.8	182.8 ± 6.8	47 ± 3	43 ± 3
Hα 6563	274 ± 13	274 ± 13	270 ± 16	270 ± 16
[N II] 6583	4.3 ± 0.4	4.2 ± 0.4	5.7 ± 0.7	5.3 ± 0.7
He I 6678	1.9 ± 0.3	1.9 ± 0.3	...	...
[S II] 6716	78.0 ± 0.5	75.9 ± 0.5	15.2 ± 1.1	14.1 ± 1.1
[S II] 6731	63.0 ± 0.4	61.3 ± 0.4	11.6 ± 0.9	10.7 ± 0.9
He I 7065	1.6 ± 0.3	1.6 ± 0.3	...	...
[Ar III] 7136	3.2 ± 0.3	3.1 ± 0.3	...	...

Table 4.11: Observed and corrected line ratios for DDO 187. Wavelengths are listed in Å. F is the observed flux ratio with respect to Hβ = 100 (van Zee et al. 1997) and I is the intensity ratio corrected for underlying Balmer absorption. The reddening was assumed to be zero.

4.4 Flux and Intensity Ratios: Virgo dIs

For the sample of Virgo dIs, observed flux and corrected intensity ratios are listed in Tables 4.12 to 4.15 inclusive. In a number of cases, the adopted reddening was zero. Errors for the observed flux ratios account for the errors in the fits to the line profiles, their surrounding continuua, and the relative error in the sensitivity function listed in Table 3.8. Errors for the observed ratios do not include the error in the flux for the Hβ reference line. Errors in the corrected intensity ratios account for errors in the flux at the specified wavelength λ, errors at the Hβ reference line, and errors in the reddening values (where nonzero).

The temperature–sensitive [O III]λ4363 emission line was detected in the spectra for H II regions VCC 0848–1 and VCC 1554–1. Because these spectra were of good quality, the following weak lines were also detected: [N I]λ5198, [N II]λ5755,[5]

[5]As an "auroral" transition, the [N II]λ5755 emission line is analogous to the [O III]λ4363 line,

[O I]λ6300, [S III]λ6312, [O I]λ6364, He Iλ6678, and [Ar III]λ7136. Upper limits to [O III]λ4363 were determined for the remaining Virgo dIs. Weak lines were also observed in VCC 0888 ([Ar III]λ7136), VCC 1179 (He Iλ6678, [Ar III]λ7136), and VCC 2037 ([O I]λ6300, He Iλ6678, [Ar III]λ7136).

but is weak in most H II regions. It can be used to derive the electron temperature in the O^+, N^+ zone of an H II region. (Osterbrock 1989).

	VCC 0512–3		VCC 0512–4		VCC 0848–1	
Identification (Å)	F	I	F	I	F	I
[O II] 3727	263 ± 76	257 ± 98	458 ± 131	430 ± 190	252 ± 1.2	254 ± 33
[Ne III] 3869	...	...	...	...	31.8 ± 2.3	31.7 ± 5.2
Hδ 4101	...	...	...	...	15.8 ± 1.3	23.0 ± 4.5
Hγ 4340	89 ± 13	86 ± 22	36 ± 14	43 ± 30	42.23 ± 0.88	47.2 ± 5.6
[O III] 4363	< 25.2 (2σ)	< 24.7 (2σ)	...	...	4.71 ± 0.70	4.6 ± 1.0
He I 4472	...	...	...	...	2.77 ± 0.45	2.66 ± 0.61
Hβ 4861	100.0 ± 6.5	100.0 ± 8.6	100 ± 13	100 ± 15	100 ± 1.2	100.0 ± 5.1
[O III] 4959	179.3 ± 7.4	175 ± 26	93 ± 13	87 ± 26	124.9 ± 1.2	117 ± 12
[O III] 5007	528.4 ± 9.2	517 ± 72	208 ± 15	193 ± 48	374.5 ± 1.5	352 ± 34
[N I] 5198	...	...	...	...	1.73 ± 0.42	1.61 ± 0.47
He I 5876	...	...	...	...	11.81 ± 0.98	10.8 ± 1.4
[O I] 6300	...	...	...	...	7.26 ± 0.93	6.6 ± 1.1
[S III] 6312	...	...	...	...	3.29 ± 0.75	2.98 ± 0.79
[O I] 6364	...	...	...	...	2.29 ± 0.73	2.07 ± 0.74
[N II] 6548	2.3 ± 4.1	2.3 ± 4.3	...	...	7.5 ± 2.0	6.7 ± 2.0
Hα 6563	265.1 ± 5.2	260 ± 37	270 ± 12	255 ± 58	314.3 ± 2.5	286 ± 23
[N II] 6583	6.2 ± 4.2	6.1 ± 4.6	24.1 ± 9.1	22 ± 12	20.8 ± 2.0	18.7 ± 2.6
He I 6678	...	...	...	...	2.95 ± 0.39	2.65 ± 0.45
[S II] 6716	33.1 ± 3.8	32.4 ± 6.8	...	...	34.13 ± 0.46	30.7 ± 2.4
[S II] 6731	24.5 ± 3.7	23.9 ± 5.9	...	...	24.11 ± 0.44	21.6 ± 1.7
He I 7065	...	...	...	...	2.46 ± 0.43	2.20 ± 0.46
[Ar III] 7136	...	...	...	...	7.65 ± 0.52	6.83 ± 0.74
	VCC 0888–1		VCC 0888–2		VCC 1114–1	
Identification (Å)	F	I	F	I	F	I
[O II] 3727	382 ± 21	390 ± 120	427 ± 22	470 ± 170	419 ± 98	400 ± 130
Hγ 4340	30.1 ± 4.4	46 ± 16	27.0 ± 3.3	50 ± 18	45 ± 10	49 ± 18
[O III] 4363	< 5.36 (2σ)	< 4.76 (2σ)	< 4.70 (2σ)	< 4.12 (2σ)	...	...
Hβ 4861	100.0 ± 6.5	100.0 ± 7.3	100.0 ± 8.1	100.0 ± 9.6	100.0 ± 7.4	100.0 ± 9.5
[O III] 4959	46.5 ± 4.2	37.5 ± 5.8	89.3 ± 6.5	67 ± 11	20.6 ± 5.9	19.8 ± 7.7
[O III] 5007	138.4 ± 8.0	111 ± 13	287 ± 15	213 ± 28	91.2 ± 8.0	87 ± 17
[N II] 6548	12.9 ± 4.0	9.0 ± 2.3	11.0 ± 5.7	6.5 ± 3.0	15.4 ± 4.8	14.8 ± 6.1
Hα 6563	396 ± 20	286 ± 36	467 ± 24	286 ± 43	291.4 ± 6.0	278 ± 42
[N II] 6583	52.9 ± 4.7	36.6 ± 4.6	56.7 ± 6.3	33.3 ± 5.0	41.3 ± 4.9	39.6 ± 8.9
[S II] 6716	78.3 ± 5.0	53.7 ± 3.8	90.3 ± 5.2	52.2 ± 3.1	38.2 ± 5.4	36.7 ± 9.0
[S II] 6731	59.5 ± 4.2	40.8 ± 3.0	64.2 ± 4.0	37.1 ± 2.6	27.8 ± 5.1	26.7 ± 7.7
[Ar III] 7136	...	...	15.3 ± 3.7	8.5 ± 2.1	...	...

Table 4.12: Observed and corrected line ratios for H II regions in Virgo dIs (1). Wavelengths are listed in Å. F is the observed flux ratio with respect to H$\beta \equiv 100$. I is the intensity ratio corrected for underlying Balmer absorption and reddening. The errors in the observed line ratios account for the errors in the fits to the line profiles, their surrounding continua, and the relative error in the sensitivity function (Table 3.8). Errors in the flux of the observed Hβ reference line are not included in the ratio relative to Hβ. However, errors in the corrected line ratios account for flux errors in both the specified line and in the reference line, and errors in the reddening where nonzero.

	VCC 1114-2		VCC 1179-1		VCC 1179-2	
Identification (Å)	F	I	F	I	F	I
[O II] 3727	304 ± 63	302 ± 92	690 ± 65	530 ± 400	506 ± 32	500 ± 170
[Ne III] 3869	...	...	110 ± 43	77 ± 78	36 ± 12	34 ± 20
Hγ 4340	33.7 ± 8.1	36 ± 13	...	...	...	...
[O III] 4363	...	...	...	...	< 4.2 (2σ)	< 3.5 (2σ)
Hβ 4861	100.0 ± 7.3	100.0 ± 9.3	100 ± 14	100 ± 22	100.0 ± 6.9	100.0 ± 8.0
[O III] 4959	...	...	153 ± 16	69 ± 21	70.6 ± 5.6	52.2 ± 7.7
[O III] 5007	29.0 ± 6.3	28.8 ± 9.1	468 ± 30	207 ± 52	207 ± 12	152 ± 19
[N II] 6548	9.5 ± 5.1	9.4 ± 6.0	35 ± 10	11.1 ± 2.7	17.3 ± 2.9	10.8 ± 1.2
Hα 6563	248.2 ± 6.3	247 ± 37	804 ± 46	286 ± 81	438 ± 25	286 ± 39
[N II] 6583	31.4 ± 5.1	31.2 ± 8.2	105 ± 12	33.5 ± 8.3	67.0 ± 4.6	41.6 ± 5.8
He I 6678	...	...	...	...	5.5 ± 2.1	3.4 ± 0.5
[S II] 6716	47.2 ± 4.5	46.9 ± 9.4	136.0 ± 9.4	43 ± 11	98.5 ± 6.0	60.6 ± 8.5
[S II] 6731	31.8 ± 4.2	31.5 ± 7.4	105.8 ± 8.0	33.2 ± 8.3	66.4 ± 4.3	40.8 ± 5.7
[Ar III] 7136	...	...	38 ± 10	11.4 ± 2.8	12.7 ± 3.5	7.6 ± 2.3
	VCC 1179-3		VCC 1179-4		VCC 1200-1 [a]	
Identification (Å)	F	I	F	I	F	I
[O II] 3727	254 ± 18	204 ± 71	334 ± 25	330 ± 170	114.1 ± 8.0	...
[Ne III] 3869	38.7 ± 9.4	31 ± 15	13 ± 13	13 ± 19	...	...
Hγ 4340	47.1 ± 5.7	52 ± 15	30.9 ± 7.7	38 ± 22	...	...
[O III] 4363	< 7.7 (2σ)	< 6.5 (2σ)	< 14 (2σ)	< 13 (2σ)	...	...
Hβ 4861	100.0 ± 7.1	100.0 ± 7.7	100 ± 12	100 ± 13	...	...
[O III] 4959	116.3 ± 8.1	102 ± 14	70.7 ± 9.0	62 ± 15	...	...
[O III] 5007	335 ± 19	295 ± 35	245 ± 17	216 ± 38	15.5 ± 2.8	...
[N II] 6548	9.2 ± 5.3	8.6 ± 4.5	9.7 ± 9.2	8.0 ± 7.1	...	...
Hα 6563	299 ± 18	286 ± 39	337 ± 22	286 ± 57	100 ± 4	...
[N II] 6583	15.4 ± 5.4	14.3 ± 4.2	37.3 ± 9.5	30.9 ± 5.8	8.2 ± 3.2	...
[S II] 6716	28.6 ± 4.6	26.7 ± 2.4	47.4 ± 7.8	39.0 ± 3.4	32.6 ± 2.9	...
[S II] 6731	14.1 ± 3.6	13.2 ± 2.4	28.7 ± 6.3	23.6 ± 3.3	26.4 ± 2.8	...
[Ar III] 7136	12.7 ± 4.8	12.0 ± 3.5	35.0 ± 8.7	28.5 ± 4.1	...	...

Table 4.13: Observed and corrected line ratios for H II regions in Virgo dIs (2). NOTE: [a] VCC 1200-1: Hβ and [O III]λ4959 lines were not detected. Observed line ratios are given with respect to Hα, where $F(\mathrm{H}\alpha) = (1.16 \pm 0.05) \times 10^{-15}$ ergs s^{-1} cm^{-2}. Corrected ratios are not computed.

	VCC 1200–2		VCC 1249–1 [a]		VCC 1554–1	
Identification (Å)	F	I	F	I	F	I
[O II] 3727	298 ± 16	246 ± 33	693 ± 166	645 ± 197	474.0 ± 6.8	440 ± 100
[Ne III] 3869	...	...	...	...	19.0 ± 1.3	17.9 ± 4.3
He II 4026	...	...	...	...	2.05 ± 0.68	1.95 ± 0.92
Hδ 4101	...	...	...	...	22.82 ± 0.74	24.6 ± 4.5
Hγ 4340	...	...	...	...	47.8 ± 1.1	48.8 ± 7.2
[O III] 4363	...	...	...	...	1.54 ± 0.86	1.48 ± 0.98
He I 4472	...	...	...	...	2.94 ± 0.48	2.85 ± 0.72
Hβ 4861	100.0 ± 7.1	100.0 ± 8.0	100 ± 17	100 ± 19	100.0 ± 2.0	100.0 ± 4.8
He I 4922	...	...	...	...	0.83 ± 0.25	0.81 ± 0.29
[O III] 4959	38.0 ± 3.6	31.4 ± 5.5	84 ± 17	79 ± 22	78.4 ± 3.2	77.2 ± 7.7
[O III] 5007	111.6 ± 6.5	92 ± 13	130 ± 22	121 ± 31	230.8 ± 4.0	228 ± 19
[N I] 5197	...	...	...	...	1.57 ± 0.24	1.56 ± 0.29
[N II] 5755	...	...	...	...	0.52 ± 0.17	0.53 ± 0.17
He I 5876	13.8 ± 3.9	11.4 ± 4.2	...	...	12.42 ± 0.30	12.5 ± 4.2
[O I] 6300	...	...	...	...	4.44 ± 0.28	4.50 ± 0.19
[S III] 6312	...	...	...	...	1.12 ± 0.22	1.13 ± 0.19
[O I] 6364	...	...	...	...	1.78 ± 0.22	1.81 ± 0.17
[N II] 6548	5.4 ± 3.4	4.4 ± 3.1	...	...	6.4 ± 2.6	6.5 ± 2.3
Hα 6563	287 ± 15	247 ± 33	289 ± 16	270 ± 54	279.9 ± 3.2	286 ± 26
[N II] 6583	22.2 ± 3.5	18.3 ± 4.4	13 ± 13	12 ± 12	21.1 ± 2.6	21.5 ± 1.8
He I 6678	...	...	...	...	2.96 ± 0.39	3.02 ± 0.27
[S II] 6716	57.0 ± 4.3	47.1 ± 7.4	...	...	25.64 ± 0.42	26.2 ± 0.1
[S II] 6731	39.5 ± 3.7	32.6 ± 5.7	...	...	17.61 ± 0.41	18.0 ± 0.4
He I 7065	...	...	...	...	1.69 ± 0.25	1.74 ± 0.16
[Ar III] 7136	...	...	...	...	4.67 ± 0.32	4.80 ± 0.8
	VCC 1554–2		VCC 1554–3		VCC 1554–4	
Identification (Å)	F	I	F	I	F	I
[O II] 3727	330 ± 18	400 ± 110	283 ± 24	272 ± 87	595 ± 39	600 ± 260
[Ne III] 3869	...	...	38.3 ± 9.6	37 ± 17	...	...
Hδ 4101	46.2 ± 6.2	43 ± 14	39.9 ± 5.6	35 ± 11	...	...
Hγ 4340	57.2 ± 5.1	54 ± 12	62.2 ± 5.3	58 ± 13	21.1 ± 8.1	73 ± 77
[O III] 4363	< 9.8 (2σ)	< 11 (2σ)	< 13 (2σ)	< 13 (2σ)	< 11 (2σ)	< 8.5 (2σ)
Hβ 4861	100.0 ± 3.2	100.0 ± 5.7	100.0 ± 4.5	100.0 ± 6.5	100.0 ± 7.6	100 ± 11
[O III] 4959	57.8 ± 4.1	61.9 ± 8.1	77.2 ± 3.4	80.9 ± 9.5	145.5 ± 8.5	97 ± 17
[O III] 5007	178.7 ± 5.0	191 ± 18	241.3 ± 4.3	254 ± 25	399 ± 10	264 ± 38
He I 5876	10.7 ± 1.7	10.9 ± 1.6	12.1 ± 1.9	13.1 ± 2.0	24.4 ± 3.4	13.7 ± 2.0
[N II] 6548	10.2 ± 3.3	10.2 ± 2.9	4.8 ± 2.8	5.3 ± 2.9	22.2 ± 8.7	11.4 ± 4.0
Hα 6563	293.5 ± 4.2	286 ± 32	262.8 ± 3.5	286 ± 30	531 ± 11	286 ± 61
[N II] 6583	29.6 ± 3.4	29.3 ± 2.2	12.0 ± 2.8	13.3 ± 2.5	55.0 ± 8.8	28.2 ± 3.2
He I 6678	5.4 ± 1.3	5.4 ± 1.0	...	...	...	...
[S II] 6716	21.4 ± 1.5	21.1 ± 0.6	45.8 ± 7.9	50.9 ± 6.4	92.5 ± 4.3	46.7 ± 0.2
[S II] 6731	18.1 ± 1.4	17.9 ± 0.7	5.8 ± 8.0	6.2 ± 8.5	67.8 ± 4.0	34.2 ± 0.5

Table 4.14: Observed and corrected line ratios for H II regions in Virgo dIs (3). NOTE: [a] The H II region, VCC 1249–1, is also labelled LR1 (Chapter 6; Lee et al. 2000).

	VCC 1554–5		VCC 1554–6 [a]	VCC 1554–7 [a]	VCC 1585–1	
Identification (Å)	F	I	F	F	F	I
[O II] 3727	455 ± 44	420 ± 170	481 ± 29	258 ± 40	338 ± 28	370 ± 190
Hγ 4340	49.9 ± 6.5	43 ± 14	...	...	53.3 ± 7.8	59 ± 23
[O III] 4363	< 16 (2σ)	< 16 (2σ)	...	...	< 16 (2σ)	< 17 (2σ)
Hβ 4861	100.0 ± 7.3	100.0 ± 9.2	100 ± 12	100 ± 18	100.0 ± 9.6	100 ± 12
[O III] 4959	42.6 ± 4.6	46.9 ± 9.3	23 ± 13	...	50.6 ± 8.4	49 ± 14
[O III] 5007	150.2 ± 5.9	166 ± 22	126 ± 17	...	120.8 ± 9.9	116 ± 23
[N II] 6548	7.6 ± 3.9	9.3 ± 4.4	...	85 ± 18	24 ± 13	22 ± 10
Hα 6563	240.2 ± 4.9	286 ± 36	...	451 ± 22	324 ± 16	286 ± 60
[N II] 6583	17.8 ± 3.9	21.8 ± 3.8	...	235 ± 20	34 ± 13	29.8 ± 9.3
[S II] 6716	41.4 ± 3.1	51.0 ± 1.5	...	...	43.4 ± 8.4	38.1 ± 4.5
[S II] 6731	26.5 ± 2.8	32.7 ± 1.9	...	...	57.3 ± 8.8	50.2 ± 4.0
	VCC 1789–1		VCC 2037–1		VCC 2037–2	
Identification (Å)	F	I	F	I	F	I
[O II] 3727	404 ± 23	490 ± 210	403 ± 23	430 ± 140	492 ± 41	450 ± 320
[Ne III] 3869	...	...	31.4 ± 5.2	33 ± 13	...	...
Hγ 4340	30.5 ± 4.7	43 ± 22	37.1 ± 3.6	50 ± 13	...	...
[O III] 4363	< 9.3 (2σ)	< 9.1 (2σ)	< 5.1 (2σ)	< 4.8 (2σ)	...	...
Hβ 4861	100.0 ± 6.4	100 ± 11	100.0 ± 6.3	100.0 ± 6.7	100 ± 15	100 ± 19
[O III] 4959	48.8 ± 3.7	41.7 ± 7.2	89.6 ± 5.3	77.9 ± 9.0	89 ± 12	59 ± 18
[O III] 5007	145.5 ± 8.6	123 ± 18	257 ± 14	222 ± 24	213 ± 18	140 ± 34
He I 5876	...	...	5.9 ± 2.5	4.7 ± 1.9	...	...
[O I] 6300	...	...	11.5 ± 3.1	8.9 ± 2.0	...	...
[N II] 6548	16.2 ± 4.7	11.2 ± 2.5	9.2 ± 4.0	7.0 ± 2.6	...	...
Hα 6563	402 ± 23	288 ± 32	366 ± 21	286 ± 21	487 ± 31	286 ± 5.6
[N II] 6583	56.4 ± 5.5	38.9 ± 3.8	30.0 ± 4.3	22.8 ± 1.8	62 ± 13	34.0 ± 4.0
He I 6678	...	...	4.9 ± 1.7	3.7 ± 1.3	...	...
[S II] 6716	82.9 ± 5.5	56.6 ± 5.4	69.2 ± 4.3	52.2 ± 0.6	135 ± 13	73.2 ± 0.3
[S II] 6731	60.4 ± 4.5	41.1 ± 3.1	48.7 ± 3.3	36.8 ± 0.2	93 ± 12	50.0 ± 1.1
[Ar III] 7136	...	...	11.2 ± 1.9	8.3 ± 0.6	...	...

Table 4.15: Observed and corrected line ratios for H II regions in Virgo dIs (4). NOTE: [a] VCC 1554–6 and VCC 1554–7: The recession velocity of emission lines for each object is $\langle v_\odot \rangle / c \simeq +0.0933$, which makes these two objects galaxies in the background of the Virgo Cluster. Corrected ratios are not computed, and their measurements are not included in the subsequent analysis.

Chapter 5

Deriving Nebular Abundances

In this chapter, the procedures for deriving oxygen abundances are presented. The direct method of computing oxygen abundances (from [O III]λ4363) is discussed in § 5.1. The bright-line method of deriving oxygen abundances (in the absence of [O III]λ4363) is discussed in § 5.2. The method by which the abundance of nitrogen relative to oxygen is obtained is stated in § 5.3. Derived properties of field and Virgo dIs are presented in § 5.4 and 5.5, respectively.

5.1 Direct ([O III]λ4363) Oxygen Abundances

The direct (or standard) method of obtaining oxygen abundances from emission lines is applicable to any object where [O III]λ4363 is detectable and for which the doubly ionized O^{+2} ion is the dominant form of oxygen (Osterbrock 1989). The standard method is summarized by the flow-chart in Figure 5.1, which is adopted from Dinerstein (1990). This method applies only when [O III]λ4363 is detected. Computations are performed with SNAP (see § 4.2) in the five-level atom approximation (DeRobertis et al. 1987).

Given a temperature and a density, an oxygen abundance is determined from

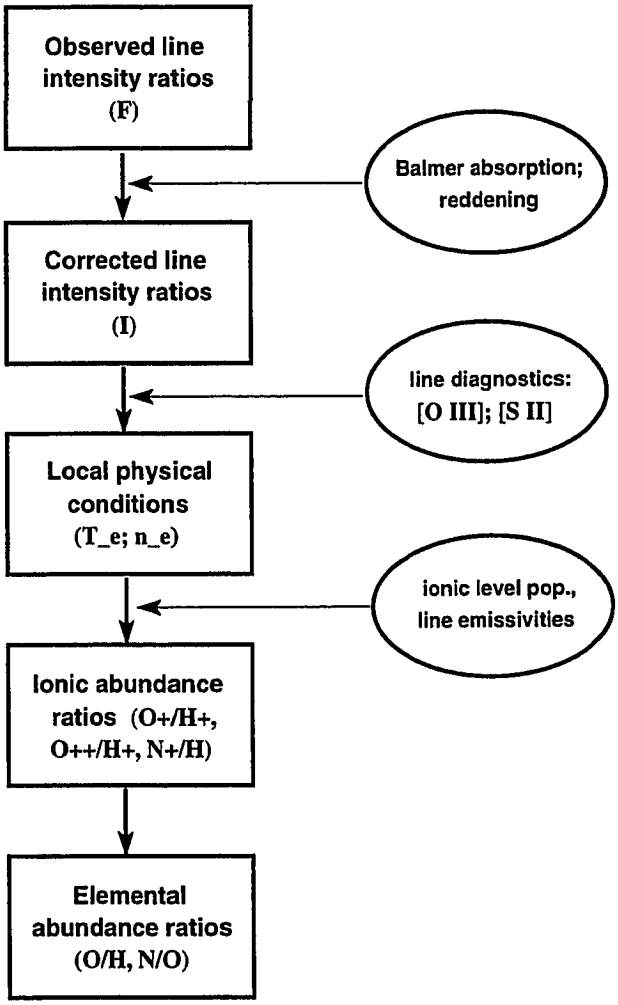

Figure 5.1: Standard method to derive nebular abundances for dIs from the spectra of H II regions. Reddening corrections are derived from $F(\mathrm{H}\alpha)/F(\mathrm{H}\beta)$ or $F(\mathrm{H}\gamma)/F(\mathrm{H}\beta)$ and are computed as described in Figure 4.2. The electron density, n_e, is usually adopted to be 100 cm^{-3}. This figure is adapted from Dinerstein (1990).

strong emission arising from singly– and doubly–ionized oxygen. At temperature T_e, the relative abundances of singly– and doubly–ionized oxygen by number are

$$\frac{N(\mathrm{O}^+)}{N(\mathrm{H})} = \frac{I([\mathrm{O\ II}]\lambda 3727)}{I(\mathrm{H}\beta)} \cdot \frac{j(\mathrm{H}\beta;\ n_e,\ T_e)}{j([\mathrm{O\ II}]\lambda 3727;\ n_e,\ T_e)}, \tag{5.1}$$

$$\frac{N(\mathrm{O}^{+2})}{N(\mathrm{H})} = \frac{I([\mathrm{O\ III}]\lambda 5007)}{I(\mathrm{H}\beta)} \cdot \frac{j(\mathrm{H}\beta;\ n_e,\ T_e)}{j([\mathrm{O\ III}]\lambda 5007;\ n_e,\ T_e)}, \tag{5.2}$$

where I is the intensity of the line at wavelength λ, j is the volume emissivity of the line at density n_e and temperature T_e, and $N(A^{+k})$ is the abundance by number of the atomic species in the kth–ionized state responsible for the line. Data for Balmer line emissivities are found in Storey and Hummer (1995). Emissivities for neutral and ionic oxygen are computed using spontaneous emission coefficients and collision strengths from the literature. References to these data are listed in Table 5.1.

Species	$A_{j,i}$	$\Omega(i,j)$
N^+	Wiese et al. (1996)	Lennon and Burke (1994)
O^0	Wiese et al. (1996)	Bhatia and Kastner (1995)
O^+	Wiese et al. (1996)	Pradhan (1976), McLaughlin and Bell (1993)
O^{+2}	Wiese et al. (1996)	Lennon and Burke (1994)

Table 5.1: Data for nitrogen and oxygen: transition probabilities, $A_{j,i}$, and collision strengths, $\Omega(i,j)$ between levels i and j.

The total oxygen abundance by number, $N(\mathrm{O})/N(\mathrm{H})$, is obtained from the sum

$$\frac{N(\mathrm{O})}{N(\mathrm{H})} = f \cdot \left[\frac{N(\mathrm{O}^+)}{N(\mathrm{H}^+)} + \frac{N(\mathrm{O}^{+2})}{N(\mathrm{H}^+)}\right], \tag{5.3}$$

where f is an ionization correction factor to account for unobserved oxygen ions. To correct for species more ionized than O^{+2}, and since the ionization potential of the O^{+2} ion is similar to the ionization potential of He^+, f may be written as

$$f = 1 + \frac{N(\mathrm{He}^{+2})}{N(\mathrm{He}^+)}. \tag{5.4}$$

By analogy to ionized hydrogen, the ions He^{+} and He^{+2} are traced by line emission from He^{0} (He I) and He^{+} (He II), respectively, which comes from the recombinations of He^{+} and He^{+2} ions (Talent 1980). The last term in Equation (5.4) is zero, because emission from He IIλ4686 is very weak or negligible in typical H II regions. Consequently, the contribution by O^{+3} (or higher ionized species) to the total oxygen abundance is negligible. Thus, the ionization correction factor for oxygen is $f = 1$.

On occasion, forbidden emission from neutral oxygen (O^{0}) is observed in [O I]λ6300 and [O I]λ6364 lines. In typical H II regions, there is very little oxygen in the form of O^{0} (see Baldwin et al. 1981; Veilleux and Osterbrock 1987; Stasińska 1990), so strong [O I] emission indicates the presence of shocks from supernova remnants (see, e.g., Skillman 1985). These lines are not be used to compute the oxygen abundance.

5.2 The Bright–Line Method

Galaxies may be sufficiently distant or contain H II regions so faint that [O III]λ4363 may not be detected within emission line spectra. For these galaxies, the "bright–line" method is used to derive oxygen abundances. Because dIs in the Virgo Cluster are much farther away than dIs in the field, only the strongest emission lines are detected generally if H II regions do not fill the slit or are of low surface brightness. To compare properly the oxygen abundances of Virgo Cluster dIs with field dIs, it is necessary to tie abundances derived from an empirical calibration founded upon the observable bright lines to abundances computed directly from [O III]λ4363 measurements. What follows is a description of the empirical calibration and how the calibration is used to obtain oxygen abundances.

When [O III]λ4363 is too weak to be measured, the "bright–line" or "empirical" method can be used to derive oxygen abundances. This method was originally devised

by Pagel et al. (1979) for metal–rich H II regions. Pagel et al. (1979) suggested that the ratio

$$R_{23} = \frac{I([\text{O II}]\lambda 3727) + I([\text{O III}]\lambda\lambda 4959, 5007)}{I(\text{H}\beta)} \tag{5.5}$$

could be used as an abundance indicator. McCall et al. (1985) showed that giant extragalactic H II regions in spiral galaxies form a well–defined sequence in a number of line–ratio diagrams constructed from bright emission lines. In particular, for metal–rich H II regions (12+log(O/H) $\gtrsim$ 8.4), a trend of decreasing oxygen abundance was found to correlate best with increasing R_{23}. R_{23} is a better sequencing index than [O III]/Hβ because the latter is very sensitive to the degree of ionization of the gas. Thus, a calibration of R_{23} against directly obtained oxygen abundances could give an indication of oxygen abundances.

There have been many efforts to calibrate the relation between R_{23} and the oxygen abundance (see, e.g., Alloin et al. 1979; Edmunds and Pagel 1984; McCall et al. 1985; Dopita and Evans 1986; Skillman 1989; Torres-Peimbert et al. 1989; Zaritsky et al. 1994). McGaugh (1991, 1994) has done much to quantify this relationship at low oxygen abundances, which is the present focus for dwarf galaxies.

Even in dwarfs, the R_{23} indicator depends strongly upon the nebular abundance (e.g., McGaugh 1991, 1994). At extremely low oxygen abundances (12+log(O/H) $\lesssim$ 8), the number of available coolants is low. Because there are few emitters, R_{23} is small and temperatures within H II regions are high. As the abundance begins to increase, cooling becomes dominated by the growing reserves of oxygen and the temperature begins to decrease. So, R_{23} increases with increasing abundance. At an oxygen abundance of 12+log(O/H) $\simeq$ 8.4, the strength of the [O III] lines eventually reaches a maximum and the relationship between R_{23} and oxygen abundance "turns around." At oxygen abundances 12+log(O/H) $\gtrsim$ 8.4, the intensities of [O II]λ3727

and [O III]$\lambda\lambda$4959, 5007 and, thus, the value of R_{23}, begin to decline as the gas becomes so cold that the burden of cooling shifts to the fine–structure infrared lines of [O III] at 52 and 88 μm. At very high abundances (12+log(O/H) $\gtrsim$ 8.7), H II regions are very cold ($T_e \lesssim$ 6000 K) and values of R_{23} are small. Infrared lines of [O III] continue to provide cooling, although other metallic species contribute significantly to the cooling process, too.

Clearly then, the R_{23} indicator is not a monotonic function of oxygen abundance. That is, at a given value of R_{23}, there are two possible choices of the oxygen abundance. Roughly, the low–abundance or "lower branch" régime is defined by 12+log(O/H) $\lesssim$ 8.4, whereas the high–abundance or "upper branch" régime is defined by 12+log(O/H) $\gtrsim$ 8.4. It should be pointed out, however, that within the "turnaround" region 8.2 $\lesssim$ 12+log(O/H) $\lesssim$ 8.6, the oxygen abundance changes quite rapidly with R_{23}. Additional discussion of models are described in § 5.2.1 below.

A plot of R_{23} versus oxygen abundance is shown in Figure 5.2 for H II regions in dwarf irregular galaxies in the field. Each point represents an H II region with an [O III]λ4363 measurement. Theoretical curves of oxygen abundance versus R_{23} are superimposed (§ 5.2.1). Horizontal dotted lines indicate solar and one–tenth solar values of the oxygen abundance, where the solar value is 12+log(O/H) = 8.87 (Grevesse et al. 1996). A long–dash short–dash horizontal line at 12+log(O/H) $\simeq$ 8.4 marks the boundary below (above) which the lower–branch (upper–branch) occurs. Oxygen abundances for H II regions in field dIs range from about one–tenth to about one–half of the solar value. The two Virgo dwarfs VCC 0848–1 and VCC 1554–1 are also indicated in Figure 5.2 and lie on the same locus defined by H II regions in field dIs. Unfortunately, H II regions in these dwarfs are clustered around the "knee" of the curves within the "turnaround" region, where ambiguity is greatest. A method must be used to distinguish between the upper branch and the lower branch to break

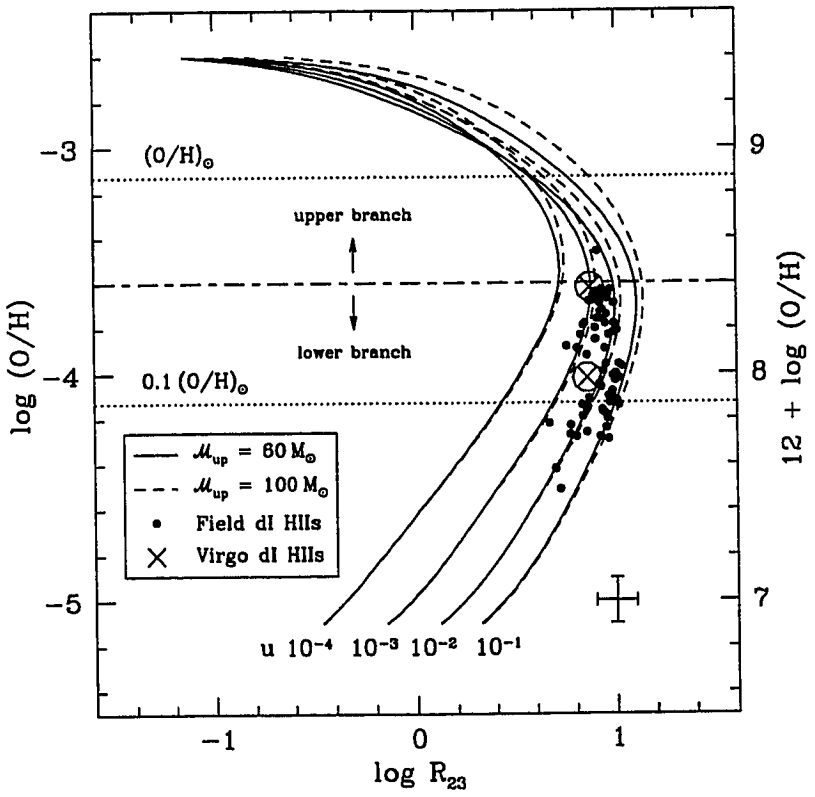

Figure 5.2: Oxygen abundance versus R_{23} for H II regions in field and Virgo dIs. The filled circles indicate H II regions from field dIs, whose oxygen abundances were obtained directly from measurements of the [O III]λ4363 emission line. Data for field dwarfs were gathered from the references in Richer and McCall (1995) and from Table 2.3 in § 2.1.3. [O III]λ4363 abundances for VCC 0848–1 and VCC 1554–1 are shown as crosses enclosed in open circles. The horizontal dotted lines indicate solar ($12+\log(O/H)_\odot = 8.87$; Grevesse et al. 1996) and one–tenth solar values of the oxygen abundance. Calibration curves for log(O/H) against log R_{23} (McGaugh 1991; 1994; 1997, personal communication) are plotted for four different values of the ionization parameter (§ 5.2.1). These curves were derived using a standard stellar initial mass function for a cluster of ionizing stars with an upper mass limit of $\mathcal{M}_{up} = 60\ M_\odot$(solid lines) and 100 $M_\odot$(dashed lines). Further discussion about the model curves is given in § 5.2.1. The long–dash short–dash horizontal line at $\log(O/H) \simeq -3.6$ marks the boundary below (above) which the lower–branch (upper–branch) occurs. [O III]λ4363 abundances are consistent with lower branch values. The error bars at the lower right indicates typical uncertainties of 0.1 dex for the R_{23} indicator and 0.1 dex for the oxygen abundance.

the degeneracy in R_{23}.

5.2.1 The McGaugh Discriminant

Skillman (1989) and McGaugh (1994) showed that the ionization state of the nebula is an important consideration when oxygen abundances are derived at low metallicities. In particular, McGaugh (1994, Figure 7) showed that model temperatures depend strongly upon the ionization for oxygen abundances 12+log(O/H) $\lesssim 8$. The form of the empirical calibration used for the remainder of this discussion is the one defined by McGaugh (1991, 1994, 1997; personal communication). Theoretical curves are plotted in Figure 5.2 for an ionizing cluster of stars and a standard stellar initial mass function with an upper mass limit of 60 $M_{\odot}$ and 100 $M_{\odot}$. Each of the four curves is plotted with a unique value of the ionization parameter, $u = \log \bar{U}$ (see § 5.2.2), where the volume–averaged ionization parameter, $\bar{U}$, is the ratio of the density of ionizing photons to the density of gas particles within an H II region (McGaugh 1991). For constant density, $\bar{U}$ is given by

$$\bar{U} = \frac{3Q}{4\pi c N R_s^2}, \tag{5.6}$$

where Q is the luminosity of ionizing stars within an H II region, c is the speed of light, N is the volume density of gas, and R_s is the Strömgren radius. In the models, the range of $\log \bar{U}$ goes from -4 to -1 in steps of 1 dex, which covers the range observed in H II regions. At low metallicities, the oxygen abundance is particularly dependent upon $\bar{U}$ at a given R_{23}, as Figure 5.2 shows.

Since H II regions in dwarfs are located near the "turnaround" region in Figure 5.2, determining the oxygen abundance from Figure 5.2 alone is impossible. Fortunately, the [N II]λ6583/[O II]λ3727 ratio (hereafter, [N II]/[O II]), can be used to resolve the degeneracy in R_{23} (McCall et al. 1985; McGaugh 1991, 1994). The

strength of the [N II]λ6583 line is roughly proportional to the nitrogen abundance and the [N II]/[O II] intensity ratio is relatively insensitive to the ionization. Thus, the [N II]/[O II] ratio can be used to derive the abundance of N^+ relative to O^+ by number, $N(N^+)/N(O^+)$ (see § 5.3). For low–metallicity H II regions such as those found in dwarf galaxies, $N(N^+)/N(O^+)$ is approximately equivalent to the nitrogen–to–oxygen abundance ratio, $N(N)/N(O) \equiv N/O$, and is roughly constant with oxygen abundance (Peimbert and Costero 1969; Garnett 1990). At higher metallicity, N/O varies monotonically with oxygen abundance (McCall et al. 1985). McGaugh (1994) has shown that [N II]/[O II] is approximately $\lesssim 0.1$ at low oxygen abundance, and $\gtrsim 0.1$ at high oxygen abundance. For objects ranging from sub–solar to solar metallicities, [N II]/[O II] can vary by one to two orders of magnitude (McGaugh 1994).

McGaugh (1991, 1994; 1997, personal communication) confirmed the usefulness of [N II]/[O II] in resolving the ambiguity in the empirical calibration of R_{23}. He claimed that log ([N II]/[O II]) $\simeq -1$ should be used as a boundary between the upper and lower branch of the calibration. So, the lower O/H branch is chosen when log ([N II]/[O II]) $\lesssim -1$ and the upper branch is indicated by log ([N II]/[O II]) $\gtrsim -1$.

For field dIs with measured [O III]λ4363 (i.e., direct oxygen abundances), values of [N II]/[O II] are obtained from the original references listed in Richer and McCall (1995). These [N II]/[O II] data are plotted against R_{23} in Figure 5.3. For the most part, [N II]/[O II] values for H II regions in field dwarfs are consistent with the choice of the lower branch of the empirical calibration of R_{23}, as required by determinations of direct oxygen abundances. The three deviants are: NGC 2366 "region 1" (Kennicutt et al. 1980) with log ([N II]/[O II]) = −0.91; NGC 5408 (Stasińska et al. 1986) with log ([N II]/[O II]) = −0.78; and WLM "object #9" (Hodge and Miller 1995) with log ([N II]/[O II]) = −0.92. Although the [N II]/[O II] values for these three H II regions lie above the lower/upper branch boundary, there are other H II regions in

their host galaxies, which have [O III]λ4363 oxygen abundances consistent with lower branch values.

Figure 5.3 shows that H II regions in Virgo dIs all occupy the same phase space as H II regions in field dIs in the lower branch of the diagram. Thus, oxygen abundances of Virgo dIs can be computed using analytical formulae for the lower branch values (§ 5.2.2).

Values of [N II]/[O II] are plotted against direct [O III]λ4363 oxygen abundances in Figure 5.4. Filled circles indicate H II regions from field dwarf galaxies. [O III]λ4363 measurements for VCC 0848–1 and VCC 1554–1 are also indicated. The horizontal dashed line indicates the boundary between the upper and lower branches in the calibration. The vertical dashed line roughly marks the oxygen abundance (12+log(O/H) $\sim$ 8.4) where the "turnaround" region occurs in the empirical calibration as R_{23} reaches a maximum value. H II regions with high oxygen abundances are expected to lie in the upper right of the diagram, while H II regions with low oxygen abundances occupy the lower left portion of the diagram. This is similar to what Webster et al. (1983) found in their early compilation of dwarf galaxies from the literature. For both field and Virgo dIs, lower branch abundances are consistent with [O III]λ4363 abundances. Clearly, the [N II]/[O II] indicator is adequate for use in distinguishing between the lower and upper branches of the calibration of R_{23}.

5.2.2 Analytical Expressions

McGaugh (1997, personal communication) has developed analytical expressions which can be used to compute the oxygen abundance based upon observations of [O II]λ3727, [O III]λ4959, and [O III]λ5007 emission lines, provided also that [N II]λ6583 is available to discriminate between the upper and lower branches of the empirical calibration. McGaugh generated a large grid of photoionization models covering a wide

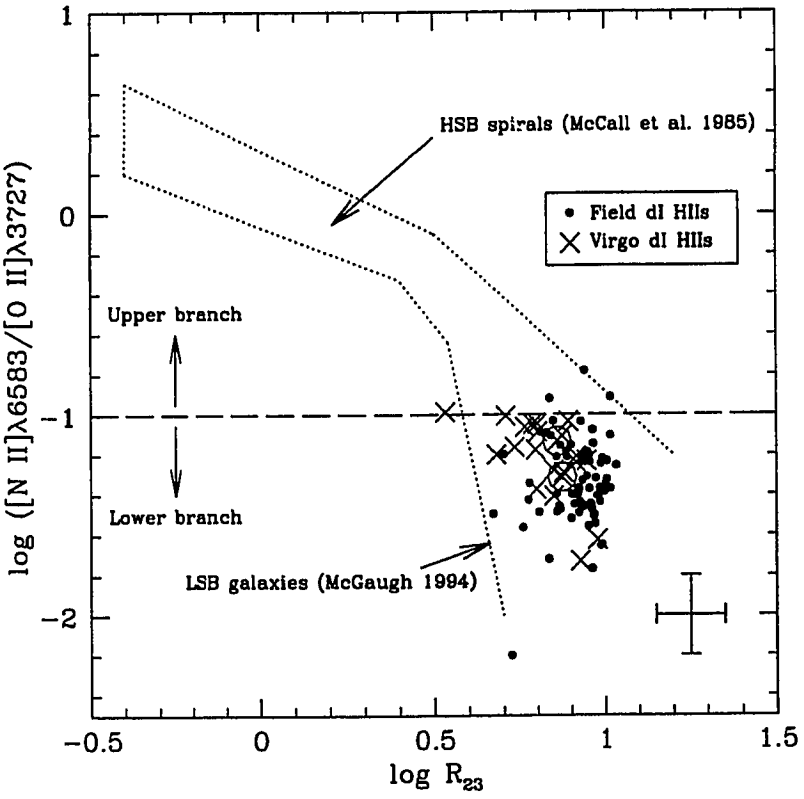

Figure 5.3: log ([N II]λ6583/[O II]λ3727) versus log R_{23} for H II regions in field and Virgo dIs. Filled circles indicate H II regions from field dIs with [O III]λ4363 detections and whose [N II]/[O II] data were obtained from the literature. Crosses indicate H II regions in Virgo dIs. [O III]λ4363 detections for VCC 0848–1 and VCC 1554-1 are indicated as crosses enclosed by open circles. The error bars at the lower right indicate typical uncertainties of 0.1 dex for the R_{23} indicator and 0.2 dex (at most) for the [N II]/[O II] ratio. The dotted lines mark roughly the regions occupied by high surface brightness (HSB) spiral galaxies (McCall et al. 1985) at the upper left and low surface brightness (LSB) galaxies (McGaugh 1994) towards the lower right. The horizontal dashed line marks the boundary below (above) which the lower (upper) branch of the empirical calibration is selected to determine a unique value of an oxygen abundance. There are only three H II regions whose [N II]/[O II] values are above the boundary and which imply empirical abundances inconsistent with direct determinations. However, the dIs in which these H II regions lie contain other H II regions whose [O III]λ4363 oxygen abundances are consistent with lower branch values. H II regions for Virgo dIs lie in the same area as H II regions for field dIs, implying that Virgo dIs have lower branch abundances.

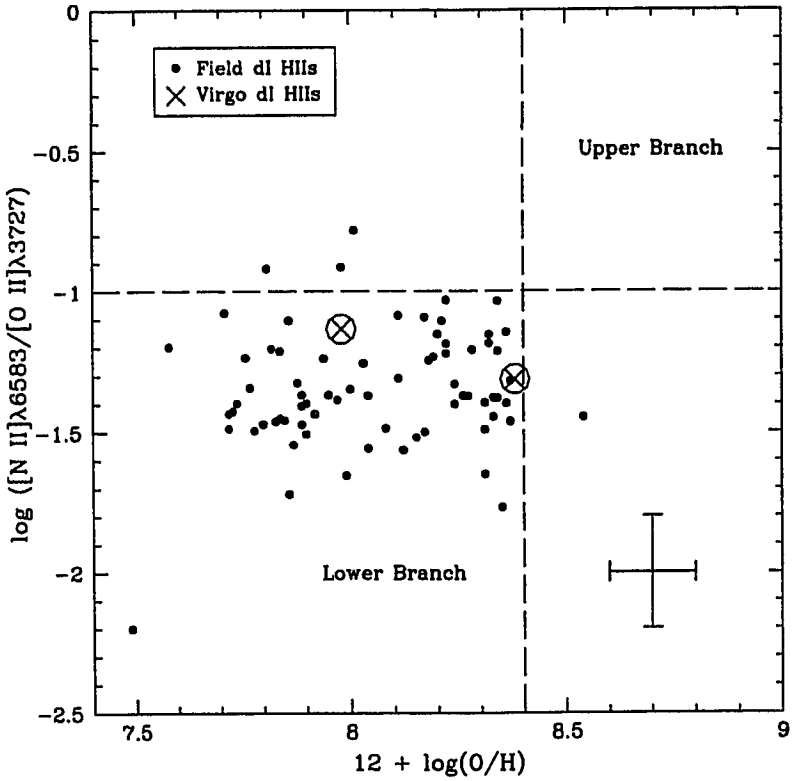

Figure 5.4: [N II]/[O II] versus direct log(O/H) for H II regions in field and Virgo dIs. The filled circles mark the positions of H II regions in field dIs. Only H II regions with [O III]λ4363 detections are shown. Oxygen abundances based on [O III]λ4363 detections for VCC 0848–1 and VCC 1554–1 are indicated as crosses enclosed by open circles. The error bars at the lower right indicate typical uncertainties of 0.1 dex for the oxygen abundance and 0.2 dex for the [N II]/[O II] ratio. The vertical dashed line at 12+log(O/H) = 8.4 indicates roughly the position where the [O III]λλ4959, 5007 lines are at their brightest and R_{23} is maximum. The horizontal dashed line indicates log [N II]/[O II] ≈ -1 below (above) which H II regions should have lower branch (upper branch) abundances (McGaugh 1991, 1994). So, H II regions with low (high) oxygen abundance are expected to lie in the lower left (upper right) of the diagram. For field dIs, oxygen abundances obtained using the empirical calibration are consistent with direct [O III]λ4363 determinations. The [N II]/[O II] indicator is clearly adequate to distinguish between the lower and upper branches of the calibration.

range in physical parameters with the primary assumption that a cluster of young OB stars is responsible for the ionizing spectrum within the H II regions. The models are not sensitive to the effective temperature[1], T_*, so long as $T_* \gtrsim 40{,}000$ K. Assuming a standard slope for the stellar initial mass function and an upper mass limit (e.g., 60 $M_\odot$), a two–parameter (oxygen abundance and ionization parameter) calibration of R_{23} can be obtained from the model grid. The models are not very sensitive to the upper mass limit adopted for the stellar initial mass function (see Figure 5.2). Oxygen abundances can be determined by interpolating between the lines of constant oxygen abundance and constant ionization parameter.

McGaugh (1991) fitted a model grid to observed H II regions (his Table 2) where most of the H II regions (70 of 82) had measured temperatures in the O^{+2} zone. His model curves were shown in Figure 5.2 above. McGaugh generated analytical expressions for O/H as a function of R_{23} and u to reproduce the same oxygen abundances and ionization parameters obtained directly using [O III]λ4363. These expressions are reproduced here and defined as follows:

$$z = \log(\mathrm{O/H}), \tag{5.7}$$

$$u = \log \bar{U}, \tag{5.8}$$

$$x = \log(R_{23}), \tag{5.9}$$

$$y = \log(O_{32}), \tag{5.10}$$

where z represents the oxygen abundance, and $\bar{U}$ is the volume–averaged ionization parameter described by Equation (5.6). The bright–line ratio, R_{23} (as defined in Equation 5.5), and the ratio of bright oxygen line intensities, O_{32}, are given by

$$R_{23} = \frac{I([\mathrm{O\ II}]\lambda 3727) + I([\mathrm{O\ III}]\lambda\lambda 4959, 5007)}{I(\mathrm{H}\beta)}, \tag{5.11}$$

[1] T_* is the temperature of a blackbody with the same exitance integrated over all wavelengths as the star.

$$O_{32} = \frac{I([\text{O III}]\lambda\lambda 4959, 5007)}{I([\text{O II}]\lambda 3727)}. \quad (5.12)$$

The oxygen abundance, $z(x, y)$, is obtained from the observable line ratios x and y. On the lower branch, z and u are given by

$$z_{\text{lower}}(x, y) = \log(\text{O/H})_{\text{lower}} \quad (5.13)$$

$$= -4.93 + 4.25x - 3.35\sin(x) - 0.26y - 0.12\sin(y) \quad (5.14)$$

$$u_{\text{lower}}(x, y) = -2.95 + 0.17x^2 + 1.02y. \quad (5.15)$$

On the upper branch, z and u are given by

$$z_{\text{upper}}(x, y) = \log(\text{O/H})_{\text{upper}} \quad (5.16)$$

$$= -2.65 - 0.91x + 0.12y\sin(x) \quad (5.17)$$

$$u_{\text{upper}}(x, y) = -2.39 - 0.35x + 1.29y - 0.15xy. \quad (5.18)$$

In the absence of [O III]λ4363, measurements of [O II]λ3727 and [O III]$\lambda\lambda$4959, 5007 lines can be combined with the formulae above to obtain a measure of the oxygen abundance and the ionization parameter. The value of [N II]/[O II] discriminates between upper and lower branches.

In Figure 5.5, oxygen abundances obtained directly from [O III]λ4363 measurements for H II regions in the samples of field and Virgo dIs are plotted against oxygen abundances obtained from the lower branch as required by [N II]/[O II] using the equations above. The solid line marks where direct abundances are equal to empirical abundances. While the general trend is indeed correct, the scatter of the data points about the line of equality is consistent with the 0.2 dex uncertainty stated by McGaugh in determining oxygen abundances from the bright-line method. This is smaller than the 0.3 dex uncertainty stated by Skillman (1989) for abundances computed below 12+log(O/H) $\sim$ 8.2.

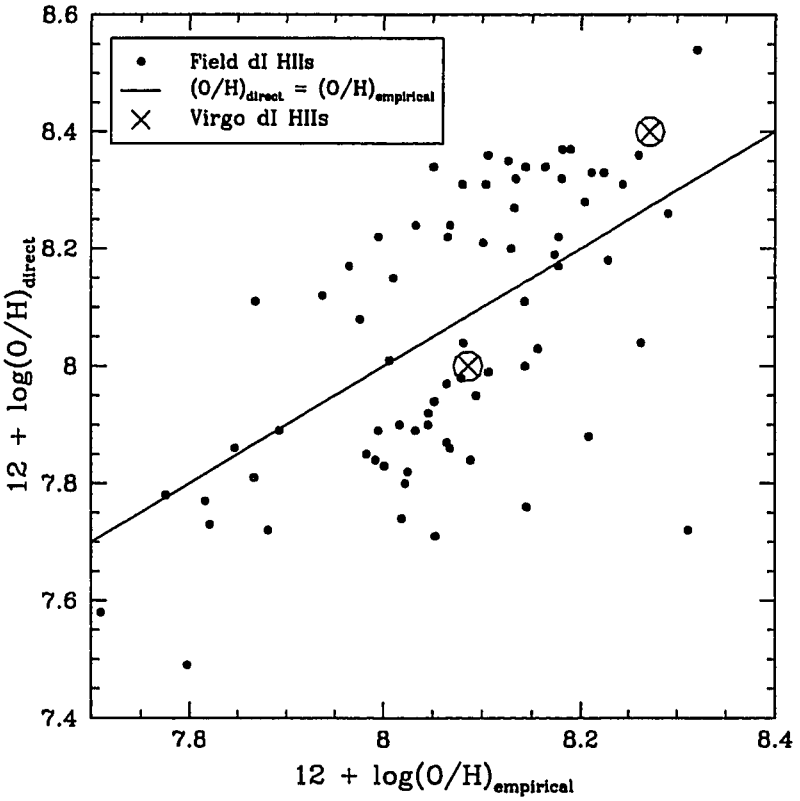

Figure 5.5: Direct ([O III]λ4363) oxygen abundances versus empirical abundances for H II regions in field and Virgo dIs. Filled circles indicate H II regions from field dIs. [O III]λ4363 abundances for VCC 0848–1 and VCC 1554–1 are indicated as crosses enclosed by open circles. The solid line is the line of equality between direct and empirical oxygen abundances. The scatter of data points about the line is consistent with the approximate 0.2 dex uncertainty in the empirical calibration of the oxygen abundance stated by McGaugh (1991, 1994).

With the agreement seen between direct and empirical abundances, the empirical calibration combined with the McGaugh discriminant can now be applied with confidence to dwarfs lacking [O III]λ4363 detections, such as the majority of Virgo dIs studied here. The previous figures have shown that H II regions in Virgo dIs are physically comparable to those in field dIs. A precise absolute calibration is not required for a *comparison* between Virgo dwarfs and field dwarfs, because oxygen abundances for both datasets will be computed in the same manner using the same form of the calibration. The primary goal of this thesis is simply to look for an offset in chemical abundances between Virgo and field dwarfs, which would reflect the effect of differences in evolution.

5.3 Abundance of Nitrogen Relative to Oxygen

The nitrogen–to–oxygen ratio, N/O, was estimated from $N(\mathrm{N}^+)/N(\mathrm{O}^+)$, if the temperature were known (Peimbert and Costero 1969; Garnett 1990). In the absence of [O III]λ4363, temperatures were derived with the aid of the empirical calibration. The precise method is shown in Figure 5.6. An estimate of the temperature was obtained from O/H using a plot of temperature versus oxygen abundance for various values of the ionization parameter (Figure 7 of McGaugh 1991). With an estimate for the electron temperature, T_e, a variation of Equation (5.2) was used to compute N/O:

$$\frac{N(\mathrm{N})}{N(\mathrm{O})} = \frac{N(\mathrm{N}^+)}{N(\mathrm{O}^+)} \tag{5.19}$$

$$= \frac{I([\mathrm{N\ II}]\lambda\,6583)}{I([\mathrm{O\ II}]\lambda\,3727)} \cdot \frac{j([\mathrm{O\ II}]\lambda\,3727;\ n_e,\ T_e)}{j([\mathrm{N\ II}]\lambda\,6583;\ n_e,\ T_e)}, \tag{5.20}$$

where $j([\mathrm{N\ II}]\lambda6583;\ n_e,\ T_e)$ and $j([\mathrm{O\ II}]\lambda3727;\ n_e,\ T_e)$ are the volume emissivities of [N II]λ6583 and [O II]λ3727, respectively. References to the appropriate data used to

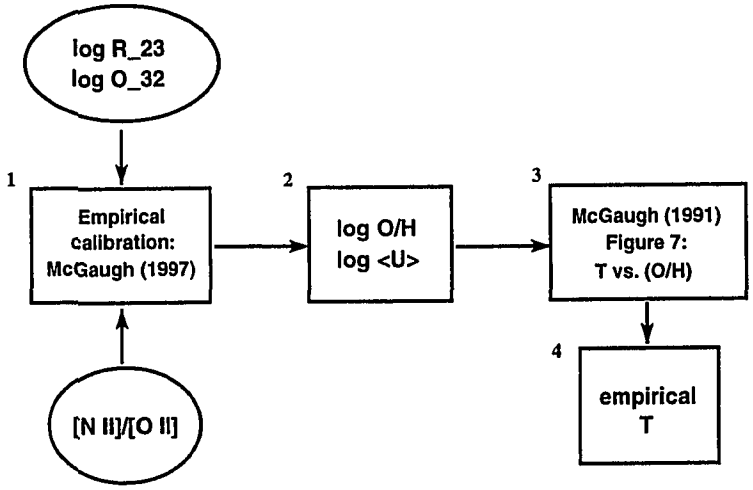

Figure 5.6: Method to obtain temperatures using the bright-line method. Box 1: Values of log R_{23} and log O_{32} are computed. The value of [N II]/[O II] is used to choose the appropriate branch in the empirical calibration. Box 2: The oxygen abundance, log(O/H), and the ionization parameter, log $\langle U \rangle$ (or log $\bar{U}$), are derived using the analytical formulae in § 5.2.2. Box 3: A plot of temperature versus oxygen abundance for various values of the ionization parameter (McGaugh 1991, Figure 7) is examined. Box 4: Given log(O/H) and log $\bar{U}$ from Box 2, an estimate of the temperature is obtained.

compute the line emissivity for [N II]λ6583 are listed in Table 5.1. SNAP (Krawchuk et al. 1997) was used to compute N/O values, which are presented in Tables 5.4 to 5.6 below.

5.4 Derived Properties for the Field dIs

Derived properties for the five dIs observed at Steward and San Pedro Mártir (see § 3.1, 3.5, and 4.3) are listed in Table 5.2. For at least one H II region in each of Holmberg II, IC 10, NGC 3109, and UGC 6456, [O III]λ4363 was detected and an oxygen abundance was derived directly. A meaningful lower limit to the oxygen abundance was obtained for NGC 1560. Properties include Hβ intensities corrected

for underlying Balmer absorption and reddening, derived values of the reddening[2], $E(B-V)$, Hβ emission equivalent widths corrected for underlying Balmer absorption, electron temperatures, T_e, and resulting oxygen abundances, 12+log(O/H). Errors in oxygen abundances were computed from the maximum and minimum possible values, given the errors in the reddening, temperature, and line intensities.

5.4.1 Holmberg II

Oxygen abundances for H II regions Ho II–5, Ho II–8, and Ho II–9 were adopted, because these H II regions are independent of each other and have the largest Hβ intensities. The abundance for Ho II–7 was not selected because the extracted spectrum is not independent of the spectrum for Ho II–8 (see also Table 3.3). Oxygen abundances for three H II regions reported by Masegosa et al. (1991) were re–analyzed in the same manner as the Steward data. The average oxygen abundance listed in Table 2.1 was computed using results for the three selected H II regions in the present analysis and results for the three H II regions in Masegosa et al. (1991).

5.4.2 IC 10

Oxygen abundances for H II regions IC 10–2 and IC 10–3 were adopted. The abundance for IC 10–1 was not selected because the extracted spectrum is not independent of the spectra extracted for IC 10–2 and IC 10–3 (see also Table 3.4). The oxygen abundance for IC 10 listed in Table 2.1 is an average of abundances for IC 10–2 and IC 10–3. Computed errors in derived oxygen abundances include errors in both reddenings and temperatures. The oxygen abundance for IC 10–2 (HL111c; Table 3.4) agrees with the value independently derived by Richer et al. (2001) for the same

[2]Reddenings were computed from values of $F(\mathrm{H}\gamma)/F(\mathrm{H}\beta)$, except for IC 10 and NGC 1560, where values of $F(\mathrm{H}\alpha)/F(\mathrm{H}\beta)$ were used; see § 4.3.

Property	Ho II-1	Ho II-2	Ho II-3	Ho II-4	Ho II-5
$I(\mathrm{H}\beta)$ ($\times 10^{-15}$)	1.97 ± 0.12	6.85 ± 0.31	4.47 ± 0.20	3.24 ± 0.17	21.44 ± 0.85
$E(B-V)$ [a]	-0.59 ± 0.29	-0.46 ± 0.20	-0.42 ± 0.20	-0.18 ± 0.24	-0.12 ± 0.16
$W(\mathrm{H}\beta)$	209 ± 79	218 ± 42	201 ± 35	104 ± 14	101.9 ± 5.0
$T_e(\mathrm{O}^{+2})$	< 17400	< 23500	< 29000	< 17300	16000 ± 1300
12+log(O/H)	> 7.64	> 7.17	> 6.89	> 7.37	7.56 ± 0.13
Property	Ho II-6	Ho II-7	Ho II-8	Ho II-9	
$I(\mathrm{H}\beta)$ ($\times 10^{-15}$)	9.46 ± 0.37	20.99 ± 0.81	11.47 ± 0.45	32.4 ± 1.3	
$E(B-V)$ [a]	$+0.05 \pm 0.22$	-0.08 ± 0.17	-0.16 ± 0.17	$+0.12 \pm 0.16$	
$W(\mathrm{H}\beta)$	113.8 ± 5.8	113.5 ± 4.6	112.3 ± 5.0	155 ± 12	
$T_e(\mathrm{O}^{+2})$	< 11700	13400 ± 2100	15100 ± 1800	14800 ± 1100	
12+log(O/H)	> 7.97	7.76 ± 0.25	7.60 ± 0.18	7.65 ± 0.13	
Property	IC 10-1	IC 10-2	IC 10-3	IC 10-4	IC 10-5
$I(\mathrm{H}\beta)$ ($\times 10^{-12}$) [b]	15.8 ± 4.1	11.8 ± 2.9	3.6 ± 1.1	6.3 ± 2.1	10.9 ± 4.0
$E(B-V)$ [c]	$+0.788 \pm 0.070$	$+0.773 \pm 0.067$	$+0.862 \pm 0.083$	$+0.897 \pm 0.091$	$+1.215 \pm 0.096$
$W(\mathrm{H}\beta)$	88.5 ± 3.9	101.0 ± 4.7	60.5 ± 2.4	92.6 ± 7.6	154 ± 28
$T_e(\mathrm{O}^{+2})$	10100 ± 560	9800 ± 580	12300 ± 1100	< 13200	< 19100
12+log(O/H)	8.29 ± 0.13	8.32 ± 0.14	8.05 ± 0.18	> 7.96	> 7.60
Property	NGC 1560-1	NGC 1560-2	NGC 1560-3	NGC 1560-4	NGC 1560-5
$I(\mathrm{H}\beta)$ ($\times 10^{-15}$)	12.45 ± 0.45	17.25 ± 0.59	7.73 ± 0.54	14.50 ± 0.77	8.26 ± 0.49
$E(B-V)$ [d]	$+0.354$	$+0.354$	$+0.354$	$+0.354$	$+0.354$
$W(\mathrm{H}\beta)$	(-189)	111 ± 11	460 ± 370	(-132)	(-81)
$T_e(\mathrm{O}^{+2})$	< 11900	< 13300	< 19900	< 17300	< 18900
12+log(O/H)	> 8.05	> 7.89	> 7.55	> 7.64	> 7.46
Property	NGC 1560-6	NGC 1560-7			
$I(\mathrm{H}\beta)$ ($\times 10^{-15}$)	5.87 ± 0.62	1.47 ± 0.29			
$W(\mathrm{H}\beta)$	8.12 ± 0.71	7.7 ± 1.3			
$T_e(\mathrm{O}^{+2})$	...	...			
12+log(O/H)	...	...			
Property	NGC 3109-1	NGC 3109-2	NGC 3109-3	NGC 3109-4	
$I(\mathrm{H}\beta)$ ($\times 10^{-15}$)	0.48 ± 0.12	2.47 ± 0.17	4.46 ± 0.20	10.27 ± 0.48	
$E(B-V)$ [a]	$+0.15 \pm 0.57$	$+0.06 \pm 0.44$	-0.03 ± 0.23	-0.02 ± 0.29	
$W(\mathrm{H}\beta)$	(-241)	149 ± 35	60.2 ± 2.6	25.65 ± 0.80	
$T_e(\mathrm{O}^{+2})$	...	...	14600 ± 2600	< 16200	
12+log(O/H)	...	...	7.73 ± 0.33	> 7.62	
Property	UGC 6456-1	UGC 6456-2			
$I(\mathrm{H}\beta)$ ($\times 10^{-15}$)	4.99 ± 0.30	21.56 ± 0.86			
$E(B-V)$ [a]	-0.07 ± 0.27	-0.18 ± 0.17			
$W(\mathrm{H}\beta)$	66.1 ± 7.6	147 ± 10			
$T_e(\mathrm{O}^{+2})$	20900 ± 4000	17600 ± 1700			
12+log(O/H)	7.21 ± 0.23	7.45 ± 0.14			

Table 5.2: Derived properties for H II regions in Holmberg II, IC 10, NGC 1560, NGC 3109, and UGC 6456. $I(\mathrm{H}\beta)$ represents the Hβ intensity, in ergs s^{-1} cm^{-2}, corrected for underlying Balmer absorption and reddening; $E(B-V)$ is the computed reddening in magnitudes; $W(\mathrm{H}\beta)$ is the emission equivalent width, in Å, corrected for underlying Balmer absorption; $T_e(O^{+2})$ is the computed electron temperature in degrees Kelvin, assuming an electron density of 100 cm^{-3}; and 12+log(O/H) is the derived oxygen abundance in dex. NOTES: [a] The reddening was assumed to be zero and no reddening corrections were applied. [b] Hβ intensities for IC 10 are much larger than for other galaxies. [c] From Hα and Hβ measurements at SPM; see Tables 4.3 and 4.4. [d] Average $E(B-V)$ computed from red spectra; see Tables 4.6 and 4.7.

Steward data: 12 + log(O/H) = 8.23 ± 0.09.

5.4.3 NGC 1560

The [O III]λ4363 line was not detected. To determine a lower limit to the galaxy's oxygen abundance, the two best spectra were selected from the seven H II regions observed. For H II regions NGC 1560–1 and NGC 1560–2, the lower limits are 12+log(O/H) ≥ 8.05 and ≥ 7.89, respectively. The mean of lower limits is a lower limit to the mean, provided that each lower limit is lower than the true abundance values (Richer and McCall 1995). So, the mean of the lower limits obtained from the present analysis was 12+log(O/H) ≥ 7.97, which was adopted as the lower limit to the oxygen abundance for NGC 1560.

Negative equivalent widths for Hβ appear for NGC 1560. This is because some windows chosen for sky subtraction contained excess signal from the galaxy, owing to the rapid variability of surface brightness along the slit.

5.4.4 NGC 3109

In H II region NGC 3109–3, [O III]λ4363 was detected, from which an oxygen abundance of 12+log(O/H) = 7.73 ± 0.33 was derived. The oxygen abundance for NGC 3109 listed in Richer and McCall (1995), which was derived from the same Steward data, is 1σ higher than the present value. The ratio F([O III]λ4363)/F(Hβ) for NGC 3109–3 is 5.73 ± 2.04, where F(Hβ) ≡ 100. The measurement has an error of 36%. From M. G. Richer (personal communication), the derived value was 3.13 ± 1.49, implying an error of 48%. The improvement here was due to a redefinition of the "aperture window" used to extract the H II region spectrum and to "no–weights" summed extraction (see Chapter 3). The new value of the oxygen abundance was adopted for NGC 3109 and listed in Table 2.1. The 0.33 dex error in

the oxygen abundance is large, because of significant ($\simeq$ 10%) errors in each of the corrected intensity ratios for [O II] and [O III], as well as an error near 40% in the corrected intensity ratio for [O III]λ4363.

5.4.5 UGC 6456

The oxygen abundance for the brighter H II region UGC 6456–2 (12+log(O/H) = 7.45) was adopted. Izotov et al. (1997), Lynds et al. (1998), and Hunter and Hoffman (1999) provide more recent measurements. A homogeneous treatment of these data gives oxygen abundances of 12+log(O/H) = 7.65, 7.74, and 7.73, respectively. The oxygen abundance for UGC 6456 listed in Table 2.1 is an average of the abundance derived here and abundances from the three measurements in the literature.

5.4.6 DDO 187

Derived values for the electron temperature and oxygen abundance are listed in Table 5.3 and agree with the results in van Zee et al. (1997). The oxygen abundance derived for DDO 187–2 is adopted: 12+log(O/H) = 7.69 $\pm$ 0.09.

Property	DDO 187–1	DDO 187–2
$I(\mathrm{H}\beta)$ (ergs s^{-1} cm^{-2})	(1.937 $\pm$ 0.072) $\times 10^{-15}$	(5.88 $\pm$ 0.28) $\times 10^{-16}$
$W(\mathrm{H}\beta)$ (Å)	75	27
n_e (cm^{-3})	200	110
$T_e(\mathrm{O}^{+2})$ (K)	13200 $\pm$ 700	...
12+log(O/H)$_{\mathrm{dir}}$	7.69 $\pm$ 0.09	...
12+log(O/H)$_{\mathrm{emp}}$	7.72	7.78

Table 5.3: Derived properties for the two H II regions in DDO 187. $I(\mathrm{H}\beta)$ represents the corrected Hβ intensity, $W(\mathrm{H}\beta)$ is the Hβ emission equivalent width corrected for underlying Balmer absorption, n_e is the computed electron density, $T_e(\mathrm{O}^{+2})$ is the derived electron temperature using [O III]λ4363, 12+log(O/H)$_{\mathrm{dir}}$ is the direct oxygen abundance, and 12+log(O/H)$_{\mathrm{emp}}$ is the empirical oxygen abundance (see § 5.2).

5.5 Derived Properties for the Virgo dIs

Derived properties for H II regions of Virgo dIs are listed in Table 5.4 to 5.6 inclusive. Values of the reddening, $E(B-V)$, were small; the adopted reddening in some cases was zero. Where [S II]$\lambda\lambda$6716, 6731 lines were observed, derived values of the electron density were consistent with the canonical value of 100 cm^{-3} typically found in H II regions (Osterbrock 1989).

Direct oxygen abundances were derived for VCC 0848–1 and VCC 1554–1. For these two H II regions, [O I]λ6300 and [O I]λ6364 lines were detected. The implied contribution to the total oxygen abundance is about 0.02 dex, which is much smaller than the error in the oxygen abundance. The contribution from neutral oxygen was not included in the reported values of the total oxygen abundance for VCC 0848–1 and VCC 1554–1.

The direct oxygen abundances for VCC 0848–1 and VCC 1554-1 were adopted as the abundances for the dwarfs, respectively. For H II regions in the remaining dIs, lower limits to oxygen abundances were obtained from upper limits to [O III]λ4363. In all cases, the lower limits were consistent with lower branch abundances. Lower branch abundances (or an average if there was more than one H II region) were adopted for VCC 0512, VCC 0888, VCC 1114, VCC 1179, VCC 1200, VCC 1249, VCC 1585, VCC 1789, and VCC 2037. Table 5.7 summarizes the abundances adopted for each dI in the Virgo sample.

Property	VCC 0512-3	VCC 0512-4	VCC 0848-1	VCC 0888-1	VCC 0888-2
$I(\mathrm{H}\beta)$ (ergs s^{-1} cm^{-2})	$(4.50 \pm 0.39) \times 10^{-16}$	$(2.91 \pm 0.45) \times 10^{-16}$	$(1.06 \pm 0.13) \times 10^{-14}$	$(1.64 \pm 0.83) \times 10^{-15}$	$(2.1 \pm 1.3) \times 10^{-15}$
$E(B-V)$ (mag)	-0.10 ± 0.14	-0.12 ± 0.23	0.048 ± 0.022	0.17 ± 0.13	0.27 ± 0.15
Adopted $E(B-V)$	0	0	0.048	0.17	0.27
$W(\mathrm{H}\beta)_{\mathrm{e}}$ (Å)	89 ± 15	26.4 ± 4.2	33.69 ± 0.57	9.01 ± 0.33	6.59 ± 0.31
$W(\mathrm{H}\beta)_{\mathrm{abs}}$ (Å)	1.59	1.59	1.59	1.38 ± 0.52	1.19 ± 0.49
n_e (cm^{-3})	68	100	100	103	100
[N II]/[O II]	0.024 ± 0.032	0.053 ± 0.066	0.074 ± 0.020	0.093 ± 0.032	0.070 ± 0.030
log R_{23}	0.977 ± 0.089	0.85 ± 0.16	0.859 ± 0.047	0.73 ± 0.11	0.88 ± 0.12
log O_{32}	0.43 ± 0.23	-0.18 ± 0.31	0.266 ± 0.099	-0.42 ± 0.19	-0.23 ± 0.21
$T_e(\mathrm{O}^{+2})_{\mathrm{emp}}$ (K)	10500	10500	11700	11000	10000
$T_e(\mathrm{O}^{+2})_{\mathrm{dir}}$ (K)	...	...	12670 ± 950	...	...
$\mathrm{O}^{+}/\mathrm{H}^{+}$	...	...	3.7×10^{-5}	...	...
$\mathrm{O}^{+2}/\mathrm{H}^{+}$	...	...	5.8×10^{-5}	...	...
$12+\log(\mathrm{O/H})_{\mathrm{dir}}$	...	...	7.98 ± 0.15	...	...
$12+\log(\mathrm{O/H})_{\mathrm{emp}}$	8.27 ± 0.19	8.22 ± 0.25	8.07 ± 0.12	8.10 ± 0.18	8.27 ± 0.15
log(N/O)	> -1.85	-1.53 ± 0.30	-1.25 ± 0.13	-1.31 ± 0.06	-1.54 ± 0.12
Property	VCC 1114-1	VCC 1114-2	VCC 1179-1	VCC 1179-2	VCC 1179-3
$I(\mathrm{H}\beta)$ (ergs s^{-1} cm^{-2})	$(3.70 \pm 0.35) \times 10^{-16}$	$(4.36 \pm 0.41) \times 10^{-16}$	$(3.15 \pm 0.69) \times 10^{-15}$	$(3.27 \pm 0.26) \times 10^{-15}$	$(4.51 \pm 0.35) \times 10^{-16}$
$E(B-V)$ (mag)	-0.03 ± 0.15	-0.15 ± 0.15	0.19 ± 0.14	-0.06 ± 0.14	0.07 ± 0.20
Adopted $E(B-V)$	0	0	0.19	0	0.07
$W(\mathrm{H}\beta)_{\mathrm{e}}$ (Å)	47.0 ± 5.9	260 ± 130	1.61 ± 0.23	6.09 ± 0.28	13.79 ± 0.66
$W(\mathrm{H}\beta)_{\mathrm{abs}}$ (Å)	1.59	1.59	2.12 ± 0.31	1.72 ± 0.43	1.59
n_e (cm^{-3})	48	100	135	100	100
[N II]/[O II]	0.099 ± 0.060	0.103 ± 0.063	0.063 ± 0.052	0.084 ± 0.029	0.070 ± 0.045
log R_{23}	0.71 ± 0.14	0.53 ± 0.13	0.90 ± 0.24	0.85 ± 0.12	0.779 ± 0.085
log O_{32}	-0.57 ± 0.25	-0.89 ± 0.24	-0.28 ± 0.42	-0.38 ± 0.20	0.29 ± 0.20
$T_e(\mathrm{O}^{+2})_{\mathrm{emp}}$ (K)	11000	11200	9500	10200	13000
$T_e(\mathrm{O}^{+2})_{\mathrm{dir}}$ (K)	...	...	...	...	...
$\mathrm{O}^{+}/\mathrm{H}^{+}$	...	...	...	...	...
$\mathrm{O}^{+2}/\mathrm{H}^{+}$	...	...	...	...	...
$12+\log(\mathrm{O/H})_{\mathrm{dir}}$	...	...	...	...	...
$12+\log(\mathrm{O/H})_{\mathrm{emp}}$	8.10 ± 0.30	7.97 ± 0.27	8.33 ± 0.30	8.26 ± 0.16	7.92 ± 0.22
log(N/O)	-1.20 ± 0.21	-1.21 ± 0.25	-1.52 ± 0.16	-1.40 ± 0.07	-1.12 ± 0.13

Table 5.4: Derived properties for H II regions in Virgo dIs (1). $I(\mathrm{H}\beta)$ represents the Hβ intensity corrected for underlying absorption and the adopted reddening. Computed and adopted reddenings, $E(B-V)$, are listed. $W(\mathrm{H}\beta)_{\mathrm{e}}$ is the Hβ emission equivalent width and $W(\mathrm{H}\beta)_{\mathrm{abs}}$ is the equivalent width of underlying absorption at Hβ (see § 4.1.1). n_e is the computed electron density. [N II]/[O II] is the corrected ratio $I([\mathrm{N\ II}]\lambda6583)/I([\mathrm{O\ II}]\lambda3727)$. log R_{23} and log O_{32} are line ratios for the empirical abundance calibration (see equations in § 5.2.2). $T_e(\mathrm{O}^{+2})_{\mathrm{emp}}$ is the O^{+2} electron temperature computed empirically as shown by Figure 5.6, and $T_e(\mathrm{O}^{+2})_{\mathrm{dir}}$ is the O^{+2} electron temperature obtained from [O III]λ4363. $12+\log(\mathrm{O/H})_{\mathrm{emp}}$ is the oxygen abundance obtained with the empirical calibration. $12+\log(\mathrm{O/H})_{\mathrm{dir}}$ is the oxygen abundance obtained from $T_e(\mathrm{O}^{+2})_{\mathrm{dir}}$. log(N/O) is the logarithm of the nitrogen to oxygen ratio from $T_e(\mathrm{O}^{+2})_{\mathrm{dir}}$ where available, $T_e(\mathrm{O}^{+2})_{\mathrm{emp}}$ otherwise.

Property	VCC 1179-4	VCC 1200-2	VCC 1249-1 [a]	VCC 1554-1	VCC 1554-2
$I(\mathrm{H}\beta)$ (ergs s^{-1} cm^{-2})	$(3.55 \pm 0.47) \times 10^{-16}$	$(1.41 \pm 0.11) \times 10^{-15}$	$(3.68 \pm 0.70) \times 10^{-16}$	$(1.86 \pm 0.68) \times 10^{-14}$	$(4.9 \pm 2.0) \times 10^{-16}$
$E(B-V)$ (mag)	0.07 ± 0.20	-0.15 ± 0.13	0	-0.037 ± 0.095	0.09 ± 0.10
Adopted $E(B-V)$	0.07	0	0	0	0.09
$W(\mathrm{H}\beta)_{\mathrm{e}}$ (Å)	16.0 ± 1.9	6.85 ± 0.43	26.8 ± 5.9	112.3 ± 6.8	(-27)
$W(\mathrm{H}\beta)_{\mathrm{abs}}$ (Å)	1.59	2.68 ± 0.66	1.59	1.59	1.59
n_e (cm^{-3})	100	100	100	100	267
[N II]/[O II]	0.094 ± 0.066	0.075 ± 0.028	0.019 ± 0.024	0.049 ± 0.015	0.073 ± 0.026
log R_{23}	0.90 ± 0.24	0.567 ± 0.061	0.93 ± 0.10	0.874 ± 0.073	0.815 ± 0.089
log O_{32}	-0.07 ± 0.29	-0.30 ± 0.12	-0.51 ± 0.19	-0.16 ± 0.14	-0.20 ± 0.16
$T_e(\mathrm{O}^{+2})_{\mathrm{emp}}$ (K)	12200	12500	9800	10500	11000
$T_e(\mathrm{O}^{+2})_{\mathrm{dir}}$ (K)	...	...	...	10000 ± 1800 [b]	...
$\mathrm{O}^+/\mathrm{H}^+$	...	...	...	1.6×10^{-4}	...
$\mathrm{O}^{+2}/\mathrm{H}^+$	...	...	...	7.9×10^{-5}	...
$12+\log(\mathrm{O/H})_{\mathrm{dir}}$	...	...	...	8.38 ± 0.41	...
$12+\log(\mathrm{O/H})_{\mathrm{emp}}$	8.05 ± 0.32	7.80 ± 0.14	8.32 ± 0.20	8.24 ± 0.13	8.15 ± 0.21
log(N/O)	-1.23 ± 0.19	-1.33 ± 0.18	< -2.05	-1.60 ± 0.18 [c]	-1.35 ± 0.07

Property	VCC 1554-3	VCC 1554-4	VCC 1554-5	VCC 1585-1	VCC 1789-1
$I(\mathrm{H}\beta)$ (ergs s^{-1} cm^{-2})	$(2.07 \pm 0.92) \times 10^{-15}$	$(4.8 \pm 3.3) \times 10^{-15}$	$(7.4 \pm 4.4) \times 10^{-16}$	$(6.0 \pm 4.9) \times 10^{-16}$	$(3.04 \pm 0.34) \times 10^{-15}$
$E(B-V)$ (mag)	-0.06 ± 0.11	0.29 ± 0.16	-0.12 ± 0.14	0.10 ± 0.19	0.23 ± 0.18
Adopted $E(B-V)$	0	0.29	0	0.10	0.23
$W(\mathrm{H}\beta)_{\mathrm{e}}$ (Å)	(-48)	4.33 ± 0.33	(-24)	66 ± 13	6.18 ± 0.18
$W(\mathrm{H}\beta)_{\mathrm{abs}}$ (Å)	1.59	1.59	1.59	1.59	0.94 ± 0.29
n_e (cm^{-3})	100	56	100	100	49
[N II]/[O II]	0.049 ± 0.025	0.046 ± 0.025	0.052 ± 0.030	0.079 ± 0.067	0.080 ± 0.037
log R_{23}	0.783 ± 0.086	0.99 ± 0.14	0.80 ± 0.14	0.73 ± 0.17	0.81 ± 0.15
log O_{32}	0.09 ± 0.18	-0.23 ± 0.24	-0.30 ± 0.24	-0.36 ± 0.30	-0.47 ± 0.25
$T_e(\mathrm{O}^{+2})_{\mathrm{emp}}$ (K)	12200	10200	11000	11200	10200
$T_e(\mathrm{O}^{+2})_{\mathrm{dir}}$ (K)	...	...	...	...	...
$\mathrm{O}^+/\mathrm{H}^+$	...	...	...	...	...
$\mathrm{O}^{+2}/\mathrm{H}^+$	...	...	...	...	...
$12+\log(\mathrm{O/H})_{\mathrm{dir}}$	...	...	...	...	...
$12+\log(\mathrm{O/H})_{\mathrm{emp}}$	7.99 ± 0.21	8.27 ± 0.34	8.16 ± 0.24	8.07 ± 0.32	8.24 ± 0.20
log(N/O)	-1.44 ± 0.16	-1.58 ± 0.11	-1.47 ± 0.10	-1.11 ± 0.07	-1.40 ± 0.08

Table 5.5: Derived properties for H II regions in Virgo dIs (2). NOTES: [a] The H II region, VCC 1249–1, is also labelled LR1 in Lee et al. (2000); see Chapter 6. [b] From [N II]λ5755 in VCC 1554–1, the [N II] temperature was computed to be 13200 ± 3000 K. [c] Derived using $T(\mathrm{O}^{+2})_{\mathrm{dir}}$. With [N II] temperature, $\log(\mathrm{N/O}) = -1.43 \pm 0.17$.

Property	VCC 2037-1	VCC 2037-2
$I(\mathrm{H}\beta)$ (ergs s^{-1} cm^{-2})	$(2.67 \pm 0.18) \times 10^{-15}$	$(6.1 \pm 1.2) \times 10^{-16}$
$E(B-V)$ (mag)	0.15 ± 0.13	0.22 ± 0.28
Adopted $E(B-V)$	0.15	0.22
$W(\mathrm{H}\beta)_{\mathrm{e}}$ (Å)	15.03 ± 0.38	3.85 ± 0.47
$W(\mathrm{H}\beta)_{\mathrm{abs}}$ (Å)	1.24 ± 0.62	1.48 ± 0.82
n_{e} (cm^{-3})	100	100
[N II]/[O II]	0.053 ± 0.021	0.076 ± 0.064
log R_{23}	0.865 ± 0.098	0.81 ± 0.23
log O_{32}	-0.16 ± 0.18	-0.35 ± 0.40
$T_{\mathrm{e}}(\mathrm{O}^{+2})_{\mathrm{emp}}$ (K)	10700	10500
$T_{\mathrm{e}}(\mathrm{O}^{+2})_{\mathrm{dir}}$ (K)	...	...
$\mathrm{O}^{+}/\mathrm{H}^{+}$	...	...
$\mathrm{O}^{+2}/\mathrm{H}^{+}$	...	...
$12+\log(\mathrm{O/H})_{\mathrm{dir}}$	...	...
$12+\log(\mathrm{O/H})_{\mathrm{emp}}$	8.22 ± 0.18	8.19 ± 0.27
log(N/O)	-1.53 ± 0.07	-1.50 ± 0.32

Table 5.6: Derived properties for H II regions in Virgo dIs (3).

Virgo dI	12+log(O/H)	Direct / Empirical
VCC 0512	8.23	Empirical
VCC 0848	7.98	Direct
VCC 0888	8.18	Empirical
VCC 1114	8.10	Empirical
VCC 1179	8.14	Empirical
VCC 1200	7.80	Empirical
VCC 1249	8.32	Empirical
VCC 1554	8.38	Direct
VCC 1585	8.07	Empirical
VCC 1789	8.24	Empirical
VCC 2037	8.21	Empirical

Table 5.7: Oxygen abundances adopted for each dI in the Virgo sample.

Chapter 6

UGC 7636 Revealed: A Stripped dI in Virgo

UGC 7636 (VCC 1249) is a gas–poor dI residing in the vicinity of the giant elliptical galaxy NGC 4472 (M 49; VCC 1226) in the southern portion of the Virgo Cluster (see Figures 2.1, 2.2, and 2.3). The dI is located about 5′.5 to the southeast of the elliptical. There is a cloud of H I gas (STE1, after its discoverers Sancisi et al. 1987) lying between the dI and the elliptical. In Lee et al. (2000), spectroscopy was presented for a newly discovered H II region (LR1), which is located at the same position as STE1.

Key observations characterizing the discovery of STE1 and evidence for a possible physical connection between STE1 and the dI are summarized in § 6.1. The serendipitous discovery of a new H II region, LR1, the acquired spectroscopy, and the derived oxygen abundance are presented in § 6.2. The case for a direct linkage of the H I cloud with the dI is presented in § 6.3. The most likely processes responsible for removing the H I gas are discussed in § 6.4.

Basic data for UGC 7636, STE1, and LR1 are listed in Table 6.1, which is adopted from Lee et al. (2000). For reference, the heliocentric velocity of the elliptical galaxy,

NGC 4472, is 969 km s^{-1} (Binggeli et al. 1993).

6.1 Recent Observations from the Literature

To place the current results in context, a review of recent observations from the literature is presented in chronological order and is summarized in Table 6.2.

In their study of atomic gas near elliptical galaxies, Kumar and Thonnard (1983) did not detect any H I at the position of NGC 4472. However, a signal was found to the southeast, which the authors claimed was attributable to the dI. Hoffman et al. (1987) measured H I fluxes of Virgo dwarfs and found a low signal at the position of UGC 7636. Their measured 21–cm flux integral for the dI was 0.167 Jy km s^{-1}, from which the resulting derived M_{HI}/L_B value was about a factor of ten lower than that found for typical dIs (Thuan 1985; Roberts and Haynes 1994; Skillman 1996; Pildis et al. 1997). With 21–cm single–dish observations at the Arecibo Observatory, Sancisi et al. (1987) discovered an H I cloud whose projected location was between the dI and NGC 4472. Here, the H I cloud is labelled "STE1" after its discoverers (Sancisi et al. 1987). Their measurement of the 21–cm flux integral for STE1 was 0.7 Jy km s^{-1}.

Gallagher and Hunter (1989) acquired Hα imaging for a number of dwarf galaxies in the Virgo Cluster. For UGC 7636 in particular, they observed no detectable compact Hα emission characteristic of H II regions.

Patterson and Thuan (1992) performed broadband imaging in B and I in addition to their own 21–cm single–dish observations at the Green Bank Telescope. They detected tails of stars whose colours were consistent with those found in the outer regions of the dwarf galaxy. Also, the inner regions of the dwarf exhibited a disturbed optical morphology. These observations were claimed as evidence of a tidal interaction

Property (1)	Value (2)	References (3)
UGC 7636 (VCC 1249)		
α (J2000)	$12^h30^m01\overset{s}{.}0$	1
δ (J2000)	$+07°55'46''$	1
Morphological type	Im III-IV	1
$B-V$	0.50 mag	3
B_T^0	14.26 mag	9
M_B	-16.86 mag	Note a
$r_{0,B}$	$31\overset{''}{.}8$	9
$\mu_{0,B}^0$ ^{b}	24.56 mag arcsec^{-2}	9
$r_{0,I}$	$38\overset{''}{.}9$	9
$\mu_{0,I}^0$ ^{b}	23.11 mag arcsec^{-2}	9
$(B-I)_T^0$	1.69 mag	9
$v_\odot$	276 ± 78 km s^{-1}	2
H I flux integral	0.167 Jy km s^{-1}	4
H I Cloud STE1 ^{c}		
α (J2000)	$12^h29^m55\overset{s}{.}5$	7
δ (J2000)	$+07°57'38''$	7
$v_\odot$	469 ± 3 km s^{-1}	7
Linear dimensions	$\sim 80'' \times 40''$	7
H I flux integral	0.7, 1.947 Jy km s^{-1}	10, 8
H II Region LR1 ^{d}		
α (J2000)	$12^h29^m56^s$	5, 6, 7 ^{e}
δ (J2000)	$+07°57'35''$	5, 6, 7 ^{e}
$v_\odot$	577 ± 91 km s^{-1}	6
$(B-R)^0$	1.12 mag	7
12+log(O/H)	8.32 ± 0.20	6

Table 6.1: Basic data for UGC 7636, STE1, and LR1. This table is adapted from Lee et al. (2000). REFERENCES : [1] Binggeli et al. 1985; [2] Binggeli et al. 1993; [3] Gallagher and Hunter 1986; [4] Hoffman et al. 1987; [5] Lee et al. 1997; [6] Lee et al. 2000; [7] McNamara et al. 1994; [8] Patterson and Thuan 1992; [9] Patterson and Thuan 1996; [10] Sancisi et al. 1987. NOTES: ^{a} Based on a distance modulus of 31.12 mag for the Virgo Cluster. ^{b} Central surface brightness corrected for reddening. ^{c} Named for discoverers Sancisi et al. (1987). ^{d} Named by M. McCall after discoverers H. Lee & M. G. Richer. ^{e} Coincident with position of a young blue star cluster (McNamara et al. 1994; Lee et al. 1997). Estimates for positional errors of LR1: $\Delta\alpha \simeq \pm 1^s$, $\Delta\delta \simeq \pm 4''$.

Reference (1)	Observations (2)	Key Result (3)
Kumar and Thonnard 1983	H I	detection near position of dI
Sancisi, Thonnard, and Ekers 1987	H I	1st discovery of H I cloud
Gallagher and Hunter 1989	Hα	no emission
Patterson and Thuan 1992	B, I; H I	tidal stellar tails
Henning, Sancisi, and McNamara 1993	H I	higher resolution imaging
McNamara et al. 1994	U, B, R; H I	low surface brightness stellar debris
Irwin and Sarazin 1996	X-rays	"hole" near H I position
Patterson and Thuan 1996	B, I	structural parameters
Irwin, Frayer, and Sarazin 1997	CO	upper limit for molecular mass
Lee, Kim, and Geisler 1997	Washington (CT_1) phot.	blue star clusters
Lee, Richer, and McCall 2000	Emission-line spectroscopy	O/H in newly found H II region

Table 6.2: Observations of UGC 7636 from the literature. Column (1) lists references from the literature in chronological order, column (2) lists the type of observation, and column (3) lists the key result.

of the dI with the elliptical. Blue "clumps" of stars at the tip of one tidal tail were indicative of recent star formation. The H I profile for STE1 was claimed to be a superposition of two Gaussian components. Their measured 21–cm flux integral was 1.947 ± 0.358 Jy km s^{-1}. Based upon the evidence, the authors suggested that tidal and ram–pressure stripping were responsible for removing the H I cloud.

Henning et al. (1993) performed 21–cm observations with higher spatial resolution at the Westerbork Synthesis radio telescope. They measured for STE1 the central heliocentric velocity (confirming the result by Sancisi et al. 1987), the linear size, and the mean H I column and volume densities. They also derived an H I mass of $5 \times 10^7\ M_\odot$ at a distance of 20 Mpc to the Virgo Cluster.

McNamara et al. (1994) obtained broadband images in U, B, and R, in addition to 21–cm imaging with the Very Large Array. A long and wide trail of stars was observed in U, extending northwards from the dI and in the direction of the giant elliptical. The interior of the dI displayed a disrupted appearance. Their H I imaging confirmed the existence of a superposition of narrow and broad velocity profiles seen

by Patterson and Thuan (1992). Their measured flux integral was 0.73 Jy km s^{-1}. McNamara et al. (1994) concluded that a relatively weak tidal encounter combined with ram–pressure could explain the disrupted stellar material seen in the dI, the fact that the H I is well separated from the dI, and that the H I had not yet been evaporated by the surrounding hot intracluster gas.

Irwin and Sarazin (1996) obtained X–ray observations of UGC 7636 and NGC 4472 with the ROSAT observatory. They found that the X–ray emission surrounding NGC 4472 was due to two sources: (1) hot halo material associated with the elliptical, and (2) the hot intracluster gas in which the elliptical is imbedded. They found no significant absorption at the position of the dI, but found reduced X–ray brightness or a "hole" near the position of STE1, implying that the gas cloud was in front of the elliptical, absorbing X–rays along our line–of–sight.

With CO observations, Irwin et al. (1997) failed to find the necessary amount of molecular gas thought to be responsible for the "hole" in X–ray emission seen by Irwin and Sarazin (1996). The upper limit for the molecular gas mass determined by Irwin et al. (1997) is an order of magnitude lower than the H I gas mass, which is roughly consistent with molecular gas masses for other dwarfs (Israel et al. 1995).

Lee et al. (1997) found a number of bright star clusters within the dI and in the region occupied by STE1. The star clusters have blue colours and relatively high luminosities. They determined that the ages of the star clusters are about 10^7 to 10^8 yr.

6.2 LR1 : A New Intergalactic H II Region

At the Canada–France–Hawaii Telescope, a five–minute Hα image of the UGC 7636 field (about 10′ by 10′) was obtained to locate potential H II regions. Inspection of

the Hα image showed only diffuse emission and no H II regions at the position of the dI, confirming the result of Gallagher and Hunter (1989). However, approximately $2'$ to the northwest of the dI, a compact object exhibiting Hα emission was found at the same general position as STE1 (see Figure 3.8). The position of the compact object appeared to be coincident with the blue object marked "A" by McNamara et al. (1994) and with the young star cluster labelled "C2" by Lee et al. (1997). M. McCall labelled the newly discovered H II region "LR1" after H. Lee and M. Richer, who were the observers at CFHT. The coordinates of LR1 are given in Table 6.1.

An object mask was constructed from the Hα image of the UGC 7636 field. Two slits were placed lengthwise across the dI and one slit was placed at the position of LR1. An 817–second spectrum was taken for the UGC 7636 field before increasing fog cover and rising humidity levels forced the termination of the exposure and closure of the dome shutter. A visual inspection of the two–dimensional spectrum showed emission lines typical for an H II region.

The spectrum was reduced in the standard manner as described in Chapter 4, and emission–line strengths were measured using locally developed software (see Chapter 4). The observed flux ratios, $F(\lambda)/F(\mathrm{H}\beta)$ were corrected for underlying Balmer absorption with equivalent width 2 Å (McCall et al. 1985) to yield corrected intensity ratios, $I(\lambda)/I(\mathrm{H}\beta)$. When observed flux ratios were corrected for underlying Balmer absorption with equivalent width 1.57 $\pm$ 0.55 Å (derived in § 4.1.1), the resulting intensity ratios were not significantly affected. The corrected value of $I(\mathrm{H}\alpha)/I(\mathrm{H}\beta)$ was found to be consistent with theory, indicating that the reddening was negligible. Thus, no reddening correction was applied to the data. An extensive discussion of the observing run at CFHT and subsequent reductions of data were presented in § 3.4. Corrections and analyses were performed with SNAP (Krawchuk et al. 1997), as discussed previously in Chapter 4.

For LR1, the observed flux and corrected intensity ratios and the derived properties were listed as "VCC 1249–1" in Tables 4.14 and 5.5, respectively. For reference, these numbers are reproduced in Tables 6.3 and 6.4, respectively.

Identification	F	I
[O II] 3727	693 ± 166	645 ± 197
Hβ 4861	100 ± 17	100 ± 19
[O III] 4959	84 ± 17	79 ± 22
[O III] 5007	130 ± 22	121 ± 31
Hα 6563	289 ± 16	270 ± 54
[N II] 6583	13 ± 13	12 ± 12

Table 6.3: Emission line data for the H II region LR1 (VCC 1249–1). Wavelengths are listed in Å. F is the observed flux ratio with respect to Hβ and I is the intensity ratio corrected for underlying Balmer absorption; zero reddening was assumed. The errors in the observed flux ratios account for the errors in the fits to the line profiles, their surrounding continua, and the relative error in the sensitivity function (Table 3.8). The error in the flux of the Hβ reference line is not included in the ratio relative to Hβ. However, errors in the corrected intensity ratios account both for flux errors in the specified line at wavelength λ and in the reference line.

From visual inspection of the Hα image, there may be another compact H II region within the H I gas cloud. However, confirmation of the candidate H II region awaits deeper Hα imaging and spectroscopy.

6.2.1 Heliocentric Velocity

The heliocentric velocity for LR1 was estimated to ensure that LR1 is in fact associated physically with STE1. To define the absolute wavelength scale (wavelength as a function of pixel on the CCD), which was not perfectly known, measured heliocentric velocities from the spectra of H II regions in VCC 1554 were used. VCC 1554 was chosen because its recessional velocity is known and because the instrumental configuration was the same used for UGC 7636 on the same night.

Velocities for the five H II regions in VCC 1554 were estimated from the Doppler displacement of the strongest emission lines. Averages for each H II region are given

Property	Value
$F(\mathrm{H}\beta)$ [a] (ergs s^{-1} cm^{-2})	3.42 ± 0.58 ($\times 10^{-16}$)
$I(\mathrm{H}\beta)$ [b] (ergs s^{-1} cm^{-2})	3.68 ± 0.70 $\times 10^{-16}$
EW ($\mathrm{H}\beta$) (Å) [c]	26.8 ± 5.9
log R_{23}	0.93 ± 0.10
log O_{32}	-0.51 ± 0.19
$I([\mathrm{N\ II}])/I([\mathrm{O\ II}])$ [d]	$< 0.019 \pm 0.024$
12+log(O/H) [e]	8.32 ± 0.20
T_{emp} (K) [f]	9800
log(N/O) [g]	< -2.05
$L(\mathrm{H}\alpha)$ (ergs s^{-1}) [h]	3.3×10^{37}
SFR ($M_\odot$ yr^{-1}) [i]	2.6×10^{-4}
$Q(H^0)$ (s^{-1}) [j]	2.4×10^{49}

Table 6.4: Derived properties for the H II region LR1 (VCC 1249–1). NOTES: [a] Observed $\mathrm{H}\beta$ flux. [b] $\mathrm{H}\beta$ intensity corrected only for underlying Balmer absorption. [c] Equivalent width of $\mathrm{H}\beta$ emission line. [d] $I([\mathrm{N\ II}]\lambda 6583)/I([\mathrm{O\ II}]\lambda 3727)$ is the discriminant used to compute empirical oxygen abundances (§ 5.2). [e] Oxygen abundance determined using empirical calibration. [f] Electron temperature derived from oxygen abundance and Figure 7 in McGaugh (1991). [g] Upper limit to N/O due to uncertain detection of [N II]λ6583. [h] Hα luminosity, assuming 31.12 mag for the distance modulus of the Virgo Cluster. [i] Present star formation rate (Kennicutt 1983; Kennicutt 1998) computed as SFR $= 7.9 \times 10^{-42}\, L(\mathrm{H}\alpha)$. [j] Number of ionizing photons (Kennicutt 1998) computed as $Q(H^0) = 7.31 \times 10^{11}\, L(\mathrm{H}\alpha)$.

in Table 6.5. The mean heliocentric velocity is 2035 km s^{-1}. This is +22 km s^{-1} larger than the accepted heliocentric velocity for VCC 1554 (Binggeli et al. 1993). This difference was used to correct the measured heliocentric velocity of LR1.

VCC 1554 H II Region	$v_{\odot}$ (km s^{-1})
1	1972
2	2149
3	2079
4	2007
5	1968

Table 6.5: Heliocentric velocities for five H II regions in VCC 1554. H II regions with the best spectra were chosen. For each H II region, an average velocity was computed from the strongest emission lines. The average of the five H II regions is 2035 km s^{-1}.

From the detected emission lines of LR1, the apparent heliocentric velocity is 599 km s^{-1}. Correcting for the offset (22 km s^{-1}) gives a true heliocentric velocity of 577 km s^{-1}. Based on the range of velocities measured for VCC 1554, the uncertainty is 91 km s^{-1}. This result is only $\sim 1.2\,\sigma$ larger than the accepted velocity for STE1 (469 km s^{-1}), but $\sim 3.3\,\sigma$ larger than the accepted velocity for the dI UGC 7636 (276 $\pm$ 78 km s^{-1}). It is therefore reasonable to presume that LR1 resides within the H I cloud, STE1.

6.2.2 Oxygen Abundance

Because [O III]λ4363 was not detected, the oxygen abundance had to be computed using the empirical calibration of the emission–line ratio, R_{23}, which was discussed in § 5.2. The value of $I([\text{N II}])/I([\text{O II}])$ was used to break the degeneracy in the empirical calibration. Although the detection of [N II]λ6583 was uncertain, the maximum possible value of $I([\text{N II}])/I([\text{O II}])$ was found to be 0.05. This is a factor of two below the threshold value of 0.1, which confirmed the choice of the low–abundance

branch of the calibration. With values for R_{23} and O_{32}, and the analytical formulae in § 5.2.2, the oxygen abundance was computed to be 12+log(O/H) = 8.32 ± 0.20.

6.3 Linking LR1 and STE1 with UGC 7636

The following is a discussion of how the oxygen abundance effectively ties the H II region and the H I gas cloud to the dwarf galaxy. In Figure 6.1, the metallicity as measured by the oxygen abundance, 12+log(O/H), is plotted against the absolute magnitude in B for field dIs. The open star marks the location of the measured oxygen abundance of LR1 and the luminosity of UGC 7636. Its position falls very close to the locus of points defined by the field dIs.

A plot of the oxygen abundance versus M_{HI}/L_B is shown in Figure 6.2. This shows the degree to which UGC 7636 is currently deficient in H I gas compared to field dIs at a comparable oxygen abundance. The open star shows the position of UGC 7636 based upon a measurement of the existing H I content within the dwarf galaxy (Hoffman et al. 1987). The dotted line shows how the location of UGC 7636 would be shifted if the H I gas of STE1 were added to the galaxy. The filled square and filled diamond connected by a solid line indicate the range of possibilities given the dispersion in single–dish H I measurements (Sancisi et al. 1987; Patterson and Thuan 1992). The shifted position is fairly close to the locus of points defined by field dIs at the upper range of oxygen abundance. UGC 7636 would appear as a fairly normal dI if STE1 were once part of the dwarf galaxy.

Within STE1, there does not appear to be present an underlying population of old or intermediate–age stars (McNamara et al. 1994; Lee et al. 1997) which could have provided the chemical enrichment observed. Indeed, Lee et al. (1997) estimate that the ages of the clusters of young stars are about 10^7 to 10^8 yr. The optical colours of

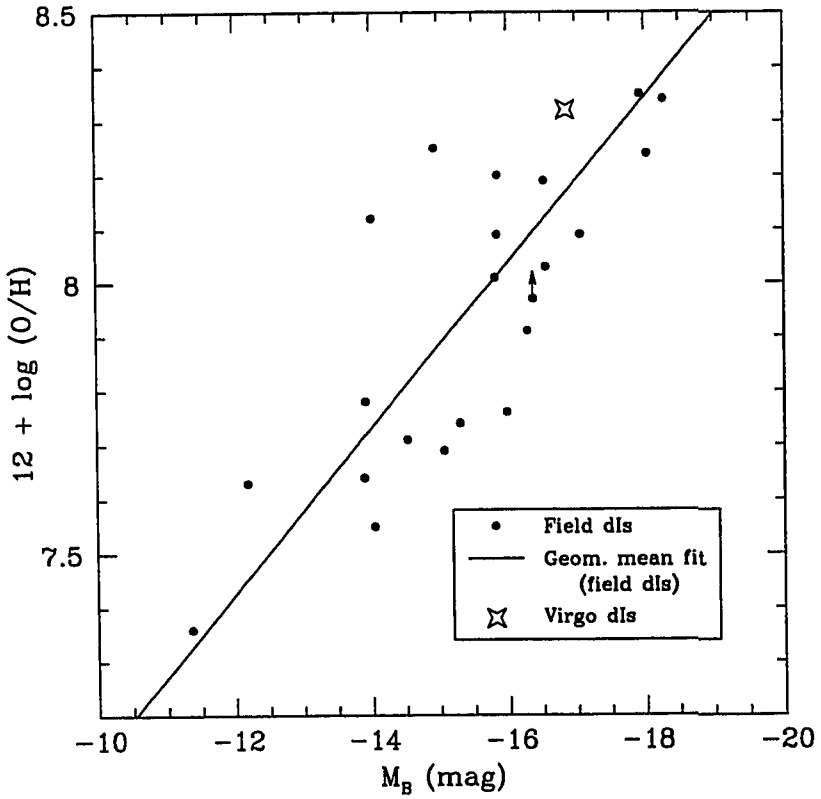

Figure 6.1: Oxygen abundance versus absolute blue magnitude for field dIs and UGC 7636. The solar value of the oxygen abundance is 12+log(O/H) = 8.87 (Grevesse et al. 1996). Field dIs are indicated by the filled circles. A lower limit to the oxygen abundance is indicated for NGC 1560. The solid line is a fit to the sample of field dIs (see § 7.4). The open star shows where UGC 7636 would lie if its oxygen abundance were equal to that measured for the H II region LR1.

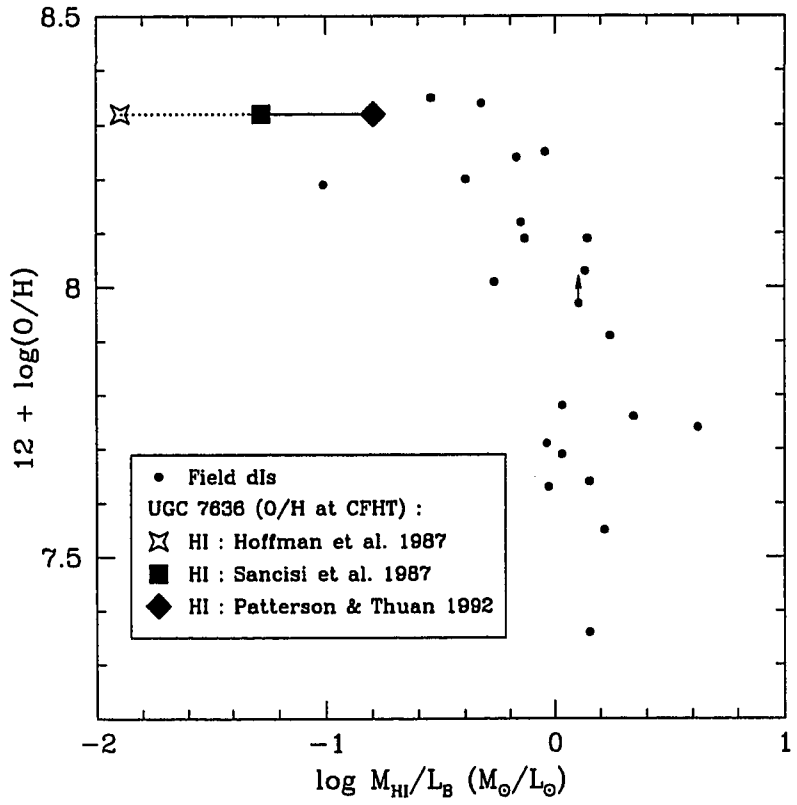

Figure 6.2: Oxygen abundance versus ratio of the H I gas mass to blue luminosity (solar units) for field dIs and UGC 7636. Field dIs are indicated by the filled circles. A lower limit to the oxygen abundance is indicated for NGC 1560. Combined with the measured oxygen abundance from the H II region, LR1, inside the H I cloud STE1, the open star shows the position of UGC 7636 based on the H I flux actually measured within the galaxy by Hoffman et al. (1987). The dotted line shows how the location of UGC 7636 would be shifted if the H I mass of STE1 were added to the galaxy. The filled square and the filled diamond indicate recent single-dish measurments of the H I mass for STE1 by Sancisi et al. (1987) and Patterson and Thuan (1992), respectively. The latter two symbols are connected with a solid line to show the allowed range of H I mass for STE1.

UGC 7636 are comparable to those of other dIs (Gallagher and Hunter 1986; Patterson and Thuan 1996; Almoznino and Brosch 1998a), which indicates that there has not been any significant fading since the gas was removed. The conclusion is that STE1 originated in UGC 7636 because (1) the metallicity of LR1 and, presumably that of STE1, agrees with what is expected for a galaxy with the same blue luminosity as UGC 7636, and (2) M_{HI}/L_B for the galaxy would be consistent with other dIs if the H I gas in STE1 were added into the galaxy. In other words, STE1 is the former interstellar medium of UGC 7636.

Measured equivalent widths for Hα and Hβ emission lines from the spectrum of LR1 were compared with recent starburst models to determine the age of the star–forming event. From the models by Leitherer et al. (1999)[1], the measured values of the Balmer equivalent widths are consistent with a recent burst ($\sim$ 4–6 Myr) of star formation in STE1, assuming that the burst was instantaneous at one–quarter solar metallicity and that the initial stellar mass function was of the standard Salpeter form[2].

The value of log $L(\mathrm{H}\alpha) \simeq 37.5$ for LR1 is at the lower end of the range expected for dIs (Kennicutt 1988). Only a handful of massive (O7 V) stars are needed to ionize the H II region (Kennicutt 1998). The low level of star formation is consistent with the observed paucity of molecular gas (Irwin and Sarazin 1996).

That there is an H II region in STE1 brings up the question of how stars form there. Schmidt (1959) described a power–law dependence of the star formation rate with gas surface density. However, the relationship breaks down at low surface densities. For star formation to occur, a minimum threshold is required and is associated with the formation of massive molecular clouds via gravitational instability (Quirk

[1]These models may be accessed at `http://www.stsci.edu/science/starburst99/`.

[2]The age of the burst is not very sensitive to the upper mass limit or to the slope of the IMF.

1972). The minimum or critical surface density, $\Sigma_{\rm cr}$ (in $M_\odot\,{\rm pc}^{-2}$), required for star formation to occur in thin, rotating, gas–rich disks (Toomre 1964; Cowie 1981; Kennicutt 1989) is given by

$$\begin{aligned}\Sigma_{\rm cr} &= 0.59\,\alpha_s\,V/R \\ &= 2.2\left(\frac{\alpha}{0.3}\right)\left(\frac{V}{50}\right)\left(\frac{R}{4}\right)^{-1}, \end{aligned} \tag{6.1}$$

where V is the maximum rotational velocity in km s^{-1}, R is the radius in kpc, and α_s is the stability constant[3]. Taking $V \approx 50$ km s^{-1} for dIs at $M_B \simeq -17$ (Skillman 1996), $R \approx 4$ kpc (Patterson and Thuan 1992; McNamara et al. 1994), and $\alpha_s \approx$ 0.3–0.7 (Kennicutt 1989; Hunter and Plummer 1996), the critical surface density is $\Sigma_{\rm cr} \approx$ 2–4 $M_\odot$ pc^{-2}. This assumes that the rotational motions are dominant over turbulent or random motions within the H I gas, and that α_s increases with increasing luminosity.

For STE1, the H I flux integral given by Patterson and Thuan (1992) was used to obtain the H I mass. The H I gas mass in solar masses (Roberts 1975; Roberts and Haynes 1994) was computed from

$$M_{HI} = 2.356 \times 10^5\, F_{21}\, D^2, \tag{6.2}$$

where F_{21} is the 21–cm flux integral in Jy km s^{-1} and $D = 16.75$ Mpc is the distance to the Virgo Cluster. The linear dimensions of the H I gas (Table 6.1) were determined by McNamara et al. (1994). Combining these quantities, the H I surface density in STE1 is $\Sigma_{\rm HI} \simeq 4\,M_\odot$ pc^{-2}. Similar results follow from the peak beam–averaged H I column density and the mean H I column density given by McNamara et al. (1994), which yield $\Sigma_{\rm HI} \simeq$ 2–4 $M_\odot$ pc^{-2}. The ratio $\Sigma_{\rm HI}/\Sigma_{\rm cr}$ is of order unity, which just satisfies the threshold criterion for star formation to occur in STE1.

[3]The stability constant is the ratio of gas to critical surface mass density at the maximum galactocentric radius where H II regions are observed in a disk (Kennicutt 1989; Hunter and Plummer 1996).

6.4 Revealing the Stripping Process

To explain how STE1 was removed from UGC 7636, a number of authors have presented arguments supporting either tidal stripping or ram–pressure stripping as the primary mechanism. A discussion of these two processes is presented, followed by remarks contending that both processes are likely responsible for removing the H I gas (see also, e.g., McNamara et al. 1994; Lee et al. 1997).

6.4.1 Tidal Stripping

Consider a galaxy of mass m and radius r which approaches a very massive galaxy M to within a distance of R. The tidal effects can be described by the following equation (van Hoerner 1957; Hodge 1966; Binney and Tremaine 1987):

$$R_{\rm crit} \sim Cr \left(\frac{M}{m}\right)^{1/3}, \tag{6.3}$$

where $R_{\rm crit}$ is the critical radius, or the Roche limit, r is the characteristic size of the low–mass object, and m and M are the masses of the galaxies in $M_\odot$. The dimensionless constant, C, is of order unity if one accounts for the fact that trajectories of dIs within clusters of galaxies are likely to be highly eccentric with respect to the giant perturber galaxies. Once the low–mass galaxy comes inside the Roche limit ($R < R_{\rm crit}$), the giant exerts tidal forces which remove material from the outer parts of the smaller object.

The Roche limit for UGC 7636 is computed as follows. For the absolute magnitude stated in Table 6.1 and assuming unity for the stellar mass-to-light ratio, the stellar mass of the dI is $m_* = 8.6 \times 10^8\ M_\odot$. The H I mass of STE1 is $1.3 \times 10^8\ M_\odot$ from the flux measurement of Patterson and Thuan (1992). For dIs at $M_B \sim -17$, the mean ratio of dark to luminous mass is adopted to be three (Skillman 1996; Côté et al. 1997). So, the total mass of UGC 7636 is $m \simeq 4.0 \times 10^9\ M_\odot$. Patterson

and Thuan (1996) found that an exponential fit best describes the surface brightness profile of UGC 7636. The last data point in their fit is at a radius of 50″. From measured X–ray emission in the hot corona surrounding NGC 4472, the total mass of the elliptical is $M = 3.5 \times 10^{12}\ M_{\odot}$ (Forman et al. 1985), adjusted for the distance to the Virgo Cluster adopted here. Substituting these quantities into Equation (6.3) gives $(M/m)^{1/3} \simeq 9.6$ and a critical radius $R_{\rm crit} \simeq 8'$. The projected angular distance between UGC 7636 and NGC 4472 is only 5′.5. Thus, the dwarf appears to lie well inside the Roche limit. From the arguments laid out by Irwin and Sarazin (1996) regarding the past trajectory of the dI, the dwarf has most likely passed perigalacticon with respect to the elliptical. Due to projection effects, the present angular separation between the dI and the elliptical is a lower limit to the true angular separation.

Equation (6.3) can be used in turn to solve for the tidal radius, $r = r_{\rm tidal}$, for UGC 7636. Any galactic material outside this radius will be pulled out by tidal forces, as appears to have been observed by Patterson and Thuan (1992) and McNamara et al. (1994). Given the present projected separation of $\sim 5'.5$ between the dI and the elliptical, the tidal radius is

$$\begin{aligned} r_{\rm tidal} &= \frac{5'.5}{9.6} \\ &\simeq 34''. \end{aligned} \tag{6.4}$$

The radius is well within the optical disk (Patterson and Thuan 1996), so it is not surprising that evidence for tidal distortion is seen.

6.4.2 Ram–Pressure Stripping

Ram–pressure stripping occurs when a galaxy moves at high speed through the intracluster medium (ICM). Pressure exerted by the ICM gas can remove the gaseous

component of the galaxy. In the case of UGC 7636, the X–ray emitting gas surrounding the elliptical galaxy NGC 4472 may be responsible for removing the H I gas (e.g., Forman et al. 1985; Fabbiano et al. 1992; Irwin and Sarazin 1996). In fact, the X–ray emission surrounding the elliptical arises from both hot gas associated directly with the elliptical and from gas in the Virgo ICM (Irwin and Sarazin 1996).

Stripping occurs when the ram–pressure encountered by a galaxy exceeds its own gravitational restoring force. Assuming a homogeneous medium, the stripping condition (Gunn and Gott 1972) is described by

$$K = \frac{\rho_{\rm ICM}\, v^2}{2\pi G\, \sigma_{\rm tot}\, \sigma_{\rm gas}} \geq 1. \tag{6.5}$$

where $\rho_{\rm ICM}$ is the ICM gas mass density, v is the component of the galaxy's velocity perpendicular to its plane, G is the gravitational constant, and $\sigma_{\rm tot}$ and $\sigma_{\rm gas}$ are the total and gas surface mass densities of the galaxy, respectively.

The value of K can be computed for UGC 7636 by deriving the mean and gas surface mass densities within a Holmberg diameter and the particle density of the ICM in the vicinity of NGC 4472. The Holmberg radius is the isophotal radius where the surface brightness in B is 26.5 mag arcsec^{-2}; for UGC 7636, it is $R_H = 84\farcs5$ (Patterson and Thuan 1996). The total dynamical mass of the galaxy (in $M_\odot$) within a Holmberg diameter can be computed using a virial analysis (Staveley-Smith et al. 1992) and is given by

$$m_{\rm tot} = 3.3 \times 10^4\, a_H\, D\, (3\sigma^2 + V_{\rm rot}^2), \tag{6.6}$$

where $a_H = 2\, R_H$ is the Holmberg diameter in arc minutes, D is the distance to the Virgo Cluster in Mpc, σ is the velocity dispersion of the H I gas, which is assumed to be 10 km s^{-1} (Mateo 1998), and $V_{\rm rot}$ is the rotation velocity in km s^{-1}. An estimate

for $V_{\rm rot}$ can be obtained from

$$V_{\rm rot} = \frac{1}{\sin i}(0.5W_{50} - 1.18\sigma), \tag{6.7}$$

where i is the inclination angle and W_{50} is the width of the H I profile at half-maximum in units of km s^{-1} (Staveley-Smith et al. 1992). Inserting $W_{50} = 70$ km s^{-1} and $i = 51°$ (Patterson and Thuan 1992, 1996) into Equation (6.7) gives a rotation velocity of 30 km s^{-1}, which is at the lower end of the range for dIs (Skillman 1996; Côté et al. 1997). From Equation (6.6), the mass of UGC 7636 is $m_{\rm tot} = 1.9 \times 10^9\ M_\odot$. The surface mass density within the Holmberg diameter is $4\,m_{\rm tot}/(\pi\,a_H^2) = 12.7\ M_\odot$ pc^{-2}, since $a_H = 13.7$ kpc at the distance of the Virgo Cluster. Using the measured H I flux of Patterson and Thuan (1992), the surface gas mass density within the Holmberg diameter is $4\,(1.36\,M_{HI})/(\pi\,a_H^2) = 1.2\ M_\odot$ pc^{-2}, where the constant 1.36 accounts for helium. From the deprojected electron density profile for NGC 4472 (Figure 6, Irwin and Sarazin 1996), the electron density, n_e, at a distance of $5'$ from NGC 4472 is about 10^{-3} cm^{-3}. Assuming that the ICM is at rest with respect to NGC 4472, the radial velocity of UGC 7636 with respect to the ICM is $v \sim 700$ km s^{-1}. The true velocity therefore is $v \gtrsim 700$ km s^{-1}. With $\rho_{\rm ICM} \simeq m_p\,n_e$ (m_p is the proton mass), and adopting 700 km s^{-1} for v, Equation (6.5) yields $K \gtrsim 5$. The condition for ram–pressure stripping is satisfied.

If K is set exactly to unity, the condition for ram–pressure stripping would be just met at an electron density

$$n_e \simeq 2.7 \times 10^{-4}\ {\rm cm}^{-3}. \tag{6.8}$$

This "threshold" value of the electron density is found at a radius of $10'$ from NGC 4472, according to the deprojected electron density profile in Figure 6 of Irwin and Sarazin (1996). The *projected* angular separation between UGC 7636 and NGC 4472 is about $5\farcm5$, which is well inside the "threshold" radius.

6.4.3 Are Both Processes Required?

Both tides and ram–pressure appear to have been necessary to strip the H I gas from UGC 7636 (e.g., Patterson and Thuan 1992; McNamara et al. 1994; Lee et al. 1997). The following observations provide evidence for tidal effects. Patterson and Thuan (1992) found a stellar "tail" and "countertail" at opposite ends of the dwarf galaxy. Lee et al. (1997) found a significant excess of blue light along the tidal tail out to an angular distance of $\geq 60''$. McNamara et al. (1994) observed a low surface brightness tail of stellar debris projected $\sim 5'$ northwards from the dI. They found that there was a "bow"–shaped structure to the southeast, and that the central regions of the dI exhibited a disrupted morphology with a lack of a distinct nucleus.

At the same time, there are observations which provide evidence for ram–pressure stripping. Both UGC 7636 and STE1 are located well within a dense ICM (Irwin and Sarazin 1996), based upon the current location of UGC 7636 with respect to the elliptical galaxy NGC 4472. The overall optical morphology of the dI and the 21–cm morphology of STE1 appear similar (McNamara et al. 1994). The radial velocity of STE1 is between that of the dI and of NGC 4472 (see Table 6.1). There is very little H I gas and no H II regions within the dwarf (present work; Gallagher and Hunter 1989; Hoffman et al. 1987), which indicates gas was lost and star formation ceased. Furthermore, the position of STE1 is shifted with respect to the tidal tails exhibited by the starlight of UGC 7636.

Abadi et al. (1999) performed simulations of ram–pressure stripping of spiral galaxies in clusters with ICM densities comparable to the Virgo and Coma clusters. The test galaxy used for their simulations was chosen to be like the Milky Way. For a spiral galaxy encountering the Virgo ICM, their models show that only $\sim 40\%$ of the gas mass is removed by ram–pressure stripping after some 50 Myr. Indeed, Abadi

et al. report that the biggest deficit of their model is that the gas is never completely removed in any of their simulations, which might suggest that tidal effects may be an important prerequisite to complete stripping of gas.

Models incorporating dwarf galaxies (Mori and Burkert 2000) suggest that ram–pressure stripping would take about 0.2 Gyr to remove the H I gas completely. With their smaller gravitational potentials, dwarf galaxies are more susceptible to ram–pressure effects and more likely to lose their gas, as Equation (1.5) implied.

The calculation in § 6.4.1 above shows that the tidal interaction with NGC 4472 must have loosened both stellar and gaseous material within the dI. As the dI travelled farther into denser regions of the ICM, the dwarf eventually "crossed" over the minimum ICM density threshold (Equation 6.8). The ram–pressure condition was satisfied and H I gas began to leave the galaxy. As the dwarf continued through the ICM, the H I gas would have been decelerated and, eventually, left "behind" the dI.

It remains unclear why the cloud has not completely "evaporated," i.e., how STE1 has maintained its integrity in the presence of surrounding hot ICM gas. Compression by ram pressure could break up the H I gas into new sites for star formation (e.g., Murakami and Babul 1999), which may explain the appearance of LR1 and other young star clusters (McNamara et al. 1994; Lee et al. 1997). Takeda et al. (1984) computed numerical models of an elliptical galaxy in a radial orbit through the intracluster medium. Subsequent ram pressure stripping results in a blob of gas which is left behind. They estimate that the remaining lifetime of the gas blob for survival is $\sim 10^8$ yr.

The H I cloud, STE1, may eventually fall into the gravitational potential well of the elliptical galaxy NGC 4472. If the cloud is fragmented by shearing and compressive forces, more young star clusters could form and eventually merge with NGC 4472.

Chapter 7

The Evolution of Dwarf Irregulars in Virgo

7.1 Introduction

In the previous chapter, UGC 7636 was presented as a prototype of a Virgo dI which has been affected by the cluster environment. A number of other dIs in the Virgo Cluster sample also have low gas masses compared to dIs in the field sample. It will be shown here that five of the twelve Virgo dIs have been stripped, but no differences between field dIs and Virgo dIs are evident in the metallicity–luminosity diagram.

Below, chemical evolution is explored via the correlation between oxygen abundance and the fraction of baryons in the form of gas. Based upon the evolution of field dwarfs, gas deficiency is defined and observed in a number of Virgo dIs. A "staged" model of chemical evolution is presented to interpret the observations of Virgo dIs relative to field dIs. A correlation between gas deficiency and the strength of the intracluster medium is examined. It will be shown that stripping must have occurred recently and that the intracluster medium in Virgo is the main cause of gas removal. The fate of stripped dIs is discussed.

7.2 Derived Parameters

Primary observables and derived parameters used to examine the evolution of dIs are listed in Table 7.1. There are "secondary" observables (e.g., $v_\odot$, $r_{\rm eff}$, extinction etc.), which may be used within intermediary steps to derive the parameters listed in Table 7.1. However, they are not relevant to discussions below.

Observable	Description (units)
B_T	total apparent magnitude in B (mag)
D	distance (Mpc)
F_{21}	integrated flux at 21 cm (Jy km s^{-1})
$B-V$	colour (mag)
log(O/H)	logarithm of oxygen abundance by number (dex)
log(N/O)	logarithm of nitrogen-to-oxygen ratio (dex)
Derived Parameter	**Description (units)**
$m-M$	distance modulus (mag)
M_B	absolute magnitude in B (mag)
M_*	mass of stars ($M_\odot$)
$M_{\rm HI}$, $M_{\rm gas}$	H I mass, total gas mass ($M_\odot$)
$M_{\rm HI}/L_B$	gas mass-to-light ratio in B ($M_\odot/L_{\odot,B}$)
$M_{\rm bary}$	total baryonic mass in stars and gas ($M_\odot$)
μ	"gas fraction:" fraction of baryons in gaseous form

Table 7.1: List of observables and derived parameters.

7.2.1 Absolute Magnitude, M_B, and Luminosity, L_B

If the distance to a galaxy, D, is known, the distance modulus, $m-M$, is obtained from

$$m - M = 5\,\log D - 5 + A, \tag{7.1}$$

where m and M represent apparent and absolute magnitudes, respectively. The final term, A, represents the total extinction of the galaxy in magnitudes, due to dust in the foreground and dust intrinsic to the target galaxies.

The absolute magnitude in the blue, M_B, is derived from the measured total apparent magnitude, B_T, after correction for extinction, and the distance modulus. Distance moduli for dIs in the field and in the Virgo Cluster were discussed in Chapter 2. For the most part, the extinction in B due to intrinsic dust is negligible or very small (Lisenfeld and Ferrara 1998). The contribution by foreground dust is $\lesssim 0.05$ mag. Moreover, galaxies in Virgo are moving slowly enough that K–corrections are negligible.

The luminosity, L_B, in units of solar luminosities is given by

$$L_B = 10^{0.4\left(M_{\odot,B} - M_B\right)}, \tag{7.2}$$

where $M_{\odot,B} = +5.48$ (Hayes 1978).

7.2.2 Gas, Stellar, and Baryonic Masses

The gas in dIs is the raw material out of which stars and metals are formed (§ 7.5), and probably consists mostly of atomic hydrogen and helium. The composition of gas in molecular form within dIs remains mostly an unknown quantity (see, e.g., Tacconi and Young 1987; Young and Scoville 1991; Hunter and Sage 1993; Israel et al. 1995). Although CO is used to trace the molecular hydrogen content in galaxies, the conversion from CO to H_2 masses is uncertain, because there is much debate about the "universality" of the conversion factor. Fortunately, molecular gas is not expected to contribute greatly to the total gas mass in dwarf galaxies, owing to low metallicities and low dust–to–gas ratios (Young and Scoville 1991; Lisenfeld and Ferrara 1998; Vidal-Madjar et al. 2001). Ionized gas contributes negligibly to the mass, too (Schombert et al. 2001).

The H I mass in solar masses is given by the following equation (Roberts 1975;

Roberts and Haynes 1994):

$$M_{HI} = 2.356 \times 10^5 \, F_{21} \, D^2, \tag{7.3}$$

where F_{21} is the 21–cm flux integral in Jy km s^{-1} and D is the distance in Mpc. Accounting for helium and other metals, the total gas mass in solar masses is given by

$$M_{\rm gas} = M_{HI}/X, \tag{7.4}$$

where X is the fraction of gas mass in the form of hydrogen. In this thesis, X is adopted to be 0.733, the solar value.

Often, the mass in stars, M_*, is computed from the product of the blue luminosity, L_B, and with the assumption of a constant mass–to–light ratio, M_*/L_B. However, this does not account for the possible contamination of the luminosity by bright star–forming regions, which may introduce significant variations in M_*/L_B. The problem may be particularly severe for dIs, because a star formation event of a given mass would have a proportionately larger effect on the light than it does in a giant spiral galaxy. A method is described below in § 7.3 which yields an estimate for M_*/L_B tailored to the particular mixture of young and old stars in a dI. This method was developed by M. L. McCall (unpublished) as part of a long–term investigation of the masses of galaxies. The total mass in baryons, $M_{\rm bary}$, is taken to be the mass of gas and stars.

7.2.3 Gas–to–Light Ratio, M_{HI}/L_B and Gas Fraction, μ

A proportional measure of how much gas is contained within galaxies is the H I gas mass–to–light ratio in B. Although near–infrared luminosities of dwarf galaxies may be more representative of the underlying stellar mass, the luminosity in B is used here, because data in B are available for all field and Virgo dIs. The gas–to–light ratio is a

distance–independent quantity, because the gas mass is derived from electromagnetic fluxes (i.e., 21–cm radiation).

The fraction of baryons in gaseous form is a "fundamental" quantity, because it determines the metallicity within the "closed box" model of chemical evolution (see § 7.5). The gas fraction is given by

$$\mu = \frac{M_{\rm gas}}{M_{\rm gas} + M_*}, \tag{7.5}$$

In this thesis, the gas fraction is a distance–independent quantity, too, because gas mass and stellar mass are both derived from electromagnetic fluxes.

7.3 Two–Component Method for Deriving M_*/L_B

Dwarf irregular galaxies consist entirely of a disk–like component, but have no spheroidal component. However, dIs are known to consist of stars with a variety of ages (e.g., Grebel 2001). Young stars can contribute significantly to the total luminosity, but they account for a minor fraction of the mass. Old stars are faint by comparison with young stars, but they dominate the mass. To account for varying rates of star formation, a computation of the stellar mass requires a synthesis of stellar populations. It would be ideal if the flux contributions by old and young stars were known across a large range of wavelengths (e.g., ultraviolet to the infrared). However, such spectral data for dwarf galaxies are very limited. Thus, syntheses are founded upon broadband optical and near–infrared colours (e.g., Krüger et al. 1991; Krüger and v. Alvensleben 1994). Unfortunately, all that is widely available for the dI samples of the present work is the $B - V$ colour.

To a first approximation, the mass in stars can be estimated by using a "two–component" formalism, where the total integrated luminosity is the sum of a "young" and an "old" component (McCall, unpublished). The young stellar component is

presumed to have properties similar to that of I Zw 18, whose light is known to be dominated by young stars. The colour and mass–to–light ratio for the ensemble of young stars are assumed to be invariant. The "old" component is assumed to consist of old stars and whatever baryonic dark matter is disk–like in its distribution. In terms of age, the young component is assumed to be less than 10 Myr old; the remaining stars are assumed to make up the old component. Knowing the colour of the ensemble of young stars (e.g., I Zw 18) and the total integrated colour of the dI, the fractions of the light contributed by old and young stars can be estimated if the colour of the old disk can be judged from its luminosity and surface brightness. The mass of stars can then be estimated using mass–to–light ratios appropriate for the young and old components separately.

The two–component formalism is founded upon the assumption that the luminosity of young stars created in a recent burst or bursts of star formation is small compared to the luminosity of old stars in the underlying population. In other words, the light of young stars cannot completely overwhelm that from the old stars. Such is the case for dIs, but not for BCDs (Papaderos et al. 1996; Patterson and Thuan 1996). The method is exact if a burst is superimposed upon an old population.

While the present method of computing stellar mass is somewhat crude in an absolute sense, stellar masses can be computed homogeneously for all dIs in both field and Virgo samples. The primary goal is to determine whether the environment has played a role in the evolution of Virgo dIs, so the focus is on differences between field and Virgo dIs. A "one–component" formalism using a "typical" M_*/L_B is not as good as the "two–component" version, because the stellar mass–to–light ratio may depend on luminosity, and may even vary greatly from galaxy to galaxy at a given luminosity. Moreover, there is no guarantee that the rates of star formation in Virgo dIs are the same as in field dIs, even in the mean. In § 7.5.3, it will be shown that the

two–component method gives a tighter correlation between oxygen abundance and the gas mass fraction than the one–component method.

What follows in the text below (up to and including § 7.3.9) is an elaboration of the work done by McCall to establish the two–component algorithm. This is necessary, because the research has not been published, yet is fundamental to this thesis. Then, in subsequent sections, the present author checks results of the two–component algorithm with other published data and compares the results with that generated by the evolutionary synthesis code of Bruzual and Charlot (1996).

7.3.1 Ingredients and Equations for M_*

The total mass in stars (in solar masses) is given by the sum of the mass in the young and old components

$$\begin{aligned} M_* &= M_{*,\mathrm{yng}} + M_{*,\mathrm{old}} \\ &= \left(\frac{M_*}{L_B}\right)_{\mathrm{yng}} L_{B,\mathrm{yng}} + \left(\frac{M_*}{L_B}\right)_{\mathrm{old}} L_{B,\mathrm{old}}, \end{aligned} \tag{7.6}$$

where $(M_*/L_B)_{\mathrm{yng}}$ and $(M_*/L_B)_{\mathrm{old}}$ represent the stellar mass–to–light ratios for the young and old components, respectively, and $L_{B,\mathrm{yng}}$ and $L_{B,\mathrm{old}}$ represent the luminosity contributions in B from the young and old components, respectively. The luminosity contributions in B from the young and old components are written as

$$L_{B,\mathrm{yng}} = (1 - f_{\mathrm{old}})L_B \tag{7.7}$$

$$L_{B,\mathrm{old}} = f_{\mathrm{old}}L_B, \tag{7.8}$$

where L_B is obtained from Equation (7.2). The fraction of light in B contributed by old stars, f_{old}, is

$$f_{\mathrm{old}} = \frac{10^{-0.4(c_{\mathrm{yng}}-c_d)} - 1}{10^{-0.4(c_{\mathrm{yng}}-c_{\mathrm{old}})} - 1}, \tag{7.9}$$

where $c_{\rm yng}$, $c_{\rm old}$, and c_d are, respectively, the $B-V$ colours of the young stars, the old stars, and the entire system.

The colour of a young population is gauged with reference to the nearby BCD I Zw 18. The optical light is completely dominated by young stars, although Östlin (2000) claims from near–infrared imaging that there exist stars at least 1 Gyr old. Another example of a limiting case is the H I cloud HI 1225+01 in Virgo, which appears only to have young stars (Salzer et al. 1991). Indeed, the observed $B-V$ colours for both I Zw 18 and HI 1225+01 are similar, despite the fact that the latter has a larger oxygen abundance by about 0.5 dex (Salzer et al. 1991; Skillman and Kennicutt 1993; Legrand et al. 2000). For these two "extreme" cases at least, it appears that the metallicity does not strongly affect the $B-V$ colour.

The dust–free $B-V$ colour assigned to the young stellar population is adopted to be

$$c_{\rm yng} = (B-V)^0_{\rm yng} = -0.03\,{\rm mag} \tag{7.10}$$

which is the colour observed for the ensemble of young dwarf stars ($M_V \leq +4$) in the solar neighbourhood (Bahcall and Soneira 1984; van der Kruit 1986). This is consistent with the colour observed for I Zw 18 (Davidson and Kinman 1985; Stevenson et al. 1993) and HI 1225+01 (Salzer et al. 1991).

The dust–free colour of old stars, $c_{\rm old} = (B-V)^0_{\rm old}$, is derived by assuming that the relationship between colour, luminosity, and surface brightness in old stars is similar to that observed for the ensemble of old stars in disk–like or exponential systems (e.g., dEs/dSphs) where star formation has stopped or is occurring at a very low rate. Dwarf elliptical galaxies in the Local Group and in the Fornax Cluster are used to set the relationship; dwarfs as faint as $M_B \approx -9$ set the low–luminosity end of the range. The disks of the Virgo dwarf IC 3475 (VCC 1448), the low surface brightness spiral

Malin 1, and the Milky Way (see below) are used to constrain colours at extremes of luminosity and surface brightness. From a multiple regression analysis to old disk systems, the relationship between colour, luminosity, and surface brightness for the B–band is found to be

$$(B-V)^0_{\rm old} = (-0.0423 \pm 0.0031)\left[M_{B,\rm old} + 1.0454\langle\mu^0_{B,\rm eff}\rangle_{\rm old}\right] + (1.177 \pm 0.019). \quad (7.11)$$

where $M_{B,\rm old}$ is the absolute magnitude in B of the old disk, and $\langle\mu^0_{B,\rm eff}\rangle_{\rm old}$ is an estimate for the dust–free mean surface brightness in B of the old disk that would be observed within a circular aperture with radius equal to the effective radius of the disk, if the disk were an oblate spheroid seen face–on. The colour of the old disk is constrained to fall within the range $+0.60 \leq (B-V)^0_{\rm old} \leq +0.98$. The lower or "blue" end of the range is set by the colours of the bluest globular clusters (Brocato et al. 1990), which should be similar to very old metal–poor stellar populations. The upper or "red" end of the range is the reddest colour observed for giant elliptical galaxies within a circle containing half of the total light.

Because the colour of the old population is related to both luminosity and surface brightness, the fraction of light from the old component (i.e., Equation 7.9) must be determined through an iterative process. First, the observed values of M_B and $\langle\mu^0_{B,\rm eff}\rangle$ for the whole galaxy are substituted for $M_{B,\rm old}$ and $\langle\mu^0_{B,\rm eff}\rangle_{\rm old}$, respectively, in Equation (7.11) to obtain an initial estimate for $c_{\rm old}$. Equation (7.9) is applied to derive a new value of $f_{\rm old}$ from the colour of the dI, c_d, and the colour of the young component, $c_{\rm yng}$ (Equation 7.10). An improved estimate for the colour of the old component is obtained from Equation (7.11) using "updated" values of the absolute magnitude, $M_{B,\rm old}$, and surface brightness, $\langle\mu^0_{B,\rm eff}\rangle_{\rm old}$. Continued iteration quickly converges to estimates of $f_{\rm old}$ and $c_{\rm old}$, which in turn lead to estimates of the luminosities of young and old stars via Equations (7.7) and (7.8).

From Equations (7.6) and (7.7), the mass in young stars, $M_{*,\mathrm{yng}}$, is expressed as

$$\begin{aligned} M_{*,\mathrm{yng}} &= \left(\frac{M_*}{L_B}\right)_{\mathrm{yng}} L_{B,\mathrm{yng}} \\ &= \left(\frac{M_*}{L_B}\right)_{\mathrm{yng}} (1 - f_{\mathrm{old}}) L_B, \end{aligned} \tag{7.12}$$

where the mass–to–light ratio in B for young stars is

$$(M_*/L_B)_{\mathrm{yng}} = 0.15\, M_\odot/L_{B,\odot}. \tag{7.13}$$

This mass–to–light ratio comes from models of the distribution of young massive main–sequence stars ($M_V \leq +4.2$) perpendicular to the Milky Way (or Galactic) disk, which employ local measures of the luminosity function and mass–luminosity relation (Bahcall 1984; Bahcall and Soneira 1984). The mass–to–light ratio for young stars is taken to be constant, because the initial mass function is found not to vary significantly from galaxy to galaxy (e.g., Massey, Johnson, and DeGioia-Eastwood 1995; Massey et al. 1995; Holtzman et al. 1997). The precise value is not too important because the mass in typical dwarf galaxies is dominated by old stars and gas.

The mass in old stars, $M_{*,\mathrm{old}}$, is given by

$$M_{*,\mathrm{old}} = \left(\frac{M_*}{L_B}\right)_{\mathrm{old}} L_{B,\mathrm{old}}. \tag{7.14}$$

Based upon what is observed for old stars in ellipticals, the mass–to–light ratio for the old component in dIs is assumed to vary as a power law in luminosity with exponent γ_d. Thus, the mass–to–light ratio of the old component is estimated from

$$\left(\frac{M_*}{L_B}\right)_{\mathrm{old}} = \left(\frac{M_*}{L_B}\right)_{\mathrm{old\,MW\,dsk}} \left(\frac{L_{B,\mathrm{old}}}{L_{B,\mathrm{old\,MW\,dsk}}}\right)^{\gamma_d}, \tag{7.15}$$

where $(\frac{M_*}{L_B})_{\mathrm{old\,MW\,dsk}}$ and $L_{B,\mathrm{old\,MW\,dsk}}$ are, respectively, the mass–to–light ratio and luminosity in B of the old component of the Milky Way disk. The mass–to–light ratio

for the old component of the disk of the Milky Way is obtained from the dispersion in vertical motions of disk matter in proximity to the solar neighbourhood. Indeed, the mass–to–light ratio for the old component is obtained without having to worry about the extragalactic distance scale (see Equation 7.47).

7.3.2 Colour and Surface Brightness of the Galactic Disk

To estimate $L_{B,\text{old MW dsk}}$, it is necessary to estimate the surface brightness and size of the old disk of the Milky Way. Here, the solar radius is adopted to be $R_{\odot} = 7.8$ kpc (Feast 1987), which is consistent with the value determined by Reid (1993).

The dust–free colour and surface brightness of light in the direction of the Galactic pole are required to compute the luminosity of the Milky Way or its components. Based upon galaxy counts and column densities of neutral hydrogen (Burstein and Heiles 1982), the reddening of an extragalactic source at a Galactic latitude of 90° (north or south) is

$$E(B-V)(90°) = 0.012 \text{ mag} \tag{7.16}$$

and the extinction in B towards the Galactic pole is

$$A_B(90°) = +0.050 \text{ mag}. \tag{7.17}$$

The colour of the spheroidal component of the Milky Way integrated along the line of sight to the Galactic pole is needed to estimate the disk colour in the vicinity of the solar neighbourhood (de Vaucouleurs and Pence 1978; Terndrup 1988). The dust–free polar colour of the spheroid is

$$(B-V)^0_{\text{sph}}(90°) = 0.60 \text{ mag} \tag{7.18}$$

and the apparent reddened polar colour of the spheroid using Equation (7.16) is

$$(B-V)_{\text{sph}}(90°) = 0.61 \text{ mag}. \tag{7.19}$$

The surface brightness of the spheroid in the direction of the Galactic pole is required to determine the disk surface brightness at the solar radius from the integrated (disk plus spheroid) polar surface brightness. Based upon star counts in the spheroid (Bahcall and Soneira 1984; Bahcall and Casertano 1986; van der Kruit 1986), the dust–free polar surface brightness of the spheroid is

$$\mu^0_{B,\mathrm{sph}}(90°) = 27.20 \text{ mag arcsec}^{-2} \tag{7.20}$$

and the apparent reddened polar surface brightness of the spheroid based upon the polar extinction in Equation (7.17) is

$$\mu_{B,\mathrm{sph}}(90°) = 27.25 \text{ mag arcsec}^{-2}. \tag{7.21}$$

The integrated polar colour of the Milky Way in the direction of the Galactic pole is required to determine the disk colour and luminosity of the old disk (de Vaucouleurs and Pence 1978; Bahcall and Soneira 1984; van der Kruit 1986; Stobie and Ishida 1987). From star counts near the North Galactic Pole, the integrated polar colour is found to be

$$(B-V)_{\mathrm{tot}}(90°) = 0.70 \text{ mag}. \tag{7.22}$$

The integrated polar surface brightness is needed to determine the surface brightness of the disk at the solar radius. This sets the surface brightness scale of the light profile and the luminosity of the disk. Based on star counts and observations by the Pioneer 10 spacecraft, the integrated polar surface brightness is determined to be

$$\mu_{B,\mathrm{tot}} = 24.50 \text{ mag arcsec}^{-2} \tag{7.23}$$

(Bahcall and Soneira 1984; van der Kruit 1986).

The vertical distributions of dust and stars are necessary to correct the polar colour and surface brightness for obscuration by dust. Vertical distributions are

approximated by an exponential (i.e., e^{-z/z_0}), whose scale is defined by a scale height, z_0. From van der Kruit (1986), the scale heights for the young disk and for dwarf stars with $M_V \geq +3$ in the old disk are

$$z_{0,\mathrm{yng}} = 90 \text{ pc} \tag{7.24}$$

and

$$z_{0,\mathrm{old}} = 325 \text{ pc} \tag{7.25}$$

respectively (van der Kruit 1986). Using the distribution of 100 μm emission measured by IRAS (Burton and Deul 1987), the scale height for dust in the Milky Way disk is

$$z_{0,\mathrm{dust}} = 155(R_\odot/7.8) \text{ pc} \tag{7.26}$$

where $R_\odot$ is in kpc.

The disk surface brightness at the solar radius sets the disk luminosity if the scale length is known. The local disk colour at the solar radius provides a way to estimate the fraction of light contributed by the old stars. Subtracting the contribution of the Milky Way spheroid (Equation 7.21) from the total polar surface brightness (Equation 7.23), the apparent local disk surface brightness towards the Galactic pole is

$$\mu_B(90°) = 24.59 \text{ mag arcsec}^{-2} \tag{7.27}$$

and the apparent local disk colour towards the Galactic pole is

$$(B-V)(90°) = 0.71 \text{ mag.} \tag{7.28}$$

Based upon the polar extinction (Equation 7.17) and the scale heights for old stars and dust (Equations 7.25 and 7.26, respectively), the extinction in B of the disk towards the Galactic pole is

$$A_B(90°) = 0.034 \text{ mag} \tag{7.29}$$

and the reddening of the disk towards the Galactic pole is

$$E(B-V)(90°) = 0.008 \text{ mag.} \tag{7.30}$$

After corrections, the dust-free local colour of the disk at the solar radius is therefore

$$(B-V)^0(r = R_\odot) = 0.70 \text{ mag} \tag{7.31}$$

and the face–on dust–free local surface brightness of the disk at the solar radius as viewed by an observer outside the Milky Way is

$$\mu_B^0(r = R_\odot) = 23.80 \text{ mag arcsec}^{-2}. \tag{7.32}$$

7.3.3 Effective Radius of the Galactic Disk

To compute the disk luminosity, the scale of the surface brightness profile is required. The disk surface brightness varies with radius as an exponential (i.e., e^{-r/r_0}) with scale length r_0. The effective radius, which contains half of the total light, is given by

$$r_{\text{eff}} = 1.678\, r_0. \tag{7.33}$$

Based upon various measurements for r_0 (van der Kruit 1986; Habing 1987; van der Kruit 1987a; van der Kruit 1987b), the adopted effective radius for the Milky Way disk is

$$r_{\text{eff}} = 8.9\, f(R_\odot) \text{ kpc}, \tag{7.34}$$

where

$$f(R_\odot) = 1 + 0.50\,[R_\odot(\text{kpc})/7.8 - 1]\,. \tag{7.35}$$

7.3.4 Surface Brightnesses of the Young and Old Galactic Disk

The dust–free surface brightness of the Milky Way's young disk is needed so that the light from young stars can be properly removed from the total to obtain the

light from the old component. The fraction of the apparent polar light from all sources which is attributable to dwarf stars with $M_V \leq +4$ is 0.17 (Bahcall and Soneira 1984; van der Kruit 1986). The extinction of the young disk towards the Galactic pole can be computed using the adopted scale heights of young stars and dust from Equations (7.24) and (7.26). From the integrated polar surface brightness (Equation 7.23) and the colour of the young component (Equation 7.10), the dust–free local surface brightness of the young disk at the solar radius is

$$\mu^0_{B,\mathrm{yng}}(R_\odot) = 24.95 \text{ mag arcsec}^{-2}. \tag{7.36}$$

Subtracting the young component from $\mu^0_B(r = R_\odot)$, the dust–free surface brightness of the old Milky Way disk at the solar radius is

$$\mu^0_{B,\mathrm{old}}(R_\odot) = 24.27 \text{ mag arcsec}^{-2}. \tag{7.37}$$

From the dust–free surface brightness in B of the old disk, the dust–free surface luminosity density of the old disk, $I^0_{B,\mathrm{old}}$, is

$$I^0_{B,\mathrm{old}} \;=\; 12.9\, L_{B,\odot}\ \mathrm{pc}^{-2}, \tag{7.38}$$

assuming 1 $L_{B,\odot}$ pc^{-2} corresponds to a surface brightness in B of 27.05 mag arcsec^{-2} (Hayes 1978).

7.3.5 Colour of the Old Galactic Disk

For old disks at high luminosity, the photometric properties of the old Milky Way disk help to anchor the dependence of colour on luminosity and surface brightness. Based upon the dust–free local surface brightness of the young disk at the solar radius (Equation 7.36), the fraction of the dust–free local surface brightness of the disk at $R_\odot$ from old stars can be computed. Given the dust–free local disk colour at the solar

radius (Equation 7.31) and the colour of the young component (Equation 7.10), the dust–free colour of the old Milky Way disk at the solar radius is

$$(B-V)^0_{\rm old}(R_\odot) = 0.95 \text{ mag.} \tag{7.39}$$

Because the solar radius is roughly similar to the effective radius of the Milky Way (e.g., van der Kruit 1986, 1987b), the colour of old stars at the solar radius should be representative of the old disk on average, because the effective radius encompasses one–half of the total light of the galaxy. Therefore, the dust–free integrated colour for the entire old disk is

$$(B-V)^0_{\rm old} = 0.95 \text{ mag.} \tag{7.40}$$

This value was adopted as an anchor point for the derivation of the dependence of $(B-V)^0_{\rm old}$ on M_B and μ_B for old disks (Equation 7.11).

7.3.6 Luminosity of the Old Galactic Disk

From the adopted effective radius (Equation 7.34) and the dust–free surface brightness of the old disk at $r = R_\odot$ (Equation 7.37), the absolute magnitude in B of the old disk of the Milky Way is

$$M_{B,\text{old MW dsk}} = -19.52 + 1.60\left[1 - \frac{R_\odot/(7.8\text{kpc})}{f(R_\odot)}\right] - 5\log f(R_\odot). \tag{7.41}$$

where $f(R_\odot)$ is given by Equation (7.35). With the choice of $R_\odot = 7.8$ kpc, the absolute magnitude in B of the old disk is -19.52. By Equation (7.2), the corresponding luminosity of the old disk is

$$L_{B,\text{old MW dsk}} = 1.0 \times 10^{10}\, L_{B,\odot}. \tag{7.42}$$

7.3.7 Mass–to–Light Ratio of the Old Galactic Disk

To compute the mass–to–light ratio of the old component of the disk, the surface mass density of the old component at the solar radius is required. This can be computed from the total surface mass density by subtracting the contributions by gas and young stars. The total surface mass density in the solar neighbourhood is derived from the vertical kinematics of nearby late–type disk stars (e.g., Bahcall 1984; Gilmore et al. 1989; Kuijken and Gilmore 1989a; Kuijken and Gilmore 1989b; Gould 1990; Bahcall et al. 1992).

Based upon the vertical kinematics of local F dwarf stars in the disk at the solar radius (Gould 1990), the surface density of disk matter in all forms (luminous and dark) is adopted to be

$$\Sigma(R_\odot) = 54\ M_\odot\ \mathrm{pc}^{-2}. \tag{7.43}$$

The surface mass density at the solar radius of the young component of the Milky Way disk is

$$\Sigma_{\mathrm{yng}}(R_\odot) = 1.1\ M_\odot\ \mathrm{pc}^{-2}, \tag{7.44}$$

which is obtained from the dust–free local surface brightness of young stars (Equation 7.36) and the mass–to–light of young stars (Equation 7.13). The sum of the surface gas mass densities in neutral, molecular, and ionized forms within the Milky Way disk at the solar radius is (Kuijken and Gilmore 1989b; Kulkarni and Heiles 1987; Scoville and Sanders 1987)

$$\Sigma_{\mathrm{gas}}(R_\odot) = 12.6\ M_\odot\ \mathrm{pc}^{-2}. \tag{7.45}$$

Subtracting the surface mass densities in gas and young stars (Equations 7.45 and 7.44, respectively) from the total surface mass density (Equation 7.43) gives the

surface mass density of the old disk:

$$\Sigma_{\rm old}(R_\odot) = 40.3\ M_\odot\ {\rm pc}^{-2}. \tag{7.46}$$

Dividing the surface mass density of the old disk (Equation 7.46) by the luminous surface density of the old disk (Equation 7.38), the mass–to–light ratio in B of the Milky Way's old disk at the solar radius is

$$(M_*/L_B)_{\rm old\,MW\,dsk}(r = R_\odot) = 3.11\ M_\odot/L_{B,\odot}. \tag{7.47}$$

Because $r_{\rm eff} \approx R_\odot$, the mass–to–light ratio of the old component at the solar radius is taken to be representative of the entire old disk component of the Milky Way.

7.3.8 The Variation of $(M_*/L_B)_{\rm old}$ with $L_{B,\rm old}$

The exponent, γ_d, of the power law describing how $(M_*/L_B)_{\rm old}$ varies with $L_{B,\rm old}$ (Equation 7.15) was derived from the relationship between rotational and photometric masses of spiral and irregular galaxies in the Virgo Cluster. From a nonlinear least squares fit to a sample of 28 Virgo Cluster galaxies with $M_{B,\rm dsk} = -19$ to -21, γ_d was determined to be 0.175. The same relation was found to hold for five dwarfs with $M_{B,\rm dsk}$ between -15 and -18 for which good rotation curves are available. The small but non–zero value of γ_d indicates that the mass–to–light ratio for the old disk varies slowly with the luminosity of the old disk over a factor of ~ 600 in luminosity.

7.3.9 A Final Equation For M_*

Combining Equations (7.14), (7.15), (7.42), and (7.47), the mass in old stars is

$$\begin{aligned} M_{*,\rm old} &= 3.11\,\frac{(L_{B,\rm old})^{1+\gamma_d}}{(L_{B,\rm old\,MW\,dsk})^{\gamma_d}} \\ &= 3.11\,\frac{(f_{\rm old}L_B)^{1+\gamma_d}}{(1.0\times10^{10})^{\gamma_d}} \end{aligned} \tag{7.48}$$

where $M_{*,\rm old}$ and L_B are in solar units. Combining Equations (7.12), (7.13), and (7.48), the total mass of stars is thus

$$\begin{aligned} M_* &= M_{*,\rm yng} + M_{*,\rm old} \\ &= 0.153\,(1 - f_{\rm old})L_B \;+\; 3.11\,\frac{(f_{\rm old}L_B)^{1+\gamma_d}}{(1.0\times 10^{10})^{\gamma_d}}. \end{aligned} \tag{7.49}$$

7.3.10 Results

For each dI, the dust–free apparent magnitude, B_T^0, the distance modulus, the total dust-free $(B-V)^0$ colour, and the effective radius, $r_{\rm eff}$ (or exponential scale length, r_0), are needed to derive the stellar mass. To compute $c_{\rm old}$ for the fraction of light contributed by old stars (see Equation 7.9), it is assumed that the photometric properties of old stars in dIs are similar to those in other disk–like systems where star formation has ceased. The relationship between $c_{\rm old}$, M_B, and $\langle\mu^0_{B,\rm eff}\rangle_{\rm old}$ is expressed by Equation (7.11). An initial estimate of luminosity is given by B_T^0; an initial estimate of surface brightness is given by

$$\begin{aligned} \mu^0_{B,\rm eff} &= B_T^0 + 2.5\log(2\pi r_{\rm eff}^2) \\ &= B_T^0 + 5\log r_{\rm eff} + 2.0, \end{aligned} \tag{7.50}$$

i.e., by the dust–free effective surface brightness in B of the whole dwarf in units of mag arcsec^{-2}.

In summary, Table 7.2 lists derived gas masses, stellar masses, stellar mass–to–light ratios, and gas fractions for field and Virgo dIs.

7.3.11 Testing the Two–Component Method

To evaluate the contribution to the total luminosity from the underlying old component, the observed luminosity in B from the old disk, $M_{B,\rm old}$, can be computed from

dI Name	M_B	log $M_{\rm HI}$	log $M_{\rm gas}$	log $M_{\rm HI}/L_B$	log M_*	M_*/L_B	μ	log log $(1/\mu)$
	(mag)	($M_\odot$)	($M_\odot$)	($M_\odot/L_{\odot,B}$)	($M_\odot$)	($M_\odot/L_{\odot,B}$)		
(1)	(2)	(3)	(4)	(5)	(6)	(7)	(8)	(9)
Field dIs								
DDO 187	−15.07	8.25	8.39	+0.032	8.01	0.61	0.706	−0.821
GR 8	−12.19	7.04	7.17	−0.027	6.74	0.47	0.731	−0.866
Ho II	−15.98	8.93	9.06	+0.344	8.54	0.90	0.771	−0.947
IC 10	−15.85	8.14	8.27	−0.394	8.62	1.21	0.312	−0.296
IC 1613	−14.53	7.97	8.10	−0.036	8.13	1.34	0.484	−0.502
IC 2574	−17.06	9.16	9.30	+0.146	8.95	0.86	0.690	−0.793
IC 4662	−15.84	8.40	8.53	−0.132	8.30	0.59	0.630	−0.697
Leo A	−11.35	6.89	7.02	+0.154	6.36	0.43	0.820	−1.066
LMC	−17.94	8.82	8.96	−0.544	9.37	1.01	0.279	−0.257
NGC 1560	−16.37	8.85	8.98	+0.107	8.74	0.99	0.638	−0.710
NGC 1569	−16.54	7.80	7.93	−1.008	8.58	0.59	0.185	−0.136
NGC 2366	−16.28	8.95	9.08	+0.243	8.79	1.22	0.662	−0.747
NGC 3109	−15.30	8.94	9.07	+0.624	8.31	1.00	0.851	−1.155
NGC 4214	−18.04	9.24	9.37	−0.169	9.40	0.98	0.485	−0.503
NGC 5408	−15.81	8.25	8.38	−0.269	8.51	0.98	0.429	−0.434
NGC 55	−18.28	9.18	9.31	−0.326	9.52	1.05	0.380	−0.377
NGC 6822	−14.95	8.13	8.26	−0.042	8.19	1.06	0.540	−0.572
Sextans A	−14.04	8.03	8.16	+0.219	7.66	0.71	0.762	−0.928
Sextans B	−14.02	7.65	7.78	−0.150	7.74	0.87	0.526	−0.554
SMC	−16.56	8.95	9.09	+0.136	8.93	1.30	0.590	−0.640
UGC 6456	−13.90	7.90	8.04	+0.154	7.61	0.72	0.729	−0.863
WLM	−13.92	7.79	7.93	+0.033	7.65	0.79	0.652	−0.731
Virgo dIs								
VCC 0512	−15.82	8.39	8.52	−0.132	8.50	0.96	0.511	−0.535
VCC 0848	−16.39	8.73	8.87	−0.014	8.62	0.74	0.640	−0.712
VCC 0888	−16.12	7.98	8.11	−0.661	8.69	1.13	0.209	−0.168
VCC 1114	−16.46	7.26	7.40	−1.512	8.79	1.03	0.039	+0.148
VCC 1179	−16.25	7.46	7.59	−1.235	8.55	0.72	0.100	+0.001
VCC 1200	−16.34	7.42	7.55	−1.311	8.74	1.03	0.061	+0.085
VCC 1249	−16.86	7.04[a]	7.18	−1.893	8.98	1.09	0.016	+0.256
VCC 1448[b]	−17.19	7.53	7.66	−1.543	9.32	1.79	0.021	+0.222
VCC 1554	−18.97	9.53	9.66	−0.253	9.69	0.82	0.483	−0.500
VCC 1585	−15.92	8.85	8.98	+0.290	8.57	1.03	0.721	−0.848
VCC 1789	−16.05	7.85	7.98	−0.764	8.73	1.30	0.153	−0.089
VCC 2037	−15.32	7.37	7.51	−0.946	8.12	0.63	0.197	−0.151

Table 7.2: Stars and gas in field and Virgo dIs. Column (1) labels the dI; column (2) lists the absolute magnitude in B; columns (3) and (4) list the logarithm of the H I gas mass and the total gas mass from Equations (7.3) and (7.4), respectively; column (5) lists the logarithm of the H I gas-to-blue-light ratio; column (6) lists the logarithm of the stellar mass from Equation (7.6); column (7) lists the stellar mass-to-light ratio in B; column (8) lists the gas fraction; and column (9) lists the inverse gas fraction, as conveyed by log log $(1/\mu)$; see § 7.5. NOTE: [a] H I measured at the actual position of VCC 1249 (see Chapter 6). [b] No H II region spectrum was detected.

Equation (7.8). Table 7.3 lists M_B, $M_{B,\mathrm{old}}$, and their difference ($\delta M_B = -2.5 \log f_{\mathrm{old}}$). The average difference for field dIs is +0.68 mag. For Virgo dIs, the average is +0.71 mag; it is +0.74 mag if VCC 1448 is excluded. These numbers are similar to those found by Papaderos et al. (1996) and Patterson and Thuan (1996), who performed photometric decompositions on star–forming dwarfs to separate recent bursts from their underlying non–burst components.

To facilitate a more detailed comparison with models below, properties of an "average" dI in each of the field and Virgo samples are computed. The field dIs are restricted to the same range of M_B encompassed by Virgo dIs ($-15.3 \gtrsim M_B \gtrsim -19.0$). Properties of the average field and the average Virgo dI are listed in Table 7.4. The average field dI and the average Virgo dI have similar properties, except for the gas fraction μ.

It is important to realize that recent observations of dIs (e.g., Gallagher and Hunter 1985; Gallagher and Hunter 1986; Grebel 2001; van Zee 2001) suggest that observed rates of star formation are consistent with the scenario that stars have formed at a constant rate on average over a Hubble time. The properties of the average dI in each sample are readily reproduced by syntheses founded upon a constant rate of star formation. Using a standard Salpeter initial mass function (IMF) (Salpeter 1955), Searle et al. (1973) created a model with $M_B = -15.6$ mag and $B - V = +0.36$ mag at an age of 10 Gyr. Larson and Tinsley (1978) produced models with $B-V$ colours of +0.44 mag, +0.50 mag, +0.56 mag at ages of 5, 10, and 20 Gyr, respectively. Models for dwarf galaxies by Krüger et al. (1991) and Krüger and v. Alvensleben (1994) yielded similar results. Beginning with a gas mass of approximately 10^9 $M_\odot$, their models resulted in dwarfs with the following properties at an age of about 10 Gyr: $M_B \approx -16.5$, $B - V \approx 0.45$ mag, and $\mu \approx 0.65$. Most important, they computed $M_*/L_B \approx 0.60$, which is in good agreement with results from the two–component

dI Name (1)	M_B (mag) (2)	$M_{B,\mathrm{old}}$ (mag) (3)	f_{old} (4)	$-2.5 \log f_{\mathrm{old}}$ (mag) (5)
Field dIs				
DDO 187	−15.070	−14.120	0.417	+0.950
GR 8	−12.185	−11.358	0.467	+0.827
Holmberg II	−15.980	−15.285	0.527	+0.695
IC 10	−15.854	−15.499	0.721	+0.355
IC 1613	−14.531	−14.490	0.963	+0.041
IC 2574	−17.061	−16.135	0.426	+0.926
IC 4662	−15.844	−14.689	0.345	+1.155
Leo A	−11.353	−10.545	0.475	+0.808
LMC	−17.936	−17.050	0.442	+0.886
NGC 1560	−16.372	−15.717	0.547	+0.655
NGC 1569	−16.536	−15.261	0.309	+1.275
NGC 2366	−16.284	−15.864	0.679	+0.420
NGC 3109	−15.299	−14.831	0.650	+0.468
NGC 4214	−18.035	−17.101	0.423	+0.934
NGC 5408	−15.812	−15.179	0.558	+0.633
NGC 55	−18.277	−17.381	0.438	+0.896
NGC 6822	−14.947	−14.592	0.721	+0.355
Sextans A	−14.038	−13.393	0.552	+0.645
Sextans B	−14.015	−13.614	0.691	+0.401
SMC	−16.556	−16.155	0.691	+0.401
UGC 6456	−13.896	−13.182	0.518	+0.714
WLM	−13.916	−13.409	0.627	+0.507
Virgo dIs				
VCC 0512	−15.820	−15.198	0.564	+0.622
VCC 0848	−16.390	−15.414	0.407	+0.976
VCC 0888	−16.120	−15.642	0.644	+0.478
VCC 1114	−16.460	−15.827	0.558	+0.633
VCC 1179	−16.250	−15.255	0.400	+0.995
VCC 1200	−16.340	−15.691	0.550	+0.649
VCC 1249	−16.860	−16.232	0.561	+0.628
VCC 1448 [a]	−17.190	−16.919	0.779	+0.271
VCC 1554	−18.970	−17.684	0.306	+1.286
VCC 1585	−15.920	−15.313	0.572	+0.607
VCC 1789	−16.050	−15.729	0.744	+0.321
VCC 2037	−15.320	−14.325	0.400	+0.995

Table 7.3: M_B, $M_{B,\mathrm{old}}$, and their difference for field and Virgo dIs. Column (1) lists the name of the dI, column (2) lists the absolute magnitude in B, column (3) lists the absolute magnitude in B for the underlying old component, column (4) lists the luminosity fraction in B for the old component given by Equation (7.9), and column (5) lists the corresponding magnitude difference. NOTE: [a] VCC 1448: no spectrum could be obtained for this dI.

Property	Field dI ($N = 13$)	Virgo dI ($N = 12$)
Mean M_B (mag)	−16.6	−16.5
Mean $B - V$ (mag)	+0.47	+0.52
log $\langle M_* \rangle$ ($M_\odot$)	8.81	8.99
Mean (M_*/L_B) $(M_\odot/L_{\odot,B})$	0.97	1.02
Mean μ	0.53	0.26
Mean 12+log(O/H)	8.07	8.15 [a]

Table 7.4: Properties of an average field and an average Virgo dI. The field dIs are restricted to the luminosity range encompassed by Virgo dIs, namely $-15.3 \gtrsim M_B \gtrsim -19.0$. Values of M_* and M_*/L_B are computed using the two-component algorithm. NOTE: [a] Average based upon 11 dwarfs; no H II region spectrum was obtained for VCC 1448.

model.

7.3.12 Comparison with the Bruzual & Charlot Code

Although precise values of M_* are not essential to studying the evolution of Virgo dIs *with respect to* field dIs, they are important for assessing how dIs have evolved in an absolute sense. Thus, it is appropriate to test the two-component population synthesis technique more rigorously. The galaxy evolutionary synthesis code by Bruzual and Charlot (1996; BC96 hereafter) has been used to evaluate whether the initial assumption of a small young burst on top of an underlying old population of stars is valid and whether computed values of M_* above are reasonable. Further details of the code are provided in Charlot and Bruzual (1991) and Bruzual and Charlot (1993).

The code[1] by Bruzual and Charlot (1996) provides a reasonably simple method to generate models for galaxies. Composite stellar populations at a given metallicity are constructed with the aid of spectral libraries and stellar evolutionary tracks (Lejeune et al. 1997). The user is permitted to perform computations with sub-solar, solar, and super-solar metallicities, with different initial stellar mass functions, and with

[1]See also § 6.4, Leitherer et al. (1996).

different star formation histories. The stellar mass function and the metallicity do not vary with time. Here, the following model is adopted: a Salpeter initial stellar mass function (Salpeter 1955) with mass limits in the range between $m_{\rm lower} = 0.1\ M_{\odot}$ and $m_{\rm upper} = 125\ M_{\odot}$, a constant star formation rate, and a metallicity equal to one–fifth solar (12+log(O/H) = 8.17), which is similar to the value for the average dI for each of our samples (Table 7.4).

The galaxy in a model is normalized to 1 $M_{\odot}$. By assigning a desired absolute magnitude, M_B(desired), a physical stellar mass, M_*(actual), is defined by

$$M_B(\text{desired}) - B_{\rm mag}(\text{model}) = -2.5 \log \left[\frac{M_*(\text{actual})}{M_*(\text{model})} \right], \qquad (7.51)$$

where $B_{\rm mag}$(model) and M_*(model) are obtained from the models. For the present discussion, the desired absolute magnitude, M_B(desired), is assigned to be -16, which is typical of the range for field and Virgo dIs, as seen in Table 7.4.

Table 7.5 lists results for a set of models founded upon a constant star formation rate (SFR). The model colours are within the range of values observed for field and Virgo dIs (see Tables 2.1 and 2.5). Note that the actual choice of the star formation rate has no bearing on the results for $B - V$ and M_*/L_B at a given age. This is because the ratio of the SFR to the actual mass of stars formed by a given age is independent of the SFR. A model with a Scalo initial mass function (Scalo 1986) yields slightly smaller stellar mass–to–light ratios and $B-V$ colours which are redder by about 0.1 mag.

The stellar mass and the stellar mass–to–light ratio are computed using the two–component method for a test dI with $M_B = -16$ and $B - V = +0.405$ and a test dI with $M_B = -16$ and $B-V = +0.438$, and are compared with BC96 models evaluated with a constant SFR at ages of 10 Gyr and 14 Gyr. Results are listed in Table 7.6. The stellar mass and total stellar mass–to–light ratio from the two–component algorithm

t (Gyr) (1)	$B_{\rm mag}$(model) (per 1 $M_\odot$) (2)	$B-V$ (mag) (3)	M_*(model) (per 1 $M_\odot$) (4)	$\log M_*$(actual) ($M_\odot$) (5)	M_*/L_B(actual) ($M_\odot/L_{\odot,B}$) (6)
SFR = constant					
10	8.0959	0.4050	0.068	8.471	0.757
12	8.0606	0.4231	0.081	8.533	0.872
14	8.0310	0.4383	0.094	8.586	0.985
16	8.0052	0.4577	0.107	8.631	1.095
18	7.9826	0.4635	0.120	8.672	1.203
20	7.9629	0.4742	0.133	8.709	1.309

Table 7.5: Models with a constant star formation rate (SFR) created with the evolutionary synthesis code by Bruzual and Charlot (1996). The model is scaled so that the final mass of the galaxy is 1 $M_\odot$. A Salpeter initial mass function and a metallicity of one–fifth solar are assumed. Column (1) lists the age of the model galaxy. Column (2) lists the B magnitude per 1 $M_\odot$ galaxy. Column (3) lists the output $B-V$ colour. Column (4) lists the output stellar mass fraction. Column (5) lists the actual stellar mass from Equation (7.51). Column (6) lists the actual stellar mass–to–light ratio from actual stellar masses in column (5) and the luminosity corresponding to $M_B = -16$. At a given age, the colours, actual stellar masses, and stellar mass–to–light ratios are independent of the SFR.

are the same as the values obtained from the evolutionary synthesis code.

7.3.13 Variation of M_*/L_B with M_B

Based on the two–component algorithm, values of the stellar mass–to–light ratio in B for the sample of field dIs range between 0.4 and 1.3. The lowest values belong to GR 8 and Leo A, which are the lowest luminosity dIs in the field sample. Values of M_*/L_B for the sample of Virgo dIs range between 0.6 and 1.8 (see Table 7.2).

Figure 7.1 shows a plot of stellar mass–to–light ratio in B versus absolute magnitude in B for field and Virgo dIs. There is little correlation of M_*/L_B with M_B for both samples of dIs; values are all clustered around $M_*/L_B \sim 1$. The range of M_*/L_B observed in field and Virgo dIs is reproduced at ages between 10 and 20 Gyr by a model with constant star formation (see Tables 7.5 and 7.6).

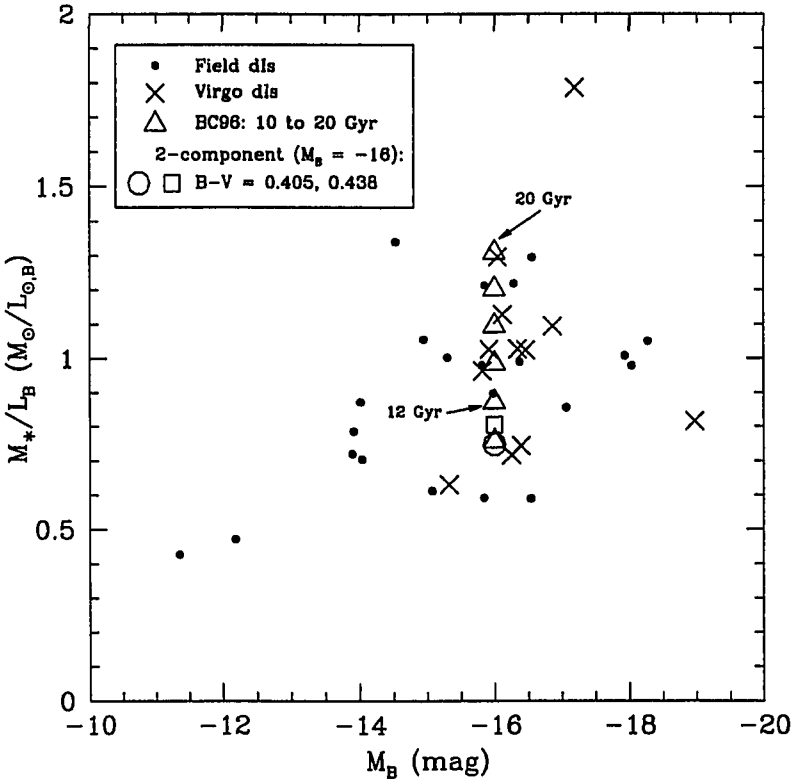

Figure 7.1: Stellar mass-to-light ratio versus absolute magnitude in B for field and Virgo dIs. Filled circles indicate field dIs and crosses indicate Virgo dIs. For ages between 10 and 20 Gyr in increments of 2 Gyr, open triangles show the locations of an $M_B = -16$ dwarf galaxy, whose properties are determined from the evolutionary synthesis code of Bruzual and Charlot (BC96) and are listed in Table 7.5. The open circle and open square show the position of dIs at $M_B = -16$ with colours $B - V = 0.405$ and 0.438, respectively, for which M_* are obtained from the two-component method (see Table 7.6).

Property of Test dI (1)	Two-Component Method (2)	BC96 (10 Gyr) (3)	Two-Component Method (4)	BC96 (14 Gyr) (5)
Assigned M_B (mag)	-16	-16	-16	-16
Assigned $B-V$ (mag)	$+0.405$ [a]	$+0.405$ [a]	$+0.438$ [b]	$+0.438$ [b]
$f_{\rm old}$	0.434	...	0.469	...
$(M_*/L_B)_{\rm old}$ $(M_\odot/L_{\odot,B})$	1.524	...	1.545	...
$\log M_*$ $(M_\odot)$	8.466	8.471 [a]	8.498	8.586 [b]
(M_*/L_B) $(M_\odot/L_{\odot,B})$	0.748	0.756 [a]	0.805	0.986 [b]

Table 7.6: Properties of a test dI: two–component formalism versus Bruzual and Charlot (1996) code. The assigned value of M_B is motivated by the approximate mean value for Virgo dIs (see Table 7.4). Columns (2) and (4) list the fraction of light in B from old stars, $f_{\rm old}$, the ratio of mass in old stars to blue luminosity, the total stellar mass, and the stellar mass–to–light ratio in B computed using the two–component algorithm in § 7.3. Columns (3) and (5) list the stellar mass and stellar mass–to–light ratio in B generated by the evolutionary synthesis code (Bruzual and Charlot 1996). NOTES: [a] Values obtained from Table 7.5 at an age of 10 Gyr. [b] Values obtained from Table 7.5 at an age of 14 Gyr.

7.4 Correlations

To explore the effects of the cluster environment on the evolution of dIs, the following correlations are examined: O/H and M_B in § 7.4.2, $B-V$ and M_B in § 7.4.3, the effect of star formation on O/H and M_B in § 7.4.4, O/H and M_* in § 7.4.5, O/H and $M_{\rm HI}/L_B$ in § 7.4.6, $M_{\rm HI}/L_B$ and M_B in § 7.4.7, O/H and $M_{\rm gas}$ in § 7.4.8, $M_{\rm gas}$ and M_* in § 7.4.9, and O/H and $M_{\rm bary}$ in § 7.4.10. The correlation between O/H and μ is extensively discussed in § 7.5.

7.4.1 Fitting Procedure

A best–fit line for the correlation between two parameters with comparable errors is obtained with the geometric mean functional relationship (Draper and Smith 1998), which assumes similar dispersions in both observables. As correlations are sought between parameters expressed in logarithms, a typical error is about 0.1 to 0.2 dex. In particular, for the two key diagnostics (O/H vs. M_B and O/H vs. μ), the errors

for both dependent and independent variables are very similar (see Figures 7.2 and 7.14). An equal weighting of points is assigned for both variables in a given fit. While maximum likelihood techniques are more appealing for asymptotic results, these methods do not work as well when the datasets are small (Draper and Smith 1998).

The geometric mean functional relationship relies upon the minimization of the sum of areas bounded by the shortest horizontal and vertical lines from each data point to the best–fit line. For the desired relation Y versus X, the fit is described by

$$Y = y_0 + mX. \tag{7.52}$$

Initially, two linear least–squares fits are obtained : $Y = b_0 + b_1 X$ and $X = a_0 + a_1 Y$. The desired slope, m, is obtained from the geometric mean of the slopes from the two linear least–squares fits

$$m = \left(\frac{b_1}{a_1}\right)^{1/2}. \tag{7.53}$$

The desired intercept, y_0, is given by

$$y_0 = \langle Y \rangle - m \langle X \rangle, \tag{7.54}$$

where $\langle X \rangle$ and $\langle Y \rangle$ are the average of X and Y values, respectively.

7.4.2 (O/H) vs. M_B

Skillman et al. (1989) and Richer and McCall (1995) showed that oxygen abundances in dIs increase with increasing galaxy luminosity in B. Hidalgo-Gámez and Olofsson (1998) claimed from their sample of dIs that this relationship is weaker than previously thought. Nevertheless, the relationship continues to spiral galaxies at higher luminosities (Garnett and Shields 1987; Roberts and Haynes 1994; Zaritsky et al. 1994). For nearby dSphs, Grebel and Guhathakurta (1999) have also observed a

similar relationship between iron abundance and galaxy luminosity in V (see also Aaronson et al. 1978; Aaronson 1986). However, Richer et al. (1995, 1998) showed that oxygen abundances for a number of field dSphs are about +0.3 dex higher than in field dIs at similar luminosities in B and concluded that the predecessors to field dSphs could not have been dIs.

Figure 7.2 shows the metallicity–luminosity diagram for the samples of field and Virgo dIs. Using the geometric mean functional relationship, the fit to all field dIs is given by

$$12 + \log(\mathrm{O/H}) = (5.59 \pm 0.54) + (-0.153 \pm 0.025)\, M_B. \qquad (7.55)$$

This fit is shown as a solid line in Figure 7.2. Equation (7.55) is consistent with the relation determined by Richer and McCall (1995) for dwarfs brighter than $M_B = -15$. From the fit, the root–mean–square deviation, or rms, in log(O/H) is computed to be $\sigma = 0.175$ dex. Two field dIs (Sextans B and NGC 6822) appear to be underluminous for their metallicities, as was noted by Richer and McCall (1995). The dispersion in log(O/H) about the fit described by Equation (7.55) does not increase significantly for dwarfs fainter than $M_B < -15$. In fact, improved distances for Leo A and GR 8 (see Chapter 2) are responsible for the smaller dispersion at lower galaxy luminosities relative to that of Richer and McCall (1995). Hereafter, Equation (7.55) will be adopted as the metallicity–luminosity relation for all field dIs.

Oxygen abundances for the sample of Virgo dIs are consistent with those for the sample of field dIs at comparable luminosities. A simultaneous fit to the 22 field and 11 Virgo dIs gives a result consistent with that expressed by Equation (7.55):

$$12 + \log(\mathrm{O/H}) = (5.43 \pm 0.52) + (-0.164 \pm 0.024)\, M_B. \qquad (7.56)$$

To judge whether there are any differences between field and Virgo dIs, residuals in oxygen abundance are plotted versus absolute magnitude in B in Figure 7.3 for

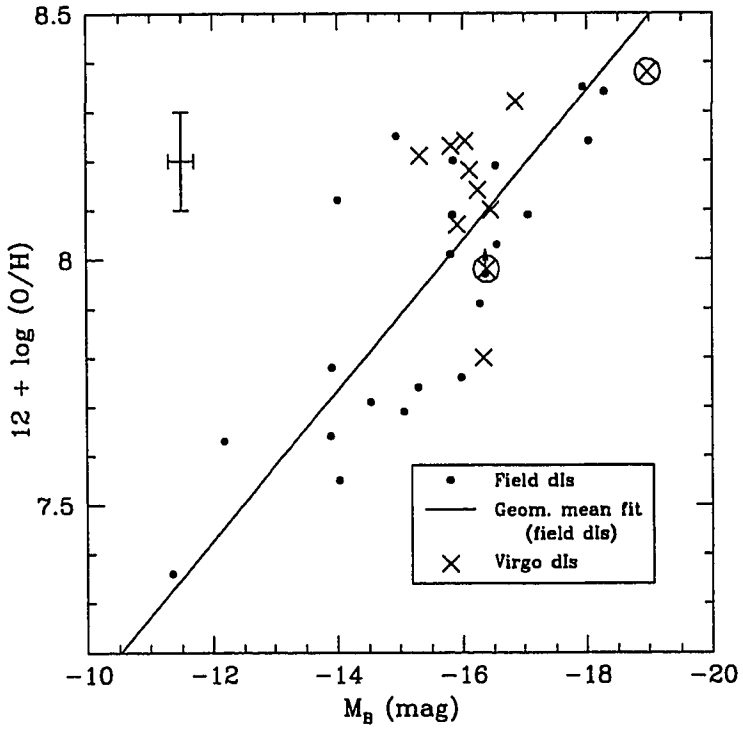

Figure 7.2: Oxygen abundance versus absolute magnitude in B for field and Virgo dIs. Galaxy luminosity increases to the right. The solid dots mark the field dIs. The arrow indicates a lower limit to the oxygen abundance for NGC 1560. Oxygen abundances for the field dwarfs were determined directly from [O III]λ4363 measurements. The solid line is a fit to the field dIs (Equation 7.55) using the geometric mean functional relation (Draper and Smith 1998). Crosses indicate Virgo dIs. [O III]λ4363 detections for VCC 0848 and VCC 1554 are marked as crosses enclosed by open circles. The error bars indicate typical uncertainties in the oxygen abundance and absolute magnitude. The uncertainty is at most 0.1 dex for oxygen abundances which were determined directly from [O III]λ4363 measurements. A typical uncertainty of 0.2 mag in absolute magnitude accounts for the various methods used to determine distances to field dIs and for possible uncertainties in the distances to Virgo dIs arising from the "depth" of the Virgo Cluster (see Chapter 2). The oxygen abundance adopted for the Sun is 12+log(O/H) = 8.87 (Grevesse et al. 1996).

objects in the magnitude range encompassed by the Virgo dIs ($-17 \lesssim M_B \lesssim -15$). Residuals in oxygen abundance are obtained by subtracting the observed abundances from the fit to all dIs in Equation (7.56) to remove the trend of abundance with luminosity within the specified magnitude interval. For the ten field dIs, the mean and standard deviation of the residuals in oxygen abundance are -0.089 dex and $+0.15$ dex, respectively. For the ten Virgo dIs, the mean and standard deviation of the residuals in oxygen abundance are $+0.048$ dex and $+0.17$ dex, respectively. A Student's t–test ($T = -1.90$; $P = 0.074$) shows that the means of residuals for the two samples are not significantly different and an F–test ($F = 1.37$; $P = 0.649$) shows that the variances are indistinguishable.

7.4.3 $B - V$ vs. M_B

Photometric properties (luminosity and colour) can reveal whether Virgo dIs exhibit significant differences in star formation rates compared to field dIs. Figure 7.4 shows a plot of $B - V$ colour versus absolute magnitude in B for the samples of field and Virgo dIs. VCC 1249 (see Chapter 6) and VCC 1448 are labelled, because they are the two most H I–poor dIs in the Virgo sample. A typical fading vector is shown. In disk–like systems, $B - V$ reddens by approximately $+0.25$ mag when M_B fades by 1 mag (McGaugh and Bothun 1994). There is no significant colour difference between field and Virgo dIs, i.e., there has been no significant fading or brightening of Virgo dwarfs with respect to field dwarfs. $B - V$ colours do not vary with luminosity in a systematic way, which suggests that if ages are invariant, a constant percentage of the baryonic mass is involved in star formation. Models with constant star formation (Table 7.5) show that different $B - V$ colours at a given luminosity reflect varying proportions of recently formed stars of different ages. The topic of fading will be re–addressed later in § 7.8.2. Because there is little difference in mean colour, there

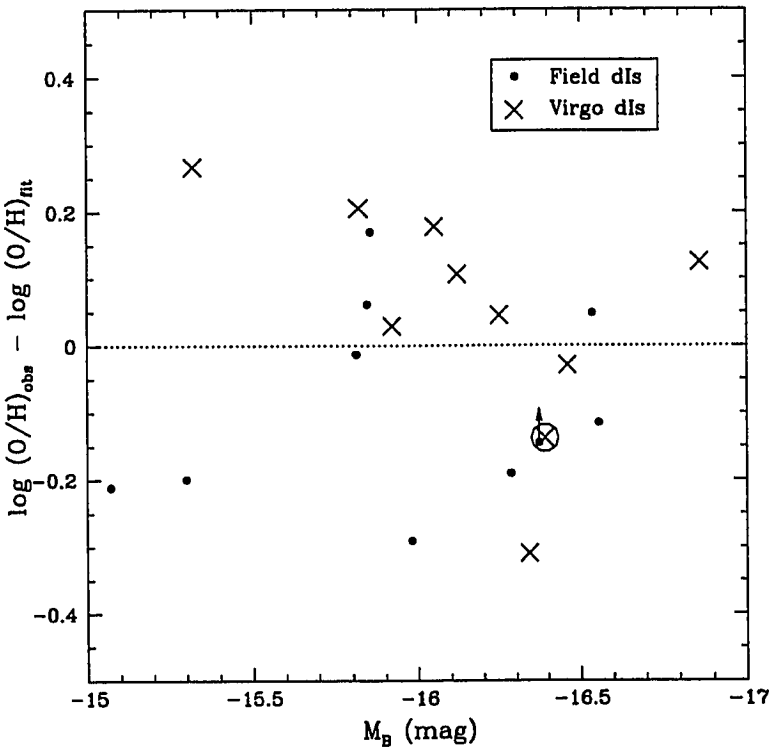

Figure 7.3: Oxygen abundance residuals versus absolute magnitude in B for field and Virgo dIs ($-15 \gtrsim M_B \gtrsim -17$). Filled circles indicate field dIs and crosses indicate Virgo dIs. The large open circle indicates the position of VCC 0848, for which [O III]λ4363 was detected. The horizontal dotted line marks where the observed abundance is equal to the abundance obtained from the fit in Equation (7.56).

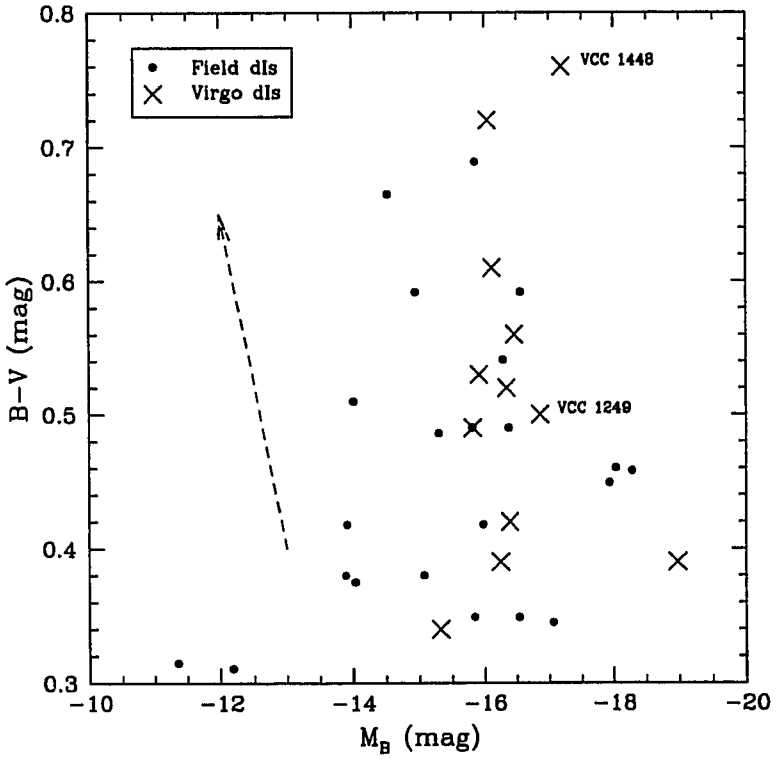

Figure 7.4: $B-V$ colour versus absolute magnitude in B for field and Virgo dIs. Filled circles and crosses indicate field dIs and Virgo dIs, respectively. VCC 1249 (see Chapter 6) and VCC 1448 are labelled, because they are the two most H I–poor dIs in the Virgo sample. A fading vector is indicated by a dashed arrow to show that $B-V$ reddens by about +0.25 mag for each magnitude of fading (McGaugh and Bothun 1994).

should be no systematic error in computing M_*/L_B in the two-component method for M_*.

7.4.4 Effect of Star Formation on (O/H) vs. M_B Relation

A plot of the oxygen abundance versus the absolute magnitude in B of the old component (Table 7.3) is examined to evaluate whether recent star formation has a significant effect on the metallicity–luminosity relationship. This plot is shown in Figure 7.5 for the samples of field and Virgo dIs. Oxygen abundances for Virgo dIs are comparable to those in field dIs at similar luminosities. A fit to the field dIs gives

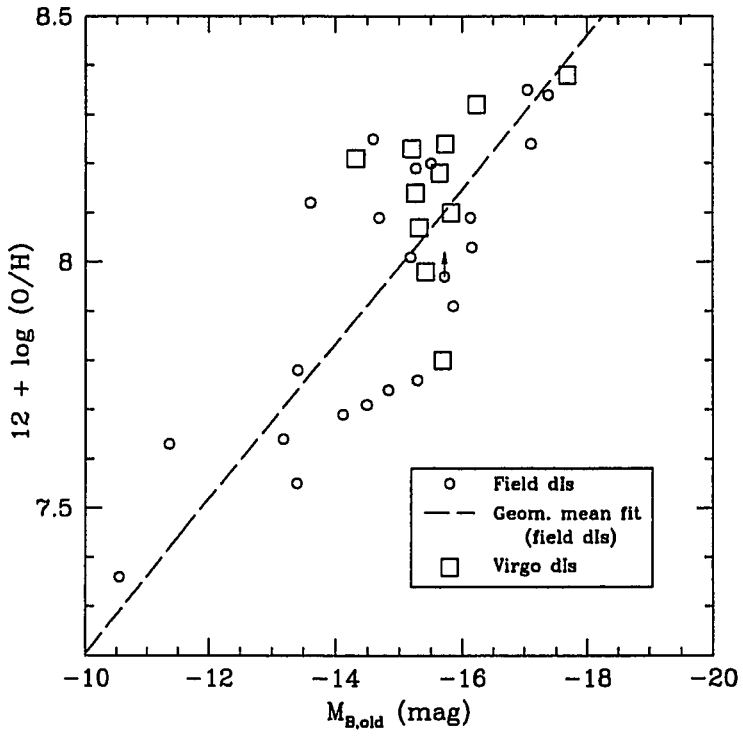

Figure 7.5: Oxygen abundance versus absolute magnitude in B of the old disk component in field and Virgo dIs. Open circles and open squares indicate field dIs and Virgo dIs, respectively. The arrow indicates a lower limit to the oxygen abundance for NGC 1560. The dashed line is a geometric mean fit to the field dIs.

$$12 + \log(\mathrm{O/H}) = (5.64 \pm 0.54) + (-0.157 \pm 0.026) M_{B,\mathrm{old}}. \qquad (7.57)$$

The rms in log(O/H) is $\sigma = 0.178$ dex. Relative to the log(O/H)–M_B relation (Equation 7.55), the fit to the field dIs is slightly shifted to fainter luminosities as expected. The slope is essentially unchanged and the dispersion is not significantly different. Figure 7.6 shows for field dIs alone a plot of the oxygen abundance versus the absolute magnitude of the whole galaxy and the old component. The average value of $-2.5 \log f_{\mathrm{old}}$ is +0.68 mag, which maps into a shift in oxygen abundance of about 0.11 dex, which is similar to the intrinsic uncertainty in oxygen abundances (see Figure 7.2). The fact that the slope of the fit does not change is further evidence of the assertion that recent star–formation activity is proportionally comparable for all field dIs. Indeed, the scatter may reflect a limit to the accuracy in (O/H) or it may reflect the fact that gas must be accommodated to obtain a proper picture of evolution.

Skillman and Bender (1995) point out an important shortcoming of the metallicity–luminosity diagnostic for dIs. If gas is the source from which stars and metals are formed, the metallicity–luminosity relation does not allow for any effects on the gas (e.g., stripping) to be shown, because the gas mass is not explicitly seen as an observable in the diagram. Furthermore, theories of chemical evolution do not show such a diagram to be fundamental. It stands to reason that both gas–normal and gas–poor dwarfs could overlap, as appears to be the case in Figure 7.2. The metallicity–luminosity diagram is by itself insufficient to determine whether the environment has affected the evolution of dIs.

7.4.5 (O/H) vs. M_*

The metallicity–luminosity diagram can be regarded as a "zeroth–order" manifestation of a relationship between metallicity and stellar mass. The actual mass of stars

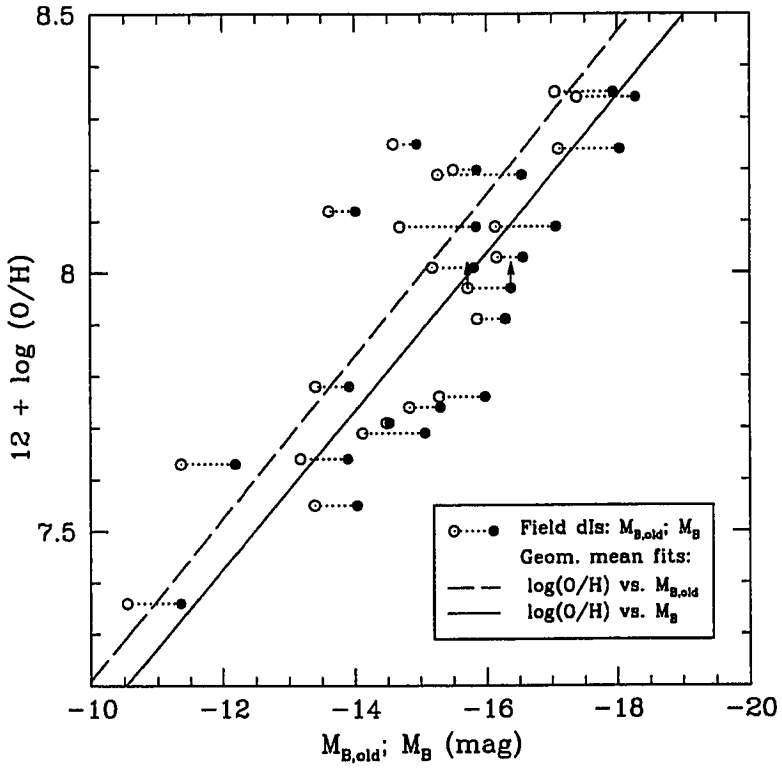

Figure 7.6: Oxygen abundance versus M_B and $M_{B,\mathrm{old}}$ for field dIs. Filled and open circles mark M_B and $M_{B,\mathrm{old}}$, respectively. A dotted line connects the pair of points for each galaxy. Arrows indicate lower limits to the oxygen abundance for NGC 1560. The solid line is a geometric mean fit to log(O/H) versus M_B for field dIs, as expressed by Equation (7.55). The dashed line is a geometric mean fit to log(O/H) versus $M_{B,\mathrm{old}}$ for field dIs, as expressed by Equation (7.57). The lines have similar slopes.

in dIs can be computed using the two–component method, which accommodates separate mass–to–light ratios for the old and young stellar populations. A plot of the oxygen abundance versus stellar mass for field and Virgo dIs is shown in Figure 7.7. Owing to the lack of any trend in $B-V$ with luminosity and the rather small impact

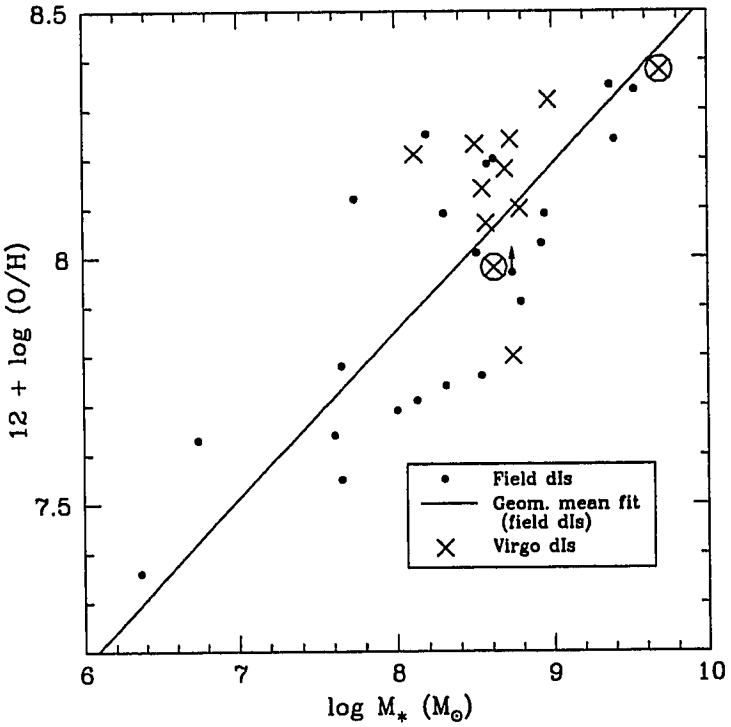

Figure 7.7: Oxygen abundance versus stellar mass (in $M_\odot$) for field and Virgo dIs. The solid dots indicate dIs in the field. The arrow indicates a lower limit to the oxygen abundance for NGC 1560. Crosses indicate Virgo dIs. [O III]λ4363 detections for VCC 0848 and VCC 1554 are marked as crosses enclosed by open circles. The solid line is a geometric mean functional fit to the field dIs.

of star formation on the total light, this diagram mimics the metallicity–luminosity diagram for the old disk component in dIs shown in Figure 7.5. The fit is given by

$$12 + \log(\mathrm{O/H}) = (5.14 \pm 0.60) + (0.339 \pm 0.055)\ \log M_* \qquad (7.58)$$

and is shown as a solid line in Figure 7.7. The rms in log(O/H) is $\sigma = 0.177$ dex.

7.4.6 (O/H) vs. $M_{\rm HI}/L_B$

A plot of metallicity against H I mass–to–light ratio ($M_{\rm HI}/L_B$) can be useful because the latter quantity is distance–independent and composed entirely of untransformed observables, yet conveys information about the gas fraction. Zaritsky et al. (1994) found a weak anti–correlation between oxygen abundance and the H I gas–to–light ratio for their sample of spiral galaxies and the sample of dIs from Skillman et al. (1989).

A plot of oxygen abundance versus $M_{\rm HI}/L_B$ for the samples of field and Virgo dIs is plotted in Figure 7.8. There is a weak inverse correlation between oxygen abundance and $M_{\rm HI}/L_B$ for field dIs. The field dI NGC 1569 exhibits an anomalously low value of $M_{\rm HI}/L_B$, which is likely due to an excess in L_B arising from its "post–starburst" nature (see next section). A number of Virgo dIs appear well separated from field dIs with similar oxygen abundances, which shows that Virgo dIs have evolved differently. This is in marked contrast to previous diagnostics of evolution based purely on stellar light.

7.4.7 $M_{\rm HI}/L_B$ vs. M_B

A plot of the H I mass–to–light ratio against absolute blue magnitude for dIs is shown in Figure 7.9. Although a spectrum was not obtained at CFHT, VCC 1448 is included in the Virgo sample as an example of an extremely H I–poor dwarf, which is clearly evident in the diagram.

For a variety of gas–rich galaxies, Staveley-Smith et al. (1992) obtained a fit of $M_{\rm HI}/L_B \propto L_B^n$, where $n = -0.3 \pm 0.1$. A fit to the field dIs using the geometric mean relationship is shown as a solid line in Figure 7.9. It is given by

$$\log \frac{M_{\rm HI}}{L_B} = (2.90 \pm 1.90) + (0.19 \pm 0.12)\, M_B, \tag{7.59}$$

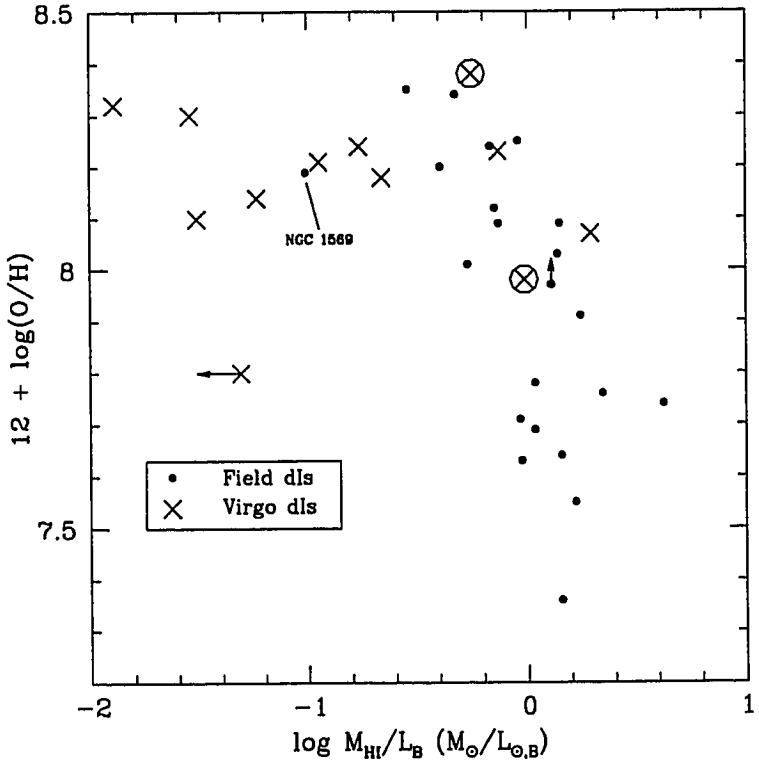

Figure 7.8: Oxygen abundance versus $M_{\rm HI}/L_B$ for field and Virgo dIs. The solid dots show dIs in the field. The arrow indicates a lower limit to the oxygen abundance for NGC 1560. NGC 1569 is labelled owing to its post–starburst nature (see text). Crosses mark Virgo dIs. [O III]λ4363 detections for VCC 0848 and VCC 1554 are marked as crosses enclosed by open circles. An upper limit to the H I mass is marked for VCC 1200.

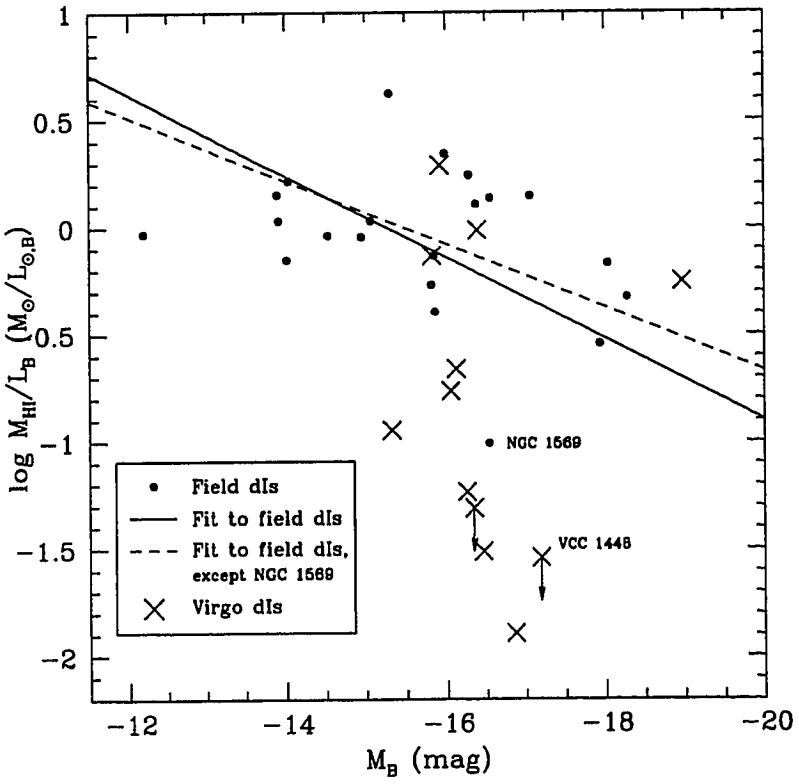

Figure 7.9: $M_{\rm HI}/L_B$ versus absolute magnitude in B for field and Virgo dIs. Solid dots mark dIs in the field. A solid line shows the fit to all field dIs given by Equation (7.59). A revised fit which excludes NGC 1569 is shown as a dashed line and is described by Equation (7.60). Crosses mark Virgo dIs. Although a spectrum was not obtained, VCC 1448 is included, because it is H I-poor. Upper limits to the H I mass are marked for VCC 1200 and VCC 1448.

which gives $n = -0.475 \pm 0.3$, consistent with the result found by Staveley-Smith et al. (1992).

The dispersion in the field dIs is rather large, thanks in part to the field dI NGC 1569, which appears anomalously "gas–deficient." As noted in Chapter 2, NGC 1569 appears to be a dwarf galaxy in a "post–starburst" phase of evolution (e.g., Heckman et al. 1995; Greggio et al. 1998), so the gas deficiency may be an illusion caused by an excess in B luminosity. Excluding NGC 1569, the fit becomes

$$\log \frac{M_{\rm HI}}{L_B} = (2.29 \pm 1.55) + (0.148 \pm 0.098)\, M_B, \tag{7.60}$$

which gives $n = -0.37 \pm 0.24$. This fit is shown as a dashed line in Figure 7.9. Although the quoted errors in the slope and the power–law index are large, this latter result is also consistent with that found by Staveley-Smith et al. (1992). The rms dispersion in $\log M_{\rm HI}/L_B$ is $\sigma = 0.362$ dex.

Figure 7.9 shows that a number of Virgo dIs are noticeably H I gas–deficient compared to field dIs in the range $-17 \lesssim M_B \lesssim -15$. Additional discussion and quantification of the gas deficiency in Virgo dIs is discussed in § 7.5.2.

7.4.8 (O/H) vs. $M_{\rm gas}$

A plot of the oxygen abundance versus gas mass for field and Virgo dIs is shown in Figure 7.10. As described previously in § 7.4.6 and 7.4.7, a number of Virgo dIs contain less gas compared to field dIs at similar abundances. Using the geometric mean functional relationship, a fit to the field dIs gives

$$12 + \log({\rm O/H}) = (4.56 \pm 0.67) + (0.401 \pm 0.065)\, \log M_{\rm gas}. \tag{7.61}$$

This equation is shown as a solid line in Figure 7.10. For field dIs, there is a rough correlation between oxygen abundance and gas mass. However, the rms in the fit is

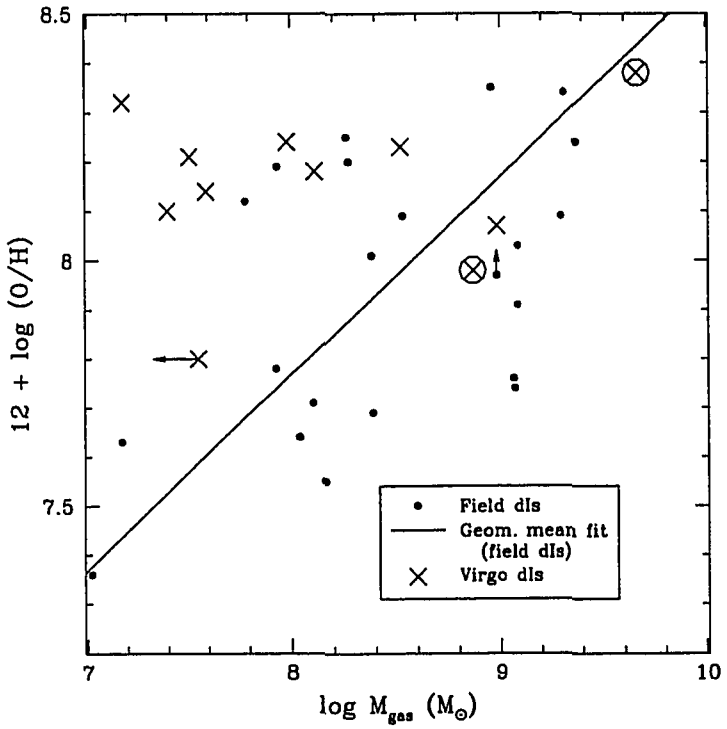

Figure 7.10: Oxygen abundance versus gas mass for field and Virgo dIs. The filled circles indicate dIs in the field. The arrow indicates a lower limit to the oxygen abundance for NGC 1560. The solid line is a geometric mean functional fit to field dIs, as expressed by Equation (7.61). Crosses mark Virgo dIs. [O III]λ4363 detections for VCC 0848 and VCC 1554 are marked as crosses enclosed by open circles. An upper limit to the gas mass is indicated for VCC 1200.

$\sigma = 0.268$ dex, which is larger than the dispersions obtained in the fits for oxygen abundance versus luminosity (§ 7.4.2) and oxygen abundance versus stellar mass (§ 7.4.5). A more fundamental relationship is that between the oxygen abundance and the gas fraction, which is a natural outcome of models of chemical evolution (see § 7.5).

7.4.9 $M_{\rm gas}$ vs. M_*

A plot of the gas mass versus stellar mass for field and Virgo dIs is shown in Figure 7.11. A number of Virgo dIs clearly show severe gas deficiency compared to field dIs at a stellar mass of about $8 \lesssim \log M_* \lesssim 9$. A geometric mean fit to the field dIs gives

$$\log M_{\rm gas} = (1.4 \pm 1.2) + (0.846 \pm 0.094)\ \log M_*, \tag{7.62}$$

which is shown as a solid line in Figure 7.11. From the fit, the rms in $\log M_{\rm gas}$ is computed to be $\sigma = 0.316$ dex. The excellent correlation for field dIs proves there must be a trend in gas mass fraction with stellar mass. The slope in Equation (7.62) is consistent with the value found (0.88) to a fit of gas–rich low surface brightness dwarf galaxies by Schombert et al. (2001). The latter authors suggested that dwarfs are less efficient than large disk systems in converting gas into stars, because the corresponding slope for disk systems is smaller than that for dwarfs. There is larger M_* at a given $M_{\rm gas}$ for giant systems than for dwarf galaxies.

7.4.10 (O/H) vs. $M_{\rm bary}$

The metallicity–luminosity relationship described in § 7.4.2 may be a manifestation of a relationship between metallicity and total mass. For a variety of gas–rich dwarf galaxies, the metallicity is found to increase with total dynamical mass (Lequeux et al. 1979; Talent 1980; Kinman and Davidson 1981; Matteucci and Chiosi 1983;

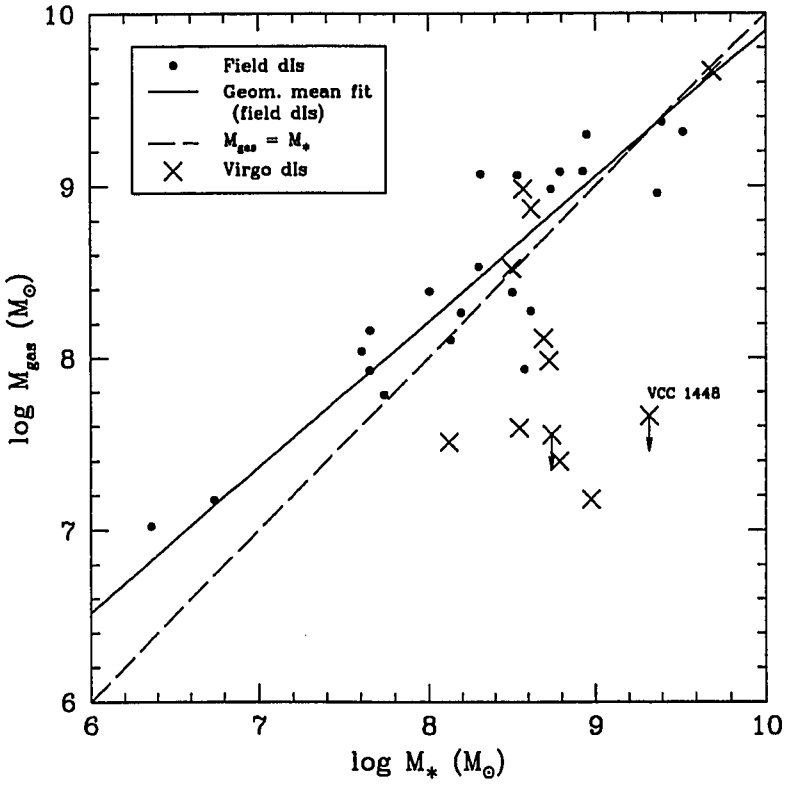

Figure 7.11: Gas mass versus stellar mass for field and Virgo dIs. The filled circles indicate dIs in the field. The solid line is a geometric mean functional fit to field dIs, as expressed by Equation (7.62). The dashed line marks gas masses equal to stellar masses. Crosses indicate Virgo dIs. Although a spectrum was not obtained, VCC 1448 is included, because it is gas–poor. Upper limits to the gas mass are marked for VCC 1200 and VCC 1448.

Pagel 1986; Skillman et al. 1988). However, dynamical masses are notoriously difficult to measure in dIs, because random or turbulent motions can dominate over ordered or rotational motions (Lo et al. 1993). Moreover, there are disagreements about the manner in which the dynamical mass should be computed.

The most fundamental definition of total mass from the standpoint of chemical evolution is the sum of the mass in gas and stars, i.e., the baryonic mass. A plot of oxygen abundance against total baryonic mass for field and Virgo dIs is shown in Figure 7.12. With the baryonic mass as the abscissa, this diagram resembles the

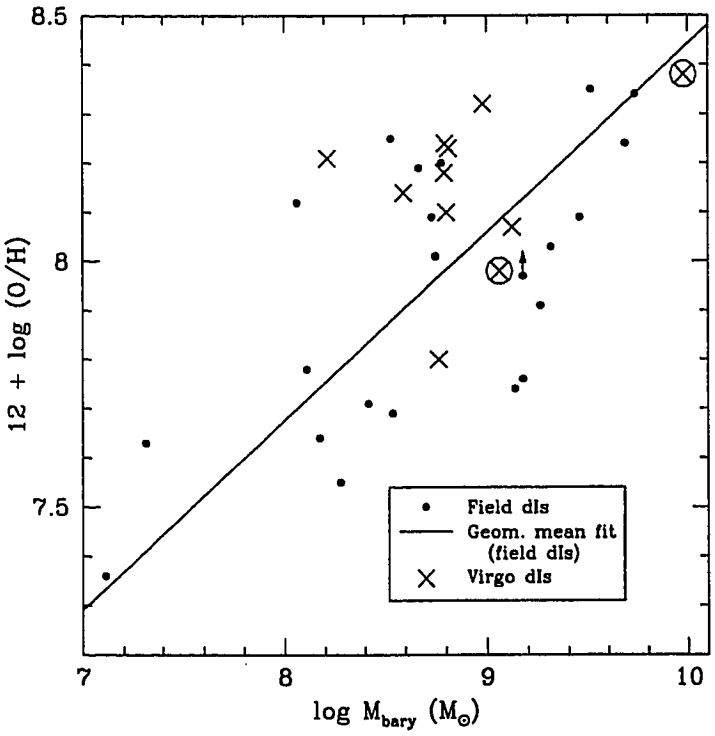

Figure 7.12: Oxygen abundance versus total baryonic mass for field and Virgo dIs. The filled circles mark dIs in the field. An arrow indicates a lower limit to the oxygen abundance for NGC 1560. Crosses mark Virgo dIs. [O III]λ4363 detections for VCC 0848 and VCC 1554 are marked as crosses enclosed by open circles. The solid line is a geometric mean fit to the field dIs.

metallicity–luminosity diagram (Figure 7.2), although the scatter is noticeably worse.

A fit to field dIs is

$$12 + \log(\mathrm{O/H}) = (4.61 \pm 0.85) + (0.384 \pm 0.086) \log M_{\mathrm{bary}}, \qquad (7.63)$$

which is shown as a solid line in Figure 7.12. From the fit, the rms is $\sigma = 0.223$ dex, which is larger than the rms for the correlation with stellar mass, but smaller than the rms for the correlation with gas mass.

A plot of linear oxygen abundance against the logarithm of total baryonic mass for field and Virgo dIs is plotted in Figure 7.13. A fit to the field dIs using the geometric

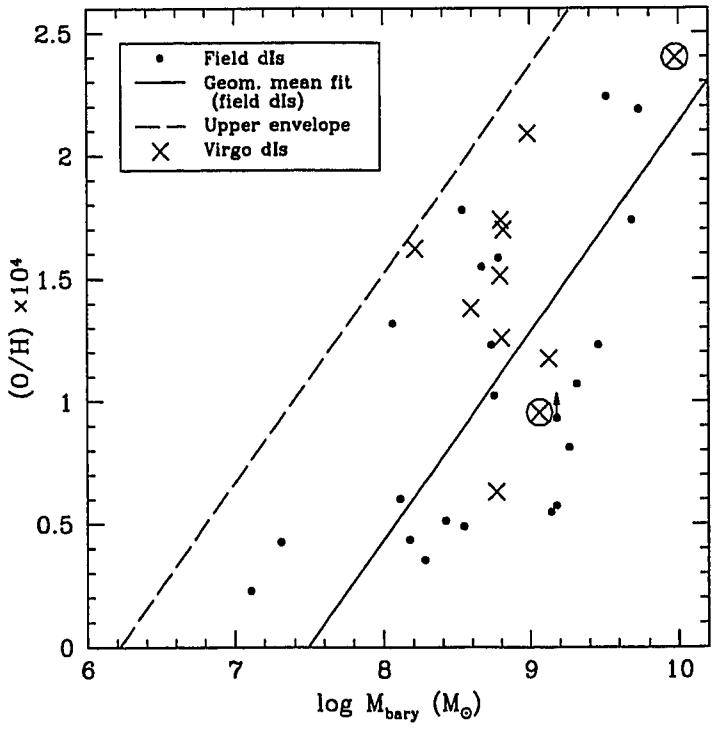

Figure 7.13: Linear oxygen abundance versus the logarithm of total baryonic mass for field and Virgo dIs. Filled circles mark dIs in the field. The arrow indicates a lower limit to the oxygen abundance for NGC 1560. Crosses mark Virgo dIs. [O III]λ4363 detections for VCC 0848 and VCC 1554 are marked as crosses enclosed by open circles. The solid line is a geometric mean fit to the field dIs. The dashed line describes the best–fit line shifted upwards to form an upper envelope to the locus defined by field dIs.

mean functional relationship gives

$$(\mathrm{O/H}) \times 10^4 = (-6.4 \pm 2.3) + (0.85 \pm 0.25)\ \log M_{\mathrm{bary}}. \qquad (7.64)$$

This is shown as a solid line in Figure 7.13. From the fit, the rms in linear (O/H) is $\sigma = 0.542 \times 10^{-4}$. The dashed line describes the best–fit line shifted upwards to form an "upper envelope" to the locus of points for field dIs. Extrapolating to zero oxygen abundance, Equation 7.64 can be solved for the minimum baryonic mass required to form metals: $\log M_{\mathrm{bary}} = 7.49$ is obtained from the best–fit line, and $\log M_{\mathrm{bary}} = 6.22$ is obtained from the "upper envelope." These masses are roughly similar to the total luminous mass in stars and gas found in low–luminosity dEs/dSphs in the Local Group (Mateo 1998). The results suggest that there are no galaxies with a stellar component which are less massive than $1.7 \times 10^6\ M_\odot$.

7.5 Chemical Abundances and Gas Fractions

Because there is little evidence for metallicity gradients within dIs (e.g., Kobulnicky and Skillman 1996, 1997), theoretical analysis of the chemical evolution of dIs is relatively straight forward. As Figures 7.8 to 7.11 have shown, a diagram which relates the abundance of metals formed within a pool of gas to some measure of the proportion of mass which is gaseous should be a good diagnostic of evolution. This observational conclusion is in fact verified by models of evolution.

A brief description of the simplest model of chemical evolution, the "closed box" model, is presented in § 7.5.1. A quantitative measure of gas–deficiency in dIs based upon the closed box model is introduced in § 7.5.2. The effect of assuming a constant value of M_*/L_B on the validity of the closed box model is evaluated in § 7.5.3. Abundances of nitrogen relative to oxygen are presented in § 7.5.4.

7.5.1 The "Closed Box" Model of Chemical Evolution

The "closed box" model (Searle and Sargent 1972; Pagel and Patchett 1975; Audouze and Tinsley 1976; Tinsley 1980; Pagel and Edmunds 1981; Edmunds 1990; Burkert 1993; Pagel 1997; Skillman 1998) serves as a useful guide to understanding the chemical evolution of galaxies. The model is constructed as follows. At the start, a galaxy is in gaseous form, from which stars form. Some stars die, polluting the interstellar medium with newly formed metals. Subsequent generations of stars form out of the enriched gas. Over time, the pool of stars and metals increases, as the pool of gas decreases.

There are several key assumptions in the closed box model:

1. Initially, a galaxy consists only of gas and no stars or metals.
2. The galaxy evolves as a closed system with no mass inflow or outflow.
3. There are two kinds of stars: stars that die immediately, and stars that live "forever." This is also known as the instantaneous recycling approximation (Searle and Sargent 1972).
4. The mixing of metals within the pool of gas is immediate.
5. The stellar initial mass function (IMF) does not change with time.

A variety of modifications can be made to the rate equations (see Edmunds 1990 and references therein) to account for inflow and outflow.

Rate equations lead to the following relation between the fraction of the gas mass in the form of a primary product of nucleosynthesis, Z (i.e., the metal abundance), and the fraction of baryonic mass in gaseous form, μ (the gas fraction):

$$Z = y \ln(1/\mu). \tag{7.65}$$

The constant y is called the yield.

A "primary" element is one formed directly from hydrogen, i.e., one which does not require pre–existing metals to be synthesized. Thus, the production of a primary element does not depend upon the initial composition of the star in which the element is synthesized. A "secondary" element is synthesized from a primary element such as carbon or oxygen, which is already present in the star as a "seed." The yield, y, is the ratio of the mass of newly formed metals to the mass of gas permanently locked into stars. The yield is constant in the model because the IMF is invariant. The assumptions above require that, at time $t = 0$, $Z = Z_0 = 0$, $M_* = M_{*,0} = 0$, and $\mu = \mu_0 = 1$. Note that there is no explicit dependence of the metal abundance on time.

Oxygen is considered a "primary" element of nucleosynthesis, which is produced mainly in massive stars and is returned to the interstellar medium when these short–lived stars explode as Type II supernovae (see Woosley and Weaver 1986; Burrows 2000; van den Bergh 2000). Oxygen is the third most abundant element in the solar neighbourhood (12+log(O/H) = 8.87; Grevesse et al. 1996), contributing approximately 45% to the total metal abundance (Peimbert and Serrano 1982). Thus, its yield by mass, y_O, is $0.45Z_\odot$, where $Z_\odot$ is the total metals abundance for the Sun. Since $Z_\odot \simeq 0.02$ (Grevesse et al. 1996), y_O is 9×10^{-3} in the solar neighbourhood.

The metal abundance is best expressed as an elemental abundance in logarithmic form. For oxygen, then,

$$\log Z_O = \log y_O + \log \ln(1/\mu), \tag{7.66}$$

where Z_O is the fraction of the gas mass in the form of oxygen. Thus, the oxygen abundance by number is given by

$$\begin{aligned} 12 + \log[n(\mathrm{O})/n(\mathrm{H})] &= 12 + \log(\mathrm{O/H}) \\ &= 12 + \log(2.303\, y_O/11.728) + \log\log(1/\mu). \end{aligned} \tag{7.67}$$

The factor 2.303 comes from the conversion from a natural logarithm to a logarithm of base ten. The factor 11.728 comes from the conversion from an oxygen abundance by mass to an oxygen abundance by number, assuming that the fraction of gas in the form of hydrogen is $X = 0.733$ (solar value). The closed box model predicts a slope of unity in a plot of oxygen abundance, 12+log(O/H), against inverse gas mass fraction, as conveyed by log log$(1/\mu)$. The oxygen yield, y_O, can be derived from the intercept.

To study chemical evolution, Lequeux et al. (1979), Matteucci and Chiosi (1983), and Pagel (1986) plotted oxygen abundances against gas fractions for gas–rich dwarf galaxies. Unfortunately, these diagrams were plagued by large dispersion, owing to the use of dynamics to judge baryonic masses. In fact, dynamics may be controlled by dark matter, which does not participate in nucleosynthesis. Also, samples included a mix of dIs and BCDs which appear to have had different evolutionary histories. In order to bring some clarity to the subject, the focus here has exclusively been upon dIs, and only those with excellent distance determinations and abundance measurements. Also, care has been taken to use the total mass in the form of baryons to gauge gas fractions.

A plot of oxygen abundance against inverse gas mass fraction for field and Virgo dIs is shown in Figure 7.14. An excellent correlation is seen for the field dIs. Using the geometrical mean function relationship, a fit to all field dIs gives

$$12 + \log(\mathrm{O/H}) = (8.63 \pm 0.40) + (1.02 \pm 0.21) \log \log(1/\mu). \qquad (7.68)$$

The rms in log(O/H) is $\sigma = 0.183$ dex.

IC 1613 appears to have an anomalously small gas mass fraction (log log $(1/\mu)$ $\simeq -0.5$) and/or a small abundance (12+log(O/H) $\simeq 7.7$). The H I mass is unlikely to be problematic, because the most recent 21–cm flux measurement obtained by

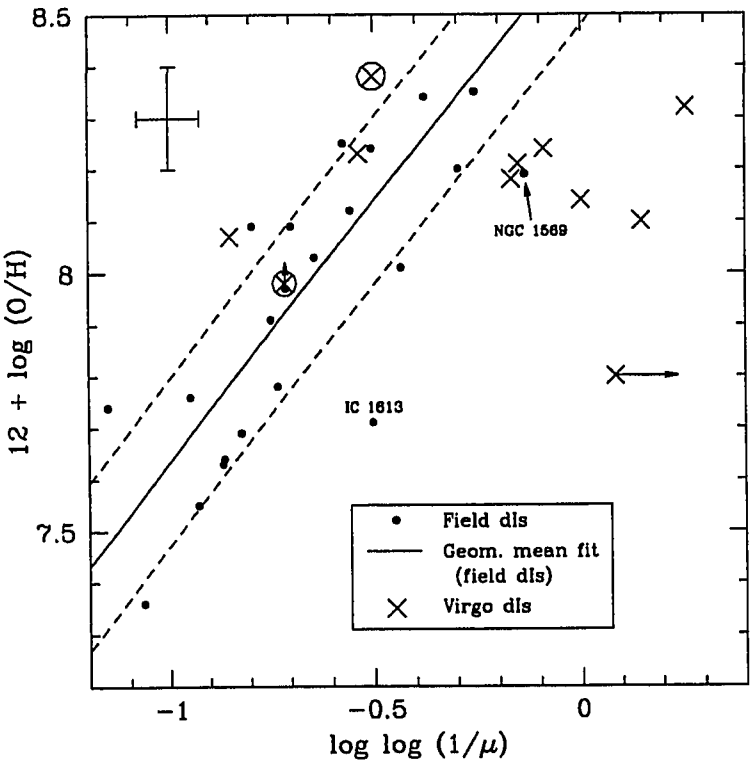

Figure 7.14: Oxygen abundance versus gas mass fraction for field and Virgo dIs. The abundance increases upwards and gas mass fraction decreases to the right. The filled circles indicate dIs in the field. The discrepant point representing the dwarf IC 1613 is labelled; it was excluded from the fit (see text). NGC 1569 is also labelled (see discussion in § 7.4.7). The upward arrow indicates a lower limit to the oxygen abundance for NGC 1560. The solid line is a geometric mean fit to the field dIs and is given by Equation (7.69). The fit is consistent with the closed box model. The dashed lines represent 1σ deviations above and below the fit. Crosses mark Virgo dIs. [O III]λ4363 detections for VCC 0848 and VCC 1554 are marked as crosses enclosed by open circles. The error bars at the upper left indicates typical uncertainties of 0.1 dex in oxygen abundance and 0.1 dex in log log $(1/\mu)$. The latter uncertainty is derived from an estimated 0.05 mag uncertainty in $B-V$, which affects the derivation of M_*, and an estimated 20% uncertainty in H I gas mass (Huchtmeier and Richter 1986 and Hoffman et al. 1987 for field and Virgo dIs, respectively).

Hoffman et al. (1996) has been employed (see § 2.1). The measurement of the oxygen abundance may be a problem though, because the most recent spectroscopic observations are over two decades old (Talent 1980). Another problem may be the reported $B-V$ colour, especially given its low Galactic latitude. If it is too red for its luminosity, there would be an overestimate of the mass of the underlying old stellar population in the dI, and in turn an underestimate of the gas fraction.

Excluding IC 1613, the fit is

$$12 + \log(\mathrm{O/H}) = (8.64 \pm 0.40) + (1.01 \pm 0.17)\ \log\log(1/\mu) \qquad (7.69)$$

and the rms is reduced to 0.162 dex. Equation (7.69) is taken as the "best fit" and is shown as a solid line in Figure 7.14. The dashed lines represent 1σ deviations above and below the fit. The fitted slope is consistent with the prediction of the closed box model (Equation 7.67). The key conclusion here is that the chemical evolution of field dIs has been *isolated.*

Comparing the intercept in Equation (7.69) with Equation (7.67), the effective oxygen yield by mass, y_O, is

$$y_O = 2.22 \times 10^{-3}. \qquad (7.70)$$

This result is consistent with that obtained from a fit to a mix of gas–rich dwarf galaxies compiled by Pagel (1986), but is one–quarter of the value for the solar neighbourhood. The oxygen yield by number is thus 1.90×10^{-4}.

7.5.2 Gas–Deficiency Index (GDI) for dIs

In Figure 7.14, a number of Virgo dIs appear in the same region as the field dIs, whereas others are noticeably gas–deficient for their oxygen abundance. In fact, Figure 7.14 reveals that it is possible to construct an index which quantifies the gas deficiency of a dI.

To compare "gas–deficient" dIs with isolated dIs, a gas–deficiency index (GDI) is defined by

$$\mathrm{GDI} \equiv \log\left[\frac{(M_{\mathrm{gas}}/M_*)_p}{(M_{\mathrm{gas}}/M_*)}\right], \tag{7.71}$$

where the subscript "p" refers to the prediction for an isolated dwarf. The gas mass to stellar mass ratio, M_{gas}/M_*, can be written as

$$\frac{M_{\mathrm{gas}}}{M_*} = \frac{\mu}{1-\mu}, \tag{7.72}$$

where μ is the gas fraction. Thus,

$$\mathrm{GDI} = \log\left(\frac{\mu_p}{\mu}\cdot\frac{1-\mu}{1-\mu_p}\right). \tag{7.73}$$

Here, μ is the observed gas fraction, and μ_p is the gas fraction predicted from the measured oxygen abundance using the closed box model (Equation 7.69). Deficiency increases with increasingly positive GDI.

Haynes and Giovanelli (1984) and Giovanelli and Haynes (1985) defined a deficiency parameter, DEF, for disk galaxies, which compares the observed H I mass of a galaxy, $M_{\mathrm{HI}}^{\mathrm{obs}}$, with the value expected for an isolated galaxy of the same morphological type, T^{obs}, and optical linear diameter $D_{\mathrm{opt}}^{\mathrm{obs}}$. Isolation was defined on the basis of association with other galaxies (Karachentseva 1973). A galaxy of angular diameter d had to lie at a projected distance of at least $20d$ from any other galaxy to be considered isolated[2]. Their deficiency parameter is written as

$$\mathrm{DEF} = \langle \log M_{\mathrm{HI}}(T^{\mathrm{obs}}, D_{\mathrm{opt}}^{\mathrm{obs}})\rangle - \log M_{\mathrm{HI}}^{\mathrm{obs}}. \tag{7.74}$$

A number of workers have computed DEF for very late–type spirals and irregulars using the relationship inferred from Sc spirals, because "normal" H I content is well–defined only for spirals of type Sa to Sc (see, e.g., Solanes et al. 2001). However, to

[2]This presumes gas flows stem only from interactions with other galaxies.

determine and quantify evolutionary effects, gas–poor dIs should be compared with gas–normal dIs.

The GDI defined above has the following advantages:

1. it is founded exclusively upon the properties of gas–rich dwarf galaxies and there is no mixing of morphological types (e.g., Sc's with Sd's or with dIs);
2. isolation is quantitatively defined via the closed box model;
3. the index is independent of absolutes, such as size; and
4. the index is distance–independent.

Table 7.7 lists GDIs for field and Virgo dIs. Histograms for the field and Virgo samples are shown in Figure 7.15. Although the total number of dwarfs in each bin is small, the field dwarfs are mostly clustered around GDI ≈ 0, whereas there are several Virgo dwarfs which are clearly gas–poor (GDI $\gtrsim 0.8$). A Kolmogorov–Smirnov test on the two distributions of GDI returned the statistic $D = 0.576$ with a significance level $P = 6.3 \times 10^{-3}$ ($N = 22$ field dIs; $N = 12$ Virgo dIs). Thus, the two data sets are significantly different and are not drawn from the same population. Simple test models of chemical evolution are presented below to show that the mechanism responsible for the observed gas deficiency has acted relatively recently. Henceforth, a gas–poor dI is defined as one for which GDI $\gtrsim 0.8$.

7.5.3 Sensitivity of μ to M_*/L_B, $(M_*/L_B)_{\rm old}$, and $(B-V)_{\rm old}$

Values of μ depend on M_*, which in turn comes from the two–component algorithm of population synthesis. It is worthwhile to examine the ingredients of the algorithm to determine the robustness of the conclusion that field dIs have evolved as closed systems. Four models are considered. In each case, M_* and μ are computed, a best

dI Name	12+log(O/H) (dex)	Measured μ	Predicted μ	GDI
(1)	(2)	(3)	(4)	(5)
Field dIs				
DDO 187	7.69	0.706	0.770	+0.143
GR 8	7.63	0.731	0.796	+0.156
Holmberg II	7.76	0.771	0.735	−0.083
IC 10	8.20	0.312	0.431	+0.224
IC 1613[a]	7.71	0.484	0.760	+0.529
IC 2574	8.09	0.690	0.520	−0.313
IC 4662	8.09	0.630	0.520	−0.196
Leo A	7.36	0.820	0.884	+0.223
LMC	8.35	0.279	0.306	+0.055
NGC 1560	> 7.97	0.638	0.608	−0.055
NGC 1569[b]	8.19	0.185	0.440	+0.537
NGC 2366	7.91	0.662	0.648	−0.027
NGC 3109	7.74	0.851	0.746	−0.290
NGC 4214	8.24	0.485	0.398	−0.154
NGC 5408	8.01	0.429	0.580	+0.265
NGC 55	8.34	0.380	0.314	−0.127
NGC 6822	8.25	0.540	0.390	−0.264
Sextans A	7.55	0.762	0.827	+0.173
Sextans B	8.12	0.526	0.496	−0.051
SMC	8.03	0.590	0.566	−0.044
UGC 6456	7.64	0.730	0.792	+0.148
WLM	7.78	0.652	0.725	+0.149
Virgo dIs				
VCC 0512	8.23	0.511	0.406	−0.183
VCC 0848	7.98	0.639	0.601	−0.071
VCC 0888	8.18	0.209	0.448	+0.487
VCC 1114	8.10	0.039	0.512	+1.409
VCC 1179	8.14	0.100	0.480	+0.922
VCC 1200	7.80	0.061	0.712	+1.585
VCC 1249	8.32	0.016	0.331	+1.491
VCC 1448	8.30[c]	0.021	0.347	+1.386
VCC 1554	8.38	0.483	0.281	−0.379
VCC 1585	8.07	0.721	0.535	−0.351
VCC 1789	8.24	0.154	0.398	+0.562
VCC 2037	8.21	0.197	0.423	+0.476

Table 7.7: Gas-deficiency indices (GDIs) for field and Virgo dIs. Column (1) lists the name of the dI, column (2) lists the measured oxygen abundance, column (3) lists the measured gas mass fraction, column (4) lists the predicted gas mass fraction from Equation (7.69), and column (5) lists the gas deficiency index derived using Equation (7.73). NOTES: [a] IC 1613 : Oxygen abundance or M_* may be anomalous. [b] NGC 1569 : Post–starburst dwarf galaxy (e.g., Heckman et al. 1995; Greggio et al. 1998). [c] VCC 1448 : A spectrum was not obtained for this dI. An estimate for its "observed" oxygen abundance is obtained using the value of M_* listed in Table 7.2 and the fit described by Equation (7.58).

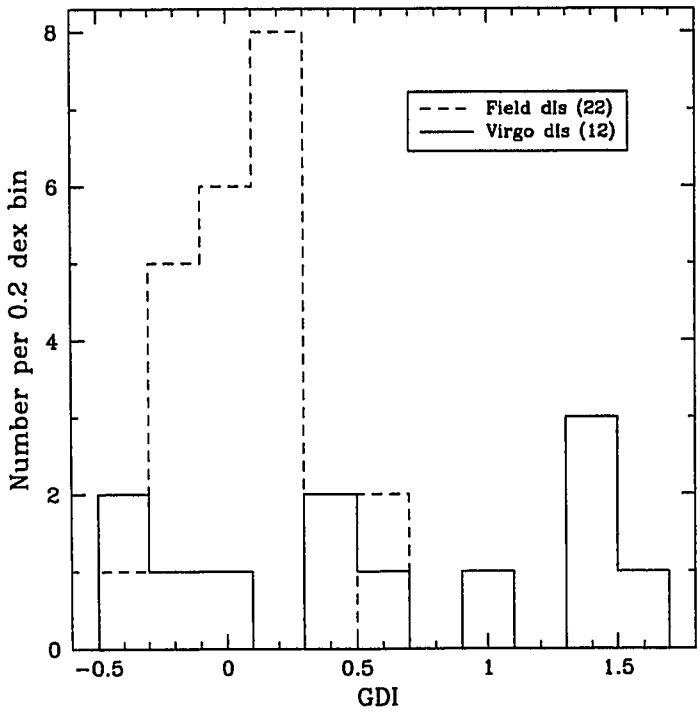

Figure 7.15: Histograms of the gas deficiency index (GDI) for field and Virgo dIs. Bins are 0.2 dex wide. Gas deficiency increases to the right. The histogram for the 22 dIs in the field sample is indicated with a dashed line. The histogram for the 12 dIs in the Virgo Cluster sample is indicated with a solid line. Most of the field dIs are clustered around GDI ≈ 0; seven Virgo dIs have similar GDIs to the field dwarfs, whereas five (including VCC 1448) have GDI $\gtrsim 0.8$.

fit to log(O/H) vs. log log $(1/\mu)$ is performed using the geometric mean functional relationship (Draper and Smith 1998), and the rms in oxygen abundance is obtained.

In applying the two–component algorithm, the mass–to–light ratio of the old component is taken to vary as a power law with the luminosity of that component (Equation 7.48); the exponent is 0.175 (see § 7.3.8). In the first model, the mass–to–light ratio for old stars is instead fixed at 3.11, which is the zero–point value in Equation (7.15) stemming from the properties of the Milky Way disk. In the second model, the mass–to–light ratio for old stars is fixed at 1.50, which is the mean over all field dIs. For the third model, the mass–to–light ratio of the old component varies with the luminosity as a power law with exponent 0.175, but the $B-V$ colour for the old component is fixed at 0.74, which is the mean over all field dIs. In the fourth model, the mass–to–light ratio of all stars is fixed at unity, which is motivated by the models of Bruzual and Charlot (1996) and the absence of any trend in $B-V$ with luminosity.

Table 7.8 lists the effects of adopting constant $(M_*/L_B)_{\rm old}$, $(B-V)_{\rm old}$, and M_*/L_B on the relationship described by Equation (7.67). The data point corresponding to IC 1613 is excluded from all models. All fits have slopes consistent with unity. The smallest dispersion in the relationship between oxygen abundance and gas fraction is obtained when the mass–to–light ratio in the old disk component has a power–law dependence on the luminosity of the old disk (Equation 7.48), as employed in the two–component algorithm. The conclusion that field dIs have evolved as isolated systems does not depend critically upon the details of the population synthesis.

7.5.4 N/O Measurements: Field and Virgo dIs

After oxygen, nitrogen is the next most abundant chemical element. Based upon observations of H II regions in spiral and dwarf galaxies, nitrogen appears to be both

Model (1)	Note (2)	Geometric Mean Fit (3)	σ (dex) (4)
$(M_*/L_B)_{\rm old} = 3.11$	[a]	$\mathcal{Y} = (8.55 \pm 0.43) + (1.38 \pm 0.41)\mathcal{X}$	0.250
$(M_*/L_B)_{\rm old} = 1.50$	[b]	$\mathcal{Y} = (8.71 \pm 0.45) + (1.19 \pm 0.38)\mathcal{X}$	0.248
$(B-V)_{\rm old} = 0.74$	[c]	$\mathcal{Y} = (8.56 \pm 0.40) + (0.92 \pm 0.14)\mathcal{X}$	0.167
$(M_*/L_B) = 1$	[d]	$\mathcal{Y} = (8.65 \pm 0.44) + (1.16 \pm 0.32)\mathcal{X}$	0.244
$(M_*/L_B)_{\rm old} \propto (L_{B,{\rm old}})^{0.175}$	[e]	$\mathcal{Y} = (8.64 \pm 0.40) + (1.01 \pm 0.17)\mathcal{X}$	0.162

Table 7.8: Effects of constant M_*/L_B, $(M_*/L_B)_{\rm old}$, and $(B-V)_{\rm old}$ on the fit to log(O/H) vs. log log$(1/\mu)$. Column (1) lists the model, column (2) provides the label for the corresponding explanatory note below, and column (3) lists the fit obtained from the geometric mean functional relationship (Draper and Smith 1998) for the model in column (1), where $\mathcal{Y}$ represents the oxygen abundance, 12+log(O/H), and $\mathcal{X}$ represents log log$(1/\mu)$. Column (4) lists the rms in oxygen abundance for field dIs. NOTES: [a]. For the old disk component, the mass–to–light ratio is fixed at 3.11, which is the zero–point value obtained from the Milky Way disk (Equation 7.47). [b]. For the old disk component, the mass–to–light ratio is fixed at 1.50, which is a mean over all field dIs. [c]. For the old disk component, the $B-V$ colour is fixed at 0.74, which is a mean over all field dIs. [d]. The mass–to–light ratio for all stars is fixed at unity. [e]. This is the premise behind Equation (7.69), additional to $(B-V)_{\rm old}$ dependent upon luminosity and surface brightness (Equation 7.11).

a primary and secondary product of nucleosynthesis. It remains uncertain, however, whether nitrogen is produced mostly from short–lived massive stars or from longer–lived intermediate–mass stars.

The closed–box model (§ 7.5.1) makes the following predictions for the primary and secondary abundances of nitrogen (Edmunds and Pagel 1978; Pagel 1997). If nitrogen is of "primary" origin, the model predicts that the nitrogen abundance varies with the gas fraction in the same way as oxygen. In other words, the nitrogen–to–oxygen abundance ratio, N/O, should be a constant, K, i.e.,

$$\log({\rm N/O}) \simeq K. \tag{7.75}$$

If nitrogen is of "secondary" origin, the model predicts that the nitrogen abundance should increase with the square of the oxygen abundance. Thus,

$$\log({\rm N/O}) \propto \log({\rm O/H}). \tag{7.76}$$

Measurements of the nitrogen–to–oxygen ratio have been used to differentiate

between the different origins for nitrogen (see e.g., (Garnett 1990)). It has been suggested that the N/O can be used as a "clock" to measure the time since the last burst of star formation (e.g., Edmunds and Pagel 1978; Garnett 1990; Skillman et al. 1997; Henry et al. 2000). This would work if bursts of star formation were separated by long quiescent periods and if the delivery of nitrogen into the interstellar gas were delayed relative to oxygen.

In Figure 7.16, a plot of log(N/O) versus log(O/H) is shown for H II regions in the sample of field dIs for which there are published data and in the sample of Virgo dIs. The two sets of galaxies overlap, although some H II regions in Virgo dIs appear to have somewhat elevated values of log(N/O) for their oxygen abundances.

A larger set of data for H II regions in a mixture of other dIs and BCDs (Garnett 1990; Kobulnicky and Skillman 1996; van Zee et al. 1997; Izotov and Thuan 1999) is shown in Figure 7.17. Although the data are rather heterogeneous, they illustrate that the range of log(N/O) values for the field and Virgo samples is not anomalous.

Figures 7.16 and 7.17 show that nitrogen in metal–poor dwarf galaxies is likely of primary origin. The considerable scatter in N/O at a given O/H may be explained by the time delay between the release of oxygen by massive stars and nitrogen by intermediate–mass stars (Garnett 1990; Skillman et al. 1997; van Zee et al. 1998; Henry et al. 2000). It is unlikely that gas flows have a bearing on the scatter, as Henry et al. (2000) suggest, because Figure 7.14 and Equation (7.69) have shown that field dIs are closed systems.

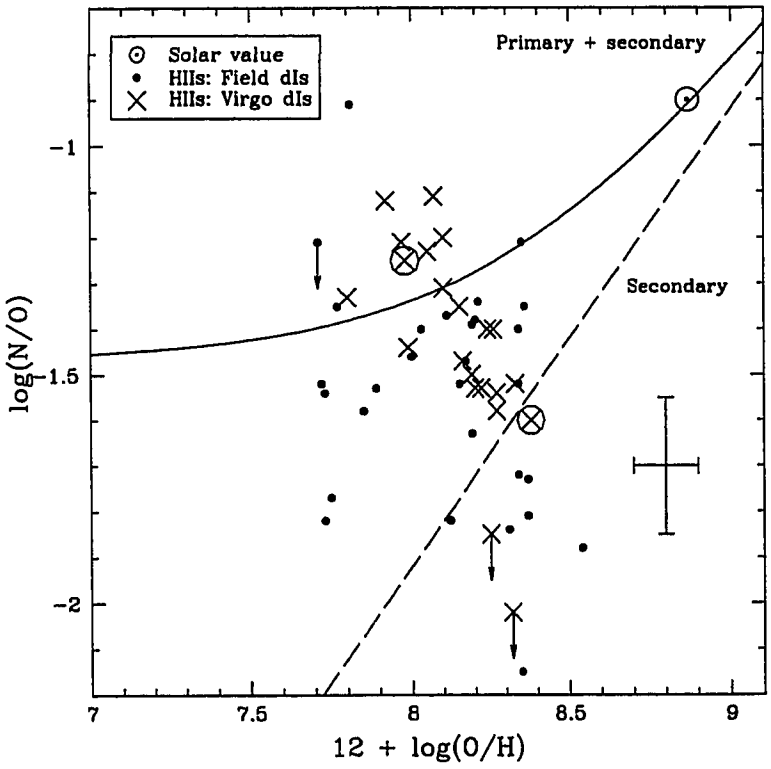

Figure 7.16: Nitrogen–to–oxygen ratio versus oxygen abundance for H II regions in field and Virgo dIs. Filled circles indicate H II regions in the sample of field dIs. An upper limit to log(N/O) is shown for IC 1613 (Talent 1980). Crosses indicate H II regions in Virgo dIs. [O III]λ4363 detections for H II regions VCC 0848–1 and VCC 1554–1 are marked as crosses enclosed by open circles. Upper limits to log(N/O) are shown for H II regions VCC 0512–3 and VCC 1249–1, owing to the low signal–to–noise ratios for [N II]λ6583. Two models for the production of nitrogen are shown (Vila-Costas and Edmunds 1993): primary (Equation 7.75) plus secondary (Equation 7.76) production of nitrogen is indicated with a solid line, whereas a purely secondary origin for nitrogen is indicated with a dashed line. The solar value (Grevesse et al. 1996) is indicated with the "$\odot$" symbol. Typical errors in log(O/H) and log(N/O) are shown.

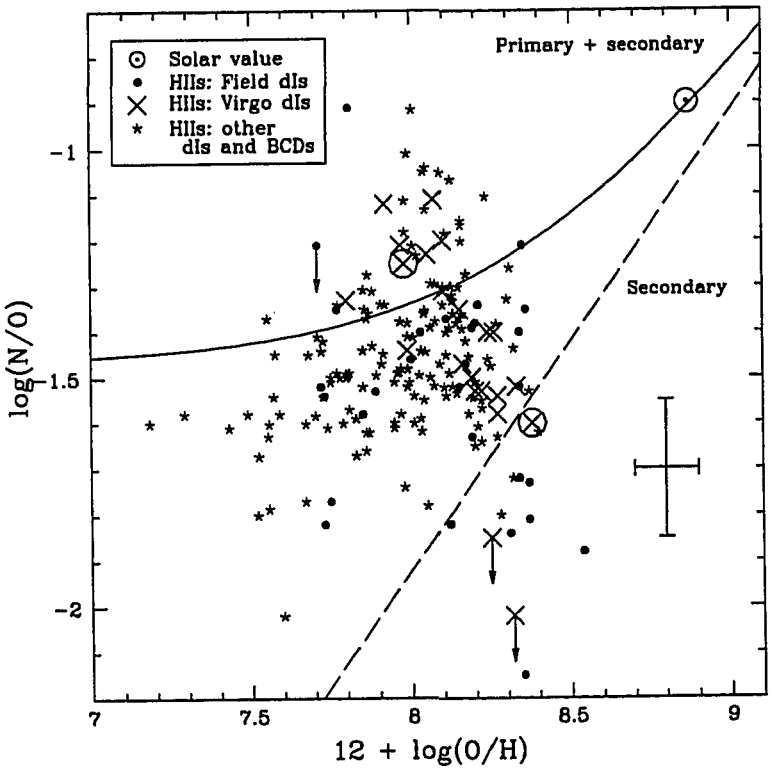

Figure 7.17: Nitrogen–to–oxygen ratio versus oxygen abundance for star–forming dwarf galaxies. Filled circles indicate H II regions in the sample of field dIs. An upper limit to log(N/O) is shown for IC 1613 (Talent 1980). Crosses indicate H II regions in Virgo dIs. [O III]λ4363 detections for H II regions VCC 0848–1 and VCC 1554–1 are marked as crosses enclosed by open circles. Upper limits to log(N/O) are shown for H II regions VCC 0512–3 and VCC 1249–1, owing to the low signal–to–noise ratios for [N II]λ6583. Stars show published data for H II regions in a variety of other dwarf galaxies, including BCDs (Garnett 1990; Kobulnicky and Skillman 1996; van Zee et al. 1997; Izotov and Thuan 1999). Two models for the production of nitrogen are shown (Vila-Costas and Edmunds 1993): primary (Equation 7.75) plus secondary (Equation 7.76) production of nitrogen is indicated with a solid line, whereas a purely secondary origin for nitrogen is indicated with a dashed line. The solar value (Grevesse et al. 1996) is indicated with the "$\odot$" symbol. Typical errors in log(O/H) and log(N/O) are shown.

7.6 The History of Virgo dIs

7.6.1 The Staged Model of Chemical Evolution

The discussions of UGC 7636 in Chapter 6 and of the gas deficiency seen in Figures 7.8, 7.10, 7.14, and 7.15 revealed that a number of Virgo dIs have lost gas. Owing to the intracluster gas in the Virgo Cluster, dwarfs should be stripped by ram–pressure on a timescale shorter than 1 Gyr, which is the crossing time. In fact, models by Mori and Burkert (2000) show that dwarf galaxies with total masses $\approx 10^9\ M_\odot$ are stripped in about 0.2 Gyr for conditions typical of the Virgo Cluster ($n \sim 10^{-3}$ cm^{-3} and $v \sim 1000$ km s^{-1}). The UGC 7636–STE1 system (Chapter 6) is the prototype for the present discussion. The H I cloud is presently observed to be intact. If stripping had occurred long ago, the cloud would have been consumed by the elliptical NGC 4472, or, since the cloud is not gravitationally bound, it would have been disrupted. Further discussion of these effects will be presented below. Moreover, no evidence of an H I trail from the cloud to the dI (Sancisi et al. 1987; Patterson and Thuan 1992; Henning et al. 1993; McNamara et al. 1994) is seen, which rules out slow continuous stripping. These observations indicate that

1. stripping has occurred,
2. stripping has occurred recently,
3. ram pressure is involved, and
4. the duration of the stripping event is short compared to the crossing timescale.

The following conjecture is made. A dI in the outskirts of the cluster forms the bulk of its stars and metals in isolation, just as if it were in the field. As the dI begins to fall into the dense, central regions of the cluster, the gas–normal dwarf is quickly stripped of most of its gas. The stellar mass and oxygen abundance are assumed

to remain constant while stripping is occurring. Stripping ceases, and whatever gas remains in the dI continues to form stars and metals in isolation. The second isolated phase of evolution would proceed from an "initial" state with nonzero metallicity ($Z_0 \neq 0$) and gas fraction less than one ($\mu_0 \neq 1$). Under these circumstances, the closed–box model gives for a primary element

$$Z - Z_0 = y \ln(\mu_0/\mu), \tag{7.77}$$

For oxygen, the yield by mass, y_O, given by Equation (7.70), was determined from the "closed–box" fit to field dIs. Equation (7.77) can be transformed to give

$$12 + \log(\mathrm{O/H}) = 12 + \log\left[\,(2.303\, y_O/11.728)\, \log(\mu_0/\mu) + (\mathrm{O/H})_0\,\right]. \tag{7.78}$$

Setting $(\mathrm{O/H})_0 = 0$ and $\mu_0 = 1$ reproduces Equation (7.67), which is conjectured to describe the first phase of isolated evolution. Equation (7.78) can be used to describe the evolution of a dI after it is stripped.

The staged model can be used to judge the state of a dwarf prior to the onset of stripping. This is accomplished with the aid of the correlations between (O/H) versus μ and (O/H) versus M_* seen for field dIs. The model is illustrated with VCC 1249. Figure 7.18 gives a plot of oxygen abundance versus the gas fraction. The solid line indicates the "closed box" fit to field dIs as expressed by Equation (7.69) and the open star indicates the position of VCC 1249 today.

Figure 7.19 gives a plot of oxygen abundance versus stellar mass for field dIs in isolation. The fit to field dIs is expressed by Equation (7.58). The position of VCC 1249 is again shown as an open star.

In both diagrams, the simplest evolutionary scenario is one where an isolated dI at position A" experiences rapid stripping and moves to position C, where no subsequent evolution occurs. Alternative staged evolutionary scenarios are also indicated in both

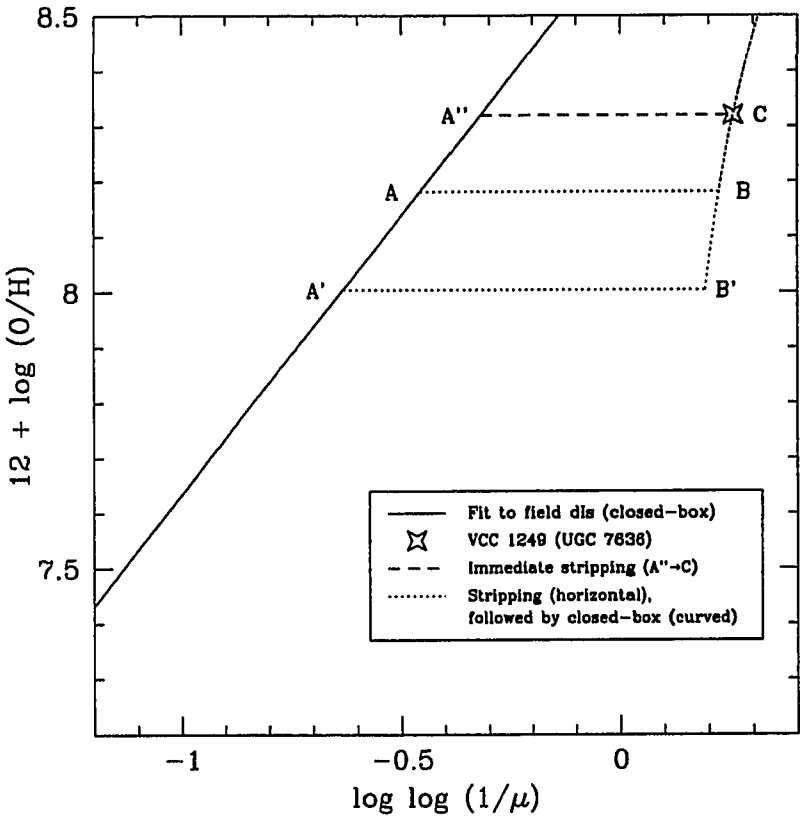

Figure 7.18: Oxygen abundance versus gas fraction: evolutionary models for VCC 1249 (UGC 7636). The solid line is the fit to field dIs described by Equation (7.69). The open star shows the observed present–day position of VCC 1249 (UGC 7636) in the diagram. The simplest evolutionary scenario is shown as a dashed line. An isolated dI at position A" experiences rapid stripping to position C. There is no subsequent evolution. Two alternative evolutionary scenarios (ABC and A'B'C) are labelled and are shown as dotted lines. Two dwarfs at A and A' have evolved in isolation. Rapid stripping takes the two dwarfs to B and B', respectively. Then, the remaining gas in the dI evolves in the second isolated evolutionary phase, described by Equation (7.78), to C.

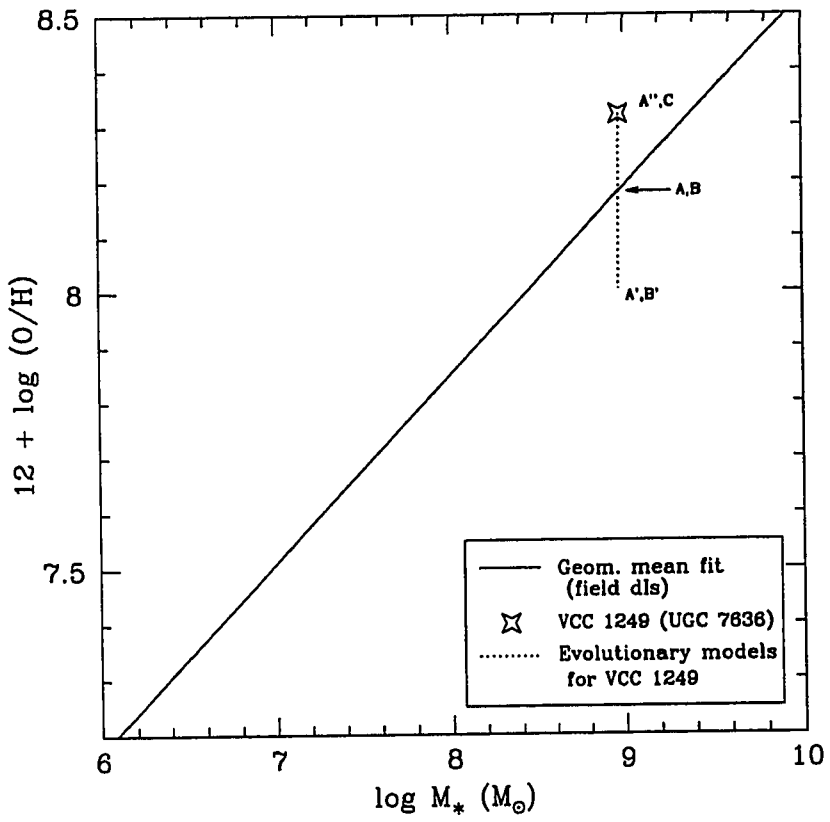

Figure 7.19: Oxygen abundance versus stellar mass (in $M_{\odot}$) for VCC 1249 (UGC 7636). The geometric mean functional fit (Draper and Smith 1998) to field dIs described by Equation (7.58) is shown as a solid line. The open star shows the position of VCC 1249 (UGC 7636) on the diagram. Labels and dotted lines correspond to the evolutionary scenarios in Figure 7.18; all scenarios terminate at the position of the open star (labelled "C" in both diagrams). The stellar mass and oxygen abundance are assumed to remain constant while stripping is occurring.

diagrams. The location of field dIs in Figures 7.18 and 7.19 define possible starting positions, i.e., where a dI which has evolved in isolation may begin to be stripped. For example, a galaxy at A (or A') moves to B (B') after stripping. If stripping is rapid, the oxygen abundance and stellar mass remain constant. Once reaching B (B'), gas loss ceases, and the remaining gas evolves in the second stage of "isolation." The galaxy moves to C along the displayed track(s). In Figure 7.19, the two tracks (ABC and A'B'C) are almost vertical, because the amount of star formation required to increase O/H adds little to the pre–existing stellar mass.

Analytical formulae describing the track ABC (or A'B'C) are derivable. The following properties of a dwarf observed today at C are known: $(\mathrm{O/H})_{\mathrm{C}}$, $M_{*,\mathrm{C}}$, $M_{\mathrm{gas,C}}$, $M_{\mathrm{bary,C}}$, and μ_{C}. The following is a prescription to derive properties of the dwarf in the past at A and B.

1. The oxygen abundance at A is fixed at the value it would have for a stellar mass as if the dwarf evolved in isolation. The relation between oxygen abundance and stellar mass for isolated dIs in the field (Equation 7.58) can be used to fix the oxygen abundance, i.e.,

$$12 + \log(\mathrm{O/H})_{\mathrm{A}} = a_1 + b_1 \log M_{*,\mathrm{C}}, \tag{7.79}$$

   where $M_{*,\mathrm{C}}$ is the present stellar mass at C, and a_1 and b_1 are the intercept and the slope. The value of the oxygen abundance at A must be less than or equal to the observed value at C.

2. If stripping is rapid, the oxygen abundance at B is set by the oxygen abundance at A.

$$(\mathrm{O/H})_{\mathrm{B}} = (\mathrm{O/H})_{\mathrm{A}} \tag{7.80}$$

3. Equation (7.78) describes the second isolated stage of evolution, i.e.,

$$(\mathrm{O/H})_{\mathrm{C}} = K_1 \log(\mu_{\mathrm{B}}/\mu_{\mathrm{C}}) + (\mathrm{O/H})_{\mathrm{B}} \tag{7.81}$$

where

$$K_1 = 2.303\, y_O/11.728 \tag{7.82}$$

$$= 4.36 \times 10^{-4} \tag{7.83}$$

where y_O is given by Equation (7.70). Thus, the gas fraction at B, μ_B, is expressed by

$$\log \mu_B = \log \mu_C + \frac{1}{K_1}[(O/H)_C - (O/H)_B]\,. \tag{7.84}$$

4. The total baryonic mass is conserved in the second isolated stage, i.e.,

$$M_{\rm bary,B} = M_{\rm bary,C} \tag{7.85}$$

So,

$$\frac{\mu_B}{\mu_C} = \frac{M_{\rm gas,B}}{M_{\rm gas,C}} \tag{7.86}$$

and the gas mass at B is

$$M_{\rm gas,B} = M_{\rm gas,C}\left(\frac{\mu_B}{\mu_C}\right). \tag{7.87}$$

5. Because baryons are conserved in the second isolated stage, the stellar mass at B is

$$M_{*,B} = M_{\rm bary,C} - M_{\rm gas,B}. \tag{7.88}$$

6. If the stripping is rapid, the stellar mass is unchanged between A and B, i.e.,

$$M_{*,A} = M_{*,B} \tag{7.89}$$

7. The dwarf at A has evolved in isolation, following Equation (7.69), i.e., at every stage of its life up to the time when stripping occurs

$$12 + \log(O/H) = a_2 + b_2 \log\log(1/\mu), \tag{7.90}$$

where a_2 is a constant related to the intercept of the fit to field dIs, and b_2 is the slope. Thus, the gas fraction at A, $\mu_{\rm A}$, is given by

$$\log(1/\mu_{\rm A}) = 10^{[\log({\rm O/H})_{\rm A} - a_2 + 12]/b_2} \tag{7.91}$$

8. Finally, the gas mass at A is

$$M_{\rm gas,A} = M_{*,{\rm A}} \left(\frac{\mu_{\rm A}}{1-\mu_{\rm A}} \right). \tag{7.92}$$

Thus, $M_{\rm gas}$, M_*, and (O/H) can be determined for positions A and B from knowledge of the properties of the dwarf at C.

Indeed, the gas fraction and the stellar mass of the original dwarf at A can be determined entirely in terms of known quantities for the dwarf observed today at C. From Equations (7.79) and (7.91), the following expression is obtained

$$\xi = \log(1/\mu_{\rm A}) = 10^{(a_1 - a_2 + b_1 \log M_{*,{\rm C}})/b_2} \tag{7.93}$$

and the gas fraction at A is given by

$$\mu_{\rm A} = 10^{-\xi} \tag{7.94}$$

From Equations (7.84), (7.87), (7.88), and (7.89), the stellar mass at A is written

$$M_{*,{\rm A}} = M_{\rm bary,C} - \frac{M_{\rm gas,C}}{\mu_{\rm C}} \cdot 10^{\{\log \mu_{\rm C} + [({\rm O/H})_{\rm C} - \eta]/K_1\}} \tag{7.95}$$

$$= M_{\rm bary,C} \left[1 - 10^{\{\log \mu_{\rm C} + [({\rm O/H})_{\rm C} - \eta]/K_1\}} \right], \tag{7.96}$$

where $\eta = 10^{(a_1 - 12 + b_1 \log M_{*,{\rm C}})}$ and $\mu_{\rm C} = M_{\rm gas,C}/M_{\rm bary,C}$.

From B to C, evolution proceeds like a closed box. The change in stellar mass is

$$\Delta M_* = M_{*,{\rm C}} - M_{*,{\rm B}}. \tag{7.97}$$

The time required to form ΔM_* can be derived from an estimate for the star formation rate (SFR). Unfortunately, the SFR is not known for the stripped Virgo dIs in the

present sample. Instead, the SFR is judged from measurements of the SFR for other dIs in Virgo, but normalized to the H I mass. The advantage of normalizing by $M_{\rm HI}$ is that the scale of the galaxies is removed. Designating the mean value of the normalized SFR by $\langle {\rm SFR}_n \rangle$, the SFR for any particular dwarf can be estimated from its H I mass using

$$ {\rm SFR} = \langle {\rm SFR}_n \rangle \cdot M_{\rm HI}. \tag{7.98} $$

Hence, the time which has elapsed since stripping (i.e., B to C) is given by

$$ t_* = \Delta M_* / {\rm SFR}. \tag{7.99} $$

Since both numerator and denominator in Equation (7.99) vary with the square of the distance, the timescale is independent of distance.

The SFR in Virgo dIs ranges from 6.9×10^{-3} $M_\odot$ yr^{-1} to 4.3×10^{-2} $M_\odot$ yr^{-1} (Heller et al. 1999). Normalized SFRs are computed by dividing each SFR by the corresponding H I mass using H I fluxes obtained by Hoffman et al. (1987) and a distance equal to 16.75 Mpc. The mean logarithmic SFR normalized by $M_{\rm HI}$ is

$$ \log \langle {\rm SFR}_n \rangle = -9.24 \pm 0.49, \tag{7.100} $$

where the error shown is the standard deviation. Thus, the mean value of ${\rm SFR}_n$ is

$$ \langle {\rm SFR}_n \rangle = 5.79 \times 10^{-10} \ {\rm yr}^{-1}. \tag{7.101} $$

7.6.2 Staged Model for VCC 1249 (UGC 7636)

Two models have been constructed for VCC 1249 (see Figures 7.18 and 7.19). The first has the galaxy begin at a position A lying exactly on the line relating O/H to M_* for field dwarfs. The second has the galaxy begin at position A', i.e., 1σ below the relation. The (O/H) for the starting position can not be pinpointed to better than

0.177 dex, which also sets how well M_* can be determined. The second model allows for an assessment of the degree to which scatter in O/H vs M_* can affect conclusions. Table 7.9 lists the relevant parameters for the models.

Position	log M_{gas} ($M_\odot$)	log M_* ($M_\odot$)	μ	log log $(1/\mu)$	12+log(O/H) (dex)	ΔM_* ($M_\odot$)	t_* (Gyr)
(1)	(2)	(3)	(4)	(5)	(6)	(7)	(8)
C	7.178	8.975	0.016	+0.256	8.32	5.31×10^6	0.023–0.22
B	7.309	8.973	0.022	+0.223	8.18	...	...
A	8.889	8.973	0.452	−0.462	8.18	...	...
C	7.178	8.975	0.016	+0.256	8.32	1.17×10^7	0.051–0.49
B'	7.428	8.970	0.028	+0.192	8.00	...	...
A'	9.123	8.970	0.587	−0.636	8.00	...	...

Table 7.9: Staged evolutionary models for VCC 1249. The first model (ABC) starts at A lying on the line describing (O/H) versus M_* for field dIs in Figure 7.19. The second model (A'B'C) starts with an oxygen abundance which is 1σ below the fit. Column (1) indicates the position in Figures 7.18 and 7.19, column (2) lists the logarithm of the gas mass, column (3) lists the logarithm of the stellar mass, columns (4) and (5) list the gas mass fraction and "inverse" gas mass fraction, column (6) lists the oxygen abundance, column (7) lists the mass of stars formed in going from position B (or B') to C, and column (8) lists the range of possible times required to form those stars between B (or B') and C.

The H I mass for STE1 is 1.3×10^8 $M_\odot$ (Patterson and Thuan 1992). Using Equations (7.101) and (7.98), the star formation rate is

$$\mathrm{SFR} = 0.0745\ M_\odot\ \mathrm{yr}^{-1}. \tag{7.102}$$

Based on the rms in H I–normalized SFRs given by Equation (7.100), the possible range in the SFR is

$$\mathrm{SFR} = 0.024\ \text{ to }\ 0.23\ M_\odot\ \mathrm{yr}^{-1}. \tag{7.103}$$

From Equation (7.99), the time since stripping for the first model is

$$t_* = 0.02\ \text{ to }\ 0.2\ \mathrm{Gyr}. \tag{7.104}$$

Because the path A'B'C in the second model is longer than ABC in the first model, more stars must be formed, and the time since stripping is longer, between 0.05 and

0.5 Gyr. In summary, if VCC 1249 is assumed to have been a "closed-box" dwarf at the outset, the staged isolation model constrains the stripping event to have ended less than 0.5 Gyr ago.

7.6.3 Evolution of an Average Gas–Poor dI in Virgo

A gas–poor dI is defined to be one with GDI $\gtrsim$ 0.8. There are five gas–poor dIs in the Virgo sample: VCC 1114, 1179, 1200, 1249, and 1448. Unfortunately, the chemical evolution of VCC 1448 cannot be studied because no H II region spectrum was obtained. The discussion here excludes VCC 1448. Because there are only four gas–poor galaxies (i.e., small numbers), properties of an "average" gas–poor are obtained to smooth out possibly large variations in properties from galaxy to galaxy. Average properties for $\log M_{\rm gas}$, $\log M_*$, and 12+log(O/H) are listed in row C in Table 7.10.

For the stellar mass at C ($\log M_* = 8.763$), Equation (7.79) yields an abundance at A (and B) of 12+log(O/H) = 8.11. This is slightly *higher* than the observed mean (8.09; Table 7.10). In other words, the abundance for a typical Virgo dI before stripping occurred happens to be larger than the present–day abundance for the stripped dwarf, which is not possible. The explanation for this problem lies in the dispersion in the relations between oxygen abundance and gas fraction and oxygen abundance and stellar mass for field dIs. The dispersion in the metallicity–stellar mass relation is a useful guide to the "phase space" that a dwarf could have once occupied. Since $\sigma = 0.177$ dex (§ 7.4.5), the lowest likely abundance at A and B is $12 + \log({\rm O/H}) = 8.11 - 0.18 = 7.93$. This value is now below the observed mean for the four gas–poor dwarfs, as it should be.

Figures 7.20 and 7.21 illustrate the evolutionary path for an average gas–poor Virgo dI, presuming it began as an isolated dI at A, rapidly evolved to B as a result

of sudden gas loss, then evolved to C as a closed system. The parameters describing

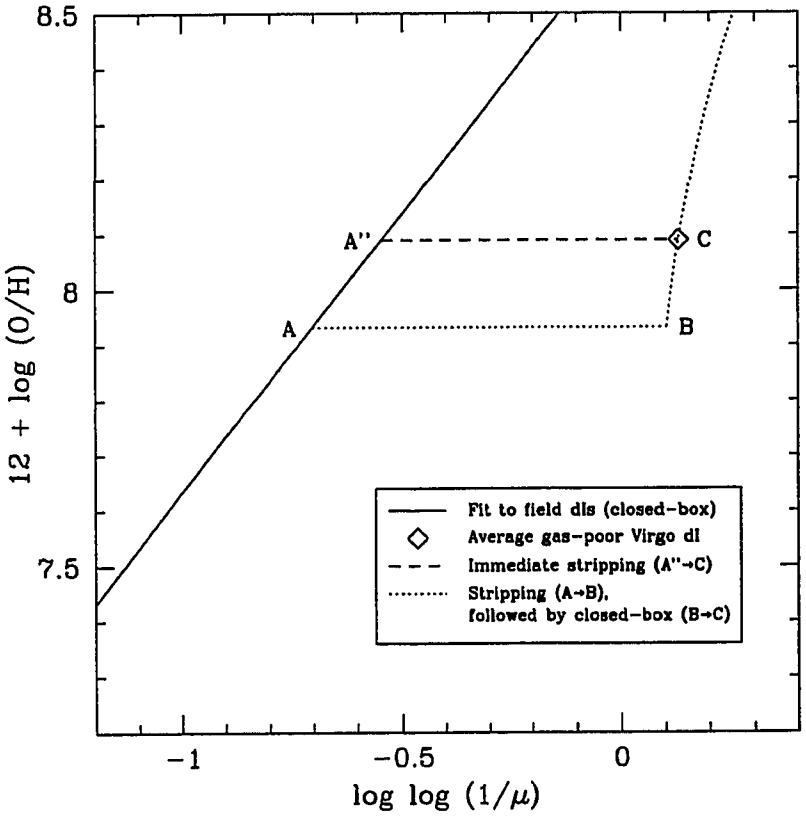

Figure 7.20: Oxygen abundance versus gas fraction: evolutionary models for an average gas–poor Virgo dI. The solid line is the fit to field dIs described by Equation (7.69). The open diamond indicates the currently observed position of an average gas–poor Virgo dI. The dashed line between A'' and C shows the path for immediate stripping with no subsequent evolution. The dotted line shows what happens if rapid stripping removes the gas (A to B) and the remaining gas in the dI subsequently evolves as an isolated system (B to C) according to Equation (7.78).

positions A and B in the Figures are given in Table 7.10. Substituting the H I gas mass at position C into Equation (7.98), the possible range in the SFR is

$$\mathrm{SFR} = 0.005 \text{ to } 0.048\ M_\odot\ \mathrm{yr}^{-1}. \tag{7.105}$$

The range of times required to form ΔM_* between B and C is between 0.1 and 1.2 Gyr. This can be regarded as a maximum, given that the initial value of (O/H)

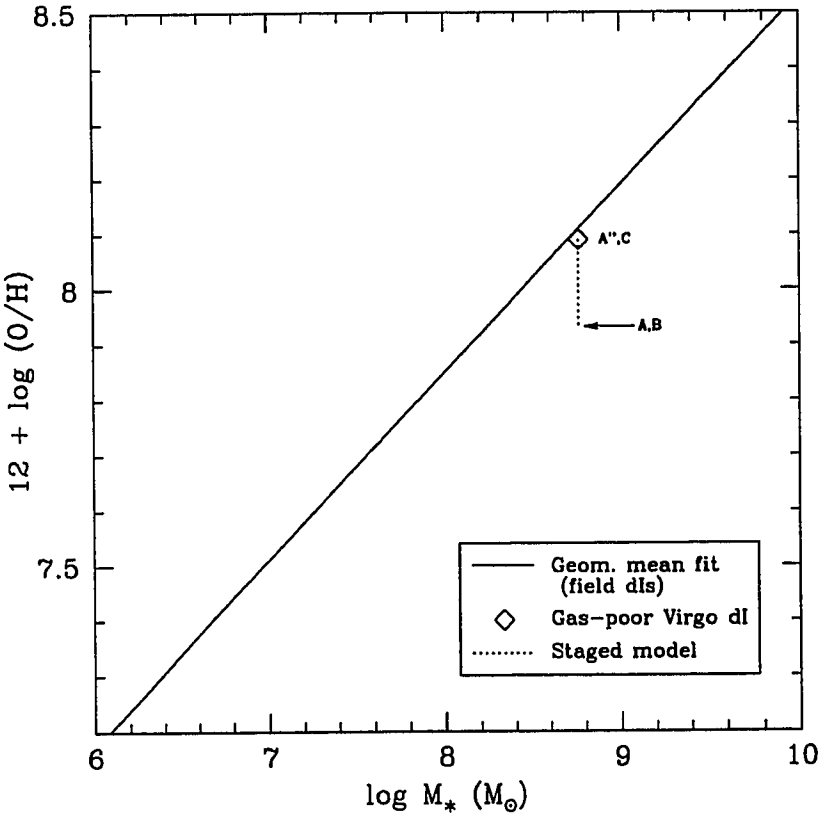

Figure 7.21: Oxygen abundance versus stellar mass (in $M_{\odot}$) for an average gas-poor Virgo dI. The geometric mean functional fit (Draper and Smith 1998) to field dIs, described by Equation (7.58), is shown as a solid line. The open diamond indicates the position of an average gas-poor Virgo dI. The dotted line indicates the evolutionary path from A to B to C seen in Figure 7.20. The stellar mass and oxygen abundance are assumed to remain constant while stripping occurs.

was probably larger than the value at A.

Position	log $M_{\rm gas}$ ($M_\odot$)	log M_* ($M_\odot$)	μ	log log $(1/\mu)$	12+log(O/H) (dex)	ΔM_* ($M_\odot$)	t_* (Gyr)
(1)	(2)	(3)	(4)	(5)	(6)	(7)	(8)
C	7.430	8.763	0.044	+0.131	8.09	5.89×10^6	0.12–1.2
B	7.516	8.759	0.054	+0.103	7.93	...	...
A	8.997	8.759	0.634	−0.704	7.93	...	...

Table 7.10: Staged evolutionary model for an average gas-poor dI in Virgo. Column (1) indicates the position in Figure 7.20, column (2) lists the logarithm of the gas mass, column (3) lists the logarithm of the stellar mass, columns (4) and (5) list the gas mass fraction and "inverse" gas mass fraction, column (6) lists the oxygen abundance, column (7) lists the mass in stars formed from position B to C, and column (8) lists the time required to form those stars.

7.7 Gas–Poor Dwarfs and the Intracluster Medium

Ram–pressure stripping by the gas in the intracluster medium (ICM) was discussed previously in § 6.4.2 to explain the observations for UGC 7636. With the construction of a gas–deficiency index for dIs and a clear indication that there are both gas–poor and gas–normal dIs in Virgo (§ 7.5.2), it is logical to seek a correlation between the GDI and the density of intracluster gas.

Previously, Figure 2.3 showed the locations of the sample of dIs within the Virgo Cluster. Figure 7.22 illustrates the positions of gas–deficient dIs within the cluster, i.e., dIs with GDI $\gtrsim 0.8$. Notably, these dIs happen to be found in regions where the number of H I–deficient spiral galaxies in the Virgo Cluster is largest (Solanes et al. 2001).

Figure 7.23 is a plot for Virgo dIs of the gas–deficiency index versus their velocity with respect to the cluster. The relative velocity, $|v_{\rm rel}|$, is defined as the difference between the heliocentric radial velocity of a dI and the heliocentric radial velocity of the entire Virgo Cluster (1050 km s^{-1}; Binggeli et al. 1993). There is no apparent

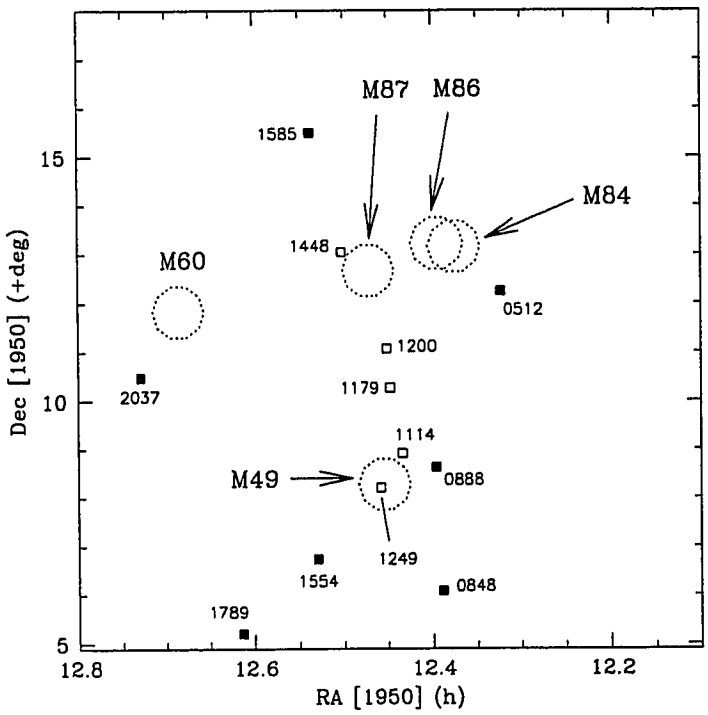

Figure 7.22: Locations of gas-deficient dIs within the Virgo Cluster. Five ellipticals are labelled by their Messier numbers; the twelve dIs are labelled by their number in the Virgo Cluster Catalog (Binggeli et al. 1985). Open squares show the positions of gas-deficient dwarfs, i.e., dwarfs for which GDI $\gtrsim 0.8$. Filled squares mark locations of dIs for which GDI $\lesssim 0.8$.

correlation of GDI with relative velocity.

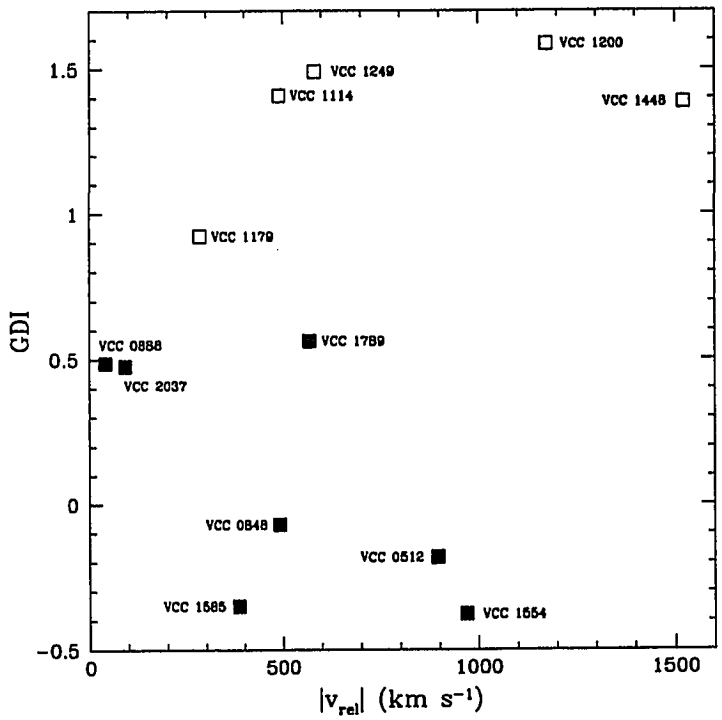

Figure 7.23: Gas–deficiency index (GDI) versus relative velocity for Virgo dIs. The relative velocity for each dI was computed as the difference between the heliocentric velocity of the dI and the heliocentric velocity of the Virgo Cluster ($v_{\odot,\mathrm{Virgo}} = 1050$ km s^{-1}; Binggeli et al. 1993). Open squares represent gas–deficient Virgo dIs for which GDI $\gtrsim 0.8$. Filled squares represent dIs for which GDI $\lesssim 0.8$.

To look for a correlation with ICM density, X–ray surface brightnesses at the positions of Virgo dIs were extracted from a map of the Virgo Cluster created by Sabine Schindler (private communication). Figure 7.24 shows a plot of the gas–deficiency index versus the X–ray surface brightness, S_X, of the ICM (Schindler et al. 1999). There appears to be a threshold in X–ray surface brightness above which gas–poor dwarfs lie. Thus, the gas deficiency appears to be related to the ICM gas density.

The correlation seen in Figure 7.24 supports the contention that ram pressure

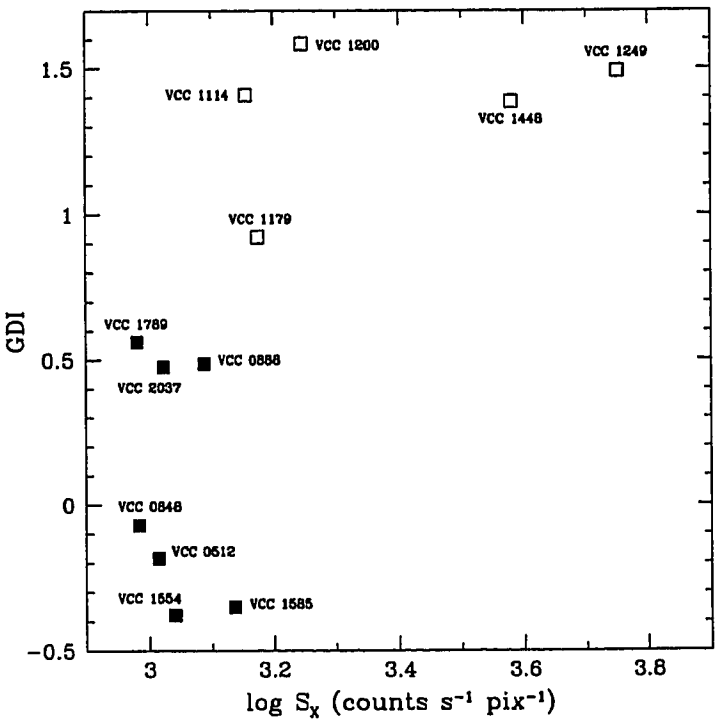

Figure 7.24: Gas–deficiency index (GDI) of dIs versus X–ray surface brightness within the Virgo Cluster. Open squares represent gas–deficient dwarfs for which GDI $\gtrsim 0.8$. Filled squares represent dIs for which GDI $\lesssim 0.8$. Note that the surface brightness for VCC 1585 may be contaminated by the background cluster Abell 1560 at $z = 0.244$ (Bothun et al. 1994).

plays a role in removal of gas from Virgo dIs. The ram pressure depends upon both density and relative velocity. The projected gas density, $\rho_{\rm ICM}$, is proportional to the square root of the X–ray surface brightness (Schindler et al. 1999). Thus, the ram pressure, $P_{\rm ram}$, is (see § 6.4.2; Gunn and Gott 1972)

$$P_{\rm ram} = \rho_{\rm icm}\, v_{\rm rel}^2 \tag{7.106}$$

$$\propto (S_X)^{1/2}\,(v_{\odot,\rm dI} - v_{\odot,\rm Virgo})^2 \tag{7.107}$$

$$\log P_{\rm ram} = \text{constant} + 0.5 \log S_X + 2 \log |v_{\rm rel}|, \tag{7.108}$$

where $v_{\rm rel}$ is the velocity of the dwarf with respect to the cluster.

In Figure 7.25, the gas deficiency index is plotted against a measure of ICM ram–pressure for the sample of Virgo dIs. Unfortunately, there is no clear correlation with ram–pressure. The correlation with X–ray surface brightness has been muddled by the relative velocities, likely because of the lack of information about transverse components. Nevertheless, the correlation of the GDI with X–ray surface brightness is compelling evidence that ram pressure plays a role in the evolution of dIs in the Virgo Cluster.

The mere existence of a correlation between the GDI and X–ray surface brightness supports the models in § 7.6.1, which showed that at most 1 Gyr has elapsed since stripping occurred. Yet, dIs should have already made about ten passages through the core of the Virgo Cluster since the Big Bang, since the time to cross the Virgo Cluster is about 1.2 Gyr (Equation 2.1). This strongly suggests that dIs are falling into the central regions and encountering the dense ICM gas for the first time. Gallagher and Hunter (1989) also claimed that most dIs have never passed through the cluster core, on the basis that only a small fraction of present–day dIs currently exhibit any signs of gas loss and that their $B-V$ colours are not significantly redder than those of field dIs.

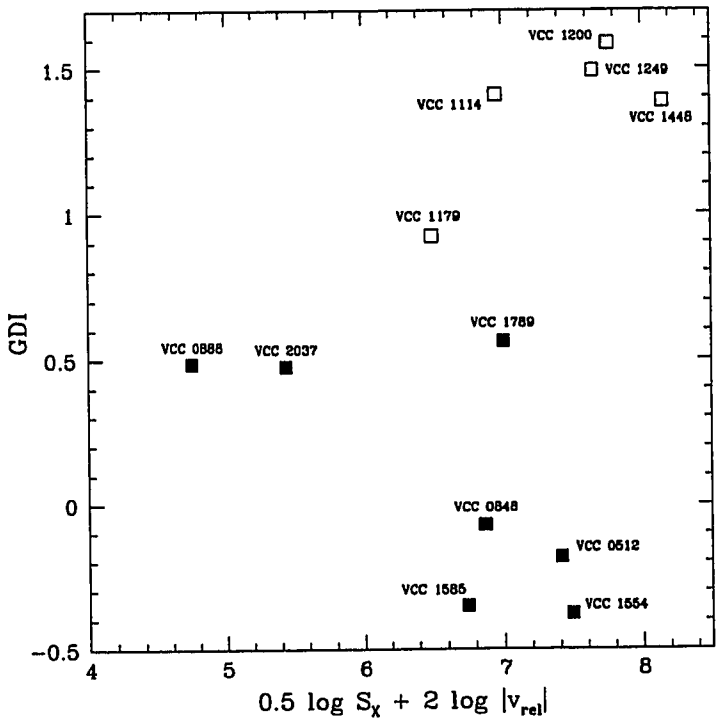

Figure 7.25: Gas–deficiency index (GDI) of Virgo dIs versus ram–pressure. The intracluster ram–pressure is gauged from Equation (7.108). Open squares represent gas–deficient dwarfs for which GDI $\gtrsim 0.8$. Filled squares represent dIs for which GDI $\lesssim 0.8$.

7.8 The Evolution of a Gas–Poor dI in Virgo

Ram–pressure stripping has been shown to be the most likely mechanism responsible for producing present–day gas–poor dIs in the Virgo Cluster. Here, comments are made regarding the recent evolution of a gas–poor dI in Virgo, the possible fate of the stripped gas, and the eventual fate of the gas–poor dwarf.

The present level of chemical enrichment of gas–poor dIs in Virgo likely was achieved well before the dIs were stripped, as the mass of the underlying population of old stars is considerable. For an average field and Virgo dI (Table 7.4), the masses in old stars are $\log M_{*,\mathrm{old}} = 8.81$ and 8.79, respectively. Based upon typical star formation rates for gas–rich dIs in Virgo (e.g., Heller et al. 1999), and assuming that most of the stars formed at a rate which has been constant on average (e.g., van Zee 2001), the time required to form the old population is at least 10 Gyr. Thus, the bulk of the stars within Virgo dIs formed well in the past, likely when the galaxies were in the outer regions of the cluster.

It appears that dIs are passing through the dense regions of the ICM on radial orbits (Dressler 1986; Giraud 1986). The dIs are unlikely to be in circular orbits in the cluster for two reasons. First, if their orbital radii were large, they would never encounter the dense ICM gas, and there would be no gas–deficient dIs, which is contrary to the observations. Second, if the orbital radii were small, the dIs would always encounter the dense ICM gas, and would have been stripped long ago. Yet, the models presented above reveal that dwarfs were stripped less than 1 Gyr ago.

Further evidence that dIs are falling into the cluster for the first time comes from analysis of the consequences of encounters. The process of dynamical friction may lead to the demise of a dwarf galaxy, if it passes near a supergiant elliptical galaxy such as M 49 or M 87. With a sufficiently close approach, the dwarf is subjected to

dynamical friction and is eventually "digested" by the giant. The time a giant needs to digest the dwarf is given by the relaxation timescale and, to within factors of unity (Shu 1986), it is given by

$$t_{\rm relax} = \frac{(rv)^3}{3\,G^2\,m\,M\ln(rv^2/Gm)}, \tag{7.109}$$

where r is the separation between the dI and the elliptical, v is the absolute value of the relative velocity between the two galaxies, G is the gravitational constant, and m and M are the masses of the dI and the elliptical, respectively. Consider an interaction between VCC 1249 (UGC 7636) and M 49. With $r \simeq 10$ kpc, $v = 700$ km s^{-1}, $m \sim 9 \times 10^8\ M_\odot$, and $M \simeq 4.6 \times 10^{12}\ M_\odot$ (Forman et al. 1985), then $t_{\rm relax} \simeq 0.2$ Gyr, which is about a factor of six smaller than the cluster crossing time (Equation 2.1; 1.2 Gyr). So, VCC 1249 and the H I cloud STE1 should have been digested long ago if the dI had made an earlier pass by M 49.

The cluster can also exert tides on dIs. Merritt (1984) showed that galaxies which come within the core redius, R_c, of a cluster and whose radii exceed some tidal radius, r_T, would be truncated significantly by cluster tides. The tidal radius is given roughly by

$$r_T \approx R_c\,\sigma_g/\sigma_{\rm cl}, \tag{7.110}$$

where σ_g and $\sigma_{\rm cl}$ are the velocity dispersions of the galaxy and of the cluster, respectively. For the Virgo Cluster (Table 2.4), the core radius is $R_c \simeq 500$ kpc and the velocity dispersion is $\sigma_{\rm cl} = 760$ km s^{-1}. Thus, the tidal radius is given by

$$r_T \approx 7\ {\rm kpc}\left(\frac{\sigma_g}{10\ {\rm km\ s^{-1}}}\right). \tag{7.111}$$

Assuming that velocity dispersions of dwarfs lie in the range between 10 and 20 km s^{-1} (Mateo 1998), dIs should be unaffected by the potential of the Virgo Cluster. In fact, based upon surface brightness profiles, Binggeli et al. (1984) have shown that tidal

stripping of high– and low–luminosity elliptical and spheroidal galaxies in the central regions of the Virgo Cluster occurs on a timescale exceeding 10^{11} yr.

7.8.1 Fate of the Stripped Gas

Given that gas is stripped from dIs, it is important to examine what happens to it. It is especially relevant to determine whether the gas remains bound to itself (e.g., STE1), and whether the gas can survive being immersed within the intracluster medium.

Hills (1980) derived analytical approximations which describe the effect of mass loss on the evolution of a stellar system. These expressions can in turn be used to evaluate whether the stripped gas remains bound. For dwarf galaxies, the characteristic size, R, is about 1 to 3 kpc and the velocity dispersion, σ, is about 10 km s^{-1} (see Mateo 1998). Thus, the dynamical time scale is

$$t_{\rm D} \approx R/\sigma \tag{7.112}$$

$$\simeq \frac{1 \text{ to } 3 \text{ kpc}}{10 \text{ km s}^{-1}}$$

$$\simeq 0.1 \text{ to } 0.3 \text{ Gyr.} \tag{7.113}$$

If 50% or more of the mass of a virialized system is lost on a timescale comparable to or shorter than a dynamical time, the remaining system is no longer bound and dissociates. The minimum fractional mass which must be lost for dissociation to occur is given by

$$\frac{\Delta M}{M_0} \gtrsim \frac{R_{\rm loss}}{2R_0}, \tag{7.114}$$

where M_0 is the mass prior to mass loss, R_0 is the radius achieved after virialization, and $R_{\rm loss}$ is the radius of the system when the mass loss occurs.

Properties of UGC 7636 and the H I cloud STE1 can be used to evaluate whether the H I gas will remain bound to itself. The H I mass of STE1 is 1.3×10^8 $M_\odot$

(Patterson and Thuan 1992), the mass of the residual H I in UGC 7636 is $1.1 \times 10^7\ M_\odot$ (Hoffman et al. 1987), and the mass of stars in UGC 7636 is $9.5 \times 10^8\ M_\odot$ (Table 7.2). The total mass is $M_0 = 1.1 \times 10^9\ M_\odot$. Assuming ΔM to be the mass of STE1, the left–hand side of Equation (7.114) is 0.12.

From the virial theorem, an estimate of R_0 is given by

$$R_0 \simeq \frac{GM_0}{2(3\sigma^2 + v_{\rm rot}^2)}. \tag{7.115}$$

Substituting for the values of M_0, $\sigma = 10$ km s^{-1}, and $v_{\rm rot} \approx 30$ km s^{-1} (see Chapter 6), R_0 is 1.97 kpc. For the dI UGC 7636 to dissociate, $R_{\rm loss} \lesssim 0.48$ kpc. Presently, the effective radius in B of UGC 7636 is 4.3 kpc (see Chapter 6). Although the dI has most likely responded to the tidal influence of NGC 4472 by expanding, UGC 7636 was probably larger than 0.5 kpc before mass loss occurred. The dI remains bound.

About 10% of the original mass of UGC 7636 was lost. This can be turned around for the gas cloud STE1. As 90% of the gravitational mass "supporting" STE1 was removed, the gas cannot remain bound in the cloud.

How long the stripped gas survives within the intracluster medium depends on the properties of the "cold" gas and the "hot" plasma. Consider a spherical cloud of hydrogen gas imbedded in a hot ICM of density $n_{\rm ICM}$ and temperature $T_{\rm ICM}$. Electrons conduct heat from the hot, fully ionized gas in the ambient medium and the cold gas in the cloud (Cowie and McKee 1977; Cowie and Songaila 1977). Energy exchange between electrons occurs over a mean free path, $\lambda_{\rm mfp}$ (in cm), given by

$$\lambda_{\rm mfp} \approx 10^4\, T_{\rm ICM}^2 / n_{\rm ICM}, \tag{7.116}$$

where $T_{\rm ICM}$ is in units of K and $n_{\rm ICM}$ is in cm^{-3}. In the Virgo Cluster, $T_{\rm ICM} \sim 10^7$ K and $n_{\rm ICM} \sim 10^{-3}$ cm^{-3}, so $\lambda_{\rm mfp} \sim 300$ pc. Since $\lambda_{\rm mfp}$ is much smaller than the radius of the Virgo Cluster, the gas in the cloud thermally evaporates. The evaporation

timescale, $t_{\rm evap}$ (in years), is given by

$$t_{\rm evap} = (3.3 \times 10^{20})\, n_{\rm cloud}\, R_{\rm cloud}^{2}\, T_{\rm ICM}^{-5/2}\, \frac{\ln \Lambda}{30}, \tag{7.117}$$

where $n_{\rm cloud}$ is the mean hydrogen density of the cloud in cm^{-3}, $R_{\rm cloud}$ is the radius of the cloud in parsecs, $T_{\rm ICM}$ is in K, and the Coulomb logarithm, $\ln \Lambda$, is given by

$$\ln \Lambda = 29.7 + \ln n_{\rm ICM}^{-1/2}\, (T_{\rm ICM}/10^{6}\ {\rm K}) \tag{7.118}$$

where $n_{\rm ICM}$ is in cm^{-3} (Cowie and McKee 1977). Ionization can be neglected because the intracluster medium is very hot ($kT_{\rm ICM} \gg 13.6$ eV). The H I mass of STE1 is $1.3 \times 10^{8}\ M_{\odot}$ (Patterson and Thuan 1992). The radius is assumed to be 60″ (McNamara et al. 1994), or about 4800 pc at the distance of the Virgo Cluster. Thus, assuming spherical symmetry, the mean hydrogen density of STE1 is approximately 0.01 to 0.02 cm^{-3}. The evaporation timescale is about 1 Gyr, which is very similar to the crossing time for the Virgo Cluster (1.2 Gyr from Equation 2.1).

During its next orbit, it can be expected that the cloud of stripped gas will dissipate and evaporate. That STE1 ought to dissipate on a time comparable to $t_{\rm D}$ and that STE1 is observed still to be intact lend additional weight to the conclusion that stripping occurred very recently.

7.8.2 Fading: The Fate of a Gas–Poor dI

Since gas–poor dIs are recognizable, it is logical to ask what they will become after fading, and whether examples of such objects exist in the present–day. The fading of a gas–poor dI can be computed in the following manner. Assuming that there is little or no gas remaining to form any more stars (e.g., VCC 1249, VCC 1448), the present population of young stars will fade to become a "new" population of old stars in the future. Thus, the mass of old stars in the future will be augmented by an amount

$$\Delta M_{*,\rm old}^{\rm future} \;=\; M_{*,\rm yng}$$

$$(M_*/L_B)_{\rm old}^{\rm future}\Delta L_{B,\rm old}^{\rm future} = (M_*/L_B)_{\rm yng}(1-f_{{\rm old},B})L_B. \quad (7.119)$$

The second line is obtained from Equations (7.6) and (7.8). The luminosity of the faded "young" population is added onto the luminosity of the present–day population of old stars to yield the total luminosity in the future:

$$\begin{aligned} L_{B,\rm old}^{\rm total} &= L_{B,\rm old}^{\rm now} + \Delta L_{B,\rm old}^{\rm future} \\ &= L_B\left[f_{{\rm old},B} + \frac{(M_*/L_B)_{\rm yng}}{(M_*/L_B)_{\rm old}^{\rm future}}(1-f_{{\rm old},B})\right]. \end{aligned} \quad (7.120)$$

The mass–to–light ratio of "future" old stars is assumed to be the same as the present value forold stars in each Virgo dwarf, i.e.,

$$(M_*/L_B)_{\rm old}^{\rm future} = (M_*/L_B)_{\rm old}. \quad (7.121)$$

With the mass–to–light ratio for the young component from Equation (7.13), the total luminosity in B of the old component can be written as

$$L_{B,\rm old}^{\rm total} = L_B\left[f_{{\rm old},B} + \frac{0.153}{(M_*/L_B)_{\rm old}}(1-f_{{\rm old},B})\right]. \quad (7.122)$$

The amount of fading in magnitudes is

$$\Delta M_{B,\rm fading} = -2.5\log(L_{B,\rm old}^{\rm total}/L_B) \quad (7.123)$$

$$= -2.5\log\left[f_{{\rm old},B} + \frac{0.153}{(M_*/L_B)_{\rm old}}(1-f_{{\rm old},B})\right]. \quad (7.124)$$

Since $f_{{\rm old},B} \approx 0.5$ (see Table 7.3) and $(M_*/L_B)_{\rm old} = 3.11$, a typical gas–poor dI in Virgo will fade by about 0.6 to 0.7 mag. This is expected to occur in about 1 Gyr (Bothun 1982).

In attempting to ascertain what the dIs will become, comparisons are made with other gas–poor dwarf galaxies in the Virgo Cluster, i.e., dEs, nucleated dwarf ellipticals (dE,Ns), "transition" dwarfs (dI/dEs), and dIs with H I fluxes comparable to or

smaller than that of VCC 1249 (gas–poor dwarfs; Hoffman et al. 1987; Binggeli and Cameron 1993). Comparisons are also made with a set of late–type dwarfs measured by Patterson and Thuan (1996). They found that dIs are segregated into two groups. Scale lengths of dIs in the first group (Type I) are similar to those of dEs/dSphs. Scale lengths of dIs in the second group (Type II) are similar to those of BCDs and about two times smaller those for dIs of Type I.

Fading vectors for gas–poor Virgo dIs are shown in Figures 7.26 and 7.27, where the exponential scale length and effective surface brightness are plotted against M_B. The scale length can be converted into an effective radius via Equation (7.33) and the effective surface brightness is computed using Equation (7.50). On the whole, the scale lengths for gas–poor Virgo dIs are similar to dIs of Type I. They are indistinguishable from those of dEs, dE,Ns, dI/dEs, and other gas–poor dwarfs at comparable luminosities.

In Figure 7.26, the scale lengths for VCC 1249 and VCC 1448 are about a factor of two larger than for the other gas–poor dIs. VCC 1249 and VCC 1448 are situated very close in projection to the supergiant elliptical galaxies M 49 and M 87, respectively (see Figure 7.22). Tidal effects from the neighbouring ellipticals have likely caused the stellar components of VCC 1249 and VCC 1448 to expand.

The effective surface brightness in B is plotted against the absolute magnitude in Figure 7.27. The dIs with GDI $\gtrsim 0.8$ lie in the upper envelope of the locus defined by dEs/dSphs and other gas–poor dwarfs identified solely by their low H I content (Hoffman et al. 1987).

Figures 7.26 and 7.27 show that there are structural differences between dEs and dE,Ns. While scale lengths of dEs and dE,Ns are similar at comparable luminosities, dEs appear to be fainter than dE,Ns at a given surface brightness. The five dIs identified here to be gas–poor appear to be structurally similar to dE,Ns. However,

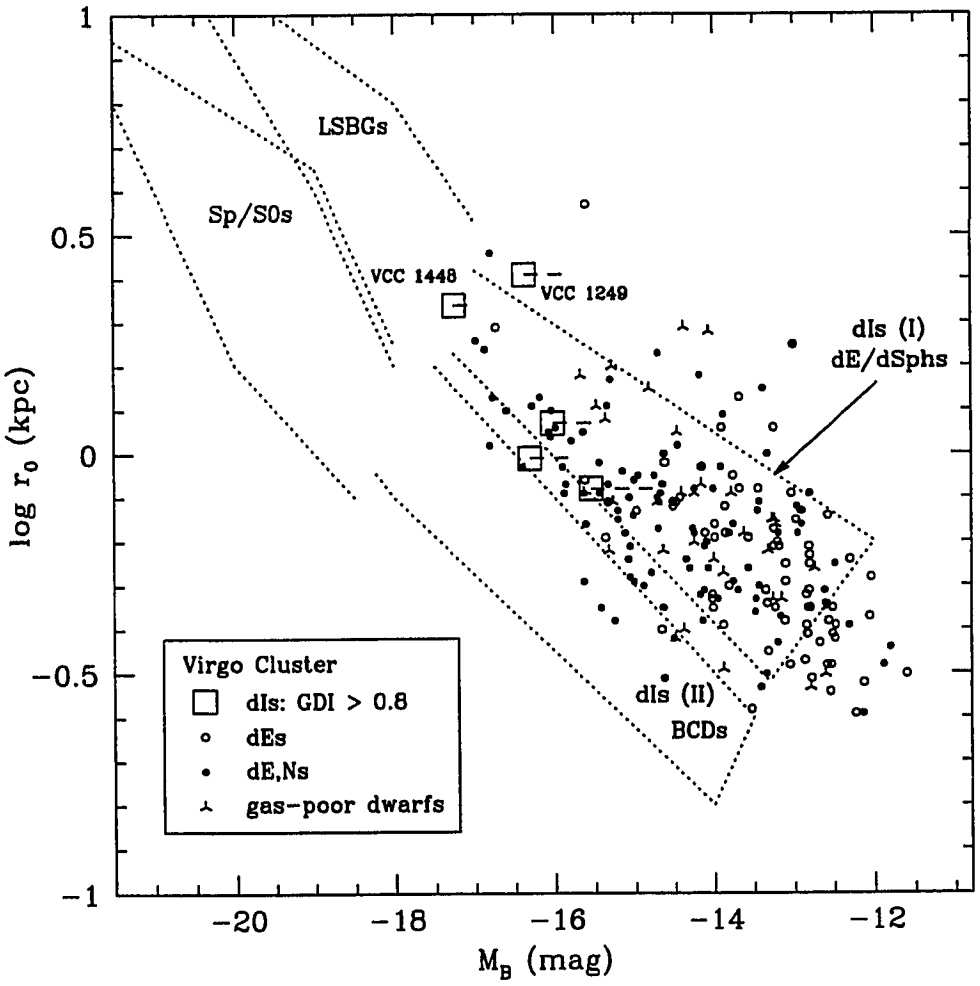

Figure 7.26: Exponential scale length, r_0, versus absolute magnitude in B for gas-poor Virgo dwarfs. Galaxy luminosity increases to the left. Adopting the nomenclature in Patterson and Thuan (1996), four regions of scale length–luminosity phase space are marked by dotted lines. "Sp/S0s" represents the region spanned by spiral and lenticular galaxies and "LSBGs" represents the region spanned by low surface brightness galaxies. Open squares indicate "gas–poor" Virgo dIs (GDI $\gtrsim$ 0.8); in particular, VCC 1249 and VCC 1448 are labelled. The scale lengths of gas–poor dIs in the present Virgo sample are consistent with dIs of type "I" defined by Patterson and Thuan (1996) (see text). Fading vectors for the five gas–poor dIs are shown as horizontal dashed lines. The fading model assumes that little or no gas remains to form new stars and that the scale length remains constant as present–day young stars fade. Open circles and filled circles indicate dEs and nucleated dEs (dE,Ns), respectively. Transition dwarfs (dI/dEs) and H I–poor dIs from Hoffman et al. (1987) are indicated as upside–down Ys. All values of the exponential scale length are taken from Binggeli and Cameron (1993), except for VCC 1249 (Patterson and Thuan 1996).

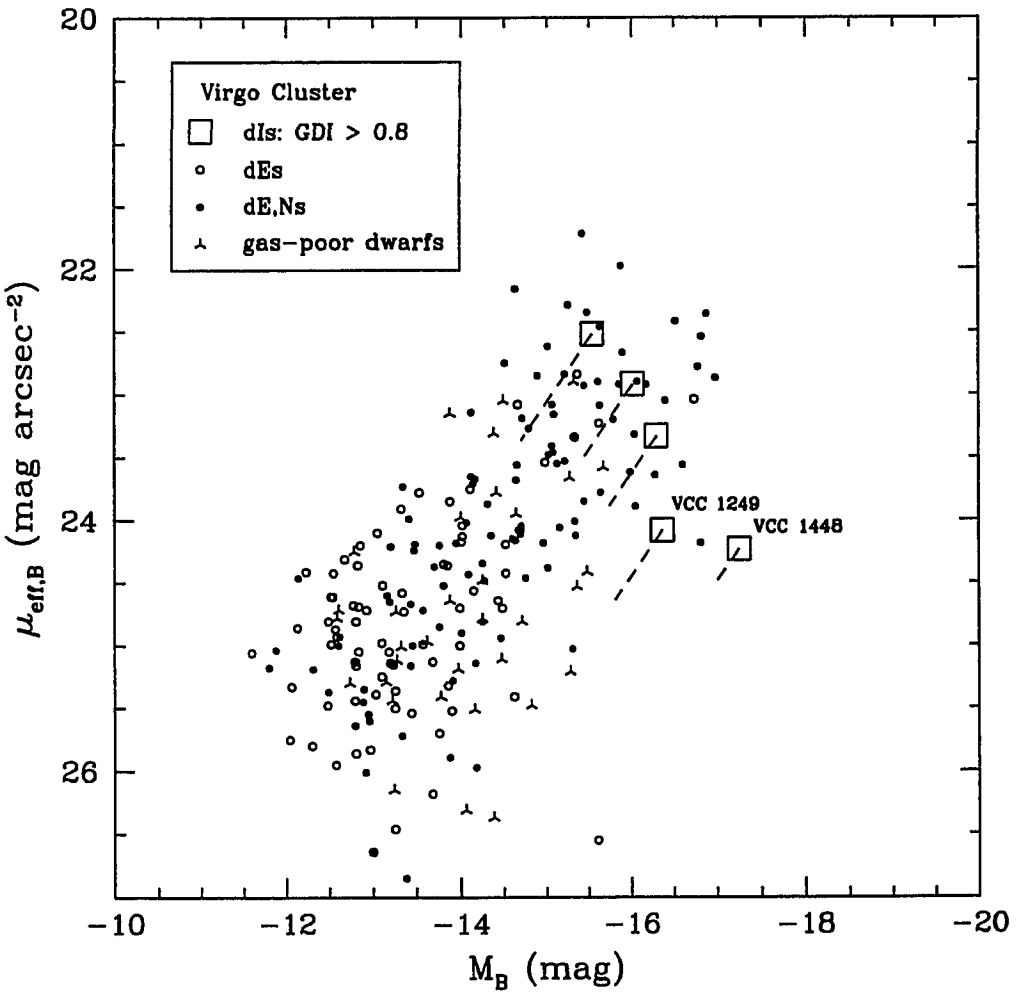

Figure 7.27: Effective surface brightness, $\mu_{\mathrm{eff},B}$, versus absolute magnitude in B for gas–poor Virgo dwarfs. Open squares indicate "gas–poor" Virgo dIs (GDI $\gtrsim$ 0.8). In particular, VCC 1249 and VCC 1448 are labelled. Fading vectors are shown as dashed lines. The fading model assumes that the scale length remains constant as the remaining young stellar component fades. Open circles and filled circles indicate dEs and nucleated dEs, respectively. Transition dwarfs (dI/dEs) and H I–poor dIs from Hoffman et al. (1987) are indicated as upside–down Ys. All effective surface brightness values are taken from Binggeli and Cameron (1993).

dIs do not have prominent nuclei; it remains unclear how non–nucleated dIs can form compact nuclei. The progenitors of nucleated Virgo dEs were not likely to have been dIs.

In conclusion, gas–poor Virgo dIs will evolve to become bright dE/dSph–like objects with scale lengths comparable to present–day dEs/dSphs. There does not appear to be an existing population of successors to present–day gas–poor dIs, lending further credence to the idea that Virgo dIs are only now falling into the cluser.

For a presently–observed gas–poor dI in the Virgo Cluster, a possible evolutionary track is shown in Figure 7.28. Throughout most of its life in the periphery of the cluster, the dwarf forms the bulk of its stars and metals. As it falls into the cluster for the first time, ICM ram pressure quickly strips the interstellar gas, perhaps aided by tidal effects from passage close to a giant galaxy. Tidal interactions and the loss of gas cause the stellar component to expand in size. In the stripped gas, star formation may occur, due to the compression of neutral gas by the intracluster medium (e.g., Mori and Burkert 2000). The cold neutral gas will eventually be "evaporated" by the hot intracluster medium and/or eventually dissipate. With little gas remaining, the gas–poor dI eventually fades to become an object resembling a present–day dE.

7.9 Final Remarks

7.9.1 Distance Variations

Based upon a revised calibration of Cepheids and a distance modulus for the LMC of (18.50 ± 0.10) mag, Freedman et al. (2001) state 30.81 mag as the distance modulus for the Virgo Cluster. Correcting to a distance modulus of 18.58 mag adopted for the LMC (§ 2.1.2), the Freedman et al. value for the Virgo Cluster distance modulus becomes 30.89 mag. This is 0.23 mag smaller than the value adopted in this thesis

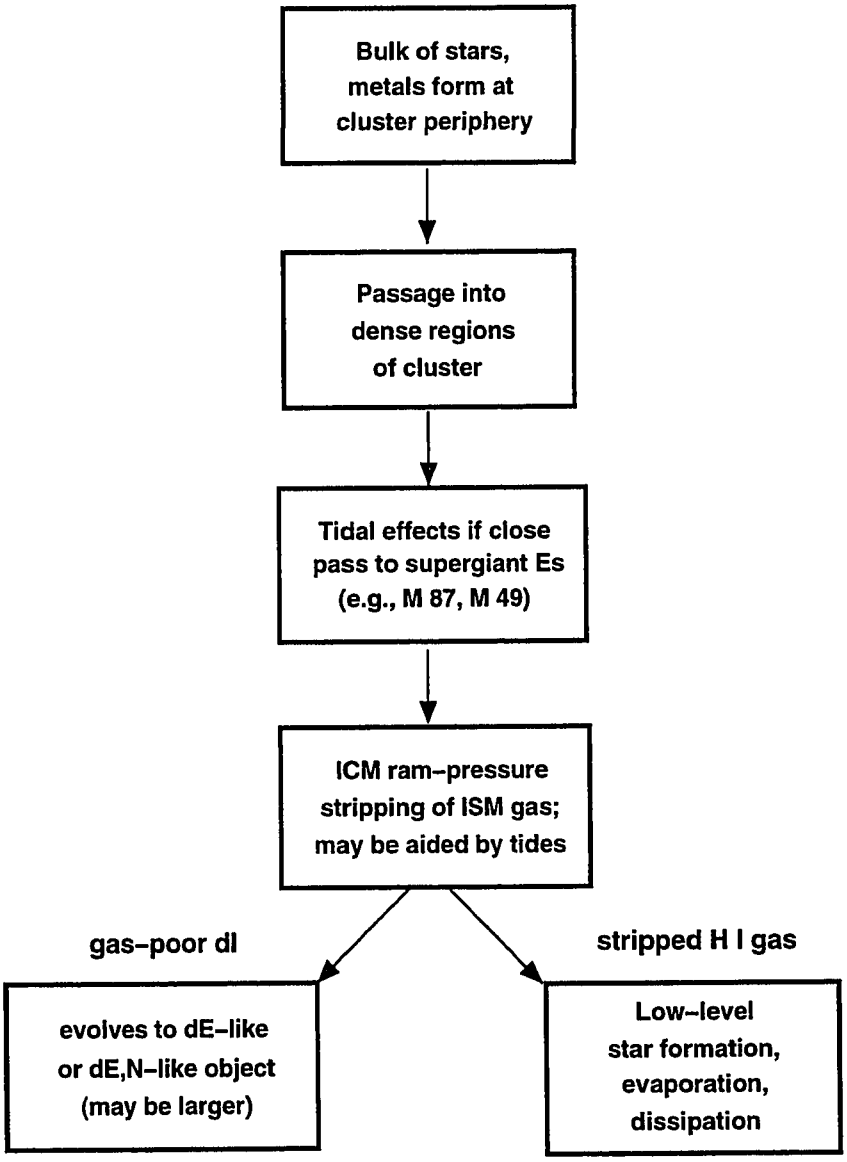

Figure 7.28: Suggested evolutionary path of a gas-poor dI in the Virgo Cluster.

(31.12 mag; § 2.2.2). Furthermore, if the distance to NGC 4258 obtained from masers is adopted as an independent zero-point (Herrnstein et al. 1999), the distance modulus for the LMC would be 18.38, placing the Virgo Cluster 0.43 mag closer than the distance adopted here. The total effect would be a systematic increase of 0.2 mag in M_B for field dIs and 0.43 mag in M_B for Virgo dIs listed in Table 7.2.

The distance revisions do not greatly affect the metallicity–luminosity diagram (Figure 7.2) or the metallicity–stellar mass diagram (Figure 7.7), because the shifts are much smaller than the dispersion of Virgo dIs around the fit to field dwarfs. More importantly, the revisions do not affect the metallicity–gas fraction diagram (Figure 7.14), because the gas fraction is independent of distance.

Conclusions stemming from evolutionary diagrams for an average gas-poor dI in Virgo (Figures 7.20 and 7.21) should not be strongly affected by revisions to distances. If the distance modulus for Virgo dIs is systematically lower, the "starting position" of an isolated dI on the evolutionary diagrams is shifted to lower M_*. Thus, ΔM_* is reduced. At the same time though, the estimated SFR goes down by an identical factor, i.e., SFR in Equation 7.98). Consequently, estimates of the time since stripping (Equation 7.99) do not depend upon the distance.

7.9.2 Dispersion in M_*–μ Relationship

Since chemical evolution requires measures of stellar and gaseous masses, a diagram of stellar mass against gas mass fraction is constructed to examine the effect of uncertainties. It is useful to examine how much of the dispersion in stellar mass observed in the metallicity–stellar mass relation arises from measurement errors and how much from some true physical dispersion in stellar mass.

Stellar mass, $\log M_*$, is plotted versus the gas fraction, $\log\log(1/\mu)$ for field and Virgo dIs in Figure 7.29. Typical errors in $\log M_*$ and $\log\log(1/\mu)$ are displayed.

These were obtained by combining the effects of a shift in distance modulus (0.2 mag for field dIs, 0.43 mag for Virgo dIs) and 0.05 mag of uncertainty in $B - V$ colour. For field dIs, errors are 0.1 dex in $\log M_*$ and 0.04 dex in $\log\log(1/\mu)$. For Virgo dIs, errors are 0.2 dex in $\log M_*$ and 0.04 dex in $\log\log(1/\mu)$. Because the gas fraction is independent of distance, the error in the gas fraction stems solely from the colour error.

Clearly, the dispersion of data points ($\sim$ 1 dex) in both the horizontal and vertical directions is much larger than the errors shown. At a given gas mass fraction, there is a wide range of stellar masses, which suggests that the time–averaged rate of conversion of gas into stars varies among individual dIs.

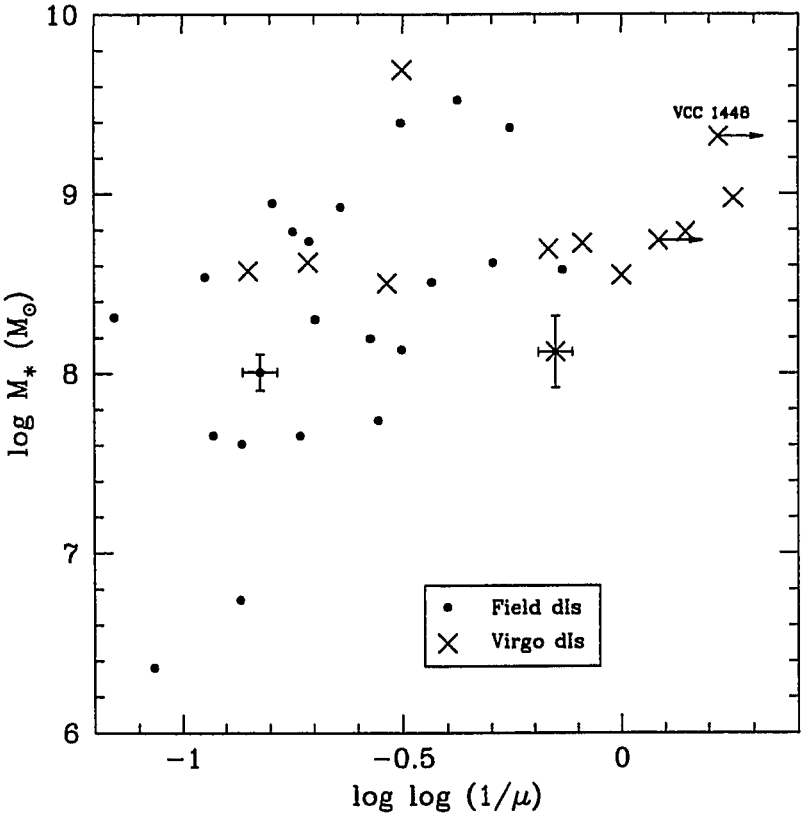

Figure 7.29: Stellar mass versus gas mass fraction for field and Virgo dIs. Filled circles and crosses represent field dIs and Virgo dIs, respectively. Upper limits to the H I gas mass are shown for VCC 1200 and VCC 1448. VCC 1448 is included, although no spectrum was measured. Error bars are displayed to indicate the effects of a 0.2 mag shift in distance modulus and 0.05 mag uncertainty in $B-V$ colour for field dIs, and the effects of a 0.43 mag shift in distance modulus and 0.05 mag uncertainty in $B-V$ colour for Virgo dIs.

Chapter 8

Conclusions

> "We do not ask for what purpose the birds do sing, for their song is pleasure since they were created for singing. Similarly, we ought not ask why the human mind troubles to fathom the secrets of the heavens. The diversity of the phenomena of Nature is so great, and the treasures hidden in the heavens so rich precisely in order that the human mind shall never be lacking in fresh nourishment." *Johannes Kepler*

Key results of this thesis are summarized in § 8.1 and perspectives on future research are discussed in § 8.2.

8.1 Summary of Results

The primary conclusion of this thesis is that a number of dwarf irregular galaxies in the Virgo Cluster have entered into dense regions of the cluster for the first time and have been rapidly stripped of their gaseous content via ram–pressure without significant effect on their luminosities and metallicities. The path to this conclusion is summarized below.

1. Dwarf irregular galaxies (dIs) are chosen for study over spirals or blue

compact dwarfs because dIs have very little dust, lack spiral arms, exhibit negligible metallicity gradients with radius, and contain H II regions whose light does not overwhelm their underlying stellar populations,

2. A sample of dIs in the field was created as a control group to study the evolution of dIs in clusters. Adopting the list constructed by Richer and McCall (1995), the sample was augmented with updates to distance determinations and oxygen abundance measurements from the literature. DDO 187 was also added to the sample. Oxygen abundances for five field dIs were updated from unpublished spectroscopy acquired at Steward Observatory and at the Mexican National Observatory.

3. A sample of dIs in the Virgo Cluster was constructed to examine the impact of the cluster environment on galaxy evolution. The dwarfs had to contain bright H II regions, they had to be spread among higher–density central regions and lower–density outer regions of the cluster, their luminosities had to lie within a narrow magnitude range between $-15 \gtrsim M_B \gtrsim -17$, and their H I masses had to vary by two orders of magnitude.

4. Optical spectroscopic data were obtained for eleven Virgo dIs at KPNO and CFHT. Because [O III]λ4363 was detected in VCC 0848 and VCC 1554, oxygen abundances could be directly determined. Oxygen abundances for the remaining dIs were derived using the bright–line method.

5. The "bright–line" method (R_{23}; also known as the empirical calibration) was used to compute oxygen abundances for objects for which [O III]λ4363 was not detected. The line ratio I([N II]λ6583)/I([O II]λ3727) was used

as a discriminant to break the degeneracy intrinsic to the method. Comparing with direct determinations, oxygen abundances obtained from the bright–line method were found to be accurate to $\sim$ 0.2 dex, with no obvious systematic differences.

6. For H II regions in Virgo dIs, equivalent widths of underlying Balmer absorption were directly measured via fits to Hβ line profiles. Resolving a long–standing problem, the equivalent width of the absorption was found to be between 3 and 7 Å, as expected for a typical OB association. However, the equivalent width of the underlying absorption effective in suppressing emission was found to be 1.59 ± 0.56 Å, consistent with previous measurements.

7. Stellar masses for field and Virgo dIs were derived using a two–component method (McCall, unpublished), which supposes that dIs consist only of a "young" component and an "old" component. The resulting stellar mass–to–light ratios in B ranged from 0.4 to 1.8, with most near unity. Stellar masses computed with the two–component method agreed with predictions of full–scale population syntheses for systems which have formed stars at a constant rate (Bruzual and Charlot 1996).

8. As found previously, a strong correlation between (O/H) and M_B exists for field dIs. Oxygen abundances of Virgo dIs were found to be comparable with field dIs at similar luminosities. The fit to field dIs in the metallicity–luminosity diagram was consistent with that found by Richer and McCall (1995). When the luminosity of the young component was removed, the slope was not significantly altered. However, the $M_{\rm HI}/L_B$ content for a number of Virgo dIs was considerably smaller than field dIs with similar

oxygen abundances, suggesting that their evolution has been affected by their environment.

9. Extrapolating to zero oxygen abundance, the range in minimum baryonic mass required to form metals is $\log M_{\rm bary}(M_\odot) \simeq 6.2$ to 7.5. This is roughly similar to galaxies with the lowest masses known.

10. A strong correlation between oxygen abundance and the gas fraction, defined as the ratio of gas mass to the total baryonic mass, was found for field dIs, revealing that they have evolved as isolated systems. This result did not depend critically upon the details of the population synthesis employed. The effective oxygen yield by mass was about one–quarter of that found in the solar neighbourhood. A number of Virgo dIs were noticeably gas–deficient compared to field dIs at a similar oxygen abundance.

11. Using the observed relation between oxygen abundance and gas fraction for field dIs, it was possible to define a gas–deficiency index for dwarfs: GDI $\equiv \log[(\mu_p/\mu) \cdot (1-\mu)/(1-\mu_p)]$, where μ and μ_p are, respectively, the observed gas fraction and the gas fraction predicted using the correlation for field dIs. A comparison of indices for field and Virgo dwarfs directly led to the quantitative identification of five gas–poor Virgo dIs. A Kolmogorov–Smirnov test showed that the field and Virgo samples could not have been drawn from the same distribution.

12. The Virgo dwarf galaxy UGC 7636 (VCC 1249) was presented as a case study for the impact of the Virgo intracluster environment on dI evolution (Lee, Richer, and McCall 2000). An H II region, LR1, was serendipitously discovered residing within the H I cloud STE1, which is located between

the dI and the giant elliptical M 49 (NGC 4472). A spectrum was obtained and an oxygen abundance was derived. The oxygen abundance was consistent with what was expected for a galaxy with the luminosity of UGC 7636. Intracluster ram–pressure and tidal forces from M 49 are believed to explain the absence of H I gas and the unusually large exponential scale length for the stellar disk of UGC 7636. Based upon the oxygen abundance for LR1 and the H I mass of STE1, the H I cloud must have once been the interstellar medium of the dwarf galaxy.

13. The existence of STE1 in proximity to UGC 7636 suggests that UGC 7636 was stripped recently and that the duration of the event was relatively short. This motivated the construction of "staged" models to evaluate the past evolution of gas–deficient dIs. The models revealed that so little time has elapsed since stripping that there has been little evolution of the stripped dI remnant. Gas loss ceased $\lesssim 1$ Gyr ago, which is comparable to the crossing timescale in the Virgo Cluster.

14. The gas deficiency was found to be correlated with X–ray surface brightness, but not with relative velocity or ram–pressure. The first correlation is compelling evidence that gas loss was a consequence of ram pressure. The lack of any strong correlation with the ram pressure itself is likely due to inadequate account of transverse motions. The results suggest that dIs are traversing the dense regions of the cluster for the first time.

15. If star formation completely stopped, stripped gas–poor dIs would fade by about 0.6 mag in B and redden by about 0.2 mag in $B-V$ in about 1 Gyr. While gas–poor dIs have been found to be structurally similar to nucleated dEs/dSphs, the former do not have prominent nuclei. The progenitors of

nucleated dEs were not likely to have been dIs. Instead, gas–poor dIs will likely fade into systems resembling present–day dEs/dSphs.

8.2 Future Projects

The following investigations would be valuable:

1. expansion of the spectroscopic sample of Virgo dwarfs to include a larger range in luminosity;
2. expansion of the sample of dwarf galaxies to include BCDs;
3. deep Hα imaging of the Virgo Cluster to search for intracluster H II regions (e.g., LR1 with UGC 7636), which may be missed by planetary nebulae surveys (Méndez et al. 1997; Ciardullo et al. 1998; Feldmeier et al. 1998);
4. a survey of dwarf galaxies in the Fornax Cluster; and
5. near–infrared imaging of dIs and BCDs.

By adding more galaxies to the sample studied, the first two investigations would augment the results obtained in this thesis in a statistical sense. Each of the aforementioned points is discussed below. Also, the Chandra AXAF observatory should be used to observe in detail the area immediately surrounding LR1 and STE1 to look for evidence of evaporation of the H I gas by the intracluster medium (e.g., Stevens et al. 1999).

The eleven dIs in the present Virgo sample are distributed in the central and outer regions of the cluster. All but one of the eleven lie within a two–magnitude interval of M_B. Because many other Virgo Cluster dwarf galaxies contain H II regions (Gallagher and Hunter 1989; Heller et al. 1999), a study of additional dwarfs is warranted to expand the coverage in luminosity and to better evaluate the effectiveness of ram pressure stripping as a function of luminosity.

A larger number of dwarfs with a wide range of gas masses and measured oxygen abundances is needed to verify that GDI ≈ 0.8 is sufficient to define a "threshold" for gas deficiency in dwarfs. The results for gas–poor dIs motivate study of the BCDs in the Virgo Cluster. The central H II regions in BCDs should be sufficiently bright for [O III]λ4363 to be detected.

The discovery of LR1 (as well as recent discoveries of intracluster stars and planetary nebulae) in the Virgo Cluster provides real impetus to search for additional intracluster H II regions. Deep Hα imaging should be directed to fields surrounding gas–poor Virgo dwarfs. If LR1 and STE1 are typical consequences of a recent passage through the intracluster medium, there may be additional signatures of recent star formation. It is very unlikely that the LR1–STE1–UGC 7636 system is the only one to be found within the Virgo Cluster.

The Fornax Cluster is approximately at the same distance as the Virgo Cluster (Madore et al. 1999), but exhibits far different properties from Virgo (Ferguson 1989b). Fornax is denser, smaller, and appears more "relaxed" (not much substructure). Compared to Virgo, Fornax has a larger central galaxy number density, a smaller core radius, and a smaller cluster velocity dispersion (Ferguson 1989b; Ferguson 1989a). Also, the X–ray luminosity, which measures the strength of the intracluster medium, is about two orders of magnitude lower in Fornax compared to Virgo (Killeen and Bicknell 1988; Edge and Stewart 1991; Böhringer et al. 1994; Jones et al. 1997). It would be timely to investigate whether the fraction of stripped systems is lower than in Virgo. Optical spectra in addition to optical and near–infrared photometry of dwarf galaxies should be obtained. Comparing the properties of dwarfs in Fornax and Virgo could highlight *intercluster* differences which lead to further insights into the effect of the intracluster environment on dwarfs. Because there are few giant galaxies and a more rarefied intracluster medium in Fornax, dwarf galaxies

are less likely to be stripped as they pass through the central regions of the cluster.

Total magnitudes for galaxies in B are perturbed by the young component, although Papaderos et al. (1996) and Patterson and Thuan (1996) claim that the contribution by H II regions is at most 0.75 mag in B. Near–infrared imaging is advantageous because the spectral energy distribution of old stars peaks in the near–infrared and the contribution of hot young stars is lessened. Thus, the contribution of light from recent bursts of star formation to the overall galaxy luminosity at near–infrared wavelengths is expected to be much smaller than at blue wavelengths. Certainly, Kunth and Östlin (2000; their § 5.1.2) and Östlin (2000) have shown that BCDs (e.g., I Zw 18) should contain old stars that dominate the underlying stellar mass. Thus, galaxy luminosities at near–infrared wavelengths should be truer measures of the underlying stellar mass.

Observing programs are already planned to obtain near–infrared images of dIs in the Local Group and dIs and BCDs in the Virgo Cluster. Global parameters (e.g., $M_{K'}$, M_*) will be derived to construct diagnostics (metallicity versus luminosity, metallicity versus gas fraction) in the near–infrared to examine whether the dispersion in these relationships will be lessened.

"El viento de la noche gira en el cielo y canta.
El viento de la noche gira en el cielo.
Oir la noche inmensa, mas inmensa sin ella.
Y el verso cae al alma como al pasto el rocío."
"Puedo Escribir" – Pablo Neruda

"Fais que ton rêve soit plus long que la nuit."

Bibliography

Aaronson, M., 1986. The Older Stellar Population of Dwarf Galaxies. In D. Kunth, T. X. Thuan, and J. T. T. Van (Eds.), *Star Forming Dwarf Galaxies and Related Objects*, pp. 125. Paris: Editions Frontiéres.

Aaronson, M., J. G. Cohen, J. Mould, and M. Malkan, 1978. *ApJ*, **223**, 824.

Abadi, M. G., B. Moore, and R. G. Bower, 1999. *MNRAS*, **308**, 947.

Afflerbach, A., E. Churchwell, J. M. Acord, P. Hofner, S. Kurtz, and C. G. Depree, 1996. *ApJS*, **106**, 423.

Aller, L. H., 1984. *Physics of Thermal Gaseous Nebulae*. Dordrecht: Reidel.

Alloin, D., S. Colin-Souffrin, M. Joly, and L. Virgroux, 1979. *A&A*, **78**, 200.

Almoznino, E. and N. Brosch, 1998a. *MNRAS*, **298**, 920.

Almoznino, E. and N. Brosch, 1998b. *MNRAS*, **298**, 931.

Aloisi, A., M. Tosi, and L. Greggio, 1999. *AJ*, **118**, 302.

Arnaud, M. and A. E. Evrard, 1999. *MNRAS*, **305**, 631.

Arnaud, M., R. Rothenflug, O. Boulade, L. Vigroux, and E. Vangioni-Flam, 1992. *A&A*, **254**, 49.

Ashman, K. M., 1992. *PASP*, **104**, 1109.

Audouze, J. and B. M. Tinsley, 1976. *ARA&A*, **14**, 43.

Babul, A. and H. C. Ferguson, 1996. *ApJ*, **458**, 100.

Babul, A. and M. J. Rees, 1992. *MNRAS*, **255**, 346.

Bahcall, J. N., 1984. *ApJ*, **287**, 926.

Bahcall, J. N. and S. Casertano, 1986. *ApJ*, **308**, 347.

Bahcall, J. N., C. Flynn, and A. Gould, 1992. *ApJ*, **389**, 234.

Bahcall, J. N. and R. M. Soneira, 1984. *ApJS*, **55**, 67.

Bahcall, N. A., 1997. "Large–Scale Structure in the Universe". In J. N. Bahcall and J. P. Ostriker (Eds.), *Unsolved Problems in Astrophysics*, pp. 61 (Chapter 4). Princeton: Princeton University Press. Also preprint: `astro-ph/9612046`.

Bahcall, N. A., 1999. Clusters and superclusters of galaxies. In A. Dekel and J. P. Ostriker (Eds.), *Formation of Structure in the Universe*, pp. 136 (Chapter 4). Cambridge: Cambridge University Press. Also preprint: `astro-ph/9611148`.

Baldwin, J. A., M. M. Phillips, and R. Terlevich, 1981. *PASP*, **93**, 5.

Barnes, J. and L. Hernquist, 1991. *ApJ*, **370**, L65.

Baugh, C. M., S. Cole, and C. S. Frenk, 1996. *MNRAS*, **283**, 1361.

Bekki, K., W. J. Couch, M. J. Drinkwater, and M. D. Gregg, 2001. *ApJ*, **557**, L39.

Bender, R., D. Burstein, and S. M. Faber, 1992. *ApJ*, **399**, 462.

Bertschinger, E., 1998. *ARA&A*, **36**, 599.

Bhatia, A. K. and S. O. Kastner, 1995. *ApJS*, **96**, 325.

Binggeli, B., 1994. A Note on the Definition and Nomenclature of Dwarf Galaxies. In G. Meylan and P. Prugniel (Eds.), *Dwarf Galaxies: ESO/OHP Conference and Workshop Proceedings*, Volume 49 of *ESO Conference and Workshop Proceedings*, pp. 13. Garching bei München: European Southern Observatory.

Binggeli, B., 2000. "The Virgo Cluster - Home of M87". Retrieved document October 1, 2000, from the World Wide Web[1]. Level 5, A Knowledgebase for Extragalactic Astronomy and Cosmology, NASA/IPAC Extragalactic Database (NED).

Binggeli, B. and L. M. Cameron, 1993. *A&AS*, **98**, 297.

Binggeli, B., C. C. Popescu, and G. A. Tammann, 1993. *A&AS*, **98**, 275.

Binggeli, B., A. Sandage, and G. A. Tammann, 1985. *AJ*, **90**, 1681.

Binggeli, B., A. Sandage, and M. Tarenghi, 1984. *AJ*, **89**, 64.

Binggeli, B., G. A. Tammann, and A. Sandage, 1987. *AJ*, **94**, 251.

Binggeli, B., M. Tarenghi, and A. Sandage, 1990. *A&A*, **228**, 42.

Binney, J. and S. Tremaine, 1987. *Galactic Dynamics.* Princeton: Princeton University Press.

Blitz, L. and T. Robishaw, 2000. *ApJ*, **541**, 675.

Böhringer, H., U. G. Briel, R. A. Schwarz, W. Voges, G. Hartner, and J. Trümper, 1994. *Nature*, **368**, 828.

Boselli, A., R. J. Tuffs, G. Gavazzi, H. Hippelein, and D. Pierini, 1997. *A&AS*, **121**, 507.

Bothun, G. D., 1982. *ApJS*, **50**, 39.

Bothun, G. D., J. Eriksen, and J. M. Schombert, 1994. *AJ*, **108**, 913.

Bothun, G. D., C. Impey, and S. McGaugh, 1997. *PASP*, **109**, 745.

Bothun, G. D., C. D. Impey, D. F. Malin, and J. R. Mould, 1987. *AJ*, **94**, 23.

[1]URL: `http://ned.ipac.caltech.edu/level5/Binggeli/Bin5.html`

Bothun, G. D., J. R. Mould, N. Caldwell, and H. T. MacGillivray, 1986. *AJ*, **92**, 1007.

Bothun, G. D., J. R. Mould, A. Wirth, and N. Caldwell, 1985. *AJ*, **90**, 697.

Brocato, E., F. Matteucci, I. Mazzitelli, and A. Tornambé, 1990. *ApJ*, **349**, 458.

Brosch, N., A. Heller, and E. Almoznino, 1998. *ApJ*, **504**, 720.

Bruzual, G. and S. Charlot, 1993. *ApJ*, **405**, 538.

Bruzual, G. and S. Charlot, 1996. Vol. 7, Astrophysics on Disc (Washington: AAS). AAS CD-ROM Series. See also § 6.4, Leitherer et al. (1996).

Burkert, A., 1993. *J. Phys. G: Nucl. Part. Phys.*, **19**, S171.

Burkert, A., 1994. *Reviews in Modern Astronomy*, **7**, 191.

Burrows, A., 2000. *Nature*, **403**, 727.

Burstein, D. and C. Heiles, 1982. *AJ*, **87**, 1165.

Burton, W. B. and E. R. Deul, 1987. The morphology of cool, diffuse gas and dust in the Galaxy. In G. Gilmore and B. Carswell (Eds.), *The Galaxy*, pp. 141. Dordrecht: Reidel.

Buta, R. J. and M. L. McCall, 1999. *ApJS*, **124**, 33.

Byrd, G. and M. Valtonen, 1990. *ApJ*, **350**, 89.

Cardelli, J. A., G. C. Clayton, and J. S. Mathis, 1989. *ApJ*, **345**, 245.

Cayatte, V., C. Kotanyl, C. Balkowski, and J. H. van Gorkom, 1994. *AJ*, **107**, 1003.

Charlot, S. and G. Bruzual, 1991. *ApJ*, **367**, 126.

Ciardullo, R., G. H. Jacoby, J. J. Feldmeier, and R. E. Bartlett, 1998. *ApJ*, **492**, 62.

Cole, A. A., E. Tolstoy, J. S. Gallagher, J. G. Hoessel, J. R. Mould, J. A. Holtzman, A. Saha, G. E. Ballester, C. J. Burrows, J. T. Clarke, D. Crisp, R. E. Griffiths, C. J. Grillmair, J. J. Hester, J. E. Krist, V. Meadows, P. A. Scowen, K. R. Stapelfeldt, J. T. Trauger, A. M. Watson, and J. R. Westphal, 1999. *AJ*, **118**, 1657.

Cole, S. M., 1991. *ApJ*, **367**, 45.

Cole, S. M., A. Aragón-Salamanca, C. S. Frenk, J. F. Navarro, and S. E. Zepf, 1994. *MNRAS*, **271**, 781.

Conselice, C. J., J. S. Gallagher, and R. F. G. Wyse, 2001. *ApJ*, **559**, 791.

Côté, S., K. Freeman, and C. Carignan, 1997. Mass–Models of Five Nearby Dwarf Irregular Galaxies. In M. Persic and P. Salucci (Eds.), *Dark and Visible Matter in Galaxies*, Volume 117 of *A.S.P. Conference Series*, pp. 52. San Francisco: Astron. Soc. of the Pacific. Also preprint: `astro-ph/9704031`.

Côté, S., K. C. Freeman, C. Carignan, and P. J. Quinn, 1997. *AJ*, **114**, 1313.

Cowie, L. L., 1981. *ApJ*, **245**, 66.

Cowie, L. L. and C. F. McKee, 1977. *ApJ*, **211**, 135.

Cowie, L. L. and A. Songaila, 1977. *Nature*, **266**, 501.

Davidson, K. and T. D. Kinman, 1985. *ApJS*, **58**, 321.

Davies, J. I. and S. Phillipps, 1988. *MNRAS*, **233**, 533.

Davies, J. I. and S. Phillipps, 1989. *Astr. Sp. Sci.*, **157**, 291.

de Vaucouleurs, G., 1948. *Annales d'Astrophysique*, **11**, 247.

de Vaucouleurs, G. and W. D. Pence, 1978. *AJ*, **83**, 1163.

Dekel, A. and J. Silk, 1986. *ApJ*, **303**, 39.

DellaCeca, R., R. E. Griffiths, and T. M. Heckman, 1997. *ApJ*, **485**, 581.

DeRobertis, M. M., R. J. Dufour, and R. W. Hunt, 1987. *JRASC*, **81**, 195.

Devost, D., J.-R. Roy, and L. Drissen, 1997. *ApJ*, **482**, 765.

Díaz, A. I., 1988. *MNRAS*, **231**, 57.

Dinerstein, H. L., 1990. Abundances in Extragalactic H II Regions. In H. A. Thronson and J. M. Shull (Eds.), *The Interstellar Medium in Galaxies*, pp. 257. Dordrecht: Kluwer Academic Publishers.

Dohm-Palmer, R. C., E. D. Skillman, J. Gallagher, E. Tolstoy, M. Mateo, R. J. Dufour, A. Saha, J. Hoessel, and C. Chiosi, 1998. *AJ*, **116**, 1227.

Donahue, M., 1998. Origins of Clusters and the Intracluster Medium. In C. E. Woodward, J. M. Shull, and H. A. Thronson (Eds.), *Origins*, Volume 148 of *A.S.P. Conference Series*, pp. 109. San Francisco: Astron. Soc. of the Pacific.

Dopita, M. A. and I. N. Evans, 1986. *ApJ*, **307**, 431.

Draper, N. R. and H. Smith, 1998. *Applied Regression Analysis*. New York: Wiley. §3.4, pg. 89.

Dressler, A., 1980. *ApJ*, **236**, 351.

Dressler, A., 1986. *ApJ*, **301**, 35.

Drinkwater, M. and E. Hardy, 1991. *AJ*, **101**, 94.

Drinkwater, M. J., M. J. Currie, C. K. Young, E. Hardy, and J. M. Yearsley, 1996. *MNRAS*, **279**, 595.

Driver, S. P. and N. Cross, 2000. The Parameter Space Occupied by Galaxies:

The Optical Window. In R. C. Kraan-Korteweg, P. A. Henning, and H. Andernach (Eds.), *Mapping the Hidden Universe*, Volume 218 of *A.S.P. Conference Series*, pp. 309. San Francisco: Astron. Soc. of the Pacific. Also preprint: `astro-ph/0004201`.

Driver, S. P., R. A. Windhorst, and R. E. Griffiths, 1995. *ApJ*, **453**, 48.

Durrell, P. R., 1997. *AJ*, **113**, 531.

Edge, A. C. and G. C. Stewart, 1991. *MNRAS*, **252**, 428.

Edmunds, M. G., 1990. *MNRAS*, **246**, 678.

Edmunds, M. G. and B. E. J. Pagel, 1978. *MNRAS*, **185**, 77P.

Edmunds, M. G. and B. E. J. Pagel, 1984. *MNRAS*, **211**, 507.

Eggen, O. J., D. Lynden-Bell, and A. Sandage, 1962. *ApJ*, **136**, 748.

Ellis, R. S., 1997. *ARA&A*, **35**, 389.

Ellis, R. S., 1998. The Hubble Deep Field: Introduction and Motivation. In M. Livio, S. M. Fall, and P. Madau (Eds.), *The Hubble Deep Field*, Volume 11 of *Space Telescope Science Institute Symposium Series*, pp. 27. Cambridge: Cambridge University Press.

Elmegreen, D. M., B. G. Elmegreen, F. R. Chromey, and M. S. Fine, 2000. *AJ*, **120**, 733.

Erasmus, D., 1510. *Moriae encomium ("In Praise of Folly")*. London: Allen & Unwin (1951).

Fabbiano, G., D.-W. Kim, and G. Trinchieri, 1992. *ApJS*, **80**, 531.

Faber, S. M. and D. N. C. Lin, 1983. *ApJ*, **266**, 17.

Feast, M. W., 1987. Galactic Distance Scales. In G. Gilmore and B. Carswell (Eds.), *The Galaxy*, pp. 1. Dordrecht: Reidel.

Feibelman, W. A., S. Hyung, and L. H. Aller, 1994. *ApJ*, **426**, 653.

Feldmeier, J. J., R. Ciardullo, and G. H. Jacoby, 1998. *ApJ*, **503**, 109.

Ferguson, H. C., 1989a. *Astrophys. Sp. Sci.*, **157**, 227.

Ferguson, H. C., 1989b. *AJ*, **98**, 367.

Ferguson, H. C. and A. Babul, 1998. *MNRAS*, **296**, 585.

Ferguson, H. C. and B. Binggeli, 1994. *A&A Rv*, **6**, 67. Also preprint: `astro-ph/9409079`.

Ferguson, H. C., N. R. Tanvir, and T. von Hippel, 1998. *Nature*, **391**, 461.

Ferrara, A. and E. Tolstoy, 2000. *MNRAS*, **313**, 291.

Ferrarese, L., W. L. Freedman, R. J. Hill, A. Saha, B. F. Madore, R. C. Kennicutt, P. B. Stetson, H. C. Ford, J. A. Graham, J. G. Hoessel, M. Han, J. Huchra, S. M. Hughes, G. D. Illingworth, D. Kelson, J. R. Mould, R. Phelps, N. A. Silbermann, S. Sakai, A. Turner, P. Harding, and F. Bresolin, 1996. *ApJ*, **464**, 568 (erratum: 1997, *ApJ*, **475**, 853).

Forman, W., C. Jones, and W. Tucker, 1985. *ApJ*, **293**, 102.

Freedman, W. L., B. F. Madore, B. K. Gibson, L. Ferrarese, D. D. Kelson, S. Sakai, J. R. Mould, R. C. Kennicutt, H. C. Ford, J. A. Graham, J. P. Huchra, S. M. G. Hughes, G. D. Illingworth, L. M. Macri, and P. B. Stetson, 2001. *ApJ*, **553**, 47.

Gallagher, J. S. and D. A. Hunter, 1984. *ARA&A*, **22**, 37.

Gallagher, J. S. and D. A. Hunter, 1985. *ApJS*, **58**, 533.

Gallagher, J. S. and D. A. Hunter, 1986. *AJ*, **92**, 557.

Gallagher, J. S. and D. A. Hunter, 1989. *AJ*, **98**, 806.

Gallagher, J. S., D. A. Hunter, and A. V. Tutukov, 1984. *ApJ*, **284**, 544.

Gallagher, J. S. and R. F. G. Wyse, 1994. *PASP*, **106**, 1225.

Gallart, C., A. Aparicio, and J. M. Vílchez, 1996. *AJ*, **112**, 1928.

Garnett, D. R., 1990. *ApJ*, **363**, 142.

Garnett, D. R. and G. A. Shields, 1987. *ApJ*, **317**, 82.

Gavazzi, G., A. Boselli, M. Scodeggio, D. Pierini, and E. Belsole, 1999. *MNRAS*, **304**, 595.

Gibson, B. K. and F. Matteucci, 1997. *ApJ*, **475**, 47.

Gilmore, G. F. and R. F. G. Wyse, 1991. *ApJ*, **367**, L55.

Gilmore, G. F., R. F. G. Wyse, and K. Kuijken, 1989. *ARA&A*, **27**, 555.

Giovanelli, R. and M. P. Haynes, 1985. *ApJ*, **292**, 404.

Giraud, E., 1986. *A&A*, **167**, 25.

González-Delgado, R. M., C. Leitherer, and T. M. Heckman, 1999. *ApJS*, **125**, 489.

González-Delgado, R. M., E. Pérez, G. Tenorio-Tagle, J. M. Vílchez, E. Terlevich, R. Terlevich, E. Telles, J. M. Rodríguez-Espinosa, M. Mas-Hesse, M. L. García-Vargas, A. I. Díaz, J. Cepa, and H. Castañeda, 1994. *ApJ*, **437**, 239.

Gorgas, J., S. Pedraz, R. Guzmán, N. Cardiel, and J. J. González, 1997. *ApJ*, **481**, L19.

Gould, A., 1990. *MNRAS*, **244**, 25.

Graham, J. A., L. Ferrarese, W. L. Freedman, R. C. Kennicutt, J. R. Mould, A. Saha, P. B. Stetson, B. F. Madore, F. Bresolin, H. C. Ford, B. K. Gibson, M. Han, J. G. Hoessel, J. Huchra, S. M. Hughes, G. D. Illingworth, D. D.

Kelson, L. Macri, R. Phelps, S. Sakai, N. A. Silbermann, and A. Turner, 1999. *ApJ*, **516**, 626.

Grebel, E. K., 1997. *Reviews in Modern Astronomy*, **10**, 29.

Grebel, E. K., 1999. Evolutionary Histories of Dwarf Galaxies in the Local Group. In P. Whitelock and R. Cannon (Eds.), *The Stellar Content of the Local Group*, IAU Symposium 192, pp. 17. San Francisco: Astronomical Society of the Pacific.

Grebel, E. K., 2000. The Star Formation History of the Local Group. In F. Favata, A. A. Kaas, and Wilson (Eds.), *Star Formation from the Small to the Large Scale*, 33rd ESLAB Symposium (ESA-SP-445). Invited review; preprint: `astro-ph/0005296`.

Grebel, E. K., 2001. Star Formation Histories of Nearby Dwarf Galaxies. In J. Vílchez, G. Stasińska, and E. Perez (Eds.), *"The Evolution of Galaxies." I. Observational Clues*, 1st Euroconference, The Evolution of Galaxies, DAEC. Dordrecht: Kluwer Academic Publishers. Invited review; preprint: `astro-ph/0011048`.

Grebel, E. K. and P. Guhathakurta, 1999. *ApJ*, **511**, L101.

Greggio, L., M. Tosi, M. Clampin, G. D. Marchi, C. Leitherer, A. Nota, and M. Sirianni, 1998. *ApJ*, **504**, 725.

Grevesse, N., A. Noels, and A. J. Sauval, 1996. Standard Abundances. In S. S. Holt and G. Sonneborn (Eds.), *Cosmic Abundances: Proceedings of the 6th Annual October Astrophysics Conference*, Volume 99 of *A.S.P. Conference Series*, pp. 117. San Francisco: Astron. Soc. of the Pacific.

Gunn, J. E. and J. R. Gott, 1972. *ApJ*, **176**, 1.

Guzman, R., J. Gallego, D. C. Koo, A. C. Phillips, J. D. Lowenthal, S. M. Faber, G. D. Illingworth, and N. P. Vogt, 1997. *ApJ*, **489**, 559.

Guzman, R., A. Jangren, D. C. Koo, M. A. Bershady, and L. Simard, 1998. *ApJ*, **495**, L13.

Habing, H. J., 1987. Highly evolved stars in the Galaxy as seen by IRAS and in OH surveys. In G. Gilmore and B. Carswell (Eds.), *The Galaxy*, pp. 173. Dordrecht: Reidel.

Hayes, D. S., 1978. The Absolute Calibration of the HR Diagram – Fundamental Effective Temperatures and Bolometric Corrections. In A. G. D. Philip and D. S. Hayes (Eds.), *IAU Symp. 80: The HR Diagram -The 100th Anniversary of Henry Norris Russell*, pp. 65. Dordrecht: Reidel.

Haynes, M. P., 1989. Evidence for Gas Deficiency in Cluster Galaxies. In W. R. Oegerle, M. J. Fitchett, and L. Danly (Eds.), *Clusters of Galaxies: Proceedings of the Clusters of Galaxies Meeting*, Space Telescope Science Institute Symposium Series 4, pp. 177. Cambridge: Cambridge University Press.

Haynes, M. P. and R. Giovanelli, 1984. *AJ*, **89**, 758.

Haynes, M. P. and R. Giovanelli, 1986. *ApJ*, **306**, 466.

He, X.-T. and C. D. Impey, 1986. *MNRAS*, **221**, 727.

Heckman, T. M., M. Dahlem, M. D. Lehnert, G. Fabbiano, D. Gilmore, and W. H. Waller, 1995. *ApJ*, **448**, 98.

Heller, A., E. Almoznino, and N. Brosch, 1999. *MNRAS*, **304**, 8.

Helmi, A., S. D. M. White, P. T. de Zeeuw, and H. Zhao, 1999. *Nature*, **402**, 53.

Henning, P. A., R. Sancisi, and B. R. McNamara, 1993. *A&A*, **268**, 536.

Henriksen, M. J. and G. Byrd, 1996. *ApJ*, **459**, 82.

Henry, R. B. C., M. G. Edmunds, and J. Köppen, 2000. *ApJ*, **541**, 660.

Henry, R. B. C., B. E. J. Pagel, and G. L. Chincarini, 1994. *MNRAS*, **266**, 421.

Henry, R. B. C., B. E. J. Pagel, D. F. Lasseter, and G. L. Chincarini, 1992. *MNRAS*, **258**, 321.

Herrnstein, J. R., J. M. Moran, L. J. Greenhill, P. J. Diamond, M. Inoue, N. Nakai, M. Miyoshi, C. Henkel, and A. Riess, 1999. *Nature*, **400**, 539.

Hidalgo-Gámez, A. M. and K. Olofsson, 1998. *A&A*, **334**, 45.

Hills, J. G., 1980. *ApJ*, **225**, 986.

Ho, L. C., A. V. Filippenko, and W. L. W. Sargent, 1995. *ApJS*, **98**, 477.

Ho, L. C., A. V. Filippenko, and W. L. W. Sargent, 1997. *ApJS*, **112**, 315.

Hodge, P., 1966. *ApJ*, **144**, 869.

Hodge, P., 1971. *ARA&A*, **9**, 35.

Hodge, P. and M. G. Lee, 1990. *PASP*, **102**, 26.

Hodge, P. and B. W. Miller, 1995. *ApJ*, **451**, 176.

Hodge, P., N. V. Strobel, and R. C. Kennicutt, 1994. *PASP*, **106**, 309.

Hoessel, J. G., A. Saha, and G. E. Danielson, 1998a. *AJ*, **115**, 573 (Holmberg II).

Hoessel, J. G., A. Saha, and G. E. Danielson, 1998b. *AJ*, **116**, 1679 (DDO 187).

Hoessel, J. G., A. Saha, J. Krist, and G. E. Danielson, 1994. *AJ*, **108**, 645.

Hoffman, G. L., J. Glosson, G. Helou, E. E. Salpeter, and A. Sandage, 1987. *ApJS*, **63**, 247.

Hoffman, G. L., G. Helou, and E. E. Salpeter, 1988. *ApJ*, **324**, 75.

Hoffman, G. L., N. Y. Lu, E. E. Salpeter, and B. M. Connell, 1999. *AJ*, **117**, 811.

Hoffman, G. L., E. E. Salpeter, B. Farhat, T. Roos, H. Williams, and G. Helou, 1996. *ApJS*, **105**, 269.

Hoffman, G. L., H. L. Williams, E. E. Salpeter, A. Sandage, and B. Binggeli, 1989. *ApJS*, **71**, 701.

Holtzman, J. A., J. R. Mould, J. S. Gallagher, A. M. Watson, C. J. Grillmair, G. E. Ballester, C. J. Burrows, J. T. Clarke, D. Crisp, R. W. Evans, R. E. Griffiths, J. J. Hester, J. G. Hoessel, P. A. Scowen, K. R. Stapelfeldt, J. T. Trauger, and J. A. Westphal, 1997. *AJ*, **113**, 656.

Huchtmeier, W. K. and O. G. Richter, 1986. *A&AS*, **63**, 323.

Hunter, D., 1997. *PASP*, **109**, 319.

Hunter, D. A. and J. S. Gallagher, 1985. *ApJS*, **58**, 533.

Hunter, D. A. and J. S. Gallagher, 1986. *PASP*, **98**, 5.

Hunter, D. A. and J. S. Gallagher, 1989. *Science*, **243**, 1557.

Hunter, D. A., W. N. Hawley, and J. S. Gallagher, 1993. *AJ*, **106**, 1797.

Hunter, D. A. and L. Hoffman, 1999. *AJ*, **117**, 2789.

Hunter, D. A. and J. D. Plummer, 1996. *ApJ*, **462**, 732.

Hunter, D. A. and L. Sage, 1993. *PASP*, **105**, 374.

Ibata, R., M. Irwin, G. Lewis, A. M. N. Ferguson, and N. Tanvir, 2001. *Nature*, **412**, 49.

Ibata, R. A., G. Gilmore, and M. J. Irwin, 1994. *Nature*, **370**, 194.

Impey, C. and G. Bothun, 1989. *ApJ*, **341**, 89.

Impey, C. and G. Bothun, 1997. *ARA&A*, **35**, 267.

Impey, C., G. Bothun, and D. Malin, 1988. *ApJ*, **330**, 634.

Irwin, J. A., D. T. Frayer, and C. L. Sarazin, 1997. *AJ*, **113**, 1580.

Irwin, J. A. and C. L. Sarazin, 1996. *ApJ*, **471**, 683.

Israel, F. P., L. J. Tacconi, and F. Baas, 1995. *A&A*, **295**, 599.

Izotov, Y. I. and N. G. Guseva, 1990. *Astrophysics (tr. Astrofizika)*, **30**, 347.

Izotov, Y. I. and T. X. Thuan, 1999. *ApJ*, **511**, 639.

Izotov, Y. I., T. X. Thuan, and V. A. Lipovetsky, 1997. *ApJS*, **108**, 1.

James, P., C. Bate, M. Wells, G. Wright, and R. Doyon, 1999. *MNRAS*, **309**, 585.

James, P. A., 1991. *MNRAS*, **250**, 544.

James, P. A., 1994. *MNRAS*, **269**, 176.

Jaschek, C. and M. Jaschek, 1995. *The Behavior of Chemical Elements in Stars.* Cambridge: Cambridge University Press.

Johnston, K. V., 1998. *ApJ*, **495**, 297.

Jones, C. and W. Forman, 1984. *ApJ*, **276**, 38.

Jones, C. and W. Forman, 1992. Imaging the Hot Intracluster Medium. In A. C. Fabian (Ed.), *Clusters and Superclusters of Galaxies*, NATO ASI Series 366, pp. 49. Dordrecht: Kluwer Academic Publishers.

Jones, C., C. Stern, W. Forman, J. Breen, L. David, and W. Tucker, 1997. *ApJ*, **482**, 143.

Kaler, J. B., 1983. *ApJ*, **264**, 594.

Karachentseva, V. E., 1973. *Comm. Spec. Astrophys. Obs.*, **8**, 1.

Kelson, D. D., G. D. Illingworth, W. F. Freedman, J. A. Graham, R. Hill, B. F. Madore, A. Saha, P. B. Stetson, R. C. Kennicutt, J. R. Mould, S. M. Hughes,

L. Ferrarese, R. Phelps, A. Turner, K. H. Cook, H. Ford, J. G. Hoessel, and J. Huchra, 1997. *ApJ*, **478**, 430.

Kelson, D. D., G. D. Illingworth, J. L. Tonry, W. L. Freedman, R. C. Kennicutt, J. R. Mould, J. A. Graham, J. P. Huchra, L. M. Macri, B. F. Madore, L. Ferrarese, B. K. Gibson, S. Sakai, P. B. Stetson, E. A. Ajhar, J. P. Blakeslee, A. Dressler, H. C. Ford, S. M. G. Hughes, K. M. Sebo, and N. A. Silbermann, 2000. *ApJ*, **529**, 768.

Kenney, J. and R. Koopmann, 1999. *AJ*, **117**, 181.

Kenney, J. and J. S. Young, 1989. *ApJ*, **344**, 171.

Kennicutt, R. C., 1983. *ApJ*, **272**, 54.

Kennicutt, R. C., 1988. *ApJ*, **334**, 144.

Kennicutt, R. C., 1989. *ApJ*, **344**, 685.

Kennicutt, R. C., 1998. *ARA&A*, **36**, 189.

Kennicutt, R. C., B. Balick, and T. Heckman, 1980. *PASP*, **92**, 134.

Kennicutt, R. C. and E. D. Skillman, 2001. *AJ*, **121**, 1461.

Killeen, N. and G. Bicknell, 1988. *ApJ*, **325**, 165.

Kinman, T. D. and K. Davidson, 1981. *ApJ*, **243**, 127.

Knezek, P. M., K. R. Sembach, and J. S. Gallagher, 1999. *ApJ*, **514**, 119.

Kobulnicky, H. A. and E. D. Skillman, 1996. *ApJ*, **471**, 211.

Kobulnicky, H. A. and E. D. Skillman, 1997. *ApJ*, **489**, 636.

Kohoutek, L. and W. Martin, 1981. *A&AS*, **44**, 325.

Koo, D. C. and R. G. Kron, 1992. *ARA&A*, **30**, 613.

Koopmann, R. and J. D. P. Kenney, 1998. *ApJ*, **497**, 75.

Kormendy, J., 1985. *ApJ*, **295**, 73.

Kotanyi, C., J. H. van Gorkom, and R. D. Ekers, 1983. *ApJ*, **273**, L7.

Krawchuk, C. A. P., M. L. McCall, M. Komljenovic, R. Kingsburgh, M. G. Richer, and C. Stevenson, 1997. SNAP: Spreadsheet nebular analysis package. In H. J. Habing and H. J. G. L. M. Lamers (Eds.), *Planetary Nebulae*, IAU Symposium 180, pp. 116. Dordrecht: Kluwer Academic Publishers.

Krüger, H. and U. F. v. Alvensleben, 1994. *A&A*, **284**, 793.

Krüger, H., U. F. v. Alvensleben, H.-H. Loose, and K. J. Fricke, 1991. *A&A*, **242**, 343.

Kuijken, K. and G. Gilmore, 1989a. *MNRAS*, **239**, 571.

Kuijken, K. and G. Gilmore, 1989b. *MNRAS*, **239**, 605.

Kulkarni, S. R. and C. Heiles, 1987. The Atomic Component. In D. J. Hollenbach and H. A. Thronson (Eds.), *Interstellar Processes*, pp. 87. Dordrecht: Reidel.

Kumar, C. K. and N. Thonnard, 1983. *AJ*, **88**, 260.

Kunth, D. and G. Östlin, 2000. *A&A Rv*, **10**, 1.

Larsen, T. I., J. Sommer-Larsen, and B. E. J. Pagel, 2001. *MNRAS*, **323**, 555.

Larson, R. B. and B. M. Tinsley, 1978. *ApJ*, **219**, 46.

Lee, H., M. G. Richer, and M. L. McCall, 2000. *ApJ*, **530**, L17.

Lee, M. G., W. L. Freedman, and B. F. Madore, 1993. *ApJ*, **417**, 553.

Lee, M. G., E. Kim, and D. Geisler, 1997. *AJ*, **114**, 1824.

Lee, M. G. and B. F. Madore, 1993. *AJ*, **106**, 66.

Lefévre, O., D. Crampton, P. Felenbock, and G. Monnet, 1994. *A&A*, **282**, 325.

Legrand, F., 2001. *A&A*, **354**, 504.

Legrand, F., D. Kunth, J.-R. Roy, J. M. Mas-Hesse, and J. R. Walsh, 2000. *A&A*, **355**, 891.

Leitherer, C., D. Alloin, U. F. v. Alvensleben, J. S. Gallagher, J. P. Huchra, F. Matteucci, R. W. O'Connell, J. E. Beckman, G. Bertelli, E. Bica, C. Boisson, C. Bonatto, G. D. Bothun, A. Bressan, J. P. Brodie, G. Bruzual, D. Burstein, R. Buser, N. Caldwell, E. Casuso, M. Cerviño, S. Charlot, M. Chavez, C. Chiosi, C. A. Delisle, A. I. Díaz, M. A. Dopita, B. Dorman, F. Fagotto, M. N. Fanelli, M. Fioc, M. L. García-Vargas, L. Girardi, J. D. Goldader, E. Hardy, T. M. Heckman, J. Iglesias, P. Jablonka, M. Joly, L. Jones, O. Kurth, A. Lançon, T. Lejeune, J. Loxen, A. Maeder, M. L. Malagnini, P. Marigo, J. M. Mas-Hesse, G. Meynet, C. S. Möller, M. L. Mollá, C. Morossi, E. Nasi, J. S. Nichols, K. J. R. Ødegaard, J. W. Parker, M. G. Pastoriza, R. Peletier, C. Robert, B. Rocca-Volmerange, D. Schaerer, A. Schmidt, H. R. Schmitt, R. A. Schommer, W. Schmutz, M. S. Roos, L. Silva, G. Stasińska, R. S. Sutherland, R. Tantalo, P. Traat, A. Vallenari, A. Vazdekis, N. R. Walborn, G. Worthey, and C.-C. Wu, 1996. *PASP*, **108**, 996.

Leitherer, C., D. Schaerer, J. D. Goldader, R. M. G. Delgado, C. Robert, D. F. Kune, D. F. de Mello, D. Devost, and T. M. Heckman, 1999. *ApJS*, **123**, 3.

Lejeune, T., F. Cuisinier, and R. Buser, 1997. *A&AS*, **125**, 229.

Lennon, D. J. and V. M. Burke, 1994. *A&AS*, **103**, 273.

Lequeux, J., M. Peimbert, J. F. Rayo, A. Serrano, and S. Torres-Peimbert, 1979. *A&A*, **80**, 155.

Lilly, S. J., O. LeFévre, F. Hammer, and D. Crampton, 1996. *ApJ*, **460**, L1.

Lin, D. N. C. and S. M. Faber, 1983. *ApJ*, **266**, L21.

Lisenfeld, U. and A. Ferrara, 1998. *ApJ*, **496**, 145.

Lo, K. Y., W. L. W. Sargent, and K. Young, 1993. *AJ*, **106**, 507.

Longair, M. S., 1998. *Galaxy Formation.* Berlin: Springer.

López-Cruz, O., K. C. Y. H, J. P. Brown, C. Jones, and W. Forman, 1997. *ApJ*, **475**, L97.

Low, M. M. and A. Ferrara, 1999. *ApJ*, **513**, 142.

Lynds, R., E. Tolstoy, E. J. O'Neil, and D. A. Hunter, 1998. *AJ*, **116**, 146.

Madore, B. F. and W. L. Freedman, 1991. *PASP*, **103**, 933.

Madore, B. F., W. L. Freedman, N. A. Silbermann, P. Harding, J. Huchra, J. R. Mould, L. Ferrarese, B. Gibson, M. Han, J. Hoessel, S. Hughes, G. D. Illingworth, R. Phelps, S. Sakai, and P. B. Stetson, 1999. *ApJ*, **515**, 29.

Marlowe, A. T., G. R. Meurer, and T. M. Heckman, 1999. *ApJ*, **522**, 183.

Marlowe, A. T., G. R. Meurer, T. M. Heckman, and R. Schommer, 1997. *ApJS*, **112**, 285.

Martin, C. L., 1996. *ApJ*, **465**, 680.

Marzke, R. O. and L. N. D. Costa, 1997. *AJ*, **113**, 185.

Masegosa, J., M. Moles, and A. del Olmo, 1991. *A&A*, **249**, 505.

Massey, P., 1992. *A User's Guide to CCD Reductions with IRAF.* IRAF Project, National Optical Astronomy Observatory.

Massey, P., J. DeVeny, B. Jannuzi, and E. Carder, 1996. *Low-to-Moderate Resolution Optical Spectroscopy Manual for Kitt Peak.* KPNO, National Optical Astronomy Observatory.

Massey, P., K. E. Johnson, and K. DeGioia-Eastwood, 1995. *ApJ*, **454**, 151.

Massey, P., C. C. Lang, K. DeGioia-Eastwood, and C. D. Garmany, 1995. *ApJ*, **438**, 188.

Massey, P., K. Strobel, J. V. Barnes, and E. Anderson, 1988. *ApJ*, **328**, 315.

Massey, P., F. Valdes, and J. Barnes, 1992. *A User's Guide to Reducing Slit Spectra with IRAF.* IRAF Project, National Optical Astronomy Observatory.

Mateo, M., 1998. *ARA&A*, **36**, 435.

Matteucci, F. and C. Chiosi, 1983. *MNRAS*, **123**, 121.

McCall, M. L., 1984. *MNRAS*, **208**, 253.

McCall, M. L., P. M. Rybski, and G. A. Shields, 1985. *ApJS*, **57**, 1.

McGaugh, S. S., 1991. *ApJ*, **380**, 140.

McGaugh, S. S., 1994. *ApJ*, **426**, 135.

McGaugh, S. S. and G. Bothun, 1994. *AJ*, **107**, 530.

McLaughlin, B. M. and K. L. Bell, 1993. *ApJ*, **408**, 753.

McNamara, B. R., R. Sancisi, P. A. Henning, and W. Junor, 1994. *AJ*, **108**, 844.

Méndez, R. H., M. A. Guerrero, K. C. Freeman, M. Arnaboldi, R. P. Kudritzki, U. Hopp, M. Capaccioli, and H. Ford, 1997. *ApJ*, **491**, L23.

Merritt, D., 1984. *ApJ*, **276**, 26.

Meurer, G. R., 1998. Starbursts, dark matter, and the evolution of dwarf galaxies. In T. X. Thuan, C. Balkowski, V. Cayatte, and J. T. T. Van (Eds.), *Dwarf*

Galaxies and Cosmology: proceedings of the XXXIIIrd Rencontres de Moriond, Moriond Astrophysics Meeting. Paris: Editions Frontiéres.

Meurer, G. R., L. Staveley-Smith, and N. E. B. Killeen, 1998. *MNRAS*, **300**, 705.

Miller, B. W., 1996. *AJ*, **112**, 991.

Miller, B. W. and P. Hodge, 1996. *ApJ*, **458**, 467.

Minniti, D. and A. A. Zijlstra, 1997. *AJ*, **114**, 147.

Minniti, D., A. A. Zijlstra, and M. V. Alonso, 1999. *AJ*, **117**, 881.

Moore, B., N. Katz, G. Lake, A. Dreesler, and A. Oemler, 1996. *Nature*, **379**, 613.

Mori, M. and A. Burkert, 2000. *ApJ*, **538**, 559.

Murakami, I. and A. Babul, 1999. *MNRAS*, **309**, 161.

Musella, I., G. Piotto, and M. Capaccioli, 1997. *AJ*, **114**, 976.

Mushotzky, R. F. and M. Loewenstein, 1997. *ApJ*, **481**, L63.

Naab, T. and A. Burkert, 2001. Formation of ellipticals by unequal mass mergers. In J. G. Funes and E. M. Corsini (Eds.), *Galaxy Disks and Disk Galaxies*, Volume 230 of *A.S.P. Conference Series*, pp. 453. San Francisco: Astron. Soc. of the Pacific. Also preprint: `astro-ph/0102251`.

Navarro, J. F. and M. Steinmetz, 1997. *ApJ*, **478**, 13.

Okazaki, T., M. Chiba, Y. Kumai, and M. Fujimoto, 1993. *PASJ*, **45**, 669.

Oke, J. B., 1990. *AJ*, **99**, 1621.

O'Neil, K., G. D. Bothun, and C. D. Impey, 1999. *AJ*, **118**, 1618 (erratum: 2000, *AJ*, **119**, 984).

Osterbrock, D. E., 1989. *Astrophysics of Gaseous Nebulae and Active Galactic Nuclei*. Mill Valley: University Science Books.

Östlin, G., 2000. *ApJ*, **535**, L99.

Pagel, B. E. J., 1986. *Highlights in Astronomy*, **7**, 551.

Pagel, B. E. J., 1997. *Nucleosynthesis and the Chemical Evolution of Galaxies.* Cambridge: Cambridge University Press.

Pagel, B. E. J. and M. G. Edmunds, 1981. *ARA&A*, **19**, 77.

Pagel, B. E. J., M. G. Edmunds, D. E. Blackwell, M. S. Chun, and G. Smith, 1979. *MNRAS*, **189**, 95.

Pagel, B. E. J., M. G. Edmunds, R. A. E. Fosbury, and B. L. Webster, 1978. *MNRAS*, **184**, 569.

Pagel, B. E. J., M. G. Edmunds, and G. Smith, 1980. *MNRAS*, **193**, 219.

Pagel, B. E. J. and B. E. Patchett, 1975. *MNRAS*, **172**, 13.

Panagia, N., 1999. Distance to SN 1987A and the LMC. In Y. H. Chu, N. Suntzeff, J. Hesser, and D. Bohlender (Eds.), *New Views of the Magellanic Clouds*, IAU Symposium 190, pp. 549. San Francisco: Astron. Soc. of the Pacific.

Papaderos, P., H.-H. Loose, K. J. Fricke, and T. X. Thuan, 1996. *A&A*, **314**, 59.

Patterson, R. J. and T. X. Thuan, 1992. *ApJ*, **400**, L55.

Patterson, R. J. and T. X. Thuan, 1996. *ApJS*, **107**, 103 (erratum: 1998, *ApJS*, **117**, 633).

Peebles, P. J. E., 1993. *Principles of Physical Cosmology.* Princeton: Princeton University Press.

Peimbert, M. and R. Costero, 1969. *Bol. Obs. Tonantzintla y Tacubaya*, **5**, 3.

Peimbert, M. and A. Serrano, 1982. *MNRAS*, **198**, 563.

Phillipps, S., Q. A. Parker, J. M. Schwartzenberg, and J. B. Jones, 1998. *ApJ*, **493**, L59.

Phillips, A. C., R. Guzman, J. Gallego, D. C. Koo, J. D. Lowenthal, N. P. Vogt, S. M. Faber, and G. D. Illingworth, 1997. *ApJ*, **489**, 543.

Pildis, R. A., J. M. Schombert, and J. A. Eder, 1997. *ApJ*, **481**, 157.

Pradhan, A. K., 1976. *MNRAS*, **177**, 31.

Puche, D., D. Westpfahl, E. Brinks, and J.-R. Roy, 1992. *AJ*, **103**, 1841.

Quirk, W., 1972. *ApJ*, **176**, L9.

Reaves, G., 1956. *AJ*, **61**, 69.

Reaves, G., 1983. *ApJS*, **53**, 375.

Reid, M. J., 1993. *ARA&A*, **31**, 345.

Richer, M. G., A. Bullejos, J. Borissova, M. L. McCall, H. Lee, R. Kurtev, L. Georgiev, R. L. Kingsburgh, R. Ross, and M. Rosado, 2001. *A&A*, **370**, 34.

Richer, M. G. and M. L. McCall, 1992. *AJ*, **103**, 54.

Richer, M. G. and M. L. McCall, 1995. *ApJ*, **445**, 642.

Richer, M. G., M. L. McCall, and G. Stasińska, 1998. *A&A*, **340**, 67.

Roberts, M. S., 1975. Radio Observations of Neutral Hydrogen in Galaxies. In A. Sandage, M. Sandage, and J. Kristian (Eds.), *Galaxies and the Universe*, pp. 309. Chicago: University of Chicago Press.

Roberts, M. S. and M. P. Haynes, 1994. *ARA&A*, **32**, 115.

Saha, A., J. G. Hoessel, J. Krist, and G. E. Danielson, 1996. *AJ*, **111**, 197.

Sakai, S., B. F. Madore, and W. L. Freedman, 1996. *ApJ*, **461**, 713.

Sakai, S., B. F. Madore, and W. L. Freedman, 1997. *ApJ*, **480**, 589.

Sakai, S., B. F. Madore, and W. L. Freedman, 1999. *ApJ*, **511**, 671.

Sakai, S., D. Zaritsky, and R. C. Kennicutt, 2000. *AJ*, **119**, 1197.

Salpeter, E. E., 1955. *ApJ*, **121**, 161.

Salzer, J. J., S. Alighieri, F. Matteucci, R. Giovanelli, and M. P. Haynes, 1991. *AJ*, **101**, 1258.

Sancisi, R., N. Thonnard, and R. D. Ekers, 1987. *ApJ*, **315**, L39.

Sandage, A. and B. Binggeli, 1984. *AJ*, **89**, 919.

Sarazin, C. L., 1988. *X-ray Emissions from Clusters of Galaxies*. Cambridge Astrophysics Series. Cambridge: Cambridge University Press.

Scalo, J. M., 1986. *Fund. Cosmic Phys.*, **11**, 1.

Schindler, S., B. Binggeli, and H. Böhringer, 1999. *A&A*, **343**, 420.

Schmidt, K.-H. and T. Boller, 1995. *Astron. Nachr.*, **2**, 69.

Schmidt, M., 1959. *ApJ*, **129**, 243.

Schombert, J., S. S. McGaugh, and J. A. Eder, 2001. *AJ*, **121**, 2420.

Schulte-Ladbeck, R. E., 1988. *PASP*, **100**, 785.

Schulte-Ladbeck, R. E. and J. A. Cardelli, 1988. *AJ*, **96**, 458.

Schulte-Ladbeck, R. E., M. M. Crone, and U. Hopp, 1998. *ApJ*, **493**, L23.

Scoville, N. Z. and D. B. Sanders, 1987. H_2 in the Galaxy. In D. J. Hollenbach and H. A. Thronson (Eds.), *Interstellar Processes*, pp. 21. Dordrecht: Reidel.

Searle, L. and W. L. W. Sargent, 1972. *ApJ*, **173**, 25.

Searle, L., W. L. W. Sargent, and W. G. Bagnuolo, 1973. *ApJ*, **179**, 427.

Searle, L. and R. Zinn, 1978. *ApJ*, **228**, 357.

Secker, J., W. E. Harris, and J. D. Plummer, 1997. *PASP*, **109**, 1377.

Shaver, P. A., R. X. McGee, L. M. Newton, A. C. Danks, and S. R. Pottasch, 1983. *MNRAS*, **204**, 53.

Shields, G. A., E. D. Skillman, and R. C. Kennicutt, 1991. *ApJ*, **371**, 82.

Shostak, G. S. and E. D. Skillman, 1989. *A&A*, **214**, 33.

Shu, F. H., 1986. *The Physical Universe: An Introduction to Astronomy.* Mill Valley: University Science Books.

Silk, J., R. F. G. Wyse, and G. A. Shields, 1987. *ApJ*, **322**, L59.

Simpson, J. P., S. W. J. Colgan, R. H. Rubin, E. F. Erickson, and M. R. Haas, 1995. *ApJ*, **444**, 721.

Skillman, E. D., 1985. *ApJ*, **290**, 449.

Skillman, E. D., 1989. *ApJ*, **347**, 883.

Skillman, E. D., 1996. Neutral Hydrogen in Dwarf Galaxies. In E. D. Skillman (Ed.), *The Minnesota Lectures on Extragalactic Neutral Hydrogen*, Volume 106 of *A.S.P. Conference Series*, pp. 208. San Francisco: Astron. Soc. of the Pacific.

Skillman, E. D., 1997. Evidence for and Against Galactic Wind Dominated Evolution of Dwarf Irregular Galaxies. In *1st Guillermo Haro Conference on Astrophysics: Starburst Activity in Galaxies*, Volume 6 of *Revista Méxicana de Astronomía y Astrofísica Serie de Conferencias*, pp. 36.

Skillman, E. D., 1998. Chemical Evolution of the ISM in Nearby Galaxies. In A. Aparicio, A. Herrero, and F. Sánchez (Eds.), *Stellar Astrophysics of the Local Group: VIII Canary Islands Winter School of Astrophysics*, pp. 457. Cambridge: Cambridge University Press.

Skillman, E. D. and R. Bender, 1995. The Dwarf Galaxy Star Formation Crisis. In E. D. Skillman (Ed.), *The Fifth Mexico-Texas Conference on Astrophysics: Gaseous Nebulae and Star Formation*, Volume 3 of *Revista Méxicana de Astronomía y Astrofísica Serie de Conferencias*, pp. 25.

Skillman, E. D., D. J. Bomans, and H. A. Kobulnicky, 1997. *ApJ*, **474**, 205.

Skillman, E. D., G. Bothun, M. Murray, and R. Warmels, 1987. *A&A*, **185**, 61.

Skillman, E. D. and G. D. Bothun, 1986. *A&A*, **165**, 45.

Skillman, E. D. and R. C. Kennicutt, 1993. *ApJ*, **411**, 655.

Skillman, E. D., R. C. Kennicutt, and P. W. Hodge, 1989. *ApJ*, **347**, 875.

Skillman, E. D., R. C. Kennicutt, G. A. Shields, and D. Zaritsky, 1996. *ApJ*, **462**, 147.

Skillman, E. D., J. Melnick, R. Terlevich, and M. Moles, 1988. *A&A*, **196**, 31.

Smartt, S. J. and W. R. J. Rolleston, 1997. *ApJ*, **481**, L47.

Solanes, J. M., A. Manrique, C. García-Gómez, G. González-Casado, R. Giovanelli, and M. P. Haynes, 2001. *ApJ*, **548**, 97.

Stasińska, G., 1990. *A&AS*, **83**, 501.

Stasińska, G., G. Comte, and L. Vigroux, 1986. *A&A*, **154**, 352.

Staveley-Smith, L., R. D. Davies, and T. D. Kinman, 1992. *MNRAS*, **258**, 334.

Stevens, I. R., D. M. Acreman, and T. J. Ponman, 1999. *MNRAS*, **310**, 663.

Stevenson, C. C., M. L. McCall, and D. L. Welch, 1993. *ApJ*, **408**, 460.

Stobie, R. S. and K. Ishida, 1987. *AJ*, **93**, 624.

Storey, P. J. and D. G. Hummer, 1995. *MNRAS*, **272**, 41.

Strickland, D. K., T. J. Ponman, and I. R. Stevens, 1997. *A&A*, **320**, 378.

Strobel, N. V., P. Hodge, and R. C. Kennicutt, 1991. *ApJ*, **383**, 148.

Tacconi, L. J. and J. S. Young, 1987. *ApJ*, **322**, 681.

Takeda, H., P. E. J. Nulsen, and A. C. Fabian, 1984. *MNRAS*, **208**, 261.

Talent, D. L., 1980. *A Spectrophotometric Study of H II Regions in Chemically Young Galaxies.* Ph. D. thesis, Rice University.

Terlevich, R., J. Melnick, J. Masegosa, M. Moles, and M. V. F. Copetti, 1991. *A&AS*, **91**, 285.

Terndrup, D. M., 1988. *AJ*, **96**, 884.

Thuan, T. X., 1985. *ApJ*, **299**, 881.

Thuan, T. X., J. R. Gott, and S. E. Schneider, 1987. *ApJ*, **315**, L93.

Tinsley, B., 1980. *Fundamentals of Cosmic Physics*, **5**, 287.

Tolstoy, E., 2001. Stellar Populations in Dwarf Galaxies: A Review of the Contribution of HST to our Understanding of the Nearby Universe. In M. Livio, K. Noll, and M. Stiavelli (Eds.), *A Decade of HST Science.* Cambridge: Cambridge University Press. Preprint: `astro-ph/0010028`.

Tolstoy, E., J. S. Gallagher, A. A. Cole, J. G. Hoessel, A. Saha, R. C. Dohm-Palmer, E. D. Skillman, M. Mateo, and D. Hurley-Keller, 1998. *AJ*, **116**, 1244.

Tolstoy, E., A. Saha, J. G. Hoessel, and G. E. Danielson, 1995. *AJ*, **109**, 579. (GR 8).

Tolstoy, E., A. Saha, J. G. Hoessel, and K. McQuade, 1995. *AJ*, **110**, 1640. (NGC 2366).

Toomre, A., 1964. *ApJ*, **139**, 1217.

Torres-Peimbert, S., M. Peimbert, and J. Fierro, 1989. *ApJ*, **345**, 186.

Tully, R. B., A. M. Boesgaard, H. M. Dyck, and W. V. Schempp, 1981. *ApJ*, **246**, 38.

Tully, R. B. and E. J. Shaya, 1984. *ApJ*, **281**, 31.

van den Bergh, S., 2000. *PASP*, **112**, 4.

van der Kruit, P. C., 1986. *A&A*, **157**, 230.

van der Kruit, P. C., 1987a. *A&A*, **173**, 59.

van der Kruit, P. C., 1987b. Comparison of the Galaxy with external spiral galaxies. In G. Gilmore and B. Carswell (Eds.), *The Galaxy*, pp. 27. Dordrecht: Reidel.

van Hoerner, S., 1957. *ApJ*, **125**, 451.

van Zee, L., 2001. *AJ*, **121**, 2003.

van Zee, L., M. P. Haynes, and J. J. Salzer, 1997. *AJ*, **114**, 2479.

van Zee, L., J. J. Salzer, and M. P. Haynes, 1998. *ApJ*, **497**, L1 (N/H, O/H).

van Zee, L., E. D. Skillman, and J. J. Salzer, 1998. *AJ*, **116**, 1186 (BCDs).

Veilleux, S., J. Bland-Hawthorn, G. Cecil, R. B. Tully, and S. T. Miller, 1999. *ApJ*, **520**, 111.

Veilleux, S. and D. E. Osterbrock, 1987. *ApJS*, **63**, 295.

Vidal-Madjar, A., D. Kunth, A. L. des Etangs, J. Lequeux, M. André, L. BenJaffel, R. Ferlet, G. Hébrard, J. C. Howk, J. W. Kruk, M. Lemoine, H. W. Moos, K. C. Roth, G. Sonneborn, and D. G. York, 2001. *ApJ*, **538**, L77.

Vigroux, L., T. X. Thuan, J. P. Vader, and M. Lachieze-Rey, 1986. *AJ*, **91**, 70.

Vila-Costas, M. B. and M. G. Edmunds, 1993. *MNRAS*, **265**, 199.

Vílchez, J. M., 1995. *AJ*, **110**, 1090.

Walborn, N. R., 1991. 30 Doradus, Starburst Rosetta. In C. Leitherer, N. R. Walborn, T. M. Heckman, and C. A. Norman (Eds.), *Massive Stars in Starbursts*, Volume 5 of *Space Telescope Science Institute Symposium Series*, pp. 145. Cambridge: Cambridge University Press.

Walsh, J. R., G. Dudziak, D. Minniti, and A. A. Zijlstra, 1997. *ApJ*, **487**, 651.

Warmels, R. H., 1988. *A&AS*, **72**, 427.

Webster, B. L., A. J. Longmore, T. G. Hawarden, and U. Mebold, 1983. *MNRAS*, **205**, 643.

Wells, L. A. and D. J. Bell, 1994. *Cleaning Images of Bad Pixels and Cosmic Rays Using IRAF*. IRAF Project, National Optical Astronomy Observatory.

Wheeler, J. C., C. Sneden, and J. W. Truran, 1989. *ARA&A*, **27**, 279.

White, S. D. M., J. F. Navarro, A. E. Evrard, and C. S. Frenk, 1993. *Nature*, **366**, 429.

Wiese, W. L., J. R. Fuhr, and T. M. Deters, 1996. *Atomic transition probabilities of carbon, nitrogen, and oxygen : a critical data compilation.* American Chemical Society for the National Institute of Standards and Technology (NIST).

Wilcots, E. M. and B. W. Miller, 1998. *AJ*, **116**, 2363.

Williams, R. E., B. Blacker, M. Dickinson, W. V. D. Dixon, H. C. Ferguson, A. S. Fruchter, M. Giavalisco, R. L. Gilliland, I. Heyer, R. Katsanis, Z. Levay, R. A. Lucas, D. B. McElroy, L. Petro, M. Postman, H. Adorf, and R. N. Hook, 1996. *AJ*, **112**, 1335.

Wilson, C. D., D. L. Welch, I. N. Reid, A. Saha, and J. Hoessel, 1996. *AJ*, **111**, 1106.

Wirth, A. and J. S. Gallagher, 1984. *ApJ*, **282**, 85.

Woosley, S. E. and T. A. Weaver, 1986. *ARA&A*, **24**, 205.

Wyse, R. F. G. and J. Silk, 1985. *ApJ*, **296**, L1.

Young, J. S., L. Allen, J. D. P. Kenney, A. Lesser, and B. K. Rownd, 1996. *AJ*, **112**, 1903.

Young, J. S. and N. Z. Scoville, 1991. *ARA&A*, **29**, 581.

Zaritsky, D., R. C. Kennicutt, and J. P. Huchra, 1994. *ApJ*, **420**, 87.